

REPORT DOCUMENTATION PAGE			Form Approved OMB NO. 0704-0188 <sup>1</sup>
<p>Public reporting burden for this collection of information is estimated to average 1 hour per response, including the time for reviewing instructions, searching existing data sources, gathering and maintaining the data needed, and completing and reviewing the collection of information. Send comment regarding this burden estimates or any other aspect of this collection of information, including suggestions for reducing this burden, to Washington Headquarters Services, Directorate for Information Operations and Reports, 1215 Jefferson Davis Highway, Suite 1204, Arlington, VA 22202-4302, and to the Office of Management and Budget, Paperwork Reduction Project (0704-0188), Washington, DC 20503.</p>			
1. AGENCY USE ONLY (Leave blank)	2. REPORT DATE 1/21/98	3. REPORT TYPE AND DATES COVERED 05/01/92 - 09/30/96 Final Report	
4. TITLE AND SUBTITLE  Numerical Investigation of Transitional and Turbulent Axisymmetric Wakes at Supersonic Speeds		5. FUNDING NUMBERS DAAL03-92-G-0228	
6. AUTHOR(S)  Dr. Hermann Fasel and Dietmar Tourbier			
7. PERFORMING ORGANIZATION NAMES(S) AND ADDRESS(ES)  Department of Aerospace and Mechanical Engineering The College of Engineering and Mines The University of Arizona Tucson, AZ 85721		8. PERFORMING ORGANIZATION REPORT NUMBER	
9. SPONSORING / MONITORING AGENCY NAME(S) AND ADDRESS(ES)  U.S. Army Research Office P.O. Box 12211 Research Triangle Park, NC 27709-2211		10. SPONSORING / MONITORING AGENCY REPORT NUMBER  ARO 30113.2-EG	
11. SUPPLEMENTARY NOTES  The views, opinions and/or findings contained in this report are those of the author(s) and should not be construed as an official Department of the Army position, policy or decision, unless so designated by other documentation.			
12a. DISTRIBUTION / AVAILABILITY STATEMENT  Approved for public release; distribution unlimited.		12 b. DISTRIBUTION CODE	
13. ABSTRACT (Maximum 200 words)  A numerical method has been developed for solving the complete compressible Navier-Stokes equations. The method was used to investigate the time dependent behavior of disturbances in the laminar and turbulent near wake of axisymmetric bluff bodies and their influence on and interaction with the global flow field. The equations are solved in a cylindrical coordinate system using finite difference approximations of fourth-order accuracy in space and time. Direct Numerical Simulations (DNS) were performed for a subsonic free stream Mach number of $M_\infty = 0.2$ and for supersonic free stream Mach numbers of $M_\infty = 1.2$ and $M_\infty = 2.46$ . Large-Eddy Simulations (LES) were carried out for a subsonic free stream Mach number of $M_\infty = 0.2$ and a global Reynolds number of $Re_D = 2,000$ and for a supersonic free stream Mach number of $M_\infty = 2.46$ and global Reynolds numbers of $Re_D = 30,000$ and $Re_D = 100,000$ . An absolute instability with regard to helical disturbances was found for the subsonic flow at $Re_D = 1,000$ and for the supersonic flows for $M_\infty = 1.2$ at $Re_D = 4,000$ and for $M_\infty = 2.46$ at $Re_D = 30,000$ . Small disturbances appear in the flow field near the corner of the base. As the disturbances are propagating downstream they grow and form intense vortical structures. These structures have a strong influence on the flow field, which results in a drastic change of the base pressure distribution and thus of the base drag.			
14. SUBJECT TERMS			15. NUMBER OF PAGES 140
			16. PRICE CODE
17. SECURITY CLASSIFICATION OR REPORT UNCLASSIFIED	18. SECURITY CLASSIFICATION OF THIS PAGE UNCLASSIFIED	19. SECURITY CLASSIFICATION OF ABSTRACT UNCLASSIFIED	20. LIMITATION OF ABSTRACT UL

Final Technical Report  
for  
Research Grant DAAL03-92-G-0228

**Numerical Investigation of Transitional and  
Turbulent Axisymmetric Wakes at  
Supersonic Speeds**

by

Hermann F. Fasel and Dietmar Tourbier

Department of Aerospace and Mechanical Engineering  
The University of Arizona  
Tucson, AZ 85721

Submitted to

Dr. Thomas L. Doligalski, Chief

Fluid Dynamics Branch  
Engineering Sciences Division  
U.S. Army Research Office

19980519 128

# Contents

<b>1</b>	<b>Introduction</b>	<b>3</b>
1.1	Technical Background . . . . .	4
1.1.1	Investigations of the Time-Averaged Flow Field . . . . .	4
1.1.2	Investigations of the Time-Dependent Flow Field . . . . .	8
1.2	Present Research . . . . .	9
<b>2</b>	<b>Governing Equations, Initial and Boundary Conditions</b>	<b>11</b>
2.1	Nondimensionalization . . . . .	12
2.2	Axisymmetric Calculations . . . . .	12
2.2.1	Equations . . . . .	12
2.2.2	Integration Domain . . . . .	14
2.2.3	Boundary Conditions . . . . .	14
2.3	Three-dimensional Calculations . . . . .	15
2.3.1	Equations . . . . .	15
2.3.2	Integration Domain . . . . .	17
2.3.3	Boundary Conditions . . . . .	17
2.4	Large-Eddy Simulations . . . . .	18
2.4.1	Spatially Filtered Three-Dimensional Equations for LES . . . . .	18
2.4.2	Spatial Filtering . . . . .	19
2.4.3	The Continuity Equation . . . . .	20
2.4.4	The Momentum Equations . . . . .	20
2.4.5	The Energy Equation . . . . .	21
2.4.6	Equation of State . . . . .	24
2.4.7	Subgrid-Scale Model . . . . .	24
2.4.8	Resolved Scale Equations . . . . .	25
2.4.9	Integration Domain and Boundary Conditions . . . . .	28
<b>3</b>	<b>Numerical Method</b>	<b>29</b>
3.1	Discretization of the Governing Equations . . . . .	29
3.1.1	Fourier Decomposition . . . . .	29
3.1.2	Spatial Derivatives . . . . .	30

3.2 Grid Stretching . . . . .	31
3.2.1 Axial Direction . . . . .	31
3.2.2 Radial Direction . . . . .	32
3.3 Discretized Equations . . . . .	33
3.4 Integration Domain . . . . .	35
3.5 Discretized Boundary Conditions . . . . .	35
3.5.1 Axisymmetric Boundary Conditions . . . . .	36
3.5.2 Three Dimensional Boundary Conditions . . . . .	38
3.6 Filtering . . . . .	40
3.7 Disturbance Generation . . . . .	41
3.7.1 Continuous Disturbances . . . . .	42
3.7.2 Pulse Disturbances . . . . .	43
3.8 Computational Procedure . . . . .	43
<b>4 Code Validation</b>	<b>45</b>
4.1 Axisymmetric Flow . . . . .	45
4.1.1 Subsonic Flow Fields . . . . .	45
4.1.2 Supersonic Flow Fields . . . . .	49
4.2 Three-dimensional Flow . . . . .	54
4.2.1 Absolute Instability . . . . .	54
4.2.2 Periodic Disturbances . . . . .	59
4.3 Large-Eddy Simulation . . . . .	66
<b>5 Results</b>	<b>70</b>
5.1 Direct Numerical Simulations . . . . .	70
5.1.1 Subsonic Flow . . . . .	70
5.1.2 Supersonic Flow at Mach 1.2 . . . . .	80
5.1.3 Supersonic Flow at Mach 2.46 . . . . .	93
5.2 Large-Eddy Simulations . . . . .	114
<b>6 Conclusions</b>	<b>125</b>
<b>A TABLES OF PARAMETERS</b>	<b>127</b>
<b>B FREE STREAM BOUNDARY CONDITIONS</b>	<b>130</b>
B.1 Subsonic Boundary Conditions . . . . .	130
B.2 Characteristic Boundary Conditions . . . . .	130
B.3 Thompson Boundary Conditions . . . . .	131
<b>C BOUNDARY CONDITIONS AT THE AXIS OF SYMMETRY</b>	<b>132</b>

# List of Figures

1.1	Total drag and base drag for axisymmetric bluff bodies with a blunt base in free flight experiments [from Rollstin (1987)]. . . . .	3
1.2	Schematic of the flow field of the near wake of axisymmetric bluff bodies with a blunt base aligned with a supersonic free stream [from Herrin & Dutton (1994c)]. . . . .	4
1.3	Region of interest. . . . .	10
2.1	Integration domain for the axisymmetric equations. . . . .	14
2.2	Integration domain for the three-dimensional equations. . . . .	17
3.1	Example for grid stretching. . . . .	32
3.2	Integration domain for the discretized equations . . . . .	36
3.3	Continuous disturbance; time signal (left) and Fourier transform (right). . . . .	41
3.4	Single pulse disturbance over three periods; time signal (left) and Fourier transform (right). . . . .	42
3.5	Single pulse disturbance over one period; time signal (left) and Fourier transform (right). . . . .	42
3.6	Spike disturbance; time signal (left) and Fourier transform (right). . . . .	43
3.7	Disturbance generation through a blowing and suction slot. . . . .	44
4.1	Steady streamlines for validation case A1. . . . .	46
4.2	Steady streamlines for validation case A2. . . . .	46
4.3	Steady azimuthal vorticity field for validation case A1. . . . .	47
4.4	Steady azimuthal vorticity field for validation case A2. . . . .	48
4.5	Spatial growth rate $\alpha_i$ for an axisymmetric disturbance of $\beta_r = 1.0$ , $\beta_i = 0.0$ ; $Re_D = 1,000$ [circles from Linear Stability Theory by Schwarz (1996)]. . . . .	50
4.6	Isolines of axial velocity at $M_\infty = 2.46$ and $Re_D = 30,000$ for two different spatial resolutions [Cases A4 (top) and A5 (below)]. . . . .	50
4.7	Isolines of radial velocity at $M_\infty = 2.46$ and $Re_D = 30,000$ for two different spatial resolutions [Cases A4 (top) and A5 (below)]. . . . .	51
4.8	Isolines of density at $M_\infty = 2.46$ and $Re_D = 30,000$ for two different spatial resolutions [Cases A4 (top) and A5 (below)]. . . . .	51

4.9 Isolines of pressure at $M_\infty = 2.46$ and $Re_D = 30,000$ for two different spatial resolutions [Cases A4 (top) and A5 (below)]. . . . .	52
4.10 Isolines of temperature at $M_\infty = 2.46$ and $Re_D = 30,000$ for two different spatial resolutions [Cases A4 (top) and A5 (below)]. . . . .	52
4.11 Isolines of local Mach number at $M_\infty = 2.46$ and $Re_D = 30,000$ for two different spatial resolutions [Cases A4 (top) and A5 (below)]. . . . .	53
4.12 Time response of radial momentum at $r=0$ to a three dimensional blowing and suction pulse disturbance in the near wake at $M_\infty = 0.2$ and $Re_D = 1,000$ . . . . .	55
4.13 Time response of radial momentum to a single pulse of Fourier mode $k = 1$ at $r=0.25$ and $z= 0.25$ at $M_\infty = 0.2$ and $Re_D = 1,000$ . . . . .	56
4.14 Flow visualization via particles at $M_\infty = 0.2$ and $Re_D = 1,000$ , viewed from $\theta = \pi/2$ (top) and from $\theta = 0$ (bottom). . . . .	57
4.15 Flow visualization via particles at $M_\infty = 0.2$ and $Re_D = 1,000$ , cross-sectional cut at $x = 2.0$ . . . . .	58
4.16 Flow visualization via particles for $Re_D = 1,000$ , cross-sectional cut at $x = 2.0$ (water channel experiment by Siegel (1994)). . . . .	58
4.17 Time response of total vorticity to a periodic disturbance of Fourier mode $k = 1$ with $St_D = 0.159$ and $A = 0.1$ at $M_\infty = 0.2$ and $Re_D = 1,000$ ( $x = 0.25$ , $r = 0.25$ ). . . . .	59
4.18 Isolines of the mean of axial velocity for three different spatial resolutions for $M_\infty = 0.2$ and $Re_D = 1,000$ [cases T3 (top) through T5 (bottom)]. . . . .	60
4.19 Isolines of the fundamental of first azimuthal mode of axial velocity for three different spatial resolutions for $M_\infty = 0.2$ and $Re_D = 1,000$ [cases T3 (top) through T5 (bottom)]. . . . .	61
4.20 Isolines of the fundamental of first azimuthal mode of radial velocity for three different spatial resolutions for $M_\infty = 0.2$ and $Re_D = 1,000$ [cases T3 (top) through T5 (bottom)]. . . . .	62
4.21 Isolines of the fundamental of first azimuthal mode of azimuthal velocity for three different spatial resolutions for $M_\infty = 0.2$ and $Re_D = 1,000$ [cases T3 (top) through T5 (bottom)]. . . . .	63
4.22 Mean flow profiles for $M_\infty = 0.2$ and $Re_D = 1,000$ at $x = 3.5$ . . . . .	63
4.23 Normalized amplitude distribution of fundamental disturbance frequency for $M_\infty = 0.2$ and $Re_D = 1,000$ at $x = 3.5$ . . . . .	64
4.24 Normalized amplitude distribution of first higher harmonic of disturbance frequency for $M_\infty = 0.2$ and $Re_D = 1,000$ at $x = 3.5$ . . . . .	64
4.25 Normalized amplitude distribution of second higher harmonic of disturbance frequency for $M_\infty = 0.2$ and $Re_D = 1,000$ at $x = 3.5$ . . . . .	65
4.26 Initial time response of total azimuthal vorticity to a single pulse disturbance of Fourier mode $k = 1$ at $r=0.25$ and $z= 0.25$ . . . . .	66
4.27 Time response of total azimuthal vorticity to a single pulse disturbance of Fourier mode $k = 1$ at $r=0.25$ and $z= 0.25$ . . . . .	67

4.28 Isolines of total vorticity at $M_\infty = 0.2$ and $Re_D = 2,000$ at $\theta = 0$ (top) and $\theta = \pi/2$ (bottom). . . . .	68
4.29 Flow visualization using particles for $M_\infty = 0.2$ and $Re_D = 2,000$ ; simulation (top) and water channel experiment by Siegel (1994) (bottom). . . . .	69
5.1 Isolines of axial velocity for $M_\infty = 0.2$ and $Re_D = 1,000$ (axisymmetric unforced calculation). . . . .	71
5.2 Isolines of radial velocity for $M_\infty = 0.2$ and $Re_D = 1,000$ (axisymmetric unforced calculation). . . . .	71
5.3 Isolines of pressure for $M_\infty = 0.2$ and $Re_D = 1,000$ (axisymmetric unforced calculation). . . . .	71
5.4 Isolines of density for $M_\infty = 0.2$ and $Re_D = 1,000$ (axisymmetric unforced calculation). . . . .	72
5.5 Isolines of temperature for $M_\infty = 0.2$ and $Re_D = 1,000$ (axisymmetric unforced calculation). . . . .	72
5.6 Instantaneous total vorticity for $Re_D = 1,000$ and $M_\infty = 0.2$ . x-z plane (top) and x-y plane (bottom). . . . .	73
5.7 Instantaneous total vorticity for $Re_D = 1,000$ and $M_\infty = 0.2$ , y-z planes at $x = 1$ (top left), $x = 2$ (top right), $x = 3$ (bottom left), and $x = 4$ (bottom right). . . . .	74
5.8 Isosurfaces of instantaneous total vorticity ( $ \omega  = 3.0$ ) for $M_\infty = 0.2$ , $Re_D = 1,000$ . . . . .	75
5.9 Isosurfaces of instantaneous axial vorticity ( $ \omega_x  = 1.0$ ) for $M_\infty = 0.2$ , $Re_D = 1,000$ . . . . .	75
5.10 Isosurfaces of instantaneous azimuthal vorticity ( $ \omega_\theta  = 3.0$ ) for $M_\infty = 0.2$ , $Re_D = 1,000$ . . . . .	76
5.11 Isosurfaces of instantaneous pressure deviation from the time-averaged mean flow ( $\Delta p = -0.02$ ) for $M_\infty = 0.2$ , $Re_D = 1,000$ . . . . .	76
5.12 Isolines of axial velocity for the time-averaged flow of $M_\infty = 0.2$ and $Re_D = 1,000$ . . . . .	77
5.13 Isolines of radial velocity for the time-averaged flow of $M_\infty = 0.2$ and $Re_D = 1,000$ . . . . .	77
5.14 Isolines of pressure for the time-averaged flow of $M_\infty = 0.2$ and $Re_D = 1,000$ . . . . .	77
5.15 Isolines of density for the time-averaged flow of $M_\infty = 0.2$ and $Re_D = 1,000$ . . . . .	77
5.16 Isolines of temperature for the time-averaged flow of $M_\infty = 0.2$ and $Re_D = 1,000$ . . . . .	77
5.17 Isolines of azimuthal vorticity for the time-averaged flow of $M_\infty = 0.2$ and $Re_D = 1,000$ . . . . .	78
5.18 Streamlines for the time-averaged flow of $M_\infty = 0.2$ and $Re_D = 1,000$ . . . . .	78
5.19 Base pressure distributions for $M_\infty = 0.2$ and $Re_D = 1,000$ . . . . .	79
5.20 Isolines of axial velocity for $M_\infty = 1.2$ and $Re_D = 4,000$ (axisymmetric steady calculation). . . . .	80
5.21 Isolines of radial velocity for $M_\infty = 1.2$ and $Re_D = 4,000$ (axisymmetric steady calculation). . . . .	80
5.22 Steady streamlines for $M_\infty = 1.2$ and $Re_D = 4,000$ (axisymmetric steady calculation). . . . .	81

5.23 Isolines of pressure for $M_\infty = 1.2$ and $Re_D = 4,000$ (axisymmetric steady calculation) . . . . .	81
5.24 Isolines of density for $M_\infty = 1.2$ and $Re_D = 4,000$ (axisymmetric steady calculation) . . . . .	82
5.25 Isolines of temperature for $M_\infty = 1.2$ and $Re_D = 4,000$ (axisymmetric steady calculation) . . . . .	82
5.26 Isolines of azimuthal vorticity field for $M_\infty = 1.2$ and $Re_D = 4,000$ (axisymmetric steady calculation) . . . . .	82
5.27 Time response of radial momentum to a single pulse of Fourier mode $k = 1$ at $r = 0.25$ and $x = 0.25$ at $M_\infty = 1.2$ and $Re_D = 4,000$ . . . . .	83
5.28 Time response of radial momentum to a single pulse of Fourier mode $k = 1$ at $r = 0.25$ and $x = 0.25$ on a logarithmic scale at $M_\infty = 1.2$ and $Re_D = 4,000$ . . . . .	84
5.29 Isolines of instantaneous total vorticity for $Re_D = 4,000$ and $M_\infty = 1.2$ , at $\theta = 0$ (top) and $\theta = \pi/2$ (bottom) at $t = 121.34$ . . . . .	84
5.30 Isolines of instantaneous total vorticity for $Re_D = 4,000$ and $M_\infty = 1.2$ , at $\theta = 0$ (top) and $\theta = \pi/2$ (bottom) at $t = 127.84$ . . . . .	85
5.31 Isolines of instantaneous total vorticity for $Re_D = 4,000$ and $M_\infty = 1.2$ , at $\theta = 0$ (top) and $\theta = \pi/2$ (bottom) at $t = 135.09$ . . . . .	86
5.32 Isolines of instantaneous total vorticity for $Re_D = 4,000$ and $M_\infty = 1.2$ , y-z planes at $x = 1$ (top left), $x = 2$ (top right), $x = 3$ (bottom left), and $x = 4$ (bottom right) at $t = 121.34$ . . . . .	87
5.33 Isolines of instantaneous total vorticity for $Re_D = 4,000$ and $M_\infty = 1.2$ , y-z planes at $x = 1$ (top left), $x = 2$ (top right), $x = 3$ (bottom left), and $x = 4$ (bottom right) at $t = 127.84$ . . . . .	88
5.34 Isolines of instantaneous total vorticity for $Re_D = 4,000$ and $M_\infty = 1.2$ , y-z planes at $x = 1$ (top left), $x = 2$ (top right), $x = 3$ (bottom left), and $x = 4$ (bottom right) at $t = 135.09$ . . . . .	89
5.35 Isosurfaces of instantaneous total vorticity ( $ \omega  = 6$ ) for $M_\infty = 1.2$ , $Re_D = 4,000$ at $t = 135.09$ . . . . .	89
5.36 Isosurfaces of instantaneous axial vorticity ( $ \omega_x  = 2$ ) for $M_\infty = 1.2$ , $Re_D = 4,000$ at $t = 135.09$ . . . . .	90
5.37 Isosurfaces of instantaneous azimuthal vorticity ( $ \omega_\theta  = 6$ ) for $M_\infty = 1.2$ , $Re_D = 4,000$ at $t = 135.09$ . . . . .	90
5.38 Isosurfaces of instantaneous pressure deviation from the time-averaged mean flow ( $\Delta p = -0.02$ ) for $M_\infty = 1.2$ , $Re_D = 4,000$ at $t = 135.09$ . . . . .	90
5.39 Flow visualization of instantaneous flow field via particles for $M_\infty = 1.2$ and $Re_D = 4,000$ , viewed from $\theta = \pi/2$ (top) and from $\theta = 0$ (bottom) (particles introduced at $x = 0.025$ , $r = 0.475$ ). . . . .	91

5.40 Flow visualization of instantaneous flow field via particles for $M_\infty = 1.2$ and $Re_D = 4,000$ , sheets of thickness 0.01 at $\theta = 0$ (top) and $\theta = \pi/2$ (bottom), (particles introduced at $x = 0.025, r = 0.475$ ). . . . .	91
5.41 Flow visualization of instantaneous flow field via particles for $M_\infty = 1.2$ and $Re_D = 4,000$ , cross-sectional cuts of thickness 0.01 at $x = 1.0, x = 2.0, x = 3.0$ , and $x = 4.0$ (particles introduced at $x = 0.025, r = 0.475$ ). . . . .	92
5.42 Isolines of pressure for a time-averaged flow at $M_\infty = 1.2$ and $Re_D = 4,000$ . . . . .	92
5.43 Isolines of density for a time-averaged flow at $M_\infty = 1.2$ and $Re_D = 4,000$ . . . . .	93
5.44 Base pressure distributions for $M_\infty = 1.2$ and $Re_D = 4,000$ . . . . .	93
5.45 Steady streamlines for $M_\infty = 2.46$ and $Re_D = 30,000$ (axisymmetric steady calculation). . . . .	94
5.46 Steady azimuthal vorticity field for $M_\infty = 2.46$ and $Re_D = 30,000$ (axisymmetric steady calculation) . . . . .	95
5.47 Time response of radial momentum to a single pulse of Fourier mode $k = 1$ at $r = 0.25$ and $x = 0.25$ for $M_\infty = 2.46$ and $Re_D = 30,000$ (unfiltered DNS). . . . .	96
5.48 Isolines of instantaneous total vorticity for $Re_D = 30,000$ and $M_\infty = 2.46$ , x-z plane (top) and x-y plane (bottom) (unfiltered DNS). . . . .	97
5.49 Isolines of instantaneous total vorticity for $Re_D = 30,000$ and $M_\infty = 2.46$ , y-z planes at $x = 1$ (top left), $x = 2$ (top right), $x = 3$ (bottom left), and $x = 4$ (bottom right) (unfiltered DNS). . . . .	98
5.50 Time signal of radial momentum at $r = 0.25$ and $x = 0.25$ for $M_\infty = 2.46$ and $Re_D = 30,000$ (filtered DNS). . . . .	99
5.51 Isolines of instantaneous total vorticity for $Re_D = 30,000$ and $M_\infty = 2.46$ at $t = 174.35$ , x-z plane (top) and x-y plane (bottom) (filtered DNS). . . . .	100
5.52 Isolines of instantaneous total vorticity for $Re_D = 30,000$ and $M_\infty = 2.46$ at $t = 176.35$ , x-z plane (top) and x-y plane (bottom) (filtered DNS). . . . .	101
5.53 Isolines of instantaneous total vorticity for $Re_D = 30,000$ and $M_\infty = 2.46$ at $t = 178.1$ , x-z plane (top) and x-y plane (bottom) (filtered DNS). . . . .	102
5.54 Isolines of instantaneous total vorticity for $Re_D = 30,000$ and $M_\infty = 2.46$ at $t = 174.35$ , y-z planes at $x = 1$ (top left), $x = 2$ (top right), $x = 3$ (bottom left), and $x = 4$ (bottom right) (filtered DNS). . . . .	103
5.55 Isolines of instantaneous total vorticity for $Re_D = 30,000$ and $M_\infty = 2.46$ at $t = 176.35$ , y-z planes at $x = 1$ (top left), $x = 2$ (top right), $x = 3$ (bottom left), and $x = 4$ (bottom right) (filtered DNS). . . . .	104
5.56 Isolines of instantaneous total vorticity for $Re_D = 30,000$ and $M_\infty = 2.46$ at $t = 178.1$ , y-z planes at $x = 1$ (top left), $x = 2$ (top right), $x = 3$ (bottom left), and $x = 4$ (bottom right) (filtered DNS). . . . .	105
5.57 Isosurfaces of instantaneous total vorticity ( $ \omega  = 7$ ) for $M_\infty = 2.46, Re_D = 30,000$ at $t = 174.35$ (filtered DNS). . . . .	106

5.58 Isosurfaces of instantaneous total vorticity ( $ \omega  = 7$ ) for $M_\infty = 2.46, Re_D = 30,000$ at $t = 176.35$ (filtered DNS). . . . .	106
5.59 Isosurfaces of instantaneous total vorticity ( $ \omega  = 7$ ) for $M_\infty = 2.46, Re_D = 30,000$ at $t = 178.1$ (filtered DNS). . . . .	106
5.60 Isosurfaces of instantaneous azimuthal vorticity ( $ \omega_\theta  = 7$ ) for $M_\infty = 2.46, Re_D = 30,000$ at $t = 174.35$ (filtered DNS). . . . .	107
5.61 Isosurfaces of instantaneous azimuthal vorticity ( $ \omega_\theta  = 7$ ) for $M_\infty = 2.46, Re_D = 30,000$ at $t = 176.35$ (filtered DNS). . . . .	107
5.62 Isosurfaces of instantaneous azimuthal vorticity ( $ \omega_\theta  = 7$ ) for $M_\infty = 2.46, Re_D = 30,000$ at $t = 178.1$ (filtered DNS). . . . .	107
5.63 Isosurfaces of instantaneous axial vorticity ( $ \omega_x  = 4$ ) for $M_\infty = 2.46, Re_D = 30,000$ at $t = 174.35$ (filtered DNS). . . . .	107
5.64 Isosurfaces of instantaneous axial vorticity ( $ \omega_x  = 4$ ) for $M_\infty = 2.46, Re_D = 30,000$ at $t = 176.35$ (filtered DNS). . . . .	108
5.65 Isosurfaces of instantaneous axial vorticity ( $ \omega_x  = 4$ ) for $M_\infty = 2.46, Re_D = 30,000$ at $t = 178.1$ (filtered DNS). . . . .	108
5.66 Isosurfaces of instantaneous pressure deviation from the time-averaged mean flow ( $\Delta p = -0.02$ ) for $M_\infty = 2.46, Re_D = 30,000$ at $t = 174.35$ (filtered DNS). . . . .	108
5.67 Isosurfaces of instantaneous pressure deviation from the time-averaged mean flow ( $\Delta p = -0.02$ ) for $M_\infty = 2.46, Re_D = 30,000$ at $t = 176.35$ (filtered DNS). . . . .	108
5.68 Isosurfaces of instantaneous pressure deviation from the time-averaged mean flow ( $\Delta p = -0.02$ ) for $M_\infty = 2.46, Re_D = 30,000$ at $t = 178.1$ (filtered DNS). . . . .	109
5.69 Flow visualization of instantaneous flow field via particles for $M_\infty = 2.46, Re_D = 30,000$ , viewed from $\theta = \pi/2$ (top) and from $\theta = 0$ (bottom) (particles introduced at $x = 0.025, r = 0.475$ ; filtered DNS). . . . .	110
5.70 Flow visualization of instantaneous flow field via particles for $M_\infty = 2.46, Re_D = 30,000$ , sheets of thickness 0.01 at $\theta = 0$ (top) and $\theta = \pi/2$ (bottom), (particles introduced at $x = 0.025, r = 0.475$ ; filtered DNS). . . . .	111
5.71 Flow visualization of instantaneous flow field via particles for $M_\infty = 2.46, Re_D = 30,000$ , cross-sectional cuts of thickness 0.01 at $x = 1.0, x = 2.0, x = 3.0$ , and $x = 4.0$ (particles introduced at $x = 0.025, r = 0.475$ ; filtered DNS). . . . .	112
5.72 Isolines of pressure for the time-averaged flow at $M_\infty = 2.46$ and $Re_D = 30,000$ . .	112
5.73 Isolines of density for the time-averaged flow at $M_\infty = 2.46$ and $Re_D = 30,000$ . .	113
5.74 Base pressure distributions for $M_\infty = 2.46$ and $Re_D = 30,000$ . . . . .	113
5.75 Isolines of instantaneous total vorticity for $M_\infty = 2.46$ and $Re_D = 30,000$ (LES). .	115
5.76 Isolines of axial velocity for the time-averaged flow field at $M_\infty = 2.46$ and $Re_D = 30,000$ (LES). . . . .	115
5.77 Isolines of radial velocity for the time-averaged flow field at $M_\infty = 2.46$ and $Re_D = 30,000$ (LES). . . . .	116

5.78 Isolines of pressure for the time-averaged flow field at $M_\infty = 2.46$ and $Re_D = 30,000$ (LES) . . . . .	116
5.79 Isolines of density for the time-averaged flow field at $M_\infty = 2.46$ and $Re_D = 30,000$ (LES) . . . . .	116
5.80 Isolines of temperature for the time-averaged flow field at $M_\infty = 2.46$ and $Re_D = 30,000$ (LES) . . . . .	117
5.81 Isolines of local Mach number for the time-averaged flow field at $M_\infty = 2.46$ and $Re_D = 30,000$ (LES) . . . . .	117
5.82 Isolines of azimuthal vorticity for the time-averaged flow field at $M_\infty = 2.46$ and $Re_D = 30,000$ (LES) . . . . .	117
5.83 Isolines of axial turbulence intensity at $M_\infty = 2.46$ and $Re_D = 30,000$ (LES) . . . . .	118
5.84 Isolines of radial turbulence intensity at $M_\infty = 2.46$ and $Re_D = 30,000$ (LES) . . . . .	118
5.85 Isolines of tangential turbulence intensity at $M_\infty = 2.46$ and $Re_D = 30,000$ (LES) . . . . .	119
5.86 Isolines of radial turbulent Reynolds stress at $M_\infty = 2.46$ and $Re_D = 30,000$ (LES) . . . . .	119
5.87 Isolines of turbulent kinetic energy at $M_\infty = 2.46$ and $Re_D = 30,000$ (LES) . . . . .	119
5.88 Isolines of instantaneous total vorticity for $M_\infty = 2.46$ and $Re_D = 100,000$ (LES) . . . . .	120
5.89 Isolines of axial velocity for the time-averaged flow field at $M_\infty = 2.46$ and $Re_D = 100,000$ (LES) . . . . .	121
5.90 Isolines of radial velocity for the time-averaged flow field at $M_\infty = 2.46$ and $Re_D = 100,000$ (LES) . . . . .	121
5.91 Isolines of pressure for the time-averaged flow field at $M_\infty = 2.46$ and $Re_D = 100,000$ (LES) . . . . .	121
5.92 Isolines of density for the time-averaged flow field at $M_\infty = 2.46$ and $Re_D = 100,000$ (LES) . . . . .	122
5.93 Isolines of temperature for the time-averaged flow field at $M_\infty = 2.46$ and $Re_D = 100,000$ (LES) . . . . .	122
5.94 Isolines of local Mach number for the time-averaged flow field at $M_\infty = 2.46$ and $Re_D = 100,000$ (LES) . . . . .	122
5.95 Isolines of vorticity for the time-averaged flow field at $M_\infty = 2.46$ and $Re_D = 100,000$ (LES) . . . . .	123
5.96 Isolines of axial turbulence intensity at $M_\infty = 2.46$ and $Re_D = 100,000$ (LES) . . . . .	123
5.97 Isolines of radial turbulence intensity at $M_\infty = 2.46$ and $Re_D = 100,000$ (LES) . . . . .	123
5.98 Isolines of tangential turbulence intensity at $M_\infty = 2.46$ and $Re_D = 100,000$ (LES) . . . . .	123
5.99 Isolines of radial turbulent Reynolds stress at $M_\infty = 2.46$ and $Re_D = 100,000$ (LES) . . . . .	124
5.100 Isolines of turbulent kinetic energy at $M_\infty = 2.46$ and $Re_D = 100,000$ (LES) . . . . .	124
C.1 Decomposition of the velocity vector within the field . . . . .	132
C.2 Decomposition of the velocity vector at the axis of symmetry . . . . .	133

# List of Tables

A.1 Parameters for axisymmetric calculations. . . . .	127
A.2 Parameters for three-dimensional subsonic DNS calculations. . . . .	128
A.3 Parameters for three-dimensional supersonic DNS calculations. . . . .	129

## Abstract

A numerical method has been developed for solving the complete compressible Navier-Stokes equations. The method is applicable for Direct Numerical Simulations (DNS) and Large-Eddy Simulations (LES) and was used here to study the evolution of three-dimensional disturbances in the laminar and turbulent near wake of axisymmetric bluff bodies with a blunt base in supersonic flows. The main objective of this research is to investigate the time dependent behavior of these disturbances and their influence on and interaction with the global flow field. The equations are solved in a cylindrical coordinate system using finite difference approximations of fourth-order accuracy in axial and radial directions and a fourth-order accurate explicit Runge-Kutta scheme for the time integration. A pseudo-spectral method is employed in the azimuthal direction. Direct Numerical Simulations (DNS) were performed for a subsonic free stream Mach number of  $M_\infty = 0.2$  and for supersonic free stream Mach numbers of  $M_\infty = 1.2$  and  $M_\infty = 2.46$ . Large-Eddy Simulations (LES) were carried out for a subsonic free stream Mach number of  $M_\infty = 0.2$  and a global Reynolds number of  $Re_D = 2,000$  and for a supersonic free stream Mach number of  $M_\infty = 2.46$  and global Reynolds numbers of  $Re_D = 30,000$  and  $Re_D = 100,000$ . Comparison of the instantaneous flow field for subsonic calculations with water channel experiments and incompressible simulations show good qualitative agreement. An absolute instability with regard to helical disturbances was found for the subsonic flow at  $Re_D = 1,000$  and for the supersonic flows for  $M_\infty = 1.2$  and  $Re_D \geq 4,000$  and for  $M_\infty = 2.46$  and  $Re_D \geq 30,000$ . Small disturbances appear in the flow field near the corner of the base. As the disturbances are propagating downstream they grow and form intense vortical structures. These structures have a strong influence on the flow field, which results in a drastic change of the base pressure distribution and thus of the base drag.

**NOMENCLATURE****Roman Symbols**

$a$	speed of sound
$c_p$	specific heat at constant pressure
$C_s$	Smagorinsky constant for Large-Eddy Simulations
$c_v$	specific heat at constant volume
$D$	diameter of the axisymmetric body
$e$	total energy per unit mass
$E_R$	resolved scale total energy
$f$	frequency
$k$	Fourier mode of Fourier decomposition in azimuthal direction
$M$	Mach number
$N$	constant used for energy equation, $N = PeEc$
$p$	pressure
$Pr$	Prandtl number
$r$	coordinate in radial direction
$R$	radius of axisymmetric body
$Re_D$	Reynolds number based on the body diameter ( $Re_D = \frac{U_\infty D}{\nu_\infty}$ )
$R_l$	specific gas constant
$S$	constant for Sutherland's law
$St_D$	Strouhal number $St_D = \frac{fD}{U_\infty}$
$t$	time
$T$	temperature
TKE	turbulent kinetic energy
$v$	velocity component
$x$	coordinate in axial direction

**Greek Symbols**

$\gamma$	adiabatic heat coefficient
$\theta$	coordinate in circumferential direction
$\vartheta$	heat conductivity
$\mu$	viscosity
$\omega$	vorticity
$\rho$	density
$\sigma$	subgrid-scale stress tensor
$\tau$	resolved stress tensor

**Superscripts**

(*)	dimensional quantities
-----	------------------------

$\langle \rangle'$	unfiltered part for spatial filter
$\langle \rangle''$	unfiltered part for Favre filter

**Subscripts**

$\infty$	dimensional quantities evaluated at the free stream
$x, r, \theta$	subscripts indicating the component of a vector or tensor

**Other Symbols**

$\overline{\langle \rangle}$	filtered quantities
$\tilde{\langle \rangle}$	Favre filtered (mass-averaged) quantities
$\langle \rangle^< >$	root-mean-squared quantity (RMS)

# Chapter 1

## Introduction

The aerodynamic drag of bodies of revolution with a blunt base is greatly affected by the low pressure immediately downstream of the base. Especially for the case of supersonic flight, even small changes in the flow behavior of the wake may affect the performance of the entire flight vehicle, e.g., missiles, rockets, or projectiles. Flight tests with projectiles (U.S. Army M549 projectile) have shown that for supersonic free stream Mach numbers the fraction of aerodynamic drag due to the low base pressure can be as high as 35 percent (compare figure 1.1) of the total drag. This suggests that controlling the near-wake flow can have a significant influence on the aerodynamic drag of bluff bodies with a blunt base.

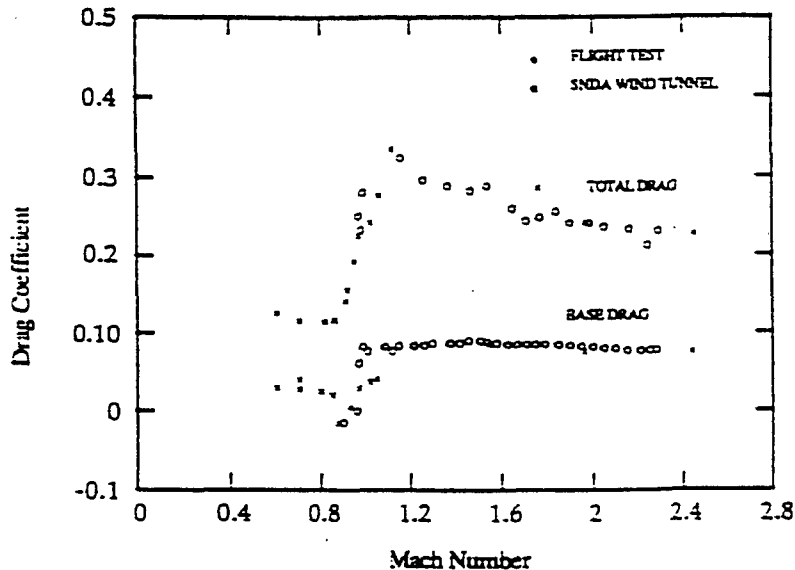


Figure 1.1: Total drag and base drag for axisymmetric bluff bodies with a blunt base in free flight experiments [from Rollstin (1987)].

For this reason, numerous research efforts, experimental, theoretical, and numerical, have focused on investigating the flow field in the near wake of blunt bodies. At the early stages the main issue of these investigations has been the prediction of the base drag for different geometries in order to provide necessary information for the design of new aerodynamic objects

(such as projectiles, rockets, supersonic planes, etc.). In more recent years, several techniques for reducing the base drag have been suggested and investigated, such as boat-tailing, base bleed, base burning, base combustion, etc. [see, for example, Sahu et al.(1985), Nietubicz and Gibeling (1993), Sahu and Heavey (1995), and Mathur and Dutton (1996a,b)]. It has been found, that with all these techniques the base drag can be reduced by a considerable amount.

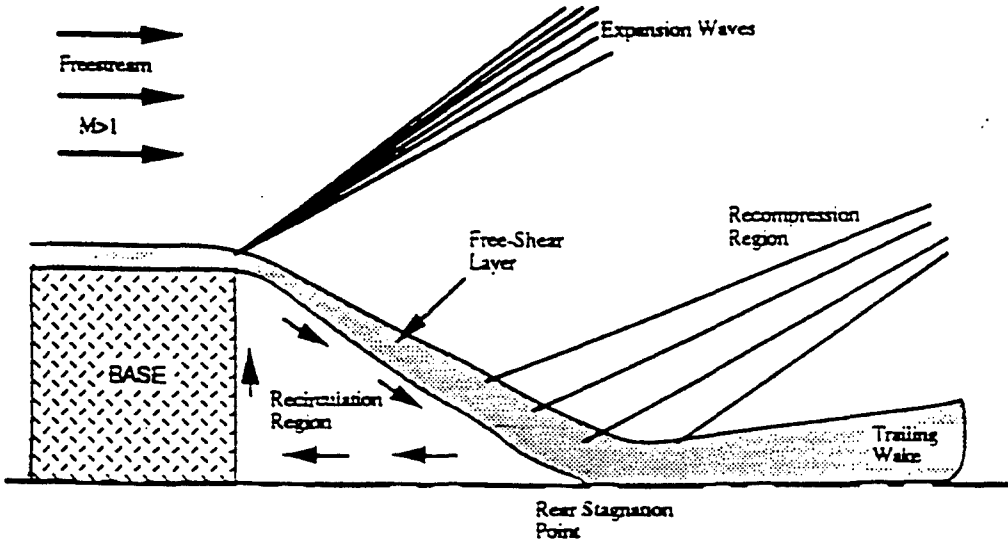


Figure 1.2: Schematic of the flow field of the near wake of axisymmetric bluff bodies with a blunt base aligned with a supersonic free stream [from Herrin & Dutton (1994c)].

A schematic diagram of the time-averaged supersonic flow field of the near wake of an axisymmetric bluff body with a blunt base is shown in figure 1.2. A boundary layer separates at the base corner and forms an axisymmetric shear layer. Outside the subsonic layer, expansion waves occur that cause the free stream to bend towards the axis. Further downstream the free stream is realigned by recompression waves. A region of recirculation, associated with low pressure, is formed immediately downstream of the base. Typically the length of this recirculation region is on the order of one to three base diameters, depending on the global Reynolds number ( $Re_D$ ) and the free stream Mach number ( $M_\infty$ ).

## 1.1 Technical Background

### 1.1.1 Investigations of the Time-Averaged Flow Field

At first, for investigating the fundamental physics of the near-wake behavior experiments were used almost exclusively. However, wind tunnel experiments suffer from the difficulty of properly supporting the (axisymmetric) base model so as not to cause undue effects on the flow field behind the base. [Chapman (1951)] conducted experiments measuring the base pressure behind a backward facing step and a circular cylinder for supersonic flows. He found that the support of the model, which in his case was supported from the rear, in general has a large effect on the base pressure if the sting diameter is larger than 30 percent of the model diameter. Another

experimental study of the effect of rear sting supports on the base pressure was conducted by [Donaldson (1955)]. He observed that the base pressure dropped monotonically with an increasing sting diameter up to 80 percent of the base diameter. Even a support rod with a diameter of 20 percent of the base diameter had a significant effect on the base pressure, in contrast to the findings of [Chapman (1951)].

Because of the problems arising from the rear support of the model, several other methods of support have been investigated in the following years. For example, [Dayman (1963)] investigated the effect of supporting wires on the wakes of spheres and cones. He concluded that any wire capable of supporting the model has a significant effect on the flow field. Thus, the only support that might not significantly influence the wake flow field is from the upstream position of the body, which has been used in most of the experimental research efforts in the following years [see, for example, [Dutton & Addy (1993)], Herrin & Dutton (1991, 1994a-c), and Mathur & Dutton (1995, 1996a,b)]. In addition, local pressure and velocity measurements in supersonic wakes have proven to be very difficult. The pressure along the body can be measured by pressure tabs, but measurements within the flow field are very difficult, because a probe has to be inserted into the flow and thus the flow field is altered. That is the reason why different, nonintruding methods such as laser Doppler velocimetry have been developed. In many recent experimental studies [see, for example, [Avidor & Schneiderman (1975)], [Herrin & Dutton (1991)]] near axisymmetric wakes have been investigated using this method.

In recent years, many experimental investigations also focused on modifying the base flow, in particular the base pressure, using several different techniques such as boat-tailing, base bleed, base burning, and base combustion. Valentine & Przirembel (1970), for example, investigated the effect of base injection on a turbulent axisymmetric wake at Mach 4. The effect of base injection on the base pressure was dependent on the injection technique. They observed an increase in the base pressure ratio of nearly 100 percent. Another way of influencing the base pressure was assessed by [Neale et al.(1978)]. They studied the effect of axisymmetric external compression fields simulating external burning on the base pressure for a cylindrical body in a supersonic flow at Mach 3. Their conclusion was that the base drag could be completely eliminated by external burning. There have been many more research efforts investigating the effects of these techniques to modify the base flow [see, for example, [Cortwright & Schroeder (1951)], [Reid & Hastings (1959)], [Clayden & Bowman (1968)], [Bowman & Clayden (1968)], [Hubbartt et al. (1981)], Ding et al. (1992)]. These experiments have shown that there are potentially considerable rewards for altering the flow field. However, it is still not understood why certain measures are more effective than others and what the optimal parameters should be. The reason for this is that the fundamental physical phenomena that are responsible for the effect of the base flow modifications are not yet understood.

More recently, Dutton and his coworkers started comprehensive experimental investigation of the near wake of an axisymmetric body with a blunt base in a supersonic flow at Mach 2.46 [see, for example, Herrin & Dutton (1991, 1994a-c), and Mathur & Dutton (1995, 1996a,b)]. In their research, they have used pressure taps along the base to measure the base pressure

and spark-schlieren photography and oil-streak visualization to qualitatively assess the flow field. Special emphasis was placed on designing the experimental facilities such that a highly uniform, axisymmetric flow field could be obtained without any interference of the support and the wind tunnel walls on the wake region. It was found that the base pressure is virtually constant along the base. In addition to the base pressure measurements they used Laser Doppler Velocimetry (LDV) to determine the time-averaged flow field and rms values of the turbulent fluctuations. The measurements of turbulent fluctuations in the flow field revealed that the highest turbulence levels occur within the free shear layer that separates the recirculating region from the free stream. Dutton and his co-workers have also investigated the effects of different techniques of drag reduction, including base bleed and boat-tailing. Their results show that all these techniques can significantly lower the base drag. At the same time, all investigated measures of drag reduction also lowered the level of the turbulent fluctuations in the free shear layer. This indicates that there might be a connection between the turbulent energy within the shear layer and the pressure drag of the aerodynamic body.

In the same publication where [Chapman (1951)] discussed his experimental measurements of compressible wakes, he also presented a semi-empirical theory for calculating the flow field of laminar, viscous wake flow. Chapman had concluded that inviscid theory was not sufficient to accurately model this flow field. He was able to predict the base pressure for two dimensional wakes with reasonable accuracy, however, he did not succeed in predicting the base pressure for axisymmetric wakes without rear sting support. Another semi-empirical theory for the prediction of turbulent flows over a two dimensional backward facing step and an axisymmetric body with rear sting support was presented by [Korst (1956)]. However, the theory was also not applicable for bodies without a rear sting. A similar theory was developed by [McDonald (1965)] which also gave fair agreement with experimental results for the base pressure of axisymmetric bodies with a rear support. A newer theory, developed by [Mueller (1968)], was able to calculate the base pressure for axisymmetric bodies without rear support fairly well. But he still had to rely on experimental data to find the recompression location for a given shape, which made it impossible to predict the base pressure for a new geometry. Several theories have been developed later trying to predict the recompression location (e.g. [Addy (1970)]), but they still had to rely on experimental data.

With the development of increasingly powerful supercomputers, numerical simulations of complex flows, such as the axisymmetric wake, have become more and more feasible. The big advantage of numerical simulations is that problems associated with wind tunnel interference, model support, probe intrusion, etc., are not present. In addition to possibly providing further understanding of the relevant physics involved, these calculations were motivated by the considerable challenge that this complicated flow field provides for computational fluid dynamicists. The computational challenge arises mainly from the combination of shock waves, thin free shear layers, boundary layers, and recirculating regions; associated with this are highly disparate length scales and local regions of very high gradients. Reliable and realistic computations can therefore only be performed if the high gradients can be adequately resolved. Furthermore,

supersonic wake flows in almost all practical applications are turbulent, requiring adequate turbulence models. In practically all previous numerical efforts, only the steady flow field was calculated. Those computations were based on the Reynolds-Averaged Navier-Stokes equations (RANS) employing typically algebraic or one- and two-equation turbulence models, such as, for example, the algebraic eddy viscosity model of Baldwin and Lomax, the two-equation  $k - \epsilon$  model, or the  $k - \omega$  model.

Numerous research efforts on calculating turbulent supersonic wake flows have been reported in the literature. The Advisory Group for Aerospace Research and Development (AGARD) formed a group to review methods to predict nozzle afterbody flows in 1982. A summary of the results is given by Putnam & Bissinger (1985). It was concluded that at the time Navier-Stokes simulations were able to predict flow fields accurately up to the point of separation, but then became unreliable. Since then there has been an increased interest in predicting wake flows using numerical techniques. [Sullins et al. (1982)], for example, calculated the turbulent mean flow of a two dimensional compressible wake with and without base injection. For the determination of the turbulent flow they used a zero equation relaxation eddy viscosity model. Comparing the pressure along the centerline of the wake showed fair agreement with experimental results. Unfortunately no comparison for the pressure distribution over the base was provided.

The flow of an axisymmetric afterbody at a free stream Mach number of 1.343 with and without a centered jet at the base was investigated by Sahu & Nietubicz (1984) using a thin layer approximation of the Navier-Stokes equation. They predicted streamlines for the near wake region and also the pressure distribution over the base. They found that the centered jet reduces the base pressure for the case of a high velocity jet. No comparison with experimental data was provided. A detailed verification of Navier-Stokes calculations was done by Nietubicz & Sturek (1988). The results show very good agreement with experiments for most flow parameters including the base drag. The study showed that current Navier-Stokes codes are able to calculate supersonic wake flows and find agreement with experimental observations in terms of certain global features fairly well. However, in all cases certain parameters for the employed turbulence models have to be set according to experimental results. Numerical computations of supersonic base flow with special emphasis on turbulence modeling were presented by [Sahu (1992)]. Comparing the results obtained by a thin layer approximation of the Navier-Stokes equations using two algebraic eddy viscosity models and a two-equation  $k-\epsilon$  model, he found that both algebraic turbulence models predicted an incorrect base pressure, while the  $k-\epsilon$  model showed very good agreement with experimental results. However, the turbulence energy distribution in the wake did not agree with the experimental results of [Herrin & Dutton (1991)].

In spite of the these shortcomings of the RANS calculations, recent applications have attacked increasingly difficult situations. As control of wake flows is now being considered as a means of drag reduction, numerical simulations have been performed to investigate, for example, the effects of base bleed [see, for example, [Sahu et al. (1985)], [Sahu & Heavey (1995)], and [Danberg & Nietubicz (1992)]] and base burning [see, for example, [Nietubicz & Sturek (1988)]]. In all simulations, the results show a correct trend for the drag reduction when compared with

experimental results. However, in some cases, even global flow field characteristics such as the centerline velocity are not in good agreement with experiments. This indicates that there are still important aspects of the physics which are not captured by the used models. Therefore empirically determined constants have to be introduced which need to be adjusted for the given geometry and thus do not allow prediction of flow fields for different geometries.

### 1.1.2 Investigations of the Time-Dependent Flow Field

All investigations mentioned above focused on calculating the time-averaged turbulent mean flow in the near wake of an axisymmetric body. If, however, the supersonic wake flow field is dominated by large structures (like its incompressible counterpart), it is necessary to investigate the time dependent evolution of the flow field. For example, the time dependent behavior of a two dimensional supersonic transitional wake has been investigated by [Chen et al. (1989)] [see also [Chen et al. (1990)]] using temporal Linear Stability Theory (LST) and Direct Numerical Simulations (DNS). In their research they found that the wake is subject to temporal instabilities. Disturbances in the shear layer get amplified and form large structures which dominate the flow field further downstream. Increasing the Mach number has a damping effect on these instabilities. It is as yet unclear if the supersonic axisymmetric wake flow is also subject to instabilities (temporal or spatial, convective or absolute) similar to its incompressible counterpart.

It is well known that for incompressible wakes the dynamics of large (coherent) structures play a dominant role in the local and global behavior of the flow. This evidence was found from both experimental investigations and numerical simulations and was confirmed by theoretical studies. For incompressible flow past bluff bodies, it has been well established that the existence of absolute and global instabilities is responsible for the development of the large structures [see, for example, [Huerre & Monkewitz (1990)]]. Using numerical simulations, absolute and global instabilities were found for a two-dimensional bluff body with a blunt base by [Hannemann & Oertel (1989)] and for an axisymmetric body with a blunt base by [Schwarz (1996)]. The absolutely or globally unstable modes for the axisymmetric case are of a helical nature. For compressible wakes, especially at supersonic speeds, however, relatively little is known about the dynamical behavior of the large structures in turbulent flows or, in particular, if absolute or global instabilities exist. This is true for supersonic flows in general and for axisymmetric wakes in particular.

Due to the lack of guidance from experimental investigations, no successful computational or theoretical attempts have been made in the past to study the unsteady, dynamical behavior of laminar, transitional, or turbulent supersonic axisymmetric wake flows. For the subsonic (incompressible) case, there is considerable evidence that the evolution of the large structures is due to the hydrodynamic instability of the (time-averaged) mean flow and that the development of these structures can be captured by stability theory. Experimental results for incompressible turbulent mixing layers, two-dimensional turbulent wakes, and axisymmetric wakes and comparisons with stability theory have shown that certain key features, such as dominant fre-

quencies, mode shapes (amplitude distributions), and streamwise spacing (wave lengths) of the structures can be well predicted by linear stability theory [see, for example, [Wygnanski (1994)] and [Marasli et al. (1989)]]]. These investigations support the notion that hydrodynamic instabilities give rise to the generation and development of the large structures. The dynamical behavior of these structures is responsible for the strong unsteady flow behavior in the wake. Thus, in reality, there is no steady turbulent wake flow, even when small-scale (high-frequency) fluctuations are not taken into consideration. Rather, the flow is highly unsteady, dominated by large-amplitude and, relative to the small scales, low-frequency fluctuations. Because of the nonlinear interaction between the various fluctuation components, the actual mean flow may be strongly dependent on the composition of the fluctuating parts of the flow field. In addition, it has been shown that, with artificial forcing, existing components (structures) can be modified or new components (structures) created and, as a consequence, that the mean flow can be strongly altered [see, for example, [Wygnanski (1994)] and [Marasli et al. (1989)]].

Due to the difficulties of the experiments, until recently it was unclear if large structures are present in supersonic wake flows or if they play a similarly dominating role. Recent experimental findings indicate that large structures indeed exist for the case of two-dimensional supersonic wakes [see, for example, Smith & Dutton (1968)]. Some quantitative evidence of the existence of dominant large structures in supersonic axisymmetric wake flows has been provided by the experiments of Demetriades (1968), who investigated the unsteady nature of the flow field. The amplitude spectra in his results display distinct peaks at certain (relatively low) frequencies, thus indicating the presence of dominant structures. If large structures are indeed dominating the near wake flow field, it is not surprising that the mean flow fields strongly depend on experimental conditions and, even for the same facility, can vary with minor changes of the experimental parameters. Also, for this reason, it is not surprising that current turbulence models for calculating mean flows using Reynolds-averaged Navier-Stokes formulations are performing poorly for these flows. Time dependent methods like Large-Eddy Simulations (LES) would be more adequate to capture the strongly time dependent behavior of the flow field. Chances to arrive at better turbulence models (for Reynolds-Averaged Navier-Stokes) are rather slim unless the physical and dynamical behavior of the large structures are better understood and this knowledge is implemented in the turbulence modeling.

## 1.2 Present Research

One way to achieve more insight into the dynamical behavior of the supersonic axisymmetric wake flow is to investigate the development of disturbances in laminar, transitional and turbulent flows. By determining the mechanisms that govern the behavior of large disturbances at the onset to turbulence one might gain more understanding about the behavior of the fully turbulent flow. This can be further supported by comparing the time dependent behavior of the laminar flow with that of the turbulent flow. As a first step, the question needs to be answered, if an absolute or a global instability also exists for the supersonic wake flow. For this reason, in the

present research the evolution of artificially generated disturbances has been investigated for laminar and for turbulent flow fields. Direct Numerical Simulations (DNS) and Large-Eddy Simulations (LES) have been employed for the investigation of the time dependent behavior of the supersonic axisymmetric wake flow. All simulations are based on solving the complete set of the compressible Navier-Stokes equations (spatially filtered for LES) in a cylindrical coordinate system.

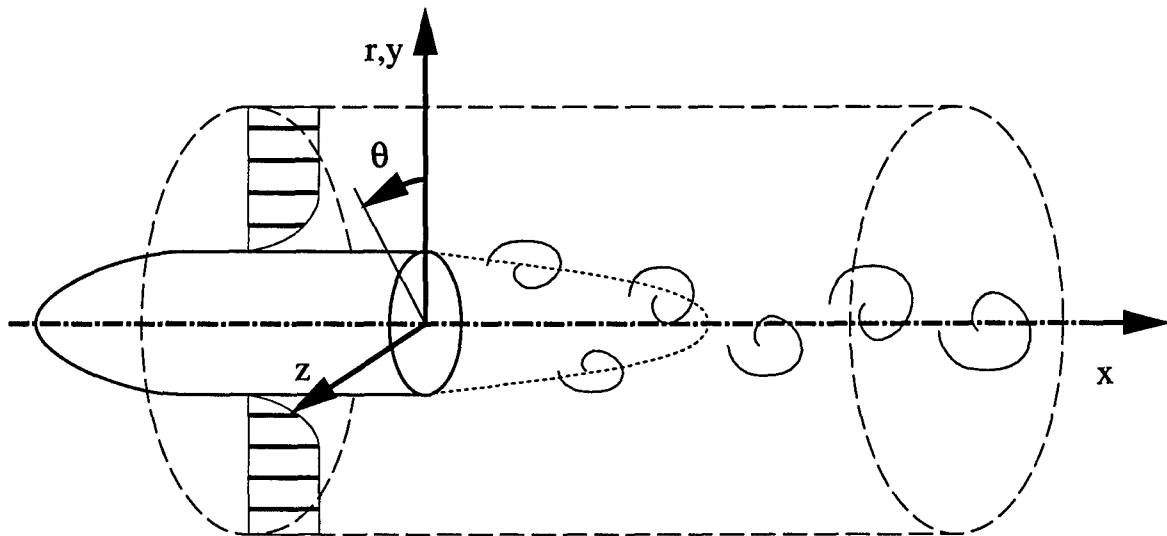


Figure 1.3: Region of interest.

The region of interest for the given problem is the near wake of the axisymmetric body as shown in figure 3.1. The last part of the boundary layer approaching the base corner was included in the calculation. This allowed the introduction of controlled disturbances through a circular blowing and suction slot on the body into the boundary layer. As the initial step, a laminar axisymmetric steady flow field was calculated. This flow field was then artificially disturbed either by blowing and suction through a circular slot on the body, or by a local pulse within the recirculating region. Then the time dependent evolution of the entire flow in response to the artificially generated disturbances was monitored. For the given flow situation, air can be treated as a calorically perfect gas, resulting in a constant heat capacity ( $c_p$ ) and a constant Prandtl number ( $Pr$ ).

One of the main interests in this research was the interaction between the recirculation region and the external flow which are connected by a shear layer. As mentioned above, it is known that for subsonic incompressible flows, large structures form in the shear layer and play a dominant role in the local and global behavior of the wake flow and, consequently, have a strong effect on the drag. However, for supersonic compressible wake flows the role of large structures in the dynamical flow behavior and in particular their influence on the base pressure is not well understood. The ultimate goal of the present research is to contribute towards the understanding of the dynamical behavior of the large structures and their effect on the global flow behavior.

## Chapter 2

# Governing Equations, Initial and Boundary Conditions

As pointed out in the literature review, previous investigations have focused on finding a time-averaged solution for turbulent axisymmetric wake flows at supersonic speeds. In almost all these research efforts the resulting flow field was assumed to be axisymmetric. Therefore, typically a set of the compressible axisymmetric Reynolds-averaged Navier-Stokes equations was used as the governing equations. In some cases, these were further simplified by using thin-layer approximations. In the present work the main emphasis was on the time-dependent evolution of the near wake flow field, which does not necessarily have to be axisymmetric. In fact, for the case of the subsonic wake flow the instantaneous flow field and sometimes even the time-averaged flow field does not exhibit axisymmetry [see, for example, [Schwarz (1996)]]]. Therefore, the governing equations chosen for the present investigation are the complete three-dimensional unsteady compressible Navier-Stokes equations. Since the given geometry is axisymmetric the equations are solved in a cylindrical coordinate system.

Three different sets of the equations are being used according to the different tasks. For the determination of laminar axisymmetric flow fields, the equations are reduced to the axisymmetric compressible Navier-Stokes equations (see section 2.2). The fully three-dimensional flow field for lower Reynolds number flows (laminar or transitional) is calculated by solving the complete three-dimensional unsteady compressible Navier-Stokes equations (see section 2.3). For the solution of turbulent flows at higher Reynolds numbers Large-Eddy Simulation (LES) is employed, where the three-dimensional equations are filtered in space in order to resolve only structures that are larger than a specified threshold (see section 2.4).

## 2.1 Nondimensionalization

All variables in the given problem are nondimensionalized. The length scale chosen for the problem is the diameter  $D$  of the axisymmetric body. Thus,

$$x = \frac{x^*}{D} ; \quad r = \frac{r^*}{D}. \quad (2.1a)$$

The velocity components are nondimensionalized by the free stream velocity  $U_\infty$

$$v_x = \frac{v_x^*}{U_\infty} ; \quad v_r = \frac{v_r^*}{U_\infty} ; \quad v_\theta = \frac{v_\theta^*}{U_\infty}. \quad (2.1b)$$

Temperature, density, viscosity, and heat conductivity are nondimensionalized by their values in the free stream:

$$T = \frac{T^*}{T_\infty} ; \quad \rho = \frac{\rho^*}{\rho_\infty} ; \quad \mu = \frac{\mu^*}{\mu_\infty} ; \quad \vartheta = \frac{\vartheta^*}{\vartheta_\infty}. \quad (2.1c)$$

This automatically leads to the following nondimensionalization for time, pressure and energy:

$$t = \frac{U_\infty t^*}{D} ; \quad p = \frac{p^*}{\rho_\infty U_\infty^2} ; \quad e = \frac{e^*}{U_\infty^2}. \quad (2.1d)$$

The global Reynolds number, the Prandtl number and the free stream Mach number are defined by

$$Re_D = \frac{\rho_\infty U_\infty D}{\mu_\infty} ; \quad Pr = \frac{\mu_\infty c_p}{\vartheta_\infty} ; \quad M_\infty = \frac{U_\infty}{a_\infty}, \quad (2.1e)$$

where the speed of sound in the free stream is given by

$$a_\infty = \sqrt{\gamma R_l T_\infty}, \quad (2.1f)$$

and

$$\gamma = \frac{c_p}{c_v} ; \quad R_l = c_p - c_v. \quad (2.1g)$$

The coefficient of the conduction term in the energy equation is given by the product of the Peclet number and the Eckert number

$$N = PeEc = (\gamma - 1)PrRe_D M_\infty^2, \quad (2.1h)$$

where

$$Pe = Re_D Pr ; \quad Ec = \frac{U_\infty^2}{c_p T_\infty}. \quad (2.1i)$$

## 2.2 Axisymmetric Calculations

### 2.2.1 Equations

For the calculation of axisymmetric flow fields, the unsteady axisymmetric compressible Navier-Stokes equations are solved. The equations are used in conservative formulation and are expressed in a cylindrical coordinate system. Then, they can be written in the following vector form

$$\frac{\partial}{\partial t} \vec{A} + \frac{\partial}{\partial x} \vec{B} + \frac{\partial}{\partial r} \vec{C} + \frac{1}{r} \vec{E} = 0, \quad (2.2a)$$

where

$$\vec{A} = \begin{pmatrix} \rho \\ \rho v_x \\ \rho v_r \\ \rho e \end{pmatrix}, \quad (2.2b)$$

$$\vec{B} = \begin{pmatrix} \rho v_x \\ \rho v_x^2 + p + \tau_{xx} \\ \rho v_x v_r + \tau_{rx} \\ v_x(\rho e + p) - \frac{\vartheta}{N} \frac{\partial T}{\partial x} + v_x \tau_{xx} + v_r \tau_{rx} \end{pmatrix}, \quad (2.2c)$$

$$\vec{C} = \begin{pmatrix} \rho v_r \\ \rho v_x v_r + \tau_{rx} \\ \rho v_r^2 + p + \tau_{rr} \\ v_r(\rho e + p) - \frac{\vartheta}{N} \frac{\partial T}{\partial r} + v_x \tau_{rx} + v_r \tau_{rr} \end{pmatrix}, \quad (2.2d)$$

and

$$\vec{E} = \begin{pmatrix} \rho v_r \\ \rho v_x v_r + \tau_{rx} \\ \rho v_r^2 + \tau_{rr} - \tau_{\theta\theta} \\ v_r(\rho e + p) - \frac{\vartheta}{N} \frac{\partial T}{\partial r} + v_x \tau_{rx} + v_r \tau_{rr} \end{pmatrix}. \quad (2.2e)$$

The stress tensor components ( $\tau_{ij}$ ) for axisymmetric flow are defined by [see, for example, [Bird et al. (1960)]]

$$\tau_{xx} = \frac{2}{3} \frac{\mu}{Re_D} \left[ -2 \frac{\partial v_x}{\partial x} + \frac{\partial v_r}{\partial r} + \frac{v_r}{r} \right], \quad (2.3a)$$

$$\tau_{rr} = \frac{2}{3} \frac{\mu}{Re_D} \left[ \frac{\partial v_x}{\partial x} - 2 \frac{\partial v_r}{\partial r} + \frac{v_r}{r} \right], \quad (2.3b)$$

$$\tau_{\theta\theta} = \frac{2}{3} \frac{\mu}{Re_D} \left[ \frac{\partial v_x}{\partial x} + \frac{\partial v_r}{\partial r} - 2 \frac{v_r}{r} \right], \quad (2.3c)$$

and

$$\tau_{xr} = \tau_{rx} = -\frac{\mu}{Re_D} \left[ \frac{\partial v_x}{\partial r} + \frac{\partial v_r}{\partial x} \right]. \quad (2.3d)$$

The energy equation is used in the form of a conservation equation for the total energy ( $e$ ), which is defined by

$$e = \frac{c_v T_\infty}{U_\infty^2} T + \frac{1}{2} \vec{v} \cdot \vec{v}. \quad (2.3e)$$

The viscosity of air is assumed to be a function of temperature, according to Sutherland's law [see, for example, [White (1991)]], which is given by

$$\mu(T) = T^{\frac{3}{2}} \left( \frac{1 + S_\infty}{T + S_\infty} \right), \text{ where } S_\infty = \frac{111\text{K}}{T_\infty}. \quad (2.4)$$

The same relationship holds for the temperature dependence of the thermal conductivity, because the Prandtl number is assumed to be constant. Since air is treated as a calorically perfect gas, the equation of state is given by [see, for example, [Thumm (1991)]]

$$p = \frac{\rho T}{\gamma M_\infty^2}. \quad (2.5)$$

### 2.2.2 Integration Domain

The domain for numerical integration of the axisymmetric equations is shown in figure 2.1. It extends from a point  $x_0$  on the body, past the base to a point  $x_1$  sufficiently far downstream of the base, such that the recirculation region is fully enclosed (typically 3 to 20 diameters behind the base). In the radial direction it starts at the axis of symmetry ( $r = 0$ ) and extends typically 2 to 10 body diameters away from the body.

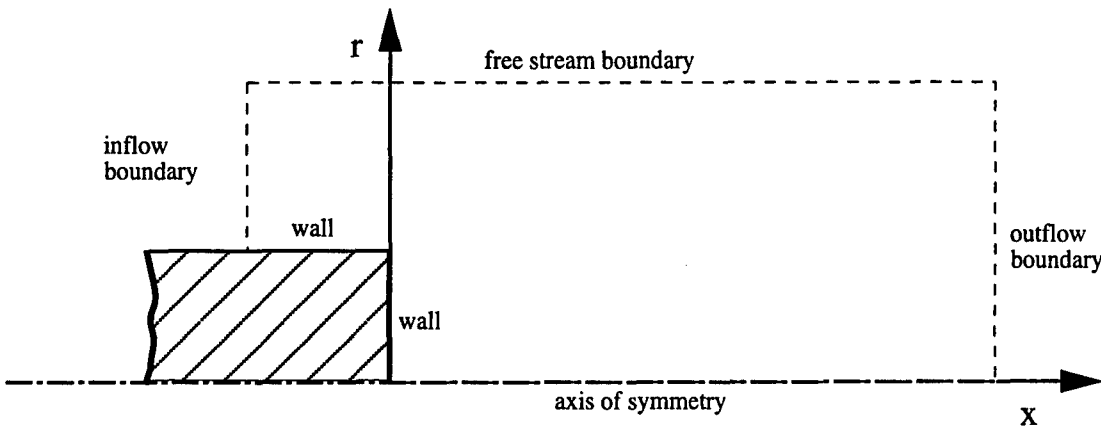


Figure 2.1: Integration domain for the axisymmetric equations.

### 2.2.3 Boundary Conditions

The integration domain for the axisymmetric problem includes five physical boundaries, as is shown in figure 2.1. These boundaries and the boundary conditions that are prescribed are listed below.

#### Inflow boundary

At the inflow boundary all flow variables ( $\rho$ ,  $v_x$ ,  $v_r$ ,  $T$ , and  $p$ ) are prescribed. In the subsonic layer the pressure ( $p$ ) is extrapolated from the field assuming a constant pressure in streamwise direction.

#### Outflow boundary

At the outflow boundary the second derivative in axial direction for all primary flow variables ( $\rho$ ,  $\rho v_x$ ,  $\rho v_r$ , and  $\rho e$ ) is set to zero. This boundary condition has been introduced

by Fasel(1976) and was found to allow disturbances to travel through the boundary without major reflections.

### Walls

At the walls, all velocities are set to zero.

$$v_x = 0 \quad ; \quad v_r = 0 \quad (2.6a)$$

For the calculation of a steady flow field the body is assumed to be adiabatic. Thus, at the horizontal wall it follows

$$\frac{\partial T}{\partial r} = 0, \quad (2.6b)$$

and at the vertical wall

$$\frac{\partial T}{\partial x} = 0. \quad (2.6c)$$

For the calculation of an unsteady flow field, the body temperature is kept constant. Thus

$$\frac{\partial T}{\partial t} = 0. \quad (2.6d)$$

### Axis of symmetry

Since the flow field is assumed to be axisymmetric, at the axis of symmetry it follows that

$$\frac{\partial v_x}{\partial r} = 0 \quad ; \quad v_r = 0 \quad ; \quad \frac{\partial \rho}{\partial r} = 0 \quad ; \quad \frac{\partial e}{\partial r} = 0. \quad (2.6e)$$

### Free stream boundary

At the free stream boundary, three different boundary conditions are applied, depending on the free stream Mach number of the problem. A detailed description of the free stream boundary conditions is given in appendix B.

### Initial condition

As an initial condition for the calculation of the steady axisymmetric flow field, the similarity solution for a compressible flat plate boundary layer is used. The radial velocity distribution is calculated by integrating the steady continuity equation. For the calculation of an unsteady axisymmetric flow field, a previously calculated steady flow field is used as initial condition.

## 2.3 Three-dimensional Calculations

### 2.3.1 Equations

The fully three-dimensional flow field is calculated by solving the complete unsteady three-dimensional compressible Navier-Stokes equations. As for the axisymmetric flow field, the equations are expressed in conservative formulation in a cylindrical coordinate system. Again they can be written in the vector form

$$\frac{\partial}{\partial t} \vec{A} + \frac{\partial}{\partial x} \vec{B} + \frac{\partial}{\partial r} \vec{C} + \frac{1}{r} \frac{\partial}{\partial \theta} \vec{D} + \frac{1}{r} \vec{E} = 0, \quad (2.7a)$$

where now

$$\vec{A} = \begin{pmatrix} \rho \\ \rho v_x \\ \rho v_r \\ \rho v_\theta \\ \rho e \end{pmatrix}, \quad (2.7b)$$

$$\vec{B} = \begin{pmatrix} \rho v_x \\ \rho v_x^2 + p + \tau_{xx} \\ \rho v_x v_r + \tau_{rx} \\ \rho v_x v_\theta + \tau_{\theta x} \\ v_x (\rho e + p) - \frac{\vartheta}{N} \frac{\partial T}{\partial x} + v_x \tau_{xx} + v_r \tau_{rx} + v_\theta \tau_{\theta x} \end{pmatrix}, \quad (2.7c)$$

$$\vec{C} = \begin{pmatrix} \rho v_r \\ \rho v_x v_r + \tau_{rx} \\ \rho v_r^2 + p + \tau_{rr} \\ \rho v_r v_\theta + \tau_{r\theta} \\ v_r (\rho e + p) - \frac{\vartheta}{N} \frac{\partial T}{\partial r} + v_x \tau_{rx} + v_r \tau_{rr} + v_\theta \tau_{r\theta} \end{pmatrix}, \quad (2.7d)$$

$$\vec{D} = \begin{pmatrix} \rho v_\theta \\ \rho v_x v_\theta + \tau_{\theta x} \\ \rho v_r v_\theta + \tau_{r\theta} \\ \rho v_\theta^2 + p + \tau_{\theta\theta} \\ v_\theta (\rho e + p) - \frac{\vartheta}{N} \frac{\partial T}{\partial \theta} + v_x \tau_{\theta x} + v_r \tau_{r\theta} + v_\theta \tau_{\theta\theta} \end{pmatrix}, \quad (2.7e)$$

and

$$\vec{E} = \begin{pmatrix} \rho v_r \\ \rho v_x v_r + \tau_{rx} \\ \rho v_r^2 - \rho v_\theta^2 + \tau_{rr} - \tau_{\theta\theta} \\ 2\rho v_r v_\theta + 2\tau_{r\theta} \\ v_r (\rho e + p) - \frac{\vartheta}{N} \frac{\partial T}{\partial r} + v_x \tau_{rx} + v_r \tau_{rr} + v_\theta \tau_{r\theta} \end{pmatrix}. \quad (2.7f)$$

For a three-dimensional flow field, the stress tensor components in a cylindrical coordinate system are defined as follows.

$$\tau_{xx} = -\frac{\mu}{Re_D} \left[ 2 \frac{\partial v_x}{\partial x} - \frac{2}{3} (\nabla \cdot \vec{v}) \right] = \frac{2}{3} \frac{\mu}{Re_D} \left[ -2 \frac{\partial v_x}{\partial x} + \frac{\partial v_r}{\partial r} + \frac{1}{r} \frac{\partial v_\theta}{\partial \theta} + \frac{v_r}{r} \right], \quad (2.8a)$$

$$\tau_{rr} = -\frac{\mu}{Re_D} \left[ 2 \frac{\partial v_r}{\partial r} - \frac{2}{3} (\nabla \cdot \vec{v}) \right] = \frac{2}{3} \frac{\mu}{Re_D} \left[ \frac{\partial v_x}{\partial x} - 2 \frac{\partial v_r}{\partial r} + \frac{1}{r} \frac{\partial v_\theta}{\partial \theta} + \frac{v_r}{r} \right], \quad (2.8b)$$

$$\tau_{\theta\theta} = -\frac{\mu}{Re_D} \left[ 2 \left( \frac{1}{r} \frac{\partial v_\theta}{\partial \theta} + \frac{v_r}{r} \right) - \frac{2}{3} (\nabla \cdot \vec{v}) \right] = \frac{2}{3} \frac{\mu}{Re_D} \left[ \frac{\partial v_x}{\partial x} + \frac{\partial v_r}{\partial r} - \frac{2}{r} \frac{\partial v_\theta}{\partial \theta} - 2 \frac{v_r}{r} \right], \quad (2.8c)$$

$$\tau_{xr} = \tau_{rx} = -\frac{\mu}{Re_D} \left[ \frac{\partial v_x}{\partial r} + \frac{\partial v_r}{\partial x} \right], \quad (2.8d)$$

$$\tau_{\theta x} = \tau_{x\theta} = -\frac{\mu}{Re_D} \left[ \frac{\partial v_\theta}{\partial x} + \frac{1}{r} \frac{\partial v_x}{\partial \theta} \right], \quad (2.8e)$$

and

$$\tau_{\theta r} = \tau_{r\theta} = -\frac{\mu}{Re_D} \left[ r \frac{\partial}{\partial r} \left[ \frac{v_\theta}{r} \right] + \frac{1}{r} \frac{\partial v_r}{\partial \theta} \right] = -\frac{\mu}{Re_D} \left[ \frac{\partial v_\theta}{\partial r} - \frac{v_\theta}{r} + \frac{1}{r} \frac{\partial v_r}{\partial \theta} \right]. \quad (2.8f)$$

As before, air is treated as a calorically perfect gas and the total energy term and the temperature dependence of the viscosity are defined in the same way, as shown in equation 2.5 (see section 2.2).

### 2.3.2 Integration Domain

The integration domain, as shown in figure 2.2, includes part of the boundary layer on the axisymmetric body and extends downstream beyond the recirculation region (typically 3 to 20 diameters downstream of the base).

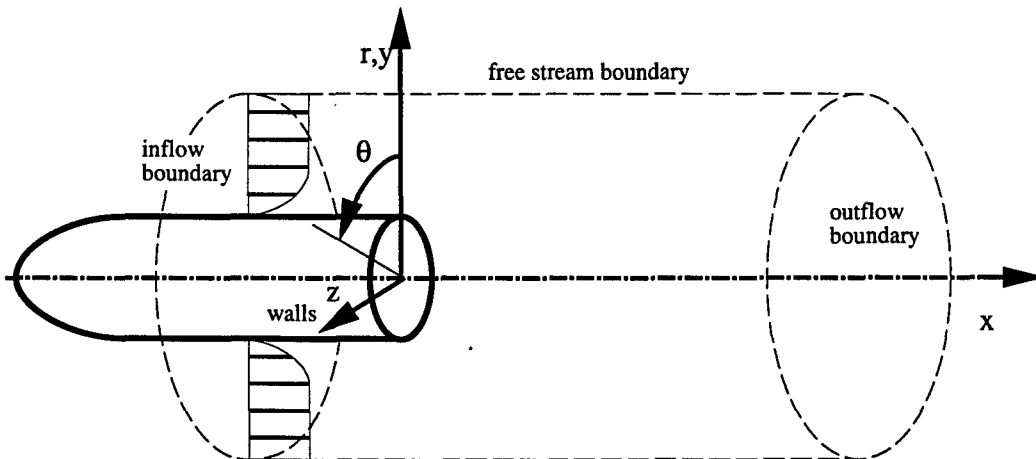


Figure 2.2: Integration domain for the three-dimensional equations.

### 2.3.3 Boundary Conditions

As can be seen in figure 2.2, the integration domain for the three-dimensional problem includes four boundaries. The boundaries and the prescribed boundary conditions are listed as follows.

#### Inflow boundary

For the three-dimensional (unsteady) calculations, all variables at the inflow boundary are specified. The only exception is the pressure in the subsonic layer, where the first derivative of the pressure in axial direction is set to zero.

#### Outflow boundary

As for the axisymmetric calculations, at the outflow boundary the second derivatives in axial direction of all primary flow variables are set to zero.

### Walls

At the walls all velocities are set to zero

$$v_x = 0 \quad ; \quad v_r = 0 \quad ; \quad v_\theta = 0 \quad (2.9a)$$

The temperature on the walls is held constant based on the assumption that the body cannot change temperature on the time scale of the disturbances. Thus

$$\frac{\partial T}{\partial t} = 0 \quad (2.9b)$$

The zero-velocity boundary condition is applied at the wall except on the circular section of blowing and suction, which is used for disturbance generation. This is described in more detail in section 3.7.

### Free stream boundary

The boundary conditions at the free stream are similar to the axisymmetric case. As before, three different kinds of boundary conditions are applied at the free stream boundary, according to the free stream Mach number ( $M_\infty$ ). The three different boundary conditions are described in more detail in appendix B.

### Initial condition

A previously calculated steady axisymmetric flow field is used as the initial condition .

## 2.4 Large-Eddy Simulations

### 2.4.1 Spatially Filtered Three-Dimensional Equations for LES

At sufficiently high Reynolds numbers the flow field eventually becomes turbulent. In that case, Direct Numerical Simulations become very memory and CPU time intensive. In order to be able to calculate the flow field for a turbulent Reynolds number the equations therefore cannot be solved directly, because of the lack of spatial resolution. In most applications, however, the small turbulent scales are not of major interest. For that reason, methods have been developed to model these small scales. In almost all previous research efforts, the turbulent compressible wake flow field was calculated by using a Reynolds-averaged form of the Navier-Stokes equations (see section 2.3). These calculations always lead to a time-averaged flow field. In the present research, however, the main focus is on the time dependent behavior of the flow field and the evolution and dynamics of large structures. Therefore, in the present research the method of Large-Eddy Simulations (LES) was chosen for the calculation of the time dependent turbulent flow field. LES has been successfully applied to isotropic turbulence and to wall bounded flows, such as flat plate boundary layers and duct flow. For LES, the Navier-Stokes equations are filtered in space, using the assumption that the small turbulent scales are separable from the larger structures (eddies). The latter can then be calculated, while the former have to be modeled. In the following sections the equations for the resolved quantities are derived. This derivation was

done for the most part by [Israel (1996)] in close collaboration with [Speziale (1996)]. Here, the derived equations are furthermore adapted to the axisymmetric geometry.

### 2.4.2 Spatial Filtering

For the filtering of the Navier-Stokes equations, any spatial filter of the form  $G(x; \Delta)$  with filter width  $\Delta$  can be used, provided that it has the following properties:

$$G(+\infty), G(-\infty) \rightarrow 0 ; \quad (2.10)$$

$$\int_{-\infty}^{+\infty} G(\xi) d\xi = 1. \quad (2.11)$$

The filtered value of property  $f$ , denoted as  $\bar{f}$ , is defined by the convolution

$$\bar{f}(x) = \int_{-\infty}^{+\infty} G(x - \xi; \Delta) f(\xi) d\xi. \quad (2.12)$$

This allows the decomposition of any quantity into a filtered and a fluctuating part by

$$f = \bar{f} + f'.$$

For spatial derivatives of filtered quantities Ghosal & Moin (1993), for example, pointed out that

$$\begin{aligned} \frac{d\bar{f}(x)}{dx} &= \frac{d}{dx} \int_{-\infty}^{+\infty} G(x - \xi) f(\xi) d\xi \\ &= \int_{-\infty}^{+\infty} \frac{dG(x - \xi)}{dx} f(\xi) d\xi \\ &= \int_{-\infty}^{+\infty} G'(x - \xi) f(\xi) d\xi \\ &= -G(x - \xi) f(\xi)|_{\xi=-\infty}^{+\infty} + \int_{-\infty}^{+\infty} G(x - \xi) f'(\xi) d\xi \\ &= \frac{df(x)}{dx}, \end{aligned}$$

since  $f$  must be finite on the boundaries and the filter vanishes at infinity. This property is only valid for filters with a uniform filter width. For non-uniform filters, it can be shown that this is only true to a second order approximation [see, for example, [Ghosal & Moin (1993)]].

In the conservative formulation of the compressible Navier-Stokes equations, the velocity always occurs in products with the density. When the equations are filtered this leads to the velocity-density correlation terms,  $\overline{\rho u_i}$ . In order to obtain separate variables (that is, not under a correlation), the so called Favre filter (denoted by a tilde) is introduced, which is defined by

$$\tilde{f} = \frac{\overline{\rho f}}{\overline{\rho}}. \quad (2.13)$$

The Favre filtered variable is also sometimes referred to as a mass averaged quantity. This allows the separation of the density-velocity correlation terms by means of the substitution  $\overline{\rho f} = \overline{\rho} \tilde{f}$ .

(Note: In the incompressible limit,  $\rho$  becomes a constant and  $\tilde{f} \rightarrow \bar{f}$ .) As before, the physical quantity can also be separated into a Favre filtered part and a fluctuating part (denoted by a double prime),

$$f = \tilde{f} + f''. \quad (2.14)$$

### 2.4.3 The Continuity Equation

The continuity equation for a compressible fluid can be written in index notation as

$$\frac{\partial \rho}{\partial t} + \frac{\partial \rho u_i}{\partial x_i} = 0. \quad (2.15)$$

Applying the spatial filter to this equation directly leads to the filtered continuity equation,

$$\frac{\partial \bar{\rho}}{\partial t} + \frac{\partial \bar{\rho} \bar{u}_i}{\partial x_i} = 0.$$

Introducing the Favre filtering the correlation in the second term can be eliminated and the continuity equation for the mass averaged velocity can be obtained as

$$\frac{\partial \bar{\rho}}{\partial t} + \frac{\partial \bar{\rho} \tilde{u}_i}{\partial x_i} = 0. \quad (2.16)$$

### 2.4.4 The Momentum Equations

Similar to the continuity equation, the momentum equations for a compressible fluid can be written in index notation as

$$\frac{\partial \rho u_i}{\partial t} + \frac{\partial \rho u_i u_j}{\partial x_j} = - \frac{\partial p}{\partial x_i} - \frac{\partial \tau_{ij}}{\partial x_j}, \quad (2.17)$$

where the stress tensor is defined by

$$\tau_{ij} = - \frac{\mu}{Re} \left( \frac{\partial u_i}{\partial x_j} + \frac{\partial u_j}{\partial x_i} - \frac{2}{3} \frac{\partial u_k}{\partial x_k} \delta_{ij} \right).$$

Spatial filtering as for the continuity equation leads directly to the filtered momentum equation

$$\frac{\partial \bar{\rho} \tilde{u}_i}{\partial t} + \frac{\partial \bar{\rho} \tilde{u}_i \tilde{u}_j}{\partial x_j} = - \frac{\partial \bar{p}}{\partial x_i} - \frac{\partial \bar{\tau}_{ij}}{\partial x_j}, \quad (2.18)$$

where the terms  $\tilde{u}_i \tilde{u}_j$  and  $\bar{\tau}_{ij}$  are not closed and have to be modeled.

To preserve the form of the unfiltered equations, the term  $\tilde{u}_i \tilde{u}_j$  needs to be replaced with  $\tilde{u}_i \tilde{u}_j$ . First, the term can be expanded as follows by substituting 2.14,

$$\begin{aligned} u_i u_j &= (\tilde{u}_i + u''_i)(\tilde{u}_j + u''_j) \\ &= \tilde{u}_i \tilde{u}_j + \tilde{u}_i u''_j + u''_i \tilde{u}_j + u''_i u''_j, \end{aligned}$$

or for the filtered term

$$\tilde{u}_i \tilde{u}_j = \widetilde{\tilde{u}_i \tilde{u}_j} + \widetilde{\tilde{u}_i u''_j} + \widetilde{u''_i \tilde{u}_j} + \widetilde{u''_i u''_j}.$$

All the terms containing unknown correlations can be moved to the right hand side. To combine them, a subgrid-scale stress tensor is defined as follows

$$\begin{aligned}\sigma_{ij} &= \bar{\rho}(\tilde{u}_i\tilde{u}_j - \widetilde{u_i u_j}) \\ &= L_{ij} + C_{ij} + R_{ij}\end{aligned}\quad (2.19)$$

where  $L_{ij}$ ,  $C_{ij}$ , and  $R_{ij}$  are typically called the Leonard stress, the cross-stress, and the Reynolds stress, respectively. They are defined by

$$\begin{aligned}L_{ij} &= -\bar{\rho}(\widetilde{\tilde{u}_i \tilde{u}_j} - \widetilde{\tilde{u}_i \tilde{u}_j}), \\ C_{ij} &= -\bar{\rho}(\widetilde{\tilde{u}_i u''_j} + \widetilde{u''_i \tilde{u}_j}), \\ R_{ij} &= -\bar{\rho}\widetilde{u''_i u''_j}.\end{aligned}$$

Substituting 2.19 into the filtered momentum equation 2.18 leads to the mass-averaged (Favre filtered) momentum equation

$$\frac{\partial \bar{\rho} \tilde{u}_i}{\partial t} + \frac{\partial \bar{\rho} \tilde{u}_i \tilde{u}_j}{\partial x_j} = -\frac{\partial \bar{p}}{\partial x_i} - \frac{\partial}{\partial x_j} [\bar{\tau}_{ij} - \sigma_{ij}] \quad (2.20)$$

The Leonard stress can be calculated explicitly. The cross-stress and Reynolds stress are not closed, and must be modeled (see section 2.4.7).

To compute the filtered viscous stress tensor,  $\bar{\tau}_{ij}$  needs to be expressed in terms of the filtered quantities. In many applications, the molecular viscosity is assumed not to vary due to the turbulent fluctuations. For example, [Erlebacher et al. (1992)] and [Zang et al. (1992)] both assume small temperature fluctuations, and therefore take  $\mu$  to be constant over the filter width. This leads to the following expression for the stress tensor

$$\bar{\tau}_{ij} = -\frac{\mu(\tilde{T})}{Re_D} \left( \frac{\partial \tilde{u}_i}{\partial x_j} + \frac{\partial \tilde{u}_j}{\partial x_i} - \frac{2}{3} \frac{\partial \tilde{u}_k}{\partial x_k} \delta_{ij} \right), \quad (2.21)$$

where the molecular viscosity  $\mu(\tilde{T})$  is a function of the Favre filtered local temperature only.

#### 2.4.5 The Energy Equation

In the formulation of the Navier-Stokes equations used in the present research the energy equation is expressed in terms of total energy. The equation in index notation is given by

$$\frac{\partial \rho e}{\partial t} = \frac{\partial}{\partial x_i} \left[ -u_i(\rho e + p) + \frac{\vartheta}{N} \frac{\partial T}{\partial x_i} - u_j \tau_{ij} \right]. \quad (2.22)$$

Unfortunately, if this equation is filtered directly several terms cannot be calculated directly and need to be modeled. This includes the filtered total energy, defined as

$$\bar{\rho} \bar{e} = \bar{\rho} \left( C_v \tilde{T} + \frac{1}{2} \widetilde{u_i u_i} \right),$$

where

$$C_v = \frac{c_v T_\infty}{U_\infty^2}.$$

This quantity is not closed since  $\tilde{u}_i \tilde{u}_i$  is not known. However, one can construct a quantity  $E_R$ , which here is called resolved scale energy, given by

$$E_R = \bar{\rho} \left( C_v \tilde{T} + \frac{1}{2} \tilde{u}_i \tilde{u}_i \right). \quad (2.23)$$

This quantity can be directly calculated from the Favre filtered velocities and temperature. In addition, it can be related to  $\bar{E}_t$  using the relation

$$\bar{E}_t = E_R - \frac{1}{2} \sigma_{ii}.$$

The governing equation for  $E_R$  can be derived in the same manner as the equation for  $E_t$ . First, the equation for the resolved kinetic energy  $\tilde{u}_i \tilde{u}_i$  can be derived by multiplying the resolved scale momentum equation 2.20 with  $\tilde{u}_i$ , which leads to

$$\begin{aligned} \tilde{u}_i \frac{\partial \bar{\rho} \tilde{u}_i}{\partial t} + \tilde{u}_i \frac{\partial \bar{\rho} \tilde{u}_i \tilde{u}_j}{\partial x_j} &= -\tilde{u}_i \frac{\partial \bar{p}}{\partial x_i} - \tilde{u}_i \frac{\partial}{\partial x_j} [\bar{\tau}_{ij} - \sigma_{ij}] \\ \frac{\partial \bar{\rho} \tilde{u}_i \tilde{u}_i}{\partial t} + \frac{\partial \bar{\rho} \tilde{u}_i \tilde{u}_i \tilde{u}_j}{\partial x_j} &= \tilde{u}_i \left[ \bar{\rho} \frac{\partial \tilde{u}_i}{\partial t} + \bar{\rho} \tilde{u}_j \frac{\partial \tilde{u}_i}{\partial x_j} \right] - \tilde{u}_i \frac{\partial \bar{p}}{\partial x_i} - \tilde{u}_i \frac{\partial}{\partial x_j} [\bar{\tau}_{ij} - \sigma_{ij}]. \end{aligned}$$

Using the continuity equation, 2.16, multiplied by  $\tilde{u}_i$  it follows

$$\frac{\partial \bar{\rho} \tilde{u}_i \tilde{u}_i}{\partial t} + \frac{\partial \bar{\rho} \tilde{u}_i \tilde{u}_i \tilde{u}_j}{\partial x_j} = \tilde{u}_i \left[ \frac{\partial \bar{\rho} \tilde{u}_i}{\partial t} + \frac{\partial \bar{\rho} \tilde{u}_i \tilde{u}_j}{\partial x_j} \right] - \tilde{u}_i \frac{\partial \bar{p}}{\partial x_i} - \tilde{u}_i \frac{\partial}{\partial x_j} [\bar{\tau}_{ij} - \tau_{ij}].$$

The right hand side can now be rewritten using the momentum equation 2.20 to yield the equation for the resolved scale turbulent kinetic energy

$$\frac{1}{2} \frac{\partial \bar{\rho} \tilde{u}_i \tilde{u}_i}{\partial t} + \frac{1}{2} \frac{\partial \bar{\rho} \tilde{u}_i \tilde{u}_i \tilde{u}_j}{\partial x_j} = \tilde{u}_i \left( -\frac{\partial \bar{p}}{\partial x_i} - \frac{\partial}{\partial x_j} [\bar{\tau}_{ij} - \sigma_{ij}] \right). \quad (2.24)$$

Similarly, the temperature equation for a compressible fluid in index notation is given by

$$\frac{\partial \rho C_v T}{\partial t} + \frac{\partial \rho C_v T u_i}{\partial x_i} = -p \frac{\partial u_i}{\partial x_i} + \frac{\partial}{\partial x_i} \left( \frac{\vartheta}{N} \frac{\partial T}{\partial x_i} \right) - \tau_{ij} \frac{\partial u_j}{\partial x_i} \quad (2.25)$$

[see, for example [Bird et al. (1960)]].

Again, the equation can be filtered in a similar manner as the momentum equation. This leads to

$$\frac{\partial \bar{\rho} C_v \tilde{T}}{\partial t} + \frac{\partial \bar{\rho} C_v \tilde{T} u_i}{\partial x_i} = -\overline{p \frac{\partial u_i}{\partial x_i}} + \frac{\partial}{\partial x_i} \left( \frac{\vartheta}{N} \frac{\partial \tilde{T}}{\partial x_i} \right) - \overline{\tau_{ij} \frac{\partial u_j}{\partial x_i}}. \quad (2.26)$$

Similar to the momentum equation, the term  $\tilde{T} u_i$  cannot be calculated directly and has to be modeled. Introducing a subgrid-scale heat flux, corresponding to the subgrid-scale stress tensor 2.19, one can define

$$\begin{aligned} Q_i &= -\bar{\rho} C_v (\tilde{T} \tilde{u}_i - \widetilde{T u_i}) \\ &= L_i^Q + C_i^Q + R_i^Q, \end{aligned}$$

where

$$L_i^Q = \bar{\rho}C_v(\widetilde{T}\tilde{u}_i - \widetilde{T}\tilde{u}_i),$$

$$C_i^Q = \bar{\rho}C_v(\widetilde{T}u''_i - \widetilde{T''}\tilde{u}_i),$$

and

$$R_i^Q = \bar{\rho}C_v\widetilde{T''}u''_i$$

are defined similarly to the Leonard stress, the cross stress and the Reynolds stress tensors, respectively. With these definitions the filtered energy equation in terms of the Favre filtered temperature becomes

$$\frac{\partial \bar{\rho}C_v\widetilde{T}}{\partial t} + \frac{\partial \bar{\rho}C_v\widetilde{T}\tilde{u}_i}{\partial x_i} = -\overline{p\frac{\partial u_i}{\partial x_i}} + \frac{\partial}{\partial x_i} \left[ \frac{\vartheta}{N} \frac{\partial \widetilde{T}}{\partial x_i} - Q_i \right] - \overline{\tau_{ij}\frac{\partial u_i}{\partial x_j}}, \quad (2.27)$$

where the right hand side is still not closed without additional assumptions to model the filtered correlations (see section 2.4.7).

Now the equation for resolved scale energy,  $E_R$ , can be determined by summing 2.24 and 2.27, and rearranging indices. This leads to

$$\frac{\partial E_R}{\partial t} + \frac{\partial \tilde{u}_i E_R}{\partial x_i} = -\overline{p\frac{\partial u_i}{\partial x_i}} + \frac{\partial}{\partial x_i} \left[ \frac{\vartheta}{N} \frac{\partial \widetilde{T}}{\partial x_i} - Q_i \right] - \overline{\tau_{ij}\frac{\partial u_i}{\partial x_j}} + \tilde{u}_i \left( -\frac{\partial \bar{p}}{\partial x_i} - \frac{\partial}{\partial x_j} [\overline{\tau_{ij}} - \sigma_{ij}] \right).$$

This equation cannot be written in a form similar to 2.22 due to the presence of disparate types of filtering in the pressure and molecular stress terms. However, following [Erlebacher et al. (1992)] the pressure terms can be rewritten as

$$\begin{aligned} -\overline{p\frac{\partial u_i}{\partial x_i}} - \tilde{u}_i \frac{\partial \bar{p}}{\partial x_i} &= -\frac{\partial \bar{p}\tilde{u}_i}{\partial x_i} + \left( \bar{p}\frac{\partial \tilde{u}_i}{\partial x_i} - \overline{p\frac{\partial u_i}{\partial x_i}} \right) \\ &= -\frac{\partial \bar{p}\tilde{u}_i}{\partial x_i} - \left( \overline{\bar{p}\frac{\partial \tilde{u}_i}{\partial x_i}} - \overline{p\frac{\partial \tilde{u}_i}{\partial x_i}} + \overline{p\frac{\partial u''_i}{\partial x_i}} + \overline{p'\frac{\partial \tilde{u}_i}{\partial x_i}} + \overline{p'\frac{\partial u''_i}{\partial x_i}} \right) \\ &= -\frac{\partial \bar{p}\tilde{u}_i}{\partial x_i} - \epsilon_p. \end{aligned}$$

In addition, according to [Erlebacher et al. (1992)] the terms combined in  $\epsilon_p$  are negligible.

The viscosity term can be handled similarly,

$$\begin{aligned} \overline{\tau_{ij}\frac{\partial u_i}{\partial x_j}} + \tilde{u}_i \frac{\partial \overline{\tau_{ij}}}{\partial x_j} &= \frac{\partial \tilde{u}_i \tau_{ij}}{\partial x_j} + \left( \overline{\tau_{ij}\frac{\partial u_i}{\partial x_j}} - \overline{\tau_{ij}\frac{\partial \tilde{u}_i}{\partial x_j}} \right) \\ &= \frac{\partial \tilde{u}_i \tau_{ij}}{\partial x_j} + \left( \overline{\tau_{ij}\frac{\partial \tilde{u}_i}{\partial x_j}} - \overline{\tau_{ij}\frac{\partial \tilde{u}_i}{\partial x_j}} + \overline{\tau_{ij}\frac{\partial u''_i}{\partial x_j}} + \overline{\tau'_{ij}\frac{\partial \tilde{u}_i}{\partial x_j}} + \overline{\tau'_{ij}\frac{\partial u''_i}{\partial x_j}} \right) \\ &= \frac{\partial \tilde{u}_i \tau_{ij}}{\partial x_j} + \epsilon_\tau, \end{aligned}$$

where the terms combined in  $\epsilon_\tau$  are neglected for similar reasons as for  $\epsilon_p$  [see, for example, [Erlebacher et al. (1992)]].

The subgrid-scale stress term can be written as (noting that  $\sigma_{ij}$  is symmetric):

$$\begin{aligned}\tilde{u}_j \frac{\partial \sigma_{ij}}{\partial x_i} &= \frac{\partial}{\partial x_i} [\tilde{u}_j \sigma_{ij}] - \sigma_{ij} \frac{\partial \tilde{u}_j}{\partial x_i} \\ &= \frac{\partial}{\partial x_i} [\tilde{u}_j \sigma_{ij}] - \frac{1}{2} \left( \sigma_{ij} \frac{\partial \tilde{u}_j}{\partial x_i} + \sigma_{ji} \frac{\partial \tilde{u}_i}{\partial x_j} \right) \\ &= \frac{\partial}{\partial x_i} [\tilde{u}_j \sigma_{ij}] - \sigma_{ij} \tilde{S}_{ij},\end{aligned}$$

where  $\tilde{S}_{ij}$  is the strain tensor formed with the Favre filtered velocities.

Introducing all the above assumptions and definitions, the final form of the resolved energy equation then becomes

$$\frac{\partial E_R}{\partial t} = \frac{\partial}{\partial x_i} \left[ -\tilde{u}_i (E_R + \bar{p}) + \left( \frac{\vartheta}{N} \frac{\partial \tilde{T}}{\partial x_i} \right) - Q_i - \tilde{u}_j (\bar{\tau}_{ij} + \sigma_{ij}) \right] - \sigma_{ij} \tilde{S}_{ij}. \quad (2.28)$$

#### 2.4.6 Equation of State

In addition to the Navier-Stokes equations, the equation of state also needs to be filtered. Recalling the equation of state for an ideal gas

$$p = \frac{\rho T}{\gamma M_\infty^2}, \quad (2.29)$$

it follows that the filtered equation is

$$\bar{p} = \frac{\bar{\rho} \tilde{T}}{\gamma M_\infty^2}. \quad (2.30)$$

#### 2.4.7 Subgrid-Scale Model

As an initial step, the subgrid model chosen for the present research is a constant coefficient Smagorinsky type model as suggested by [Speziale (1996)] [see also [Smagorinsky (1963)]]]. The Smagorinsky model is an eddy viscosity type model, as are most turbulent models currently used in fluid dynamics simulations. In this initial study the isotropic part of the turbulent stress tensor is assumed to be negligible. Thus, the turbulent stress tensor takes the form

$$\sigma_{ij} = 2\bar{\rho} \ell^2 (2\tilde{S}_{kl} \tilde{S}_{kl})^{\frac{1}{2}} \left( \tilde{S}_{ij} - \frac{1}{3} \tilde{S}_{kk} \delta_{ij} \right), \quad (2.31)$$

where the turbulent length scale  $\ell$  is given by

$$\ell = C_s \left( \prod_i \Delta_i \right)^{\frac{1}{3}},$$

where  $\Delta_i$  is the filter width in the  $i$ -th coordinate. Here,  $C_s$  is the so called Smagorinsky constant. At this point the most appropriate value for this constant for the given flow problem is unclear. It has been found for other applications that this constant can vary between approximately 0.05

and 0.2, where the lower values have been used for wall bounded flows and the higher values have been used for isotropic turbulence [[Speziale (1996)]].

In addition, for wall bounded flows a wall damping function was suggested by [Speziale (1996)], which ramps down the effect of the model in the wall-near region (For the present research the turbulence model was only used downstream of the blunt base. Thus, in this case the wall of interest is the base itself.)

$$\ell = C_s \left( \prod_i \Delta_i \right)^{\frac{1}{3}} \left( 1 - e^{-\left(\frac{x^+}{A^+}\right)^3} \right),$$

where  $x$  is the wall normal direction and

$$A^+ = 25 \quad ; \quad x^+ = \frac{\bar{\rho}xu_\tau}{\mu(\tilde{T})} \sqrt{Re_D} \quad ; \quad u_\tau = \sqrt{\frac{\tilde{S}_{rx}}{\bar{\rho}}} \Big|_{x=0}.$$

For the first investigations, the constant was chosen to be <sup>1</sup>

$$C_s = 0.065$$

For the subgrid-scale heat stress, a gradient transport hypothesis is used [see, for example [Erlebacher et al. (1992)]], which leads to the following model

$$Q_i = -\frac{\bar{\rho}C_v\ell^2}{Pr_T} \sqrt{2\tilde{S}_{kl}\tilde{S}_{kl}} \frac{\partial \tilde{T}}{\partial x_i}, \quad (2.32)$$

where the turbulent Prandtl number,  $Pr_T$  is assumed to be unity for the present research. Using a turbulent conductivity  $\vartheta_t$ , defined as

$$\vartheta_t = \frac{\bar{\rho}C_v\ell^2}{Pr_T} \sqrt{2\tilde{S}_{kl}\tilde{S}_{kl}}, \quad (2.33)$$

the subgrid heat stress can be expressed by

$$Q_i = -\vartheta_t \frac{\partial \tilde{T}}{\partial x_i}. \quad (2.34)$$

#### 2.4.8 Resolved Scale Equations

In the cylindrical coordinate system that has been used here, the final equation for the resolved (filtered) quantities is given by

$$\frac{\partial}{\partial t} \vec{A} + \frac{\partial}{\partial x} \vec{B} + \frac{\partial}{\partial r} \vec{C} + \frac{1}{r} \frac{\partial}{\partial \theta} \vec{D} + \frac{1}{r} \vec{E} + \vec{F} = 0. \quad (2.35a)$$

---

<sup>1</sup>Note:  $\sqrt{2}C_s^2 = C_R$ , or  $C_R \approx 0.8409\sqrt{C_s}$  where  $C_R$  is the Smagorinsky coefficient as defined in [Erlebacher et al. (1992)].

Here the vectors are defined by

$$\vec{A} = \begin{pmatrix} \bar{\rho} \\ \bar{\rho}\tilde{v}_x \\ \bar{\rho}\tilde{v}_r \\ \bar{\rho}\tilde{v}_\theta \\ E_R \end{pmatrix}, \quad (2.35b)$$

$$\vec{B} = \begin{pmatrix} \bar{\rho}\tilde{v}_x \\ \bar{\rho}\tilde{v}_x^2 + \bar{p} + \bar{\tau}_{xx} - \sigma_{xx} \\ \bar{\rho}\tilde{v}_x\tilde{v}_r + \bar{\tau}_{rx} - \sigma_{rx} \\ \bar{\rho}\tilde{v}_x\tilde{v}_\theta + \bar{\tau}_{\theta x} - \sigma_{\theta x} \\ \tilde{v}_x(E_R + \bar{p}) - (\vartheta_t + \vartheta_r)\frac{\partial \bar{T}}{\partial x} + \tilde{v}_x(\bar{\tau}_{xx} - \sigma_{xx}) + \tilde{v}_r(\bar{\tau}_{rx} - \sigma_{rx}) + \tilde{v}_\theta(\bar{\tau}_{\theta x} - \sigma_{\theta x}) \end{pmatrix}, \quad (2.35c)$$

$$\vec{C} = \begin{pmatrix} \bar{\rho}\tilde{v}_r \\ \bar{\rho}\tilde{v}_x\tilde{v}_r + \bar{\tau}_{rx} - \sigma_{rx} \\ \bar{\rho}\tilde{v}_r^2 + p + \bar{\tau}_{rr} - \sigma_{rr} \\ \bar{\rho}\tilde{v}_r\tilde{v}_\theta + \bar{\tau}_{r\theta} - \sigma_{r\theta} \\ \tilde{v}_r(E_R + \bar{p}) - (\vartheta_t + \vartheta_r)\frac{\partial \bar{T}}{\partial r} + \tilde{v}_x(\bar{\tau}_{rx} - \sigma_{rx}) + \tilde{v}_r(\bar{\tau}_{rr} - \sigma_{rr}) + \tilde{v}_\theta(\bar{\tau}_{r\theta} - \sigma_{r\theta}) \end{pmatrix}, \quad (2.35d)$$

$$\vec{D} = \begin{pmatrix} \bar{\rho}\tilde{v}_\theta \\ \bar{\rho}\tilde{v}_x\tilde{v}_\theta + \bar{\tau}_{\theta x} - \sigma_{\theta x} \\ \bar{\rho}\tilde{v}_r\tilde{v}_\theta + \bar{\tau}_{r\theta} - \sigma_{r\theta} \\ \bar{\rho}\tilde{v}_\theta^2 + \bar{p} + \bar{\tau}_{\theta\theta} - \sigma_{\theta\theta} \\ \tilde{v}_\theta(E_R + \bar{p}) - (\vartheta_t + \vartheta_r)\frac{\partial \bar{T}}{\partial \theta} + \tilde{v}_x(\bar{\tau}_{\theta x} - \sigma_{\theta x}) + \tilde{v}_r(\bar{\tau}_{r\theta} - \sigma_{r\theta}) + \tilde{v}_\theta(\bar{\tau}_{\theta\theta} - \sigma_{\theta\theta}) \end{pmatrix}, \quad (2.35e)$$

$$\vec{E} = \begin{pmatrix} \bar{\rho}\tilde{v}_r \\ \bar{\rho}\tilde{v}_x\tilde{v}_r + \bar{\tau}_{rx} - \sigma_{rx} \\ \bar{\rho}\tilde{v}_r^2 - \bar{\rho}\tilde{v}_\theta^2 + \bar{\tau}_{rr} - \sigma_{rr} - \bar{\tau}_{\theta\theta} - \sigma_{\theta\theta} \\ 2\bar{\rho}\tilde{v}_r\tilde{v}_\theta + 2\bar{\tau}_{r\theta} - \sigma_{r\theta} \\ \tilde{v}_r(E_R + \bar{p}) - (\vartheta_t + \vartheta_r)\frac{\partial \bar{T}}{\partial r} + \tilde{v}_x(\bar{\tau}_{rx} - \sigma_{rx}) + \tilde{v}_r(\bar{\tau}_{rr} - \sigma_{rr}) + \tilde{v}_\theta(\bar{\tau}_{r\theta} - \sigma_{r\theta}) \end{pmatrix}, \quad (2.35f)$$

and

$$\vec{F} = \begin{pmatrix} 0 \\ 0 \\ 0 \\ 0 \\ \bar{\rho}\ell^2\|\tilde{S}\| \left[ \|\tilde{S}\|^2 - \frac{2}{3}(\tilde{S}_{xx} + \tilde{S}_{rr} + \tilde{S}_{\theta\theta})^2 \right] \end{pmatrix}, \quad (2.35g)$$

where the norm of the strain tensor is defined as

$$\|\tilde{S}\| = \sqrt{2\sqrt{\tilde{S}_{xx}^2 + \tilde{S}_{rr}^2 + \tilde{S}_{\theta\theta}^2 + 2\tilde{S}_{rx}^2 + 2\tilde{S}_{r\theta}^2 + 2\tilde{S}_{\theta x}^2}}, \quad (2.36)$$

and the strain tensor components are given by

$$\tilde{S}_{xx} = -\frac{\partial \tilde{v}_x}{\partial x}, \quad (2.37a)$$

$$\tilde{S}_{rr} = -\frac{\partial \tilde{v}_r}{\partial r}, \quad (2.37b)$$

$$\tilde{S}_{\theta\theta} = -\left(\frac{1}{r}\frac{\partial \tilde{v}_\theta}{\partial \theta} + \frac{\tilde{v}_r}{r}\right), \quad (2.37c)$$

$$\tilde{S}_{xr} = \tilde{S}_{rx} = -\frac{1}{2}\left[\frac{\partial \tilde{v}_x}{\partial r} + \frac{\partial \tilde{v}_r}{\partial x}\right], \quad (2.37d)$$

$$\tilde{S}_{\theta x} = \tilde{S}_{x\theta} = -\frac{1}{2}\left[\frac{\partial \tilde{v}_\theta}{\partial x} + \frac{1}{r}\frac{\partial \tilde{v}_x}{\partial \theta}\right], \quad (2.37e)$$

and

$$\tilde{S}_{\theta r} = \tilde{S}_{r\theta} = -\frac{1}{2}\left[r\frac{\partial}{\partial r}\left[\frac{\tilde{v}_\theta}{r}\right] + \frac{1}{r}\frac{\partial \tilde{v}_r}{\partial \theta}\right] = -\frac{1}{2}\left[\frac{\partial \tilde{v}_\theta}{\partial r} - \frac{\tilde{v}_\theta}{r} + \frac{1}{r}\frac{\partial \tilde{v}_r}{\partial \theta}\right]. \quad (2.37f)$$

Then the components of the filtered stress tensor can be written as

$$\bar{\tau}_{xx} = 2\frac{\mu}{Re_D}\left(\tilde{S}_{xx} + \frac{1}{3}\nabla \cdot \tilde{\vec{v}}\right), \quad (2.38a)$$

$$\bar{\tau}_{rr} = 2\frac{\mu}{Re_D}\left(\tilde{S}_{rr} + \frac{1}{3}\nabla \cdot \tilde{\vec{v}}\right), \quad (2.38b)$$

$$\bar{\tau}_{\theta\theta} = 2\frac{\mu}{Re_D}\left(\tilde{S}_{\theta\theta} + \frac{1}{3}\nabla \cdot \tilde{\vec{v}}\right), \quad (2.38c)$$

$$\bar{\tau}_{xr} = \bar{\tau}_{rx} = 2\frac{\mu}{Re_D}\tilde{S}_{rx}, \quad (2.38d)$$

$$\bar{\tau}_{\theta x} = \bar{\tau}_{x\theta} = 2\frac{\mu}{Re_D}\tilde{S}_{x\theta}, \quad (2.38e)$$

and

$$\bar{\tau}_{\theta r} = \bar{\tau}_{r\theta} = 2\frac{\mu}{Re_D}\tilde{S}_{r\theta}, \quad (2.38f)$$

and the components of the turbulent stress tensor are given by

$$\sigma_{xx} = 2\tilde{\rho}\ell^2\|\tilde{S}\|\left(\tilde{S}_{xx} + \frac{1}{3}\nabla \cdot \tilde{\vec{v}}\right), \quad (2.39a)$$

$$\sigma_{rr} = 2\tilde{\rho}\ell^2\|\tilde{S}\|\left(\tilde{S}_{rr} + \frac{1}{3}\nabla \cdot \tilde{\vec{v}}\right), \quad (2.39b)$$

$$\sigma_{\theta\theta} = 2\tilde{\rho}\ell^2\|\tilde{S}\|\left(\tilde{S}_{\theta\theta} + \frac{1}{3}\nabla \cdot \tilde{\vec{v}}\right), \quad (2.39c)$$

$$\sigma_{xx} = \sigma_{rx} = 2\tilde{\rho}\ell^2 \|\tilde{S}\| \tilde{S}_{rx}, \quad (2.39d)$$

$$\sigma_{\theta x} = \sigma_{x\theta} = 2\tilde{\rho}\ell^2 \|\tilde{S}\| \tilde{S}_{x\theta}, \quad (2.39e)$$

and

$$\sigma_{\theta r} = \sigma_{r\theta} = 2\tilde{\rho}\ell^2 \|\tilde{S}\| \tilde{S}_{r\theta}, \quad (2.39f)$$

where the turbulent length scale  $\ell$  is given by

$$\ell = C_s \Delta, \quad (2.39g)$$

and the filter width  $\Delta$  for a cylindrical coordinate system by

$$\Delta = (\Delta_x \Delta_r r \Delta_\theta)^{\frac{1}{3}}. \quad (2.39h)$$

#### 2.4.9 Integration Domain and Boundary Conditions

The integration domain and the boundary conditions for the Large-Eddy Simulations are the same as for the three-dimensional Direct Numerical Simulations (see sections 2.3.2 and 2.3.3).

# Chapter 3

## Numerical Method

For both the Direct Numerical Simulations (DNS) and the Large-Eddy Simulations (LES), the governing equations and the boundary conditions are discretized using fourth-order accurate difference approximations in the axial ( $x$ ) and radial ( $r$ ) directions. To achieve higher resolution inside the shear layer, a geometric stretching is applied in both directions. Because of the truly periodic nature of the flow field in the azimuthal direction a pseudo-spectral approximation is employed in  $\theta$ , using a truncated Fourier series. According to the pseudo-spectral method, the non-linear terms are calculated in physical space and then transformed into spectral space. This method is based on the numerical method used by [Thumm (1991)]. Here, the discretization of the governing equations is only shown for the three-dimensional equations of the Direct Numerical Simulation. The axisymmetric equations are just a subset of those and for the Large-Eddy Simulations the equations of the resolved scales are very similar.

### 3.1 Discretization of the Governing Equations

The numerical method for solving the governing equations consists of a fourth-order accurate explicit Runge-Kutta scheme for the time integration, and fourth-order accurate central finite differences for the approximation of the spatial derivatives in the radial and axial directions.

#### 3.1.1 Fourier Decomposition

Due to the periodic nature of the flow field a truncated Fourier series transform is applied in the circumferential direction. Thus, the flow quantities in physical space can be expressed by their representation in Fourier space as follows:

$$\vec{f}(x, r, \theta) = \sum_{k=-K}^K \vec{F}_k(x, r) \cdot e^{ik\theta}, \quad (3.1)$$

where  $i = \sqrt{-1}$ .

Since  $\vec{f}$  has to be real, it follows that

$$\vec{F}_{-k} = \text{conj.} \left( \vec{F}_k \right). \quad (3.2)$$

Substituting the Fourier representation into the governing equation and using the fact that

$$\left( \frac{1}{r} \frac{\partial}{\partial \theta} \vec{D} \right) = \frac{ik}{r} \vec{D}_k \quad (3.3)$$

one gets a set of  $K + 1$  coupled equations of the following form

$$\frac{\partial}{\partial t} \vec{A}_k + \frac{\partial}{\partial z} \vec{B}_k + \frac{\partial}{\partial r} \vec{C}_k + \frac{ik}{r} \vec{D}_k + \frac{1}{r} \vec{E}_k = 0 \quad (3.4)$$

The coupling terms arising from cross products in the convective and the dissipative terms are calculated using a pseudo-spectral method, where the products are calculated in physical space and then transformed back into Fourier space (see, for example, [Toubier (1991)]).

The Fourier representation reduces the original three-dimensional problem to a set of  $K + 1$  two-dimensional problems. The integration domain for this problem set is the same as for the axisymmetric problem, shown in figure 2.1. This results in an artificial boundary at the axis of symmetry that was not present in the original three-dimensional problem. For this boundary, an additional set of boundary conditions has to be specified. This will be further explained in section 5.2.2.

### 3.1.2 Spatial Derivatives

In order to enhance numerical stability, the fourth-order accurate central finite differences that are employed for the approximation of the spatial derivatives are split into one-sided backward and forward finite differences. The splitting directions are alternated at intermediate time steps. The method is similar to the MacCormack method [see, for example, [MacCormack (1969)]]. This way artificial viscosity is added to the discretized equations, damping grid mesh oscillations. The resulting difference formulation is shown the following example.

The fourth order central differences are split into a second order backward and a second order forward difference in the following manner:

$$f'_{b_i} = \frac{1}{6h} (7f_i - 8f_{i-1} + f_{i-2}) \quad ; \quad f'_{f_i} = \frac{1}{6h} (-7f_i + 8f_{i+1} - f_{i+2}). \quad (3.5)$$

Adding both derivatives leads to

$$2f'_i = \frac{1}{6h} (f_{i-2} - 8f_{i-1} + 8f_{i+1} - f_{i+2}), \quad (3.6)$$

which is the same formula as the commonly used fourth order central difference, except that here the one sided differences are evaluated at different intermediate time steps.

Second derivatives are separated into two first order derivatives, with the splitting applied in the opposite direction for the first derivative inside, as follows:

$$\begin{aligned} f''_{b_i} &= \frac{1}{6h} (7f'_{f_i} - 8f'_{f_{i-1}} + f'_{f_{i-2}}) \\ &= \frac{1}{36h^2} (-7f_{i-2} + 64f_{i-1} - 114f_i + 64f_{i+1} - 7f_{i+2}), \end{aligned} \quad (3.7)$$

and

$$\begin{aligned} f''_{f_i} &= \frac{1}{6h} (-7f'_{b_i} + 8f'_{b_{i+1}} - f'_{b_{i+2}}) \\ &= \frac{1}{36h^2} (-7f_{i-2} + 64f_{i-1} - 114f_i + 64f_{i+1} - 7f_{i+2}). \end{aligned} \quad (3.8)$$

After adding, this leads to the following approximation for the second derivative

$$2f''_i = \frac{1}{18h^2} (-7f_{i-2} + 64f_{i-1} - 114f_i + 64f_{i+1} - 7f_{i+2}). \quad (3.9)$$

Applying Taylor series to the difference formula shows that the approximation is fourth-order accurate:

$$\begin{aligned} 2f''_i &= \frac{1}{18} (-14f''(x_i) + 32f''(x_i) + 32f''(x_i) - 14f''(x_i)) + O(h^4) \\ &= 2f''(x_i) + O(h^4). \end{aligned} \quad (3.10)$$

Since the formulation for the second derivative is the same for all intermediate time steps, no additional artificial viscosity is introduced.

## 3.2 Grid Stretching

As mentioned above, a geometrical stretching is applied in the axial and radial directions. For the stretching functions in both directions, higher order polynomials have been chosen [see, for example, [Toubier (1991)]]. Through the grid stretching, extra factors are added to the derivatives of the original equations. Changing from the  $(x, r)$  coordinate system to the  $(\xi, \eta)$  coordinate system, these factors are given by  $\frac{dx}{d\xi}$  and  $\frac{dr}{d\eta}$  for the axial and the radial direction, respectively. The stretching functions that were chosen here and the factors are given in the following two sections. A sample of the stretched grid is shown in figure 3.1.

### 3.2.1 Axial Direction

For the grid stretching in the axial direction, a third order polynomial was chosen as the stretching function. The polynomial is of the following form:

$$x(\xi) = A_x \xi^3 + B_x \xi + C_x. \quad (3.11)$$

To guarantee the highest resolution to be at the base ( $x = 0$ ), the equation has to satisfy the condition  $\frac{d^2x}{d\xi^2}\Big|_{x=0} = 0$ . For convenience, the following conditions were added:

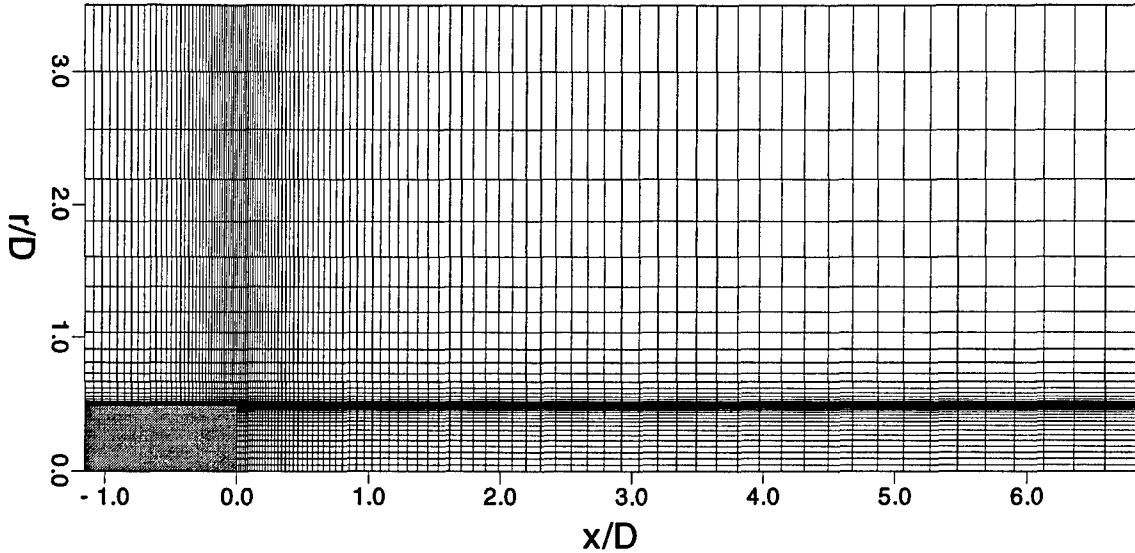


Figure 3.1: Example for grid stretching.

$$\begin{aligned} \text{at } x = 0: \quad & \frac{dx}{d\xi} \Big|_{x=0} = s_x \quad ; \quad \xi = 0 \\ \text{at } x = 1: \quad & \xi = 1. \end{aligned}$$

Here,  $s_x$  is a stretching parameter that can range between zero and one, where  $s_x = 0$  means infinite stretching and  $s_x = 1$  means no stretching. Using these conditions, the three constants for the stretching function are given by

$$A_x = 1 - s_x \quad ; \quad B_x = s_x \quad ; \quad C_x = 0. \quad (3.12)$$

Thus, the stretching in the axial direction is given by

$$x(\xi) = (1 - s_x)\xi^3 + s_x\xi. \quad (3.13)$$

The additional factor that is added to the axial derivatives is given by

$$\frac{d\xi}{dx}(\xi) = \frac{1}{3(1 - s_x)\xi^2 + s_x}. \quad (3.14)$$

### 3.2.2 Radial Direction

In the radial direction a fifth order polynomial was chosen for the stretching function, because the point of highest resolution is at  $r = 0.5$  and the function needs to have two inflection points. The general form of the polynomial is given by

$$r(\eta) = A_r\eta^5 + B_r\eta^3 + C_r\eta + D_r. \quad (3.15)$$

In order to assure the highest resolution at  $r = 0.5$ , the polynomial needs to satisfy the condition  $\frac{d^2r}{d\eta^2} \Big|_{x=0.5} = 0$ . For convenience, the following conditions were added:

$$\begin{aligned} \text{at } r = 0: \quad & \eta = 0 \\ \text{at } r = 0.5: \quad & \left. \frac{dr}{d\eta} \right|_{x=0.5} = s_r \quad ; \quad \eta = 1. \end{aligned}$$

Again,  $s_r$  is a stretching parameter that can range between zero and one, where  $s_r = 0$  means infinite stretching and  $s_r = 0.5$  means no stretching. Using these conditions, the three constants for the stretching function are given by

$$A_r = -\frac{3}{8} \left( s_r - \frac{1}{2} \right) \quad ; \quad B_r = \frac{5}{4} \left( s_r - \frac{1}{2} \right) \quad ; \quad C_r = \frac{1}{2} - \frac{7}{8} \left( s_r - \frac{1}{2} \right), \quad (3.16)$$

and the stretching function in radial direction is

$$r(\eta) = -\frac{3}{8} \left( s_r - \frac{1}{2} \right) \eta^5 + \frac{5}{4} \left( s_r - \frac{1}{2} \right) \eta^3 + \left[ \frac{1}{2} - \frac{7}{8} \left( s_r - \frac{1}{2} \right) \right] \eta. \quad (3.17)$$

The stretching factor for the radial derivatives is given by

$$\frac{d\eta}{dr}(\eta) = \frac{1}{-\frac{15}{8} \left( s_r - \frac{1}{2} \right) \eta^4 + \frac{15}{4} \left( s_r - \frac{1}{2} \right) \eta^2 + \left[ \frac{1}{2} - \frac{7}{8} \left( s_r - \frac{1}{2} \right) \right]}. \quad (3.18)$$

### 3.3 Discretized Equations

The resulting discretized equations are shown here for the example of the continuity equation for the time  $t = t_0 + l\Delta t$  at the point  $\xi = \xi_0 + m\Delta\xi$  and  $\eta = \eta_0 + n\Delta\eta$ . The continuity equation for the  $k$ -th Fourier mode in the stretched coordinate system is given by

$$\frac{\partial \hat{\rho}_k}{\partial t} = -\frac{d\xi}{dx} \frac{\partial (\widehat{\rho u})_k}{\partial \xi} - \frac{d\eta}{dr} \frac{\partial (\widehat{\rho v})_k}{\partial \eta} - \frac{ik \widehat{(\rho w)}_k}{r(\eta)} - \frac{\widehat{(\rho v)}_k}{r(\eta)}. \quad (3.19)$$

For this equation the discretized Runge-Kutta intermediate steps are:

#### First Predictor:

Forward Euler half step with backward spatial finite differences

$$\hat{\rho}_k^*|_{m,n,l+\frac{1}{2}} = \hat{\rho}_k|_{m,n,l} + \frac{\Delta t}{2} \text{RHS}|_{m,n,l}. \quad (3.20)$$

#### First Corrector:

Backward Euler half step with forward spatial finite differences

$$\hat{\rho}_k^{**}|_{m,n,l+\frac{1}{2}} = \hat{\rho}_k|_{m,n,l} + \frac{\Delta t}{2} \text{RHS}^*|_{m,n,l+\frac{1}{2}}. \quad (3.21)$$

#### Second Predictor:

Midpoint rule full step with backward spatial finite differences

$$\hat{\rho}_k^{***}|_{m,n,l+1} = \hat{\rho}_k|_{m,n,l} + \Delta t \text{RHS}^{**}|_{m,n,l+\frac{1}{2}}. \quad (3.22)$$

#### Second Corrector:

Simpson's rule full step with forward spatial finite differences

$$\begin{aligned} \hat{\rho}_k|_{m,n,l+1} = \hat{\rho}_k|_{m,n,l} & + \frac{\Delta t}{6} \left[ \text{RHS}|_{m,n,l} + 2 \text{RHS}^*|_{m,n,l+\frac{1}{2}} \right. \\ & \left. + 2 \text{RHS}^{**}|_{m,n,l+\frac{1}{2}} + \text{RHS}^{***}|_{m,n,l+1} \right], \end{aligned} \quad (3.23)$$

where the ride hand sides for the intermediate time steps are given by

$$\begin{aligned}
 \text{RHS } |_{m,n,l} = & \\
 - \frac{1}{6\Delta\xi} \frac{d\xi}{dx} \Big|_m & \left[ 7 (\widehat{\rho u})_k \Big|_{m,n,l} - 8 (\widehat{\rho u})_k \Big|_{m-1,n,l} + (\widehat{\rho u})_k \Big|_{m-2,n,l} \right] \\
 - \frac{1}{6\Delta\eta} \frac{d\eta}{dr} \Big|_n & \left[ 7 (\widehat{\rho v})_k \Big|_{m,n,l} - 8 (\widehat{\rho v})_k \Big|_{m,n-1,l} + (\widehat{\rho v})_k \Big|_{m,n-2,l} \right] \\
 - \frac{ik}{r(\eta)} (\widehat{\rho w})_k \Big|_{m,n,l} & - \frac{(\widehat{\rho v})_k \Big|_{m,n,l}}{r(\eta)}, \tag{3.24}
 \end{aligned}$$

$$\begin{aligned}
& \text{RHS}^*|_{m,n,l+\frac{1}{2}} = \\
& - \frac{1}{6\Delta\xi} \frac{d\xi}{dx}|_m \left[ -7 (\widehat{\rho u})_k^*|_{m,n,l+\frac{1}{2}} + 8 (\widehat{\rho u})_k^*|_{m+1,n,l+\frac{1}{2}} - (\widehat{\rho u})_k^*|_{m+2,n,l+\frac{1}{2}} \right] \\
& - \frac{1}{6\Delta\eta} \frac{d\eta}{dr}|_n \left[ -7 (\widehat{\rho v})_k^*|_{m,n,l+\frac{1}{2}} + 8 (\widehat{\rho v})_k^*|_{m,n+1,l+\frac{1}{2}} - (\widehat{\rho v})_k^*|_{m,n+2,l+\frac{1}{2}} \right] \\
& - \frac{ik}{r(\eta)} (\widehat{\rho w})_k^*|_{m,n,l+\frac{1}{2}} - \frac{(\widehat{\rho v})_k^*|_{m,n,l+\frac{1}{2}}}{r(\eta)}, \tag{3.25}
\end{aligned}$$

$$\begin{aligned}
& \text{RHS}^{**}|_{m,n,l+\frac{1}{2}} = \\
& - \frac{1}{6\Delta\xi} \frac{d\xi}{dx}|_m \left[ 7 (\widehat{\rho u})_k^{**}|_{m,n,l+\frac{1}{2}} - 8 (\widehat{\rho u})_k^{**}|_{m-1,n,l+\frac{1}{2}} + (\widehat{\rho u})_k^{**}|_{m-2,n,l+\frac{1}{2}} \right] \\
& - \frac{1}{6\Delta\eta} \frac{d\eta}{dr}|_n \left[ 7 (\widehat{\rho v})_k^{**}|_{m,n,l+\frac{1}{2}} - 8 (\widehat{\rho v})_k^{**}|_{m,n-1,l+\frac{1}{2}} + (\widehat{\rho v})_k^{**}|_{m,n-2,l+\frac{1}{2}} \right] \\
& - \frac{ik}{r(\eta)} (\widehat{\rho w})_k^{**}|_{m,n,l+\frac{1}{2}} - \frac{(\widehat{\rho v})_k^{**}|_{m,n,l+\frac{1}{2}}}{r(\eta)}, \tag{3.26}
\end{aligned}$$

and

$$\begin{aligned}
& \text{RHS}^{***}|_{m,n,l+1} = \\
& - \frac{1}{6\Delta\xi} \frac{d\xi}{dx}|_m \left[ -7 (\widehat{\rho u})_k^{***}|_{m,n,l+1} + 8 (\widehat{\rho u})_k^{***}|_{m+1,n,l+1} - (\widehat{\rho u})_k^{***}|_{m+2,n,l+1} \right] \\
& - \frac{1}{6\Delta\eta} \frac{d\eta}{dr}|_n \left[ -7 (\widehat{\rho v})_k^{***}|_{m,n,l+1} + 8 (\widehat{\rho v})_k^{***}|_{m,n+1,l+1} - (\widehat{\rho v})_k^{***}|_{m,n+2,l+1} \right] \\
& - \frac{ik}{r(\eta)} (\widehat{\rho w})_k^{***}|_{m,n,l+1} - \frac{(\widehat{\rho v})_k^{***}|_{m,n,l+1}}{r(\eta)}. \tag{3.27}
\end{aligned}$$

### 3.4 Integration Domain

For the discretized governing equations, the integration domain (shown in figure 3.2) is two-dimensional. The whole domain is divided into two subdomains. The first part includes part of the boundary layer on the axisymmetric body and extends from the inflow boundary to the base corner and from the wall of the axisymmetric body to the free stream boundary. Adjacent to the first domain, the second part extends from the base to a location downstream of the recirculation region. The second domain extends in the radial direction from the axis of symmetry to the free stream boundary. For the three-dimensional problem this adds an additional boundary at the axis and boundary conditions have to be specified (see the following section).

### 3.5 Discretized Boundary Conditions

As in the previous chapter, the boundary conditions for the discretized problem are divided into the conditions for the axisymmetric case and the conditions for the three-dimensional problem.

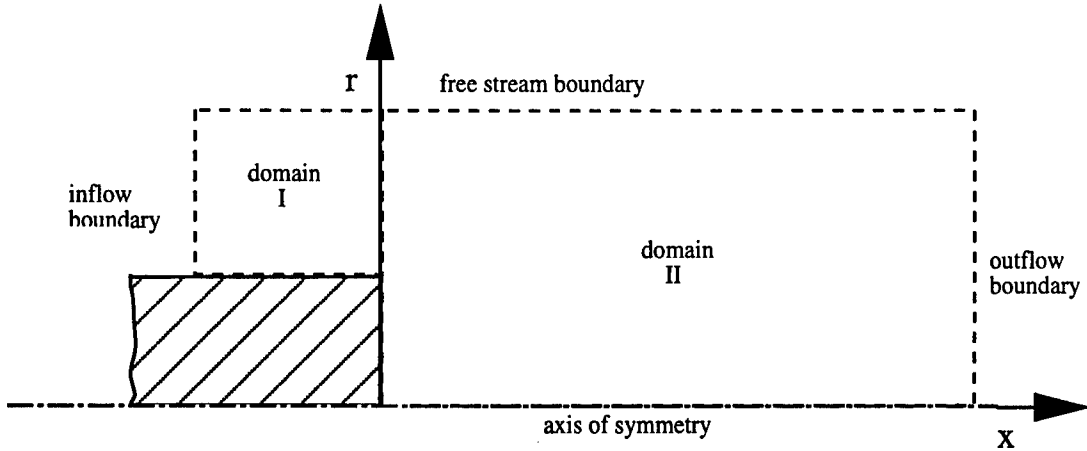


Figure 3.2: Integration domain for the discretized equations

### 3.5.1 Axisymmetric Boundary Conditions

For the given flow field, there are five boundaries, where boundary conditions have to be specified.

#### Inflow

At the inflow boundary all flow variables, except for the pressure within the subsonic layer, are specified, given by a flat plate boundary layer similarity solution. In the subsonic layer the pressure at the inflow boundary is assumed to be constant in streamwise direction and is extrapolated from the flow field, using

$$p_{1,n} = p_{2,n}, \quad \text{if } M_{1,n} < 1. \quad (3.28a)$$

#### Outflow

At the outflow boundary the second derivative in the axial direction,  $\frac{\partial^2 \phi}{\partial \xi^2}$ , is set to zero. This leads to the following fourth-order accurate one-sided finite difference approximations for the first derivatives near the outflow boundary:

$$\left. \frac{\partial \phi}{\partial \xi} \right|_{M-1,n} \approx \frac{34\phi_{M,n} + 3\phi_{M-1,n} - 42\phi_{M-2,n} + 5\phi_{M-3,n}}{66\Delta\xi}, \quad (3.28b)$$

and

$$\left. \frac{\partial \phi}{\partial \xi} \right|_{M,n} \approx \frac{85\phi_{M,n} - 108\phi_{M-1,n} + 27\phi_{M-2,n} - 4\phi_{M-3,n}}{66\Delta\xi}. \quad (3.28c)$$

#### Walls

At the walls, all velocities are set to zero. For the calculation of a steady flow field, the body is assumed to be adiabatic. Therefore the normal gradient of the temperature is zero. For the calculation of an unsteady flow field, the wall temperature is kept constant in time. The pressure at the wall is extrapolated from the flow field, using the wall normal momentum equation. Thus, the conditions are

At the horizontal wall:

$$\begin{aligned}
 v_x|_{m,w} &= 0, \\
 v_r|_{m,w} &= 0, \\
 T_{m,w} &= \frac{1}{137} [300(T_{m,w+1} - T_{m,w+2}) + 200T_{m,w+3} - 75T_{m,w+4} + 12T_{m,w+5}], \\
 &\quad \text{for a steady flow field,} \\
 T_{m,w} &= T_0|_{m,w}, \quad \text{for an unsteady flow field,} \\
 p_{m,w} &= -\tau_{rrm,w} + \frac{1}{137} [300(p_{m,w+1} + \rho_{m,w+1}v_{m,w+1}^2 + \tau_{rrm,w+1} - p_{m,w+2} \\
 &\quad - \rho_{m,w+2}v_{m,w+2}^2 - \tau_{rrm,w+2}) + 200(p_{m,w+3} + \rho_{m,w+3}v_{m,w+3}^2 \\
 &\quad + \tau_{rrm,w+3}) - 75(p_{m,w+4} + \rho_{m,w+4}v_{m,w+4}^2 + \tau_{rrm,w+4}) \\
 &\quad + 12(p_{m,w+5} + \rho_{m,w+5}v_{m,w+5}^2 + \tau_{rrm,w+5})] \\
 &\quad - 60\Delta\eta \left[ \frac{d\xi}{dx}\Big|_m \frac{1}{12\Delta\xi} (\tau_{rxm-2,w} - 8\tau_{rxm-1,w} + 8\tau_{rxm+1,w} - \tau_{rxm+2,w}) \right. \\
 &\quad \left. + \tau_{rrm,w} - \tau_{\theta\theta m,w} \right] \frac{dr}{d\eta}\Big|_w. \tag{3.28d}
 \end{aligned}$$

At the base:

$$\begin{aligned}
 v_x|_{b,n} &= 0, \\
 v_r|_{b,n} &= 0, \\
 T_{b,n} &= \frac{1}{137} [300(T_{b+1,n} - T_{b+2,n}) + 200T_{b+3,n} - 75T_{b+4,n} + 12T_{b+5,n}], \\
 &\quad \text{for a steady flow field,} \\
 T_{b,n} &= T_0|_{b,n}, \quad \text{for an unsteady flow field,} \\
 p_{b,n} &= -\tau_{xxb,n} + \frac{1}{137} [300(p_{b+1,n} + \tau_{xxb+1,n} - p_{b+2,n} - \tau_{xxb+2,n}) \\
 &\quad + 200(p_{b+3,n} + \tau_{xxb+3,n}) - 75(p_{b+4,n} + \tau_{xxb+4,n}) \\
 &\quad + 12(p_{b+5,n} + \tau_{xxb+5,n})] - 60\Delta\xi \left[ \frac{d\eta}{dr}\Big|_n \frac{1}{12\Delta\eta} (\tau_{rxb,n-2} - 8\tau_{rxb,n-1} \right. \\
 &\quad \left. + 8\tau_{rxb,n+1} - \tau_{rxb,n+2}) + \frac{\tau_{rxb,n}}{r(\eta)} \right] \frac{dx}{d\xi}\Big|_b. \tag{3.28e}
 \end{aligned}$$

### Axis

At the axis the symmetry of the flow field is used to determine the flow quantities at locations outside the integration domain. Therefore, it follows

$$\begin{aligned}
 \rho|_{m,-1} &= \rho|_{m,2} \quad ; \quad \rho|_{m,-2} = \rho|_{m,3}, \\
 \rho v_x|_{m,-1} &= \rho v_x|_{m,2} \quad ; \quad \rho v_x|_{m,-2} = \rho v_x|_{m,3},
 \end{aligned}$$

$$\begin{aligned}\rho v_r|_{m,-1} &= -\rho v_r|_{m,2} & ; \rho v_r|_{m,-2} &= -\rho v_r|_{m,3}, \\ \rho e|_{m,-1} &= \rho e|_{m,2} & ; \rho e|_{m,-2} &= \rho e|_{m,3}.\end{aligned}\quad (3.28f)$$

For all  $\frac{\phi}{r}$  terms the rule of l'Hôpital is applied as described in appendix C.

### Free stream

At the free stream boundary, three different boundary conditions are applied, according to the free stream Mach number of the flow field. The conditions are described in detail in Appendix B.

### Initial condition

As initial condition for the calculation of a steady axisymmetric flow field the similarity solution of a compressible flat plate boundary layer is used. In addition, the radial velocity is determined by integration of the steady continuity equation. For the calculation of an unsteady axisymmetric flow field, a previously calculated steady axisymmetric flow field is used as initial condition.

## 3.5.2 Three Dimensional Boundary Conditions

### Inflow

For the three-dimensional (unsteady) calculations, all variables at the inflow boundary are specified. The only exception is the pressure in the subsonic layer, where the first derivative of the pressure is set to zero. So,

$$p_{1,n} = p_{2,n} \quad \text{if} \quad M_{1,n} < 1 . \quad (3.29a)$$

### Outflow

As for the axisymmetric calculations, the second derivatives of all flow quantities are set to zero at the outflow boundary. For the first derivatives, the same difference formulas as for the axisymmetric flow are used.

### Walls

At the walls, all velocities are set to zero. The temperature along the walls is kept constant in time, assuming the body cannot change temperature on the given time scale. The wall pressure is extrapolated in physical space in the same fashion as for the axisymmetric problem. This leads to the following boundary conditions at the azimuthal location  $\theta = h\Delta\theta$ :

At the horizontal wall:

$$\begin{aligned}v_x|_{m,w,h} &= 0, \\ v_r|_{m,w,h} &= 0, \\ v_\theta|_{m,w,h} &= 0,\end{aligned}$$

$$\begin{aligned}
T_{m,w,h} &= T_0|_{m,w,h}, \\
p_{m,w,h} &= -\tau_{rrm,w,h} + \frac{1}{137} \left[ 300 \left( p_{m,w+1,h} + \rho_{m,w+1,h} v_{m,w+1,h}^2 + \tau_{rrm,w+1,h} \right. \right. \\
&\quad \left. \left. - p_{m,w+2,h} - \rho_{m,w+2,h} v_{m,w+2,h}^2 - \tau_{rrm,w+2,h} \right) \right. \\
&\quad + 200 \left( p_{m,w+3,h} + \rho_{m,w+3,h} v_{m,w+3,h}^2 + \tau_{rrm,w+3,h} \right) \\
&\quad - 75 \left( p_{m,w+4,h} + \rho_{m,w+4,h} v_{m,w+4,h}^2 + \tau_{rrm,w+4,h} \right) \\
&\quad \left. + 12 \left( p_{m,w+5,h} + \rho_{m,w+5,h} v_{m,w+5,h}^2 + \tau_{rrm,w+5,h} \right) \right] \\
&\quad - 60\Delta\eta \frac{dr}{d\eta} \Big|_w \left[ \frac{d\xi}{dx} \Big|_m \frac{1}{12\Delta\xi} (\tau_{rxm-2,w,h} - 8\tau_{rxm-1,w,h} \right. \\
&\quad \left. + 8\tau_{rxm+1,w,h} - \tau_{rxm+2,w,h}) + \tau_{rrm,w,h} - \tau_{\theta\theta m,w,h} + \frac{\partial\tau_{\theta r}}{\partial\theta} \Big|_{m,w,h} \right], 
\end{aligned} \tag{3.29b}$$

where the azimuthal derivative  $\frac{\partial\tau_{\theta r}}{\partial\theta} \Big|_{m,w,h}$  is calculated in Fourier space and then transformed into physical space.

At the base:

$$\begin{aligned}
v_x|_{b,n,h} &= 0, \\
v_r|_{b,n,h} &= 0, \\
v_\theta|_{b,n,h} &= 0, \\
T_{b,n,h} &= T_0|_{b,n,h}, \\
p_{b,n,h} &= -\tau_{xxb,n,h} + \frac{1}{137} \left[ 300 (p_{b+1,n,h} + \tau_{xxb+1,n,h} - p_{b+2,n,h} - \tau_{xxb+2,n,h}) \right. \\
&\quad + 200 (p_{b+3,n,h} + \tau_{xxb+3,n,h}) - 75 (p_{b+4,n,h} + \tau_{xxb+4,n,h}) \\
&\quad \left. + 12 (p_{b+5,n,h} + \tau_{xxb+5,n,h}) \right] - 60\Delta\xi \frac{dx}{d\xi} \Big|_b \left[ \frac{d\eta}{dr} \Big|_n \frac{1}{12\Delta\eta} (\tau_{rxb,n-2,h} \right. \\
&\quad - 8\tau_{rxb,n-1,h} + 8\tau_{rxb,n+1,h} - \tau_{rxb,n+2,h}) \\
&\quad \left. + \frac{1}{r(\eta)} \left( \tau_{rxb,n,h} + \frac{\partial\tau_{\theta x}}{\partial\theta} \Big|_{b,n,h} \right) \right]. 
\end{aligned} \tag{3.29c}$$

### Axis

The Fourier expansion of the three-dimensional governing equations results in an additional boundary at the axis of symmetry. Therefore, a set of boundary conditions has to be described for the discretized equations. At the axis, the even Fourier modes are of symmetric nature and the odd modes are of antisymmetric nature. They can be prescribed at the boundary as follows. The derivation of the boundary conditions for the different Fourier modes is described in detail in appendix C.

$$k = 0$$

The boundary conditions for Fourier mode  $k = 0$  are exactly the same as for the

axisymmetric case,

$$\begin{aligned}\hat{\rho}|_{m,-1,0} &= \hat{\rho}|_{m,2,0} & ; \quad \hat{\rho}|_{m,-2,0} &= \hat{\rho}|_{m,3,0}, \\ \widehat{\rho v_x}|_{m,-1,0} &= \widehat{\rho v_x}|_{m,2,0} & ; \quad \widehat{\rho v_x}|_{m,-2,0} &= \widehat{\rho v_x}|_{m,3,0}, \\ \widehat{\rho v_r}|_{m,-1,0} &= -\widehat{\rho v_r}|_{m,2,0} & ; \quad \widehat{\rho v_r}|_{m,-2,0} &= -\widehat{\rho v_r}|_{m,3,0}, \\ \widehat{\rho e}|_{m,-1,0} &= \widehat{\rho e}|_{m,2,0} & ; \quad \widehat{\rho e}|_{m,-2,0} &= \widehat{\rho e}|_{m,3,0},\end{aligned}\tag{3.29d}$$

while for  $k = 1$

$$\begin{aligned}\hat{\rho}|_{m,1,1} &= 0, \\ \widehat{\rho v_x}|_{m,1,1} &= 0, \\ \widehat{\rho v_r}|_{m,1,1} + i \widehat{\rho v_\theta}|_{m,1,1} &= 0, \\ \widehat{\rho e}|_{m,1,1} &= 0,\end{aligned}\tag{3.29e}$$

and for  $k \geq 2$

$$\begin{aligned}\hat{\rho}|_{m,1,k} &= 0, \\ \widehat{\rho v_x}|_{m,1,k} &= 0, \\ \widehat{\rho v_r}|_{m,1,k} &= 0, \\ \widehat{\rho v_\theta}|_{m,1,k} &= 0, \\ \widehat{\rho e}|_{m,1,k} &= 0.\end{aligned}\tag{3.29f}$$

For all  $\frac{\phi}{r}$  terms the rule of l'Hôpital is applied as described in appendix C.

### Free stream

As for the axisymmetric flow, three different types of boundary conditions are applied at the free stream boundary, according to the free stream Mach number. These are described in more detail in appendix B.

### Initial condition

As initial condition a previously calculated steady axisymmetric flow field is used.

## 3.6 Filtering

For the Large-Eddy Simulations the flow quantities  $\bar{\rho}$ ,  $\bar{\rho v_x}$ ,  $\bar{\rho v_r}$ , and  $\bar{\rho v_\theta}$  are filtered at every Runge-Kutta stage. In the present research a sixth-order compact filter has been chosen [see, for example, [Lele (1992)]]]. This filter has been tested extensively by [Bachman (1996)]. As an example, the equation for a quantity filtered in the axial direction at a given location ( $x_i$ ) is

$$\begin{aligned}\beta_F \bar{f}_{i-2} + \alpha_F \bar{f}_{i-1} + \bar{f}_i + \alpha_F \bar{f}_{i+1} + \beta_F \bar{f}_{i+2} \\ = af_i + \frac{b}{2}(f_{i-1} + f_{i+1}) + \frac{c}{2}(f_{i-2} + f_{i+2}) + \frac{d}{2}(f_{i-3} + f_{i+3})\end{aligned}\tag{3.30}$$

where  $f_i$  are the unfiltered quantities and  $\bar{f}_i$  are the filtered quantities.

The coefficients are given by

$$\begin{aligned}\alpha_F &= 0.6522474 & \beta_F &= 0.1702929 \\ a &= (2 + 3\alpha_F)/4 & b &= (9 + 16\alpha_F + 10\beta_F)/16 \\ c &= (\alpha_F + 4\beta_F)/4 & d &= (6\beta_F - 1)/16\end{aligned}\quad (3.31)$$

This filter has been successfully used for Large-Eddy Simulations of incompressible flat plate boundary layers by [Bachman (1996)].

At all Reynolds numbers calculated in the present research, the boundary layer approaching the corner of the base remained laminar and turbulence modeling was not needed in that region. The filtering, thus, is applied solely in the second subdomain, downstream of the base of the axisymmetric body. In the transition region between the two domains, the turbulence model is slowly ramped in, using the same formula as for the wall damping function (see section 2.4.7).

### 3.7 Disturbance Generation

For the unsteady (disturbed) calculations, disturbances are introduced into the flow field. In general, there are two different types of disturbances that can be generated, pulse disturbances and continuous disturbances. The main difference between the two types of disturbances lies in their frequency spectra. A continuous disturbance typically has a fixed frequency and thus, only an isolated single frequency disturbance is introduced into the flow field (see figure 3.3). This allows the investigation of the stability behavior for one given frequency.

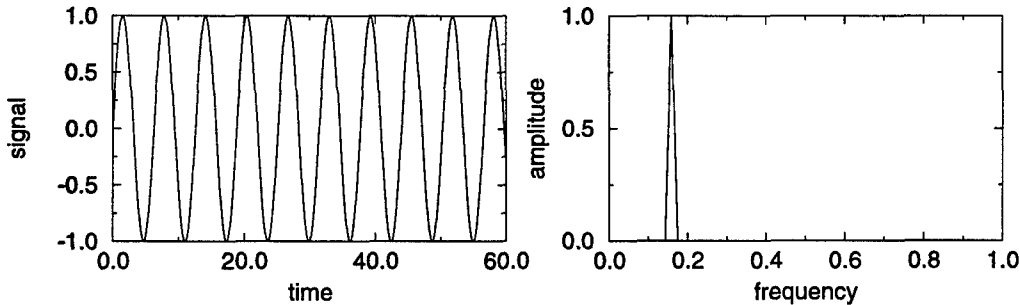


Figure 3.3: Continuous disturbance; time signal (left) and Fourier transform (right).

On the other hand, a pulse disturbance generates a broad spectrum of frequencies in the flow field. The broadness of the spectrum depends on the length of the pulse (see figure 3.4 and figure 3.5). Thus, the broadest spectrum, or in other words the widest frequency band, is generated by a single spike disturbance in time (see figure 3.6).

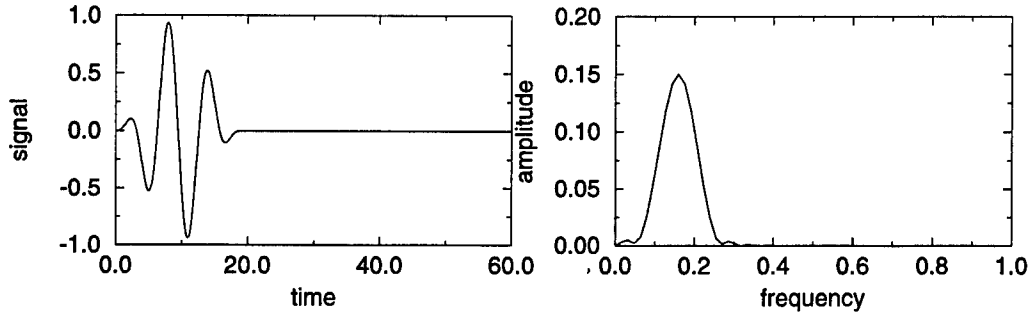


Figure 3.4: Single pulse disturbance over three periods; time signal (left) and Fourier transform (right).

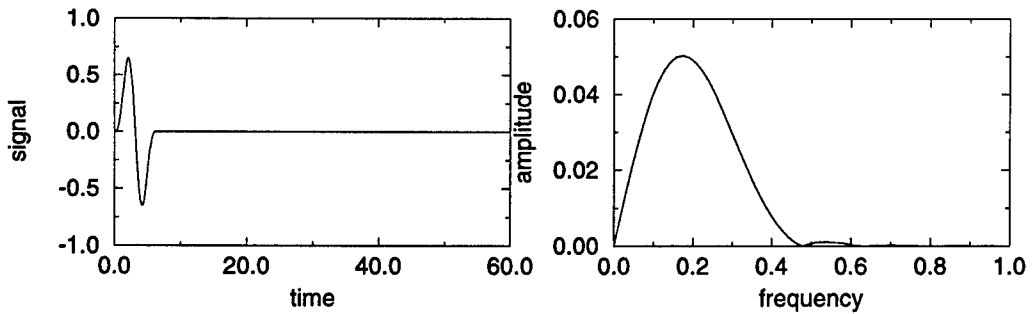


Figure 3.5: Single pulse disturbance over one period; time signal (left) and Fourier transform (right).

### 3.7.1 Continuous Disturbances

Disturbances of different Fourier modes are introduced into the flow field by radial blowing and suction through a circular slot near the base of the axisymmetric body (see figure 3.7). When a normal velocity distribution of the form shown in figure 3.7 is used, the net mass flow through the disturbance slot is zero at every instant of time. This technique produces predominantly vorticity disturbances and only to a lesser extent undesirable "sound" disturbances. The disturbances first develop within the boundary layer region and then travel into the free shear layer region and the recirculation zone.

By varying the real and imaginary parts of the Fourier component of the disturbed radial velocity at the blowing and suction slot, rotating disturbances can be introduced, thus producing a helical wave that travels downstream. It has been shown for incompressible wake flows that the flow field is unstable with respect to these helical disturbances [see, for example, [Schwarz (1996)]].

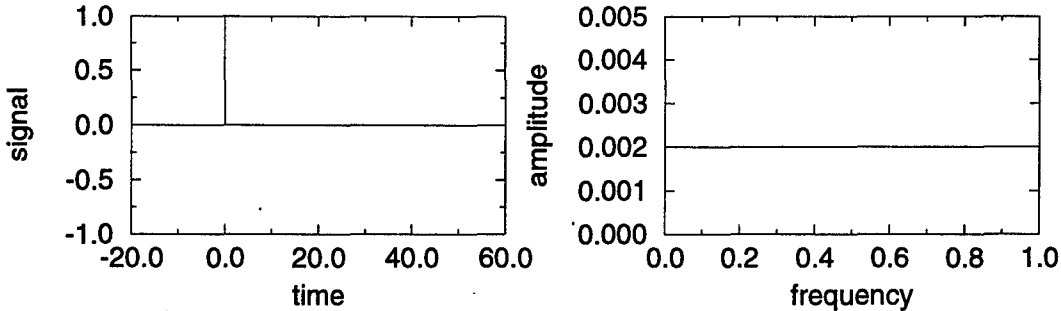


Figure 3.6: Spike disturbance; time signal (left) and Fourier transform (right).

### 3.7.2 Pulse Disturbances

A pulse disturbance can also be introduced through the blowing and suction slot, by varying the amplitude over time. This generates a wave packet and allows investigation of the disturbance behavior for a spectrum of frequencies as the wave packet travels downstream.

In addition to blowing and suction, a second method is used for the generation of pulse disturbances. In this case, a discrete pulse is introduced locally into the flow field at a location within the recirculation region. Usually, a pulse in form of a single spike in the first azimuthal Fourier mode of the density at a specified grid point and only one instance in time is used. This method generates disturbances with the broadest possible spectrum of frequencies. It is mainly used to investigate the existence and behavior of absolute instabilities.

## 3.8 Computational Procedure

For the investigation of the behavior of three dimensional flow disturbances, an axisymmetric initial undisturbed flow field has to be determined. Since no similarity solution exists for the compressible axisymmetric wake, the first step in the computational procedure is to calculate a steady flow field using an unsteady axisymmetric Navier-Stokes program. As initial condition for this axisymmetric calculation, a similarity solution for a compressible flat plate boundary layer is used. The unsteady calculation is terminated once the temporal changes of the flow variables are much smaller than the expected disturbance amplitudes.

This axisymmetric flow field is then used as initial condition for the three dimensional disturbance calculation . Disturbances are introduced either through a blowing and suction slot along the circular body near the base or locally into the flow field as a single pulse of width  $\Delta t$  (see section 3.7). The time dependent evolution of the disturbances is monitored over several time periods to investigate growth or decay and influences on the global flow field.

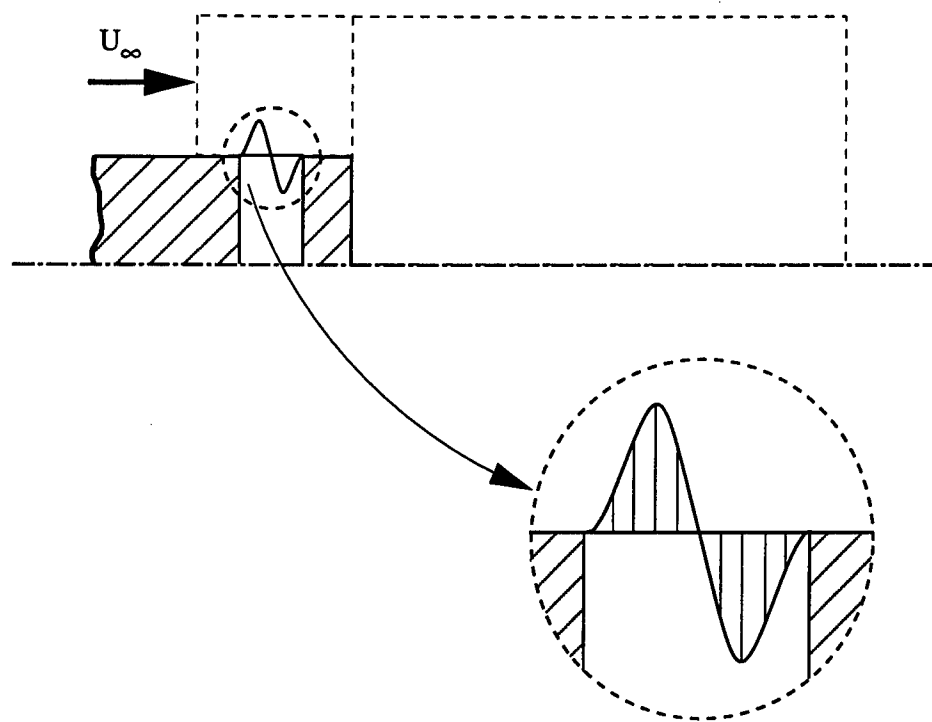


Figure 3.7: Disturbance generation through a blowing and suction slot.

For sufficiently high Reynolds numbers, local regions of very high velocity gradients appear in the flow field. In that case, the calculation with DNS is terminated before the gradients become so large that they would cause numerical instability and eventually a termination of the program. The instantaneous flow field at this point is used as an initial condition for a Large-Eddy Simulation.

# Chapter 4

## Code Validation

At the present time, no data are available for supersonic axisymmetric wake flow fields in the Reynolds number range between  $Re_D = 500$  and  $Re_D = 30,000$ . Therefore, most of the code validation was performed by comparing the results of very low Mach number subsonic calculations to DNS data for an incompressible axisymmetric wake that was obtained by [Schwarz (1996)] [see also [Schwarz et al. (1994)]] and by further comparison to experimental results that were obtained in our own water channel by [Siegel (1996)]. In addition, for supersonic flow a step size analysis was performed for the axisymmetric flow case.

### 4.1 Axisymmetric Flow

As a first step, the code validation was performed for steady and unsteady axisymmetric flow calculations. The code validation was done for a low Mach number subsonic flow by comparison with results from incompressible calculations and from experiments. For supersonic flow a step size analysis was performed, because of the lack of experimental data and previous numerical results.

#### 4.1.1 Subsonic Flow Fields

For validation of the Navier-Stokes code for the steady (undisturbed) axisymmetric flow, the flow field for a free stream Mach number of  $M_\infty = 0.2$  and a global Reynolds number of  $Re_D = 1,000$  was calculated for two different spatial resolutions. In both cases the grid was stretched in the axial and radial directions with the same stretching factor. The results were compared to results from a calculation for an incompressible axisymmetric wake by [Schwarz (1996)]. For the incompressible calculations no grid stretching was used. The parameters for the incompressible calculation by Schwarz (1996) and cases A1 and A2 of the current compressible calculations are listed in table A.1.

For comparisons of the compressible and the incompressible simulations, the length of the recirculation zone was chosen as a global characteristic of the steady flow field, and the azimuthal vorticity at the corner of the base was chosen as a local characteristic. The recirculation length,

which is the distance of the free stagnation point from the base, for the current calculation is

$$L_{rec} \cong 2.1, \quad (4.1)$$

for all three cases. Thus, both compressible calculations compare very well with the result of the incompressible calculations. Figures 4.1 and 4.2 show the steady streamlines for both validation cases. The streamlines clearly exhibit the region of recirculation. From the corner of the base, the flow separates geometrically and bends gradually towards the axis of symmetry. The free stagnation point can be found at  $x = 2.1$  for both grid resolutions. Both cases show basically identical streamlines and are in very good agreement with the incompressible results.

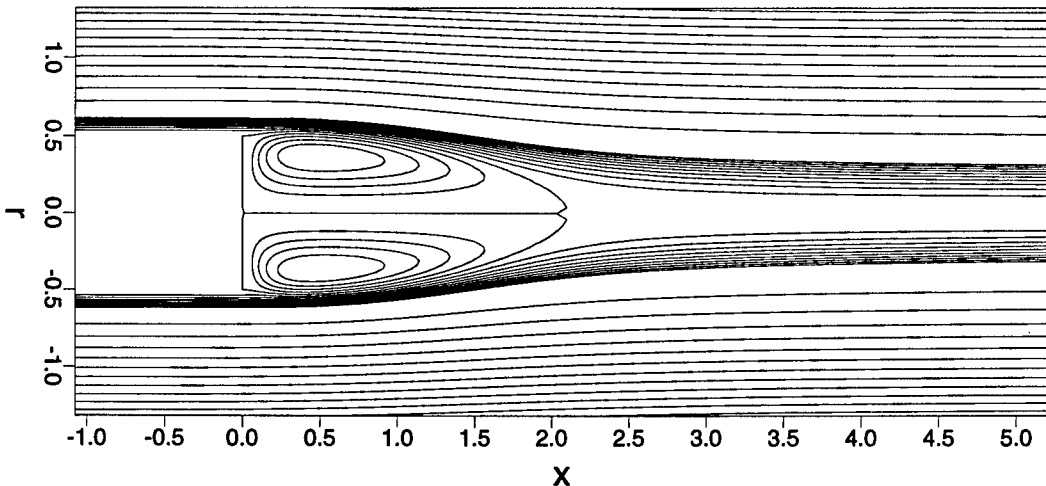


Figure 4.1: Steady streamlines for validation case A1.

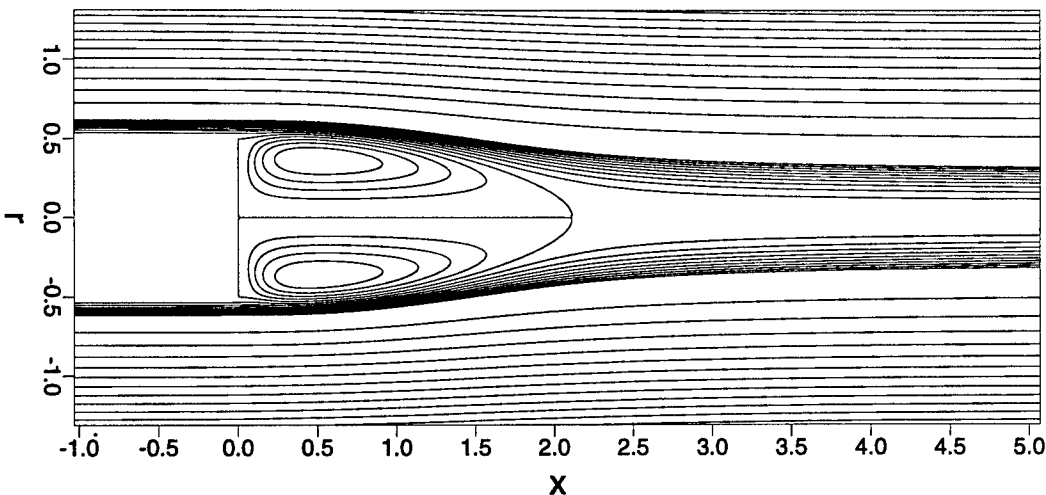


Figure 4.2: Steady streamlines for validation case A2.

The azimuthal vorticity at the corner of the base, which is defined as

$$\vec{\omega} = -\nabla \times \vec{u}, \quad (4.2)$$

turns out to be dependent on the grid resolution at the corner in both the incompressible and the compressible calculations. At the corner one-sided differences have been used for approximation of the spatial derivatives of the velocity. For the incompressible calculation, corner vorticity was found to be

$$\omega_{\theta,\text{incomp}}|_{x=0,r=0.5} = 6.8, \quad (4.3)$$

whereas for cases A1 and A2 the values are

$$\omega_{\theta,1}|_{x=0,r=0.5} = 7.2, \quad \text{and} \quad \omega_{\theta,2}|_{x=0,r=0.5} = 7.6. \quad (4.4)$$

Considering the different resolution in the three cases and the different methods, the values are in reasonable agreement. Figures 4.3 and 4.4 show isolines of azimuthal vorticity for the two compressible validation cases. In both plots, the vorticity levels for the isolines are identical ( $|\omega_{\theta}| = 1, 2, 3, \dots$ ). The lines in the two cases are almost identical and also coincide with the plot shown in Schwarz (1996). In conclusion, the agreement for the steady axisymmetric flow for the case of a very low subsonic free stream Mach number is very good.

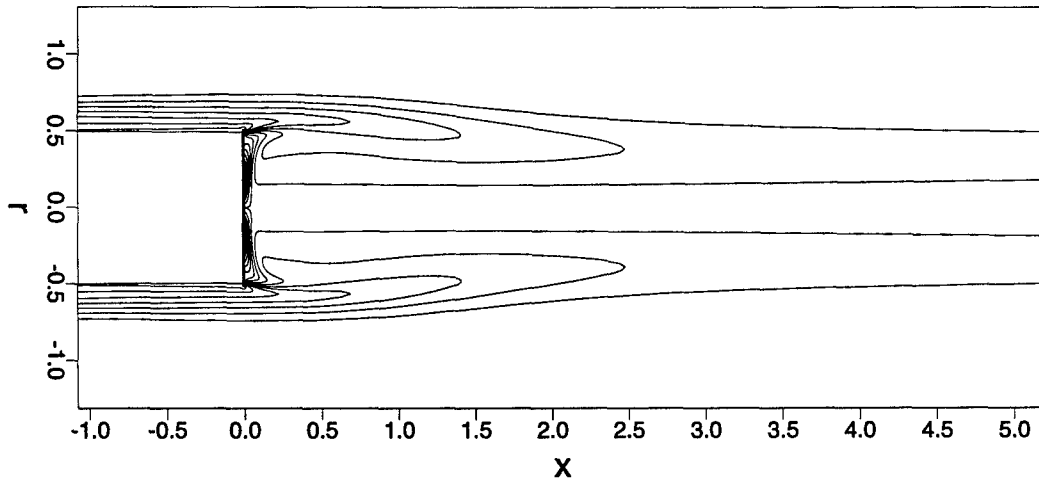


Figure 4.3: Steady azimuthal vorticity field for validation case A1.

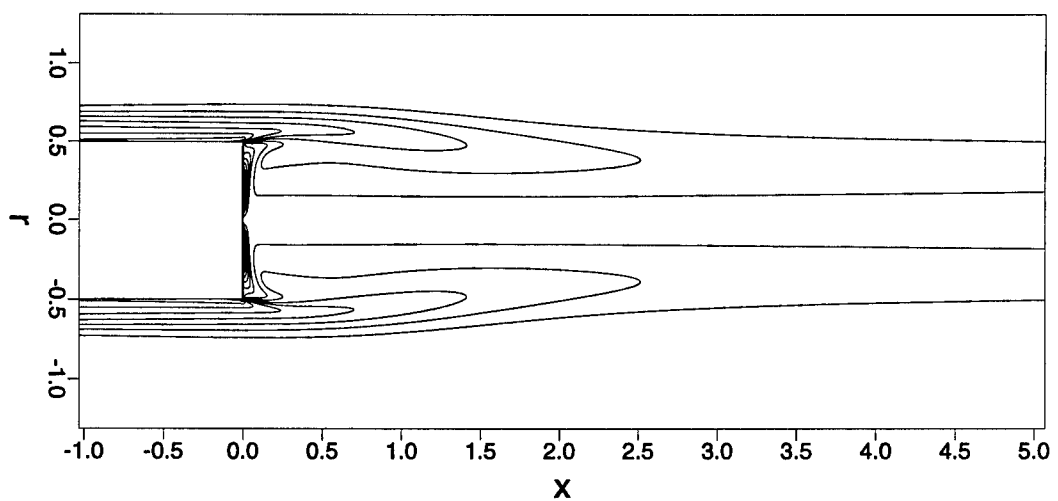


Figure 4.4: Steady azimuthal vorticity field for validation case A2.

For validation of the Navier-Stokes code for the unsteady (disturbed) axisymmetric flow, the response of the subsonic flow field of case A1 (obtained from the steady calculation as discussed above) to a small axisymmetric disturbance was calculated (case A3). In this calculation, the steady axisymmetric flow was disturbed with a continuous axisymmetric disturbance at a frequency of  $\beta = 1.0$ . The disturbance was generated through a blowing and suction slot as described in section 3.6. The amplitude of the blowing and suction distribution was 0.001 percent of the free stream velocity. Therefore, a linear behavior of the generated disturbance wave can be expected.

The calculation was carried out until the entire flow field reached a time periodic state. At this point the spatial development of the disturbance waves in the wake region was investigated to obtain the spatial growth rates. Figure 4.6 shows the spatial growth rate of the disturbance frequency versus downstream location. For comparison with the incompressible calculations the disturbance waves were monitored in the form of the square root of the kinetic disturbance energy. Assuming a behavior of the disturbance waves of the form

$$\sqrt{E} = Ae^{-i(\alpha x - \beta t)}, \quad (4.5)$$

with complex  $\alpha$  and  $\beta$ , the spatial growth rate is given by the imaginary part of the wavenumber as follows

$$-\alpha_i = \frac{\partial}{\partial x} [\ln (\sqrt{E})], \quad (4.6)$$

where

$$E = \int_0^{r_{max}} [v_x'^2 + v_r'^2] r dr. \quad (4.7)$$

The results show a region of positive growth (denoted by a negative  $\alpha_i$ ), which reaches up to about 1.2 diameters downstream of the base. Downstream of this location the disturbances are damped and eventually die out. Comparing these growth rates to linear stability theory and incompressible calculations [Figure 4.4 in Schwarz (1996)] very good agreement was found (see figure 4.5). Thus, also for the unsteady axisymmetric calculations very good agreement was found between the compressible and the incompressible calculations.

#### 4.1.2 Supersonic Flow Fields

As mentioned earlier, no experimental data are available for supersonic wakes in the Reynolds number regime that is applicable for Direct Numerical Simulations. For that reason a step-size investigation was performed for an axisymmetric flow at a free stream Mach number of  $M_\infty = 2.46$  and a global Reynolds number of  $Re_D = 30,000$ . The flow field was calculated for two different spatial resolutions. The computational parameters for both cases (A4 and A5) are given in table A.1.

Comparisons were made for the axial and radial velocities, the density, the pressure, the temperature and the local Mach number. The results in form of isolines are shown in figures 4.6 through 4.11, respectively. In all the figures, the results for the lower resolution (case A4)

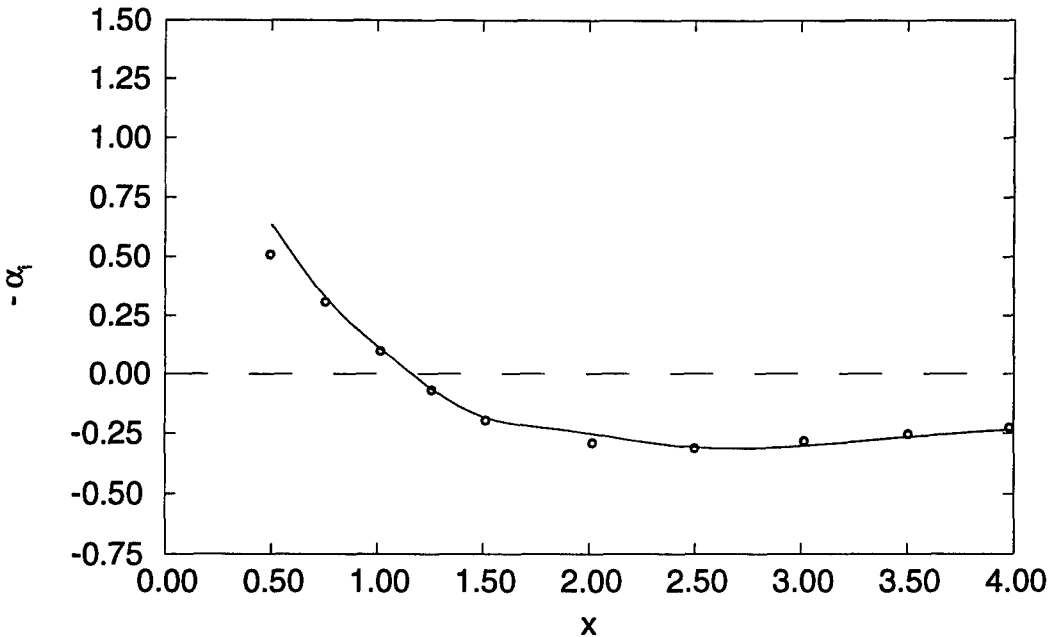


Figure 4.5: Spatial growth rate  $\alpha_i$  for an axisymmetric disturbance of  $\beta_r = 1.0$ ,  $\beta_i = 0.0$ ;  $Re_D = 1,000$  [circles from Linear Stability Theory by Schwarz (1996)].

are shown at the top and for the higher resolution (case A5) below. All flow quantities show excellent agreement between the two different cases. The wiggles at some isolines for the pressure in the lower resolved case (see figures 4.7 through 4.9) are due to the plotting software (linear interpolation). These results indicate that the lower resolution was sufficient for the calculation of this flow field. Coincidentally, this resolution was the lowest possible to avoid numerical instabilities in the calculations.

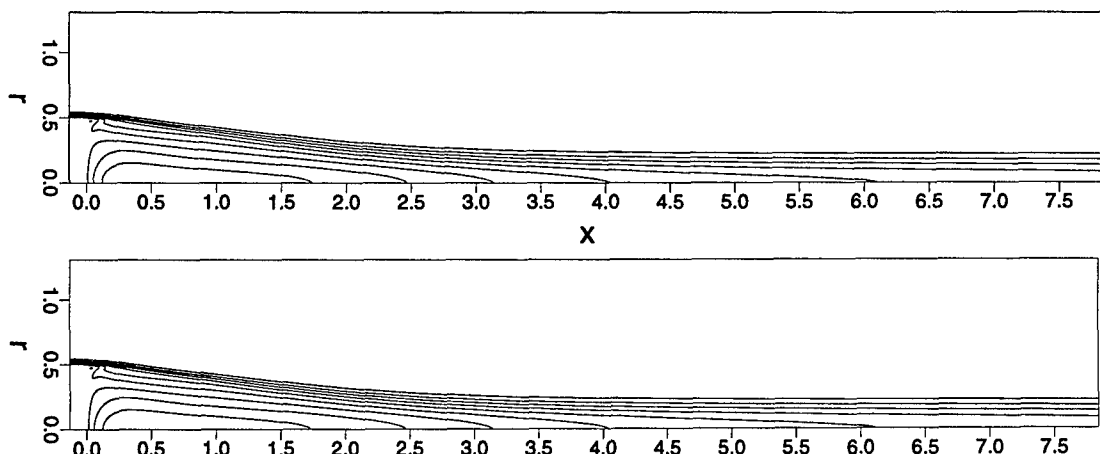


Figure 4.6: Isolines of axial velocity at  $M_\infty = 2.46$  and  $Re_D = 30,000$  for two different spatial resolutions [Cases A4 (top) and A5 (below)].

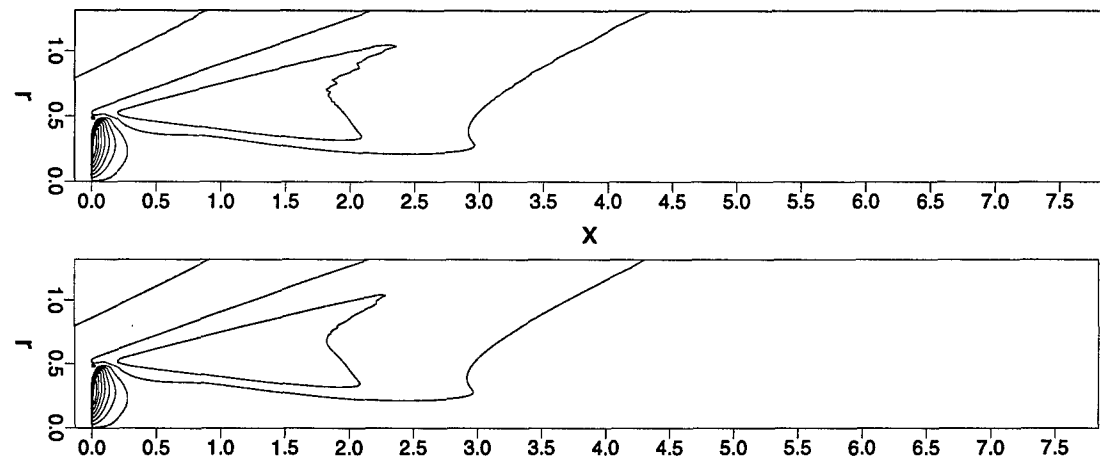


Figure 4.7: Isolines of radial velocity at  $M_\infty = 2.46$  and  $Re_D = 30,000$  for two different spatial resolutions [Cases A4 (top) and A5 (below)].

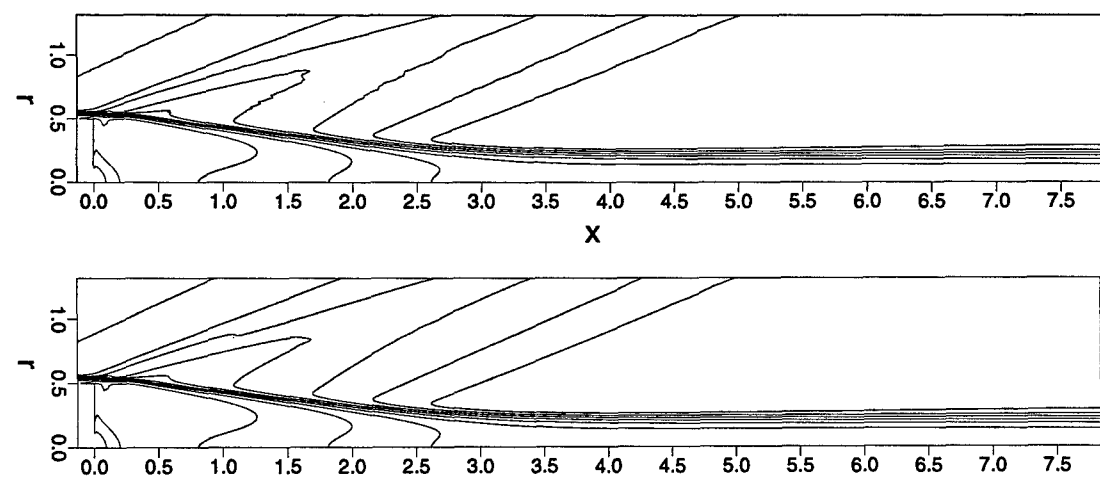


Figure 4.8: Isolines of density at  $M_\infty = 2.46$  and  $Re_D = 30,000$  for two different spatial resolutions [Cases A4 (top) and A5 (below)].

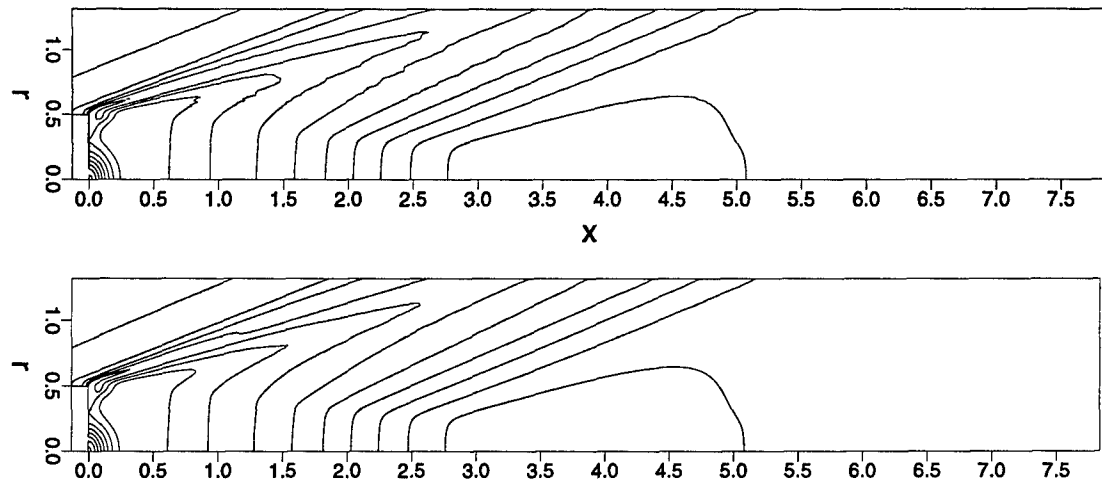


Figure 4.9: Isolines of pressure at  $M_\infty = 2.46$  and  $Re_D = 30,000$  for two different spatial resolutions [Cases A4 (top) and A5 (below)].

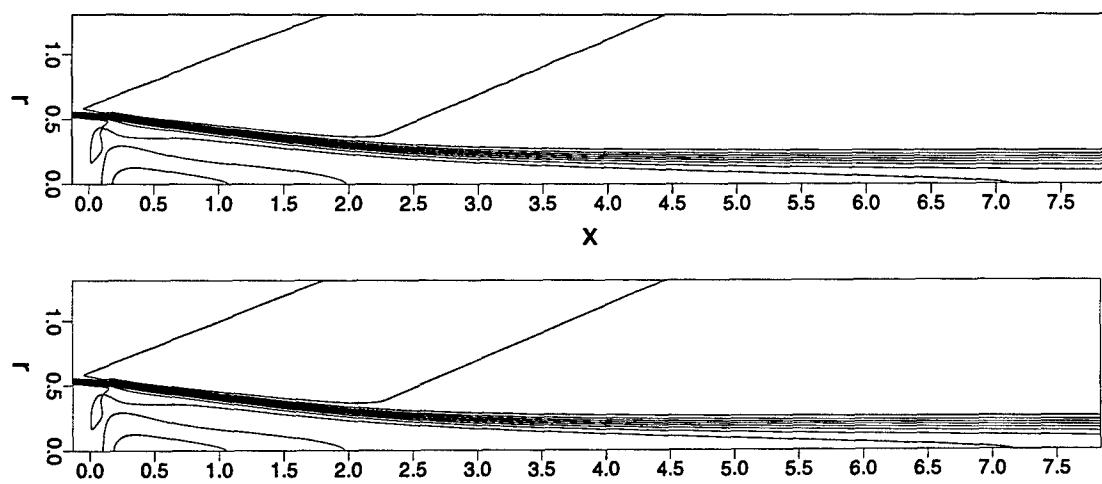


Figure 4.10: Isolines of temperature at  $M_\infty = 2.46$  and  $Re_D = 30,000$  for two different spatial resolutions [Cases A4 (top) and A5 (below)].

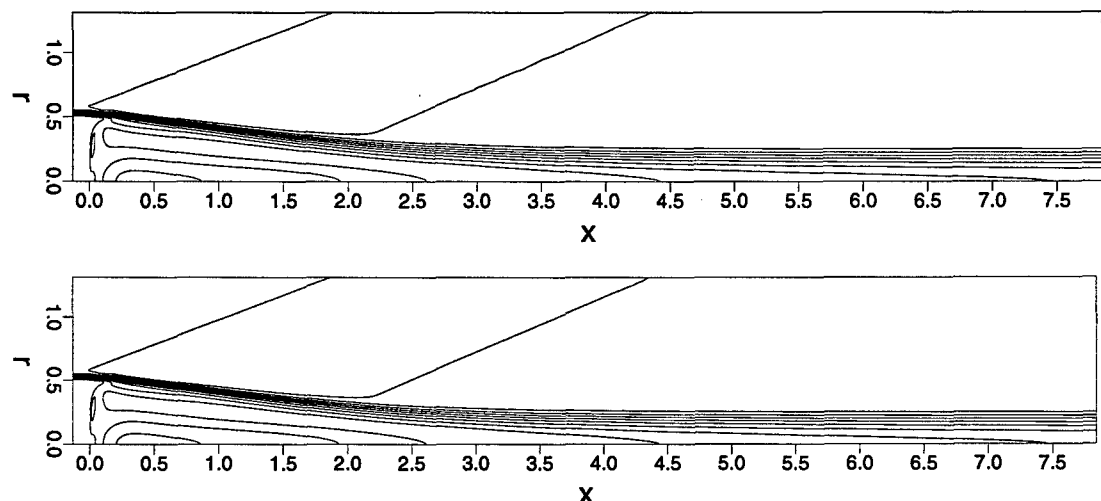


Figure 4.11: Isolines of local Mach number at  $M_\infty = 2.46$  and  $Re_D = 30,000$  for two different spatial resolutions [Cases A4 (top) and A5 (below)].

## 4.2 Three-dimensional Flow

A more thorough validation would be desirable at this point for the codes used for the calculation of three-dimensional, time dependent supersonic flow. However, the three-dimensional simulations at the chosen resolution for the supersonic flows were already very CPU time and memory intensive (see chapter 5). A three-dimensional calculation at the given resolution of case A4 typically required 600 MBytes of main memory and in the order of 1,000 CPU hours on a CRAY C90. Therefore, the three-dimensional code was validated for a subsonic flow at  $M_\infty = 0.2$  and  $Re_D = 1,000$ .

For the validation of the Navier-Stokes code for calculating the three-dimensional unsteady (disturbed) flow, the response of the subsonic flow field of case A1 (obtained from the steady calculation as discussed above) to a three dimensional disturbance input was calculated and the results were compared to results from incompressible calculations by [Schwarz (1996)] and to water channel experiments carried out in the Hydrodynamic Laboratory at the University of Arizona. The simulation was performed with up to eight complex Fourier modes in azimuthal direction and the same spatial resolution as for case A1.

### 4.2.1 Absolute Instability

For a first calculation (case T1), the flow was disturbed with a pulse disturbance of the frequency  $\beta = 0.1$  through the blowing and suction slot. The pulse had a duration of two full periods and was ramped up and down in time, using a  $\sin^2$  function. In a second calculation, the flow was disturbed only at the very first time step locally within the recirculation region (as described in section 3.6) at  $x = 0.25$  and  $r = 0.25$ . The flow response is similar for both the compressible and the incompressible calculations.

In incompressible simulations, [Schwarz (1996)] found that for the global Reynolds number  $Re_D = 1,000$  the flow field includes a region of absolute instability with regard to helical disturbances of the first azimuthal Fourier mode. Figure 4.12 shows the time response of the radial momentum at the centerline in the near wake, half a radius downstream of the base. In this case, the disturbance was generated through blowing and suction. The response clearly shows an exponential growth of the disturbance, which indicates the existence of an absolute instability, as has been found in the incompressible simulations.

For a second calculation (case T2), a disturbance was generated by a single pulse in the near wake region, as explained before. Figure 4.13 shows the time response of the flow in the form of the radial momentum of four different azimuthal Fourier modes at the location of the disturbance input. In this case the flow starts to deviate from the axisymmetric state and the signal keeps oscillating in time in a non-periodic fashion. This was also observed for the incompressible calculations. From this point, quantitative comparison is not very meaningful, since the fluctuations are not periodic.

Therefore, the comparison of the instantaneous flow field with experiments and incompressible simulations can only be of a qualitative nature. For this qualitative comparison, particles

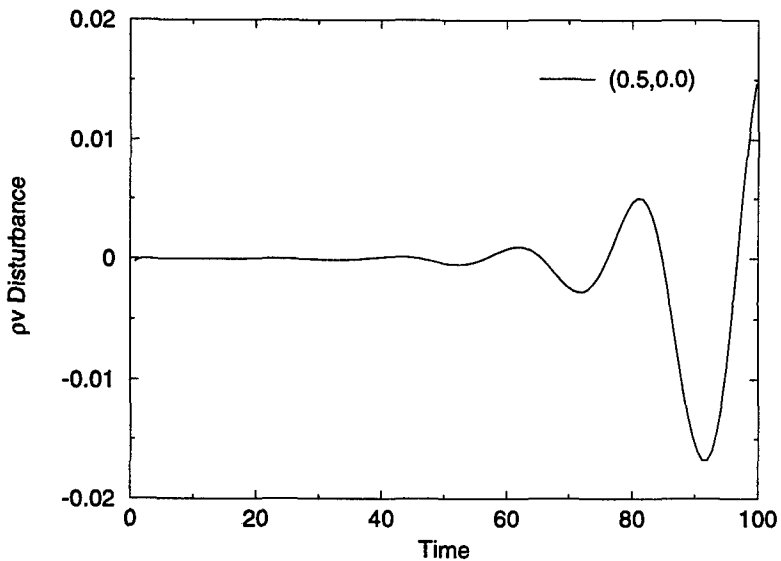


Figure 4.12: Time response of radial momentum at  $r=0$  to a three dimensional blowing and suction pulse disturbance in the near wake at  $M_\infty = 0.2$  and  $Re_D = 1,000$ .

have been released into the flow. The method is described in section 5.1.1. Figure 4.14 shows side views of the instantaneous flow field. The views are perpendicular to each other. They show that the flow is symmetric to the  $x$ - $y$  plane ( $\theta = 0$ ). This phenomenon could also be observed in experiments and incompressible simulations as presented by Schwarz.

Comparing the structures to pictures shown in Schwarz (1996) a good similarity in the shape of the structures is seen. For further simulations this symmetry was prescribed, so that only half of the points in physical space need to be calculated and main memory and CPU time are saved. In figure 4.15, cuts through the  $y$ - $z$  plane at four different  $x$  locations are presented. The plots show structures very similar to the structures that have been observed in water channel experiments by [Siegel (1994)] [see, for example, figure 4.16]. To further investigate the development of the disturbances and allow a better comparison with the experimental results, the flow was disturbed by a periodic disturbance [see section 4.2.2].

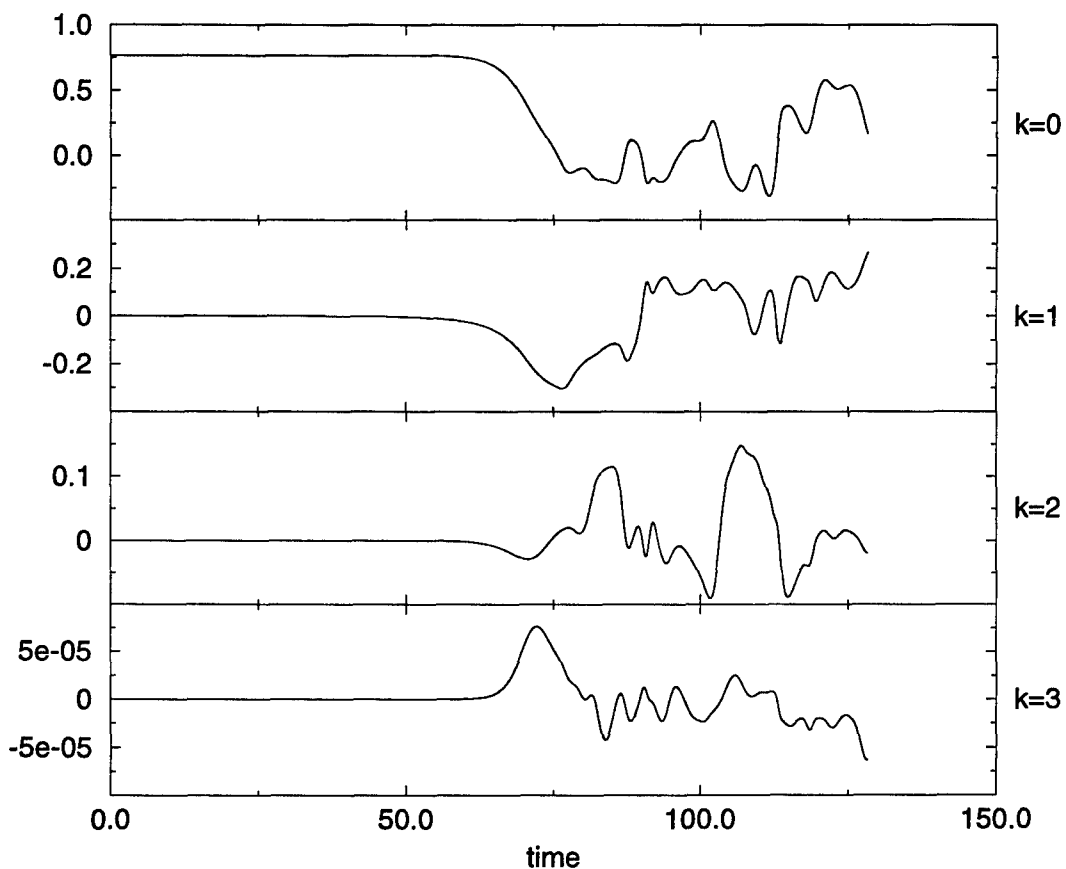


Figure 4.13: Time response of radial momentum to a single pulse of Fourier mode  $k = 1$  at  $r=0.25$  and  $z= 0.25$  at  $M_\infty = 0.2$  and  $Re_D = 1,000$ .

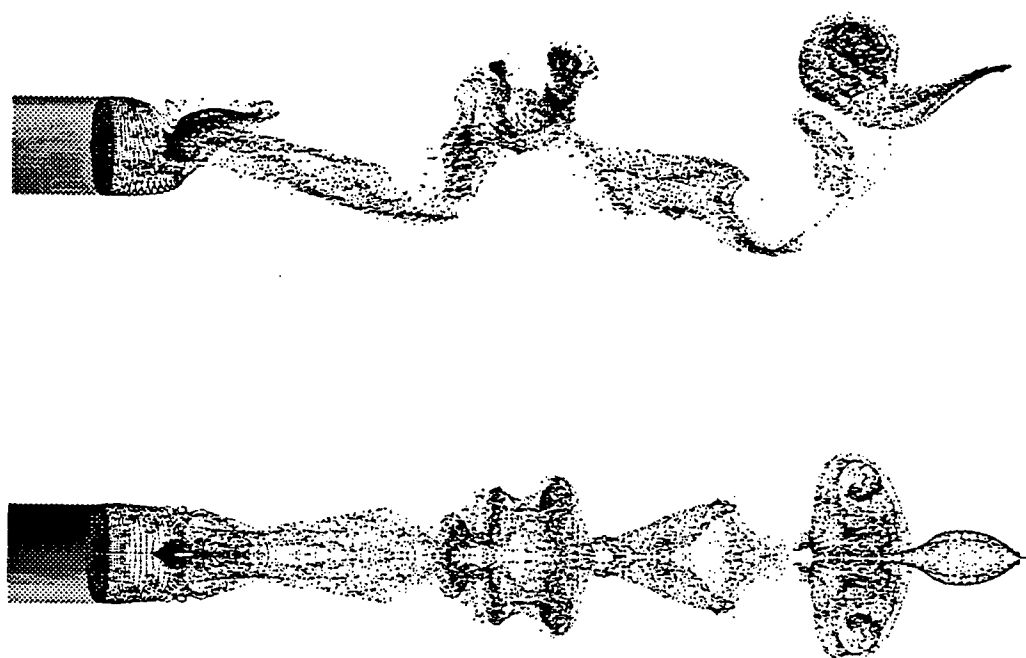


Figure 4.14: Flow visualization via particles at  $M_\infty = 0.2$  and  $Re_D = 1,000$ , viewed from  $\theta = \pi/2$  (top) and from  $\theta = 0$  (bottom).



Figure 4.15: Flow visualization via particles at  $M_\infty = 0.2$  and  $Re_D = 1,000$ , cross-sectional cut at  $x = 2.0$ .

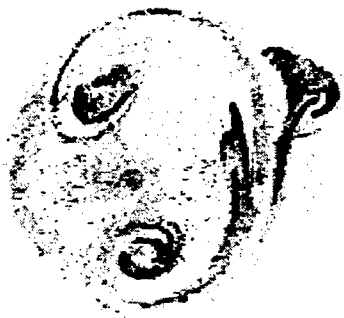


Figure 4.16: Flow visualization via particles for  $Re_D = 1,000$ , cross-sectional cut at  $x = 2.0$  (water channel experiment by Siegel (1994)).

### 4.2.2 Periodic Disturbances

In order to perform a quantitative comparison with the experimental results the same flow field as above (case A1) was disturbed continuously with a fixed disturbance frequency (case A3). For the generation of the periodic disturbances, the blowing and suction slot was used. The disturbances consisted purely of azimuthal modes  $k = -1$  and  $k = 1$ , resembling two counter-rotating disturbances of the first helical Fourier mode. The Strouhal number of the disturbance based on the free stream velocity and the base diameter was chosen to

$$St_D = \frac{fD}{U_\infty} = 0.159. \quad (4.8)$$

A first attempt, using a disturbance amplitude of  $A_{1,1} = 0.01$  did not show any significant influence of the disturbance on the flow field. Therefore, in a second and final calculation (T3), a disturbance amplitude of

$$A_{1,1} = 0.1 \quad (4.9)$$

was used. The amplitude resembles the maximum blowing and suction velocity, based on the free stream velocity.

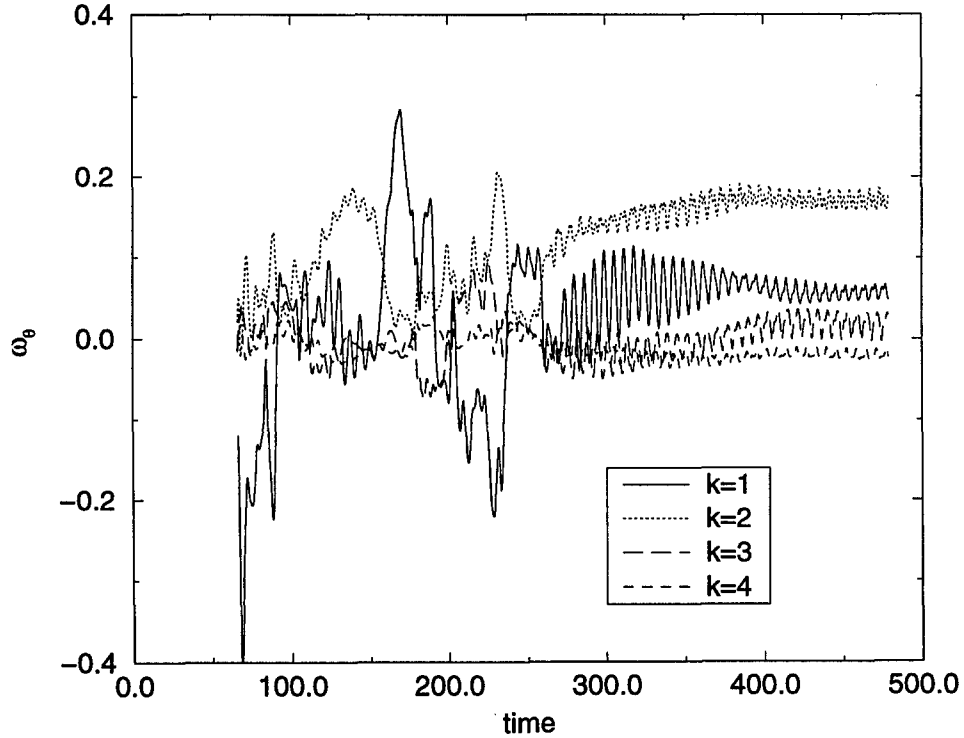


Figure 4.17: Time response of total vorticity to a periodic disturbance of Fourier mode  $k = 1$  with  $St_D = 0.159$  and  $A = 0.1$  at  $M_\infty = 0.2$  and  $Re_D = 1,000$  ( $x = 0.25$ ,  $r = 0.25$ ).

The local time response of the total vorticity at a point within the recirculating region ( $x = 0.25$ ,  $r = 0.25$ ) is shown in figure 4.17. The generation of a small amplitude disturbance ( $A_{1,1} = 0.01$ ) was started at the beginning of the calculation ( $t = 70$ ). As mentioned earlier, the

flow did not show any visible reaction to the disturbance (see figure 4.17). The signal remains non-periodic. At a later stage ( $t = 250$ ) the amplitude was raised to the final value. After several time periods the response of the flow becomes periodic with the same frequency as the generated disturbance (see figure 4.17). At this point, the structures also appear in a periodic fashion.

For a first validation, the periodic flow was calculated over two time periods for three different spatial resolutions. The different parameters are shown in table A.2 for the cases T3 through T5. The results for the three different cases were Fourier transformed in time to separate the fundamental disturbance frequency and its higher harmonics. Figures 4.18 through 4.21 show the resulting velocity fields for the several Fourier modes in time and azimuthal direction for the three different cases. It appears that they all compare very well in the region immediately downstream of the base. Further downstream the results for the different cases show small but noticeable differences. This is due to the grid stretching, which results in a lower resolution in the region further downstream. This inaccuracy, however, does not seem to affect the solution in the near wake region. Therefore, for further comparison with the experiments the lower resolution case was used.

Because of the lower resolution, all simulations could be performed on a single processor of a Silicon Graphics Power Challenge at the Computational Fluid Dynamics Laboratory of the Aerospace and Engineering Department at the University of Arizona. A typical simulation used about 20 CPU hours for the calculation of one time period.

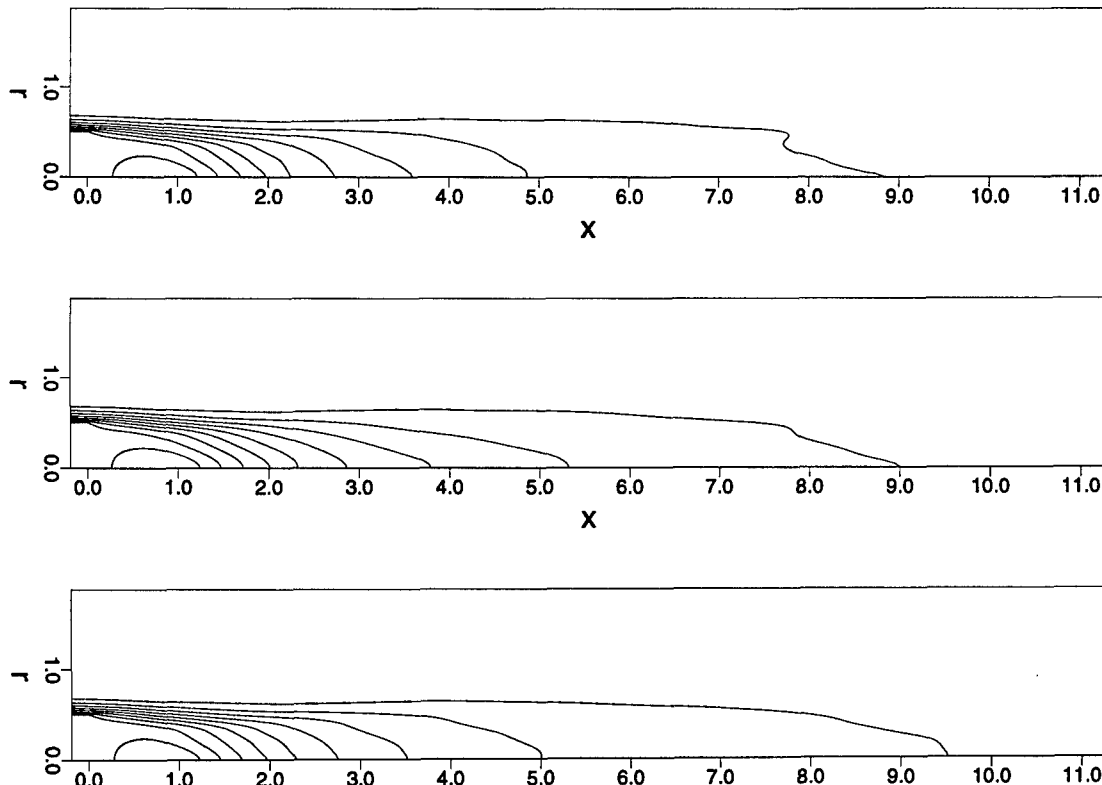


Figure 4.18: Isolines of the mean of axial velocity for three different spatial resolutions for  $M_\infty = 0.2$  and  $Re_D = 1,000$  [cases T3 (top) through T5 (bottom)].

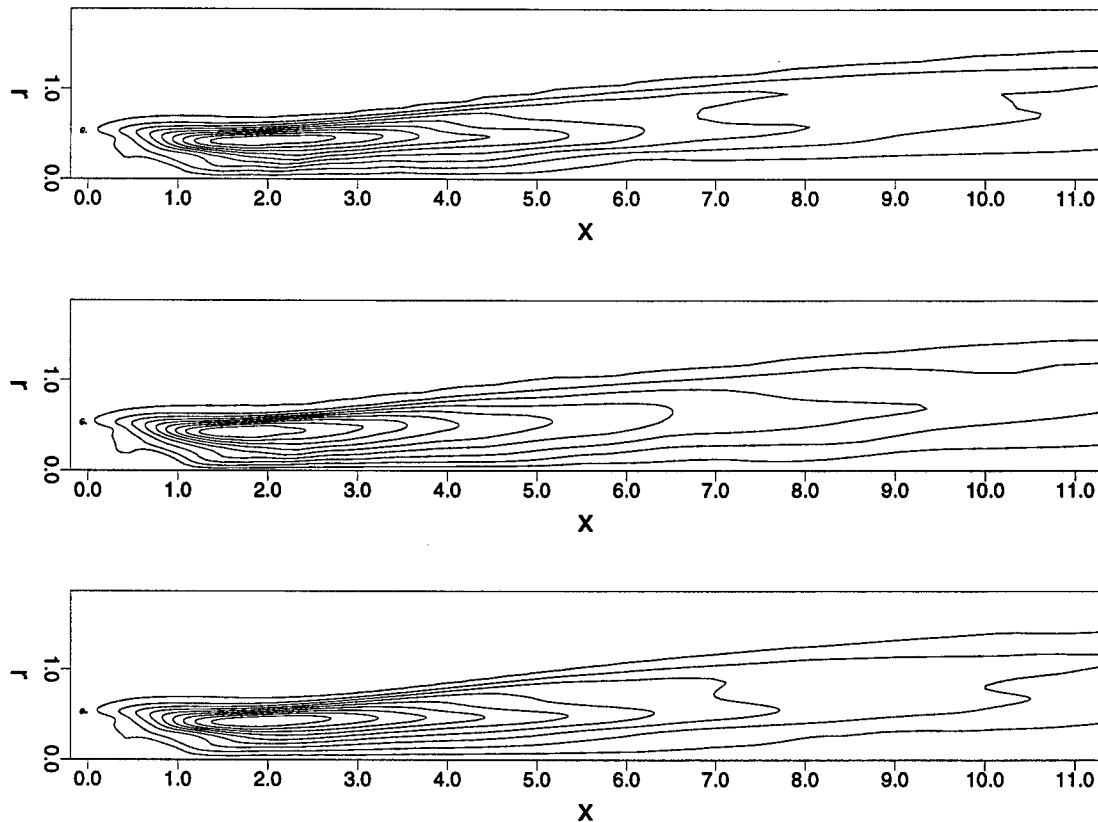


Figure 4.19: Isolines of the fundamental of first azimuthal mode of axial velocity for three different spatial resolutions for  $M_\infty = 0.2$  and  $Re_D = 1,000$  [cases T3 (top) through T5 (bottom)].

In the experiment, which was conducted in the water channel at the Hydrodynamics Laboratory of the Aerospace and Mechanical Engineering Department by [Siegel (1996)], the flow was disturbed using a vibrating ribbon. The Strouhal number was the same as for the numerical simulation. However, the amplitude of the disturbance in the experiment was not determined. As in the numerical simulation, the flow becomes periodic after several periods of the generated disturbance. In addition, the structures appeared to remain symmetric to the symmetry plane of the vibrating ribbon. Thus, the plane of symmetry was fixed, in contrast to the self excited axisymmetric wake.

For a comparison between the simulations and the experiments, velocity measurements were made at a cross section which was about 3.5 diameters downstream of the blunt base. For the measurements a hot film anemometer was used. This allowed only a measurement of the combination of two velocity components. The hot film probe was directed such that in the plane of symmetry it would measure the combination of axial and radial velocity. Thus, results were compared for the combined quantity

$$q = \sqrt{v_x^2 + v_r^2}. \quad (4.10)$$

The measured data, as well as the calculated results, were Fourier transformed in time in

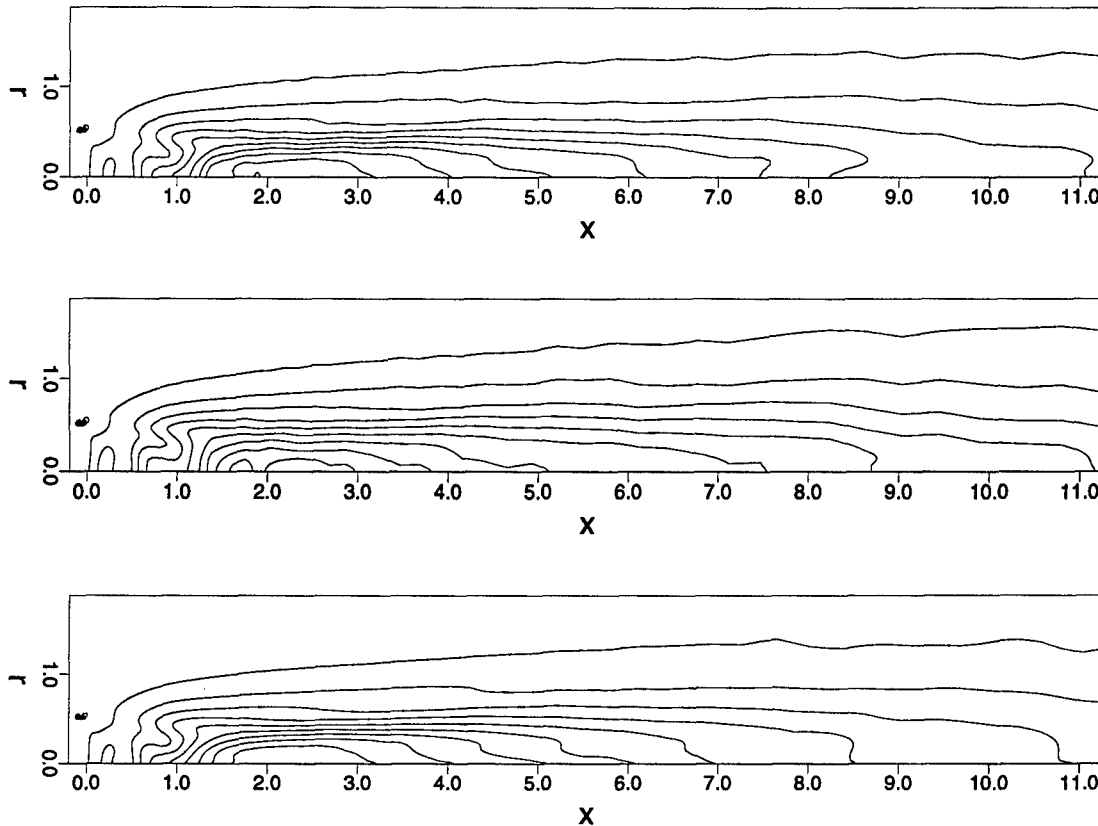


Figure 4.20: Isolines of the fundamental of first azimuthal mode of radial velocity for three different spatial resolutions for  $M_\infty = 0.2$  and  $Re_D = 1,000$  [cases T3 (top) through T5 (bottom)].

order to separate the amplitudes of the fundamental disturbance frequency and its higher harmonics, as mentioned earlier. Figures 4.22 through 4.25 show the mean flow and the amplitude distribution over the radius for  $q$  of the fundamental, the first, and the second higher harmonic at the cross section  $x = 3.5$ . As these figures show, the results compare very well, in spite of the different disturbance methods used in the experiment and the simulation. At this point it is unclear why the maximum at the axis of symmetry for the first harmonic shows appears to be lower for the numerical simulation. A possible explanation could be the low resolution near the axis due to the grid stretching or insufficient data points in time for the Fourier transformation.

In summary, it was found that with the compressible code it is possible to accurately calculate axisymmetric and three-dimensional flow fields for a subsonic Mach number of  $M_\infty = 0.2$ . Exceptionally good agreement was found with the water channel experiments by Siegel (1996) and the incompressible simulations by [Schwarz (1996)]. Further, it was found that the compressible simulation can be a valuable tool for the calculation of incompressible wake flow fields. As mentioned earlier, all simulations were performed on a single processor of a Silicon Graphics Inc. Power Challenge L with 4 R8000 CPUs (90 MHz, 4MB cache each) and 512 MBytes of main memory.

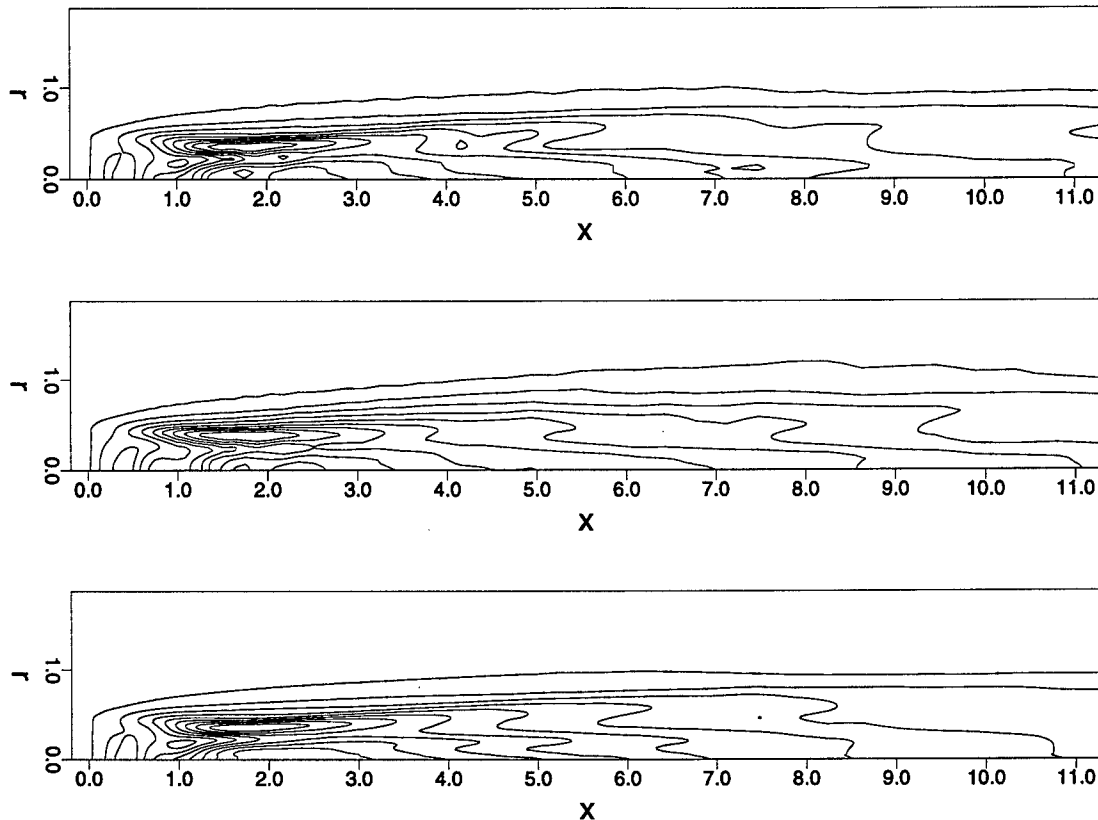


Figure 4.21: Isolines of the fundamental of first azimuthal mode of azimuthal velocity for three different spatial resolutions for  $M_\infty = 0.2$  and  $Re_D = 1,000$  [cases T3 (top) through T5 (bottom)].

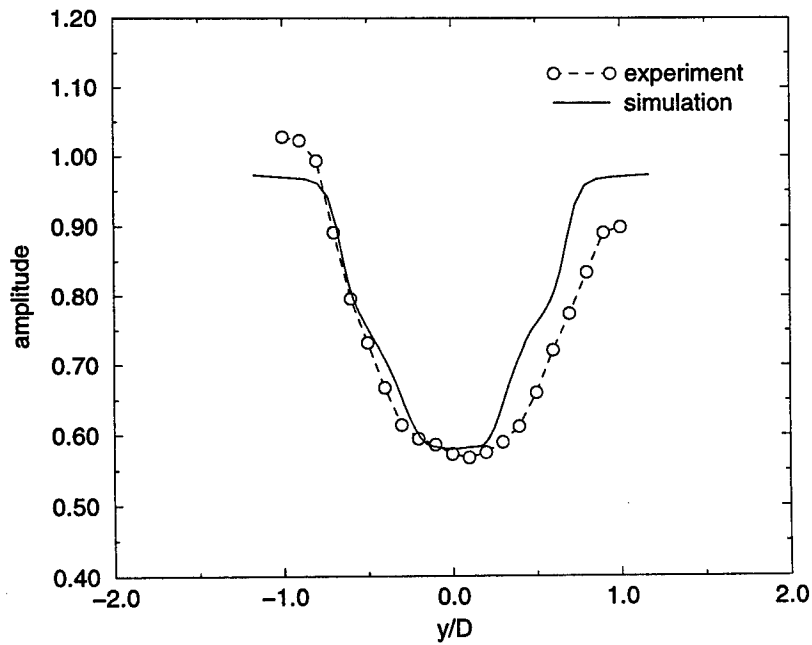


Figure 4.22: Mean flow profiles for  $M_\infty = 0.2$  and  $Re_D = 1,000$  at  $x = 3.5$ .

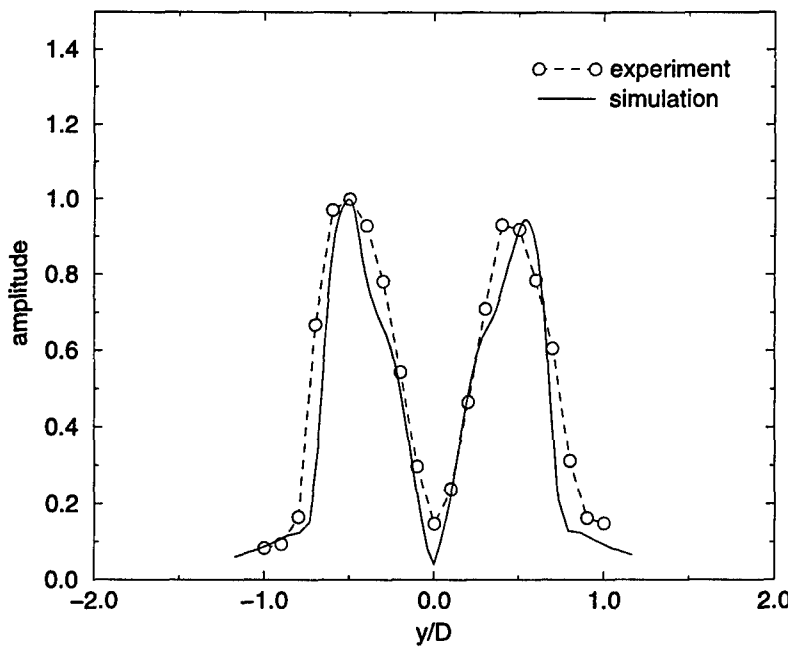


Figure 4.23: Normalized amplitude distribution of fundamental disturbance frequency for  $M_\infty = 0.2$  and  $Re_D = 1,000$  at  $x = 3.5$ .

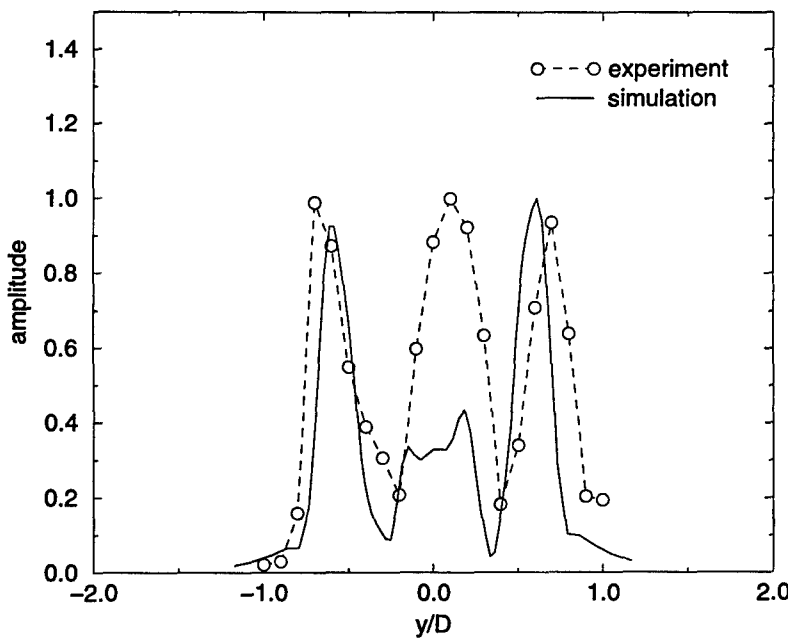


Figure 4.24: Normalized amplitude distribution of first higher harmonic of disturbance frequency for  $M_\infty = 0.2$  and  $Re_D = 1,000$  at  $x = 3.5$ .

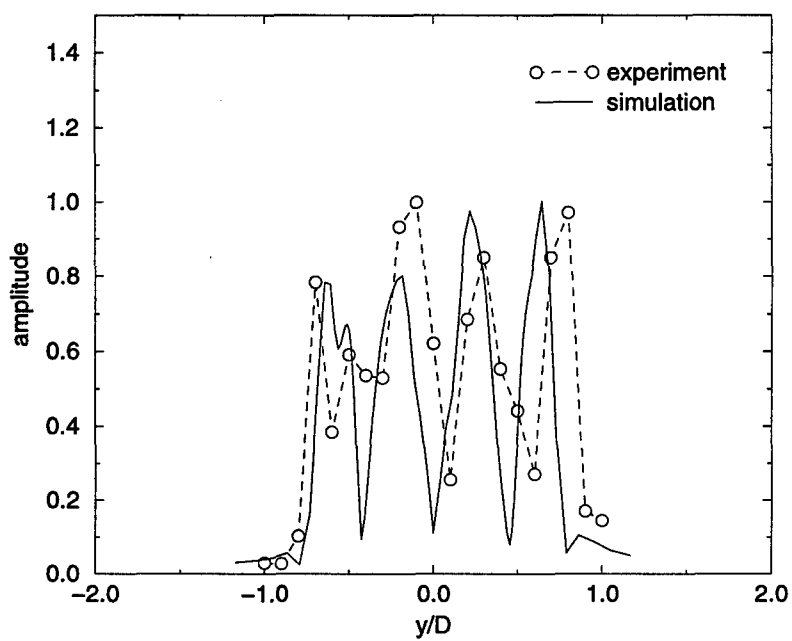


Figure 4.25: Normalized amplitude distribution of second higher harmonic of disturbance frequency for  $M_\infty = 0.2$  and  $Re_D = 1,000$  at  $x = 3.5$ .

### 4.3 Large-Eddy Simulation

A preliminary validation for the LES code was performed for a free stream Mach number of  $M_\infty = 0.2$  and a global Reynolds number of  $Re_D = 2,000$ . As before, the results were directly compared qualitatively to experimental measurements obtained in the water channel of the Hydrodynamics Laboratory of the Aerospace and Mechanical Engineering Department at the University of Arizona by [Siegel (1996)]. The experiments have shown that the flow is fully turbulent and exhibits large coherent structures, which are very similar to the laminar structures that appeared at  $Re_D = 1,000$ .

For the numerical simulation, at first the flow field was calculated with DNS in exactly the same way as the flow at  $Re_D = 1,000$ . During the initial stage a periodic disturbance in the first azimuthal mode was generated through the blowing and suction slot. After five time periods the disturbance was ramped down to zero. Figure 4.26 shows the time response of the flow at  $x = 0.25$  and  $r = 0.25$  in form of the total azimuthal vorticity for the first five periods in time. As for the lower Reynolds number case, the disturbance grows exponentially in time.

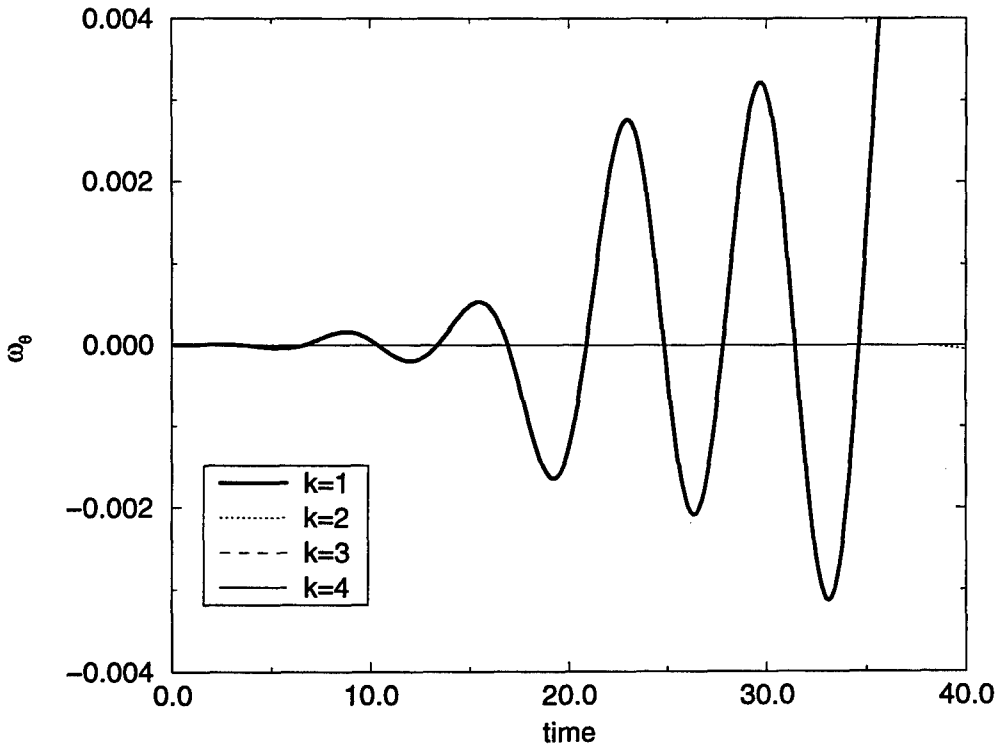


Figure 4.26: Initial time response of total azimuthal vorticity to a single pulse disturbance of Fourier mode  $k = 1$  at  $r=0.25$  and  $z= 0.25$ .

In contrast to the lower Reynolds number case, however, the structures that appear in the free shear layer became too small for the spatial resolution of the DNS. This resulted in high local gradients. Shortly after  $t = 72$  the calculation was underresolved and terminated. At this

point the simulation was continued with the LES code, using the same spatial resolution as before for the DNS. Figure 4.27 shows the continued response of the flow at the same location as before. As for the laminar case, the response remains highly unsteady and non-periodic even though the flow is not disturbed any further.

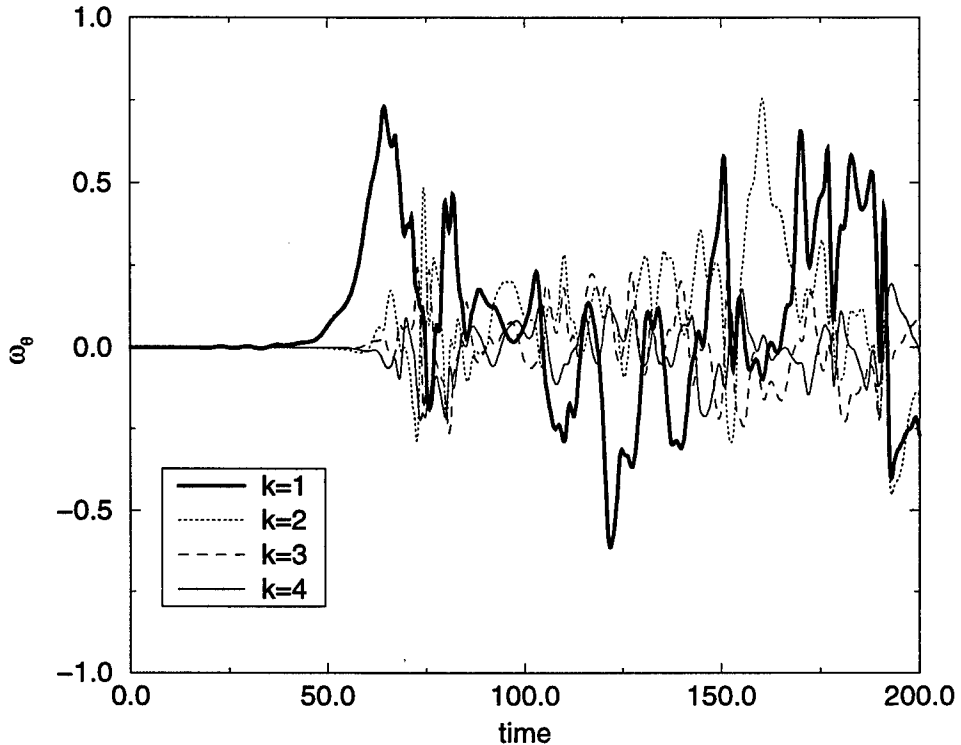


Figure 4.27: Time response of total azimuthal vorticity to a single pulse disturbance of Fourier mode  $k = 1$  at  $r=0.25$  and  $z= 0.25$ .

At this point, large coherent structures appear as shown, for example, in figure 4.28 in the form of isolines of instantaneous total vorticity. The structures look very similar to the laminar structures for the lower Reynolds number case. In addition, flow visualization via particles shows that the larger structures are similar to the structures that were observed in the water channel experiments (see figure 4.29)..

More code validation for the LES code is needed at this point, especially for supersonic flows. So far, flow fields at a supersonic Mach number of  $M_\infty = 2.46$  and global Reynolds numbers up to  $Re_D = 400,000$  have been calculated (see chapter 7). In order to perform a direct comparison with experiments, however, flows at higher Reynolds numbers ( $Re_D = O(1,000,000)$ ) need to be calculated.

Therefore, in the present work only preliminary results are presented for the LES calculations of the higher Reynolds number (turbulent) supersonic flow fields.

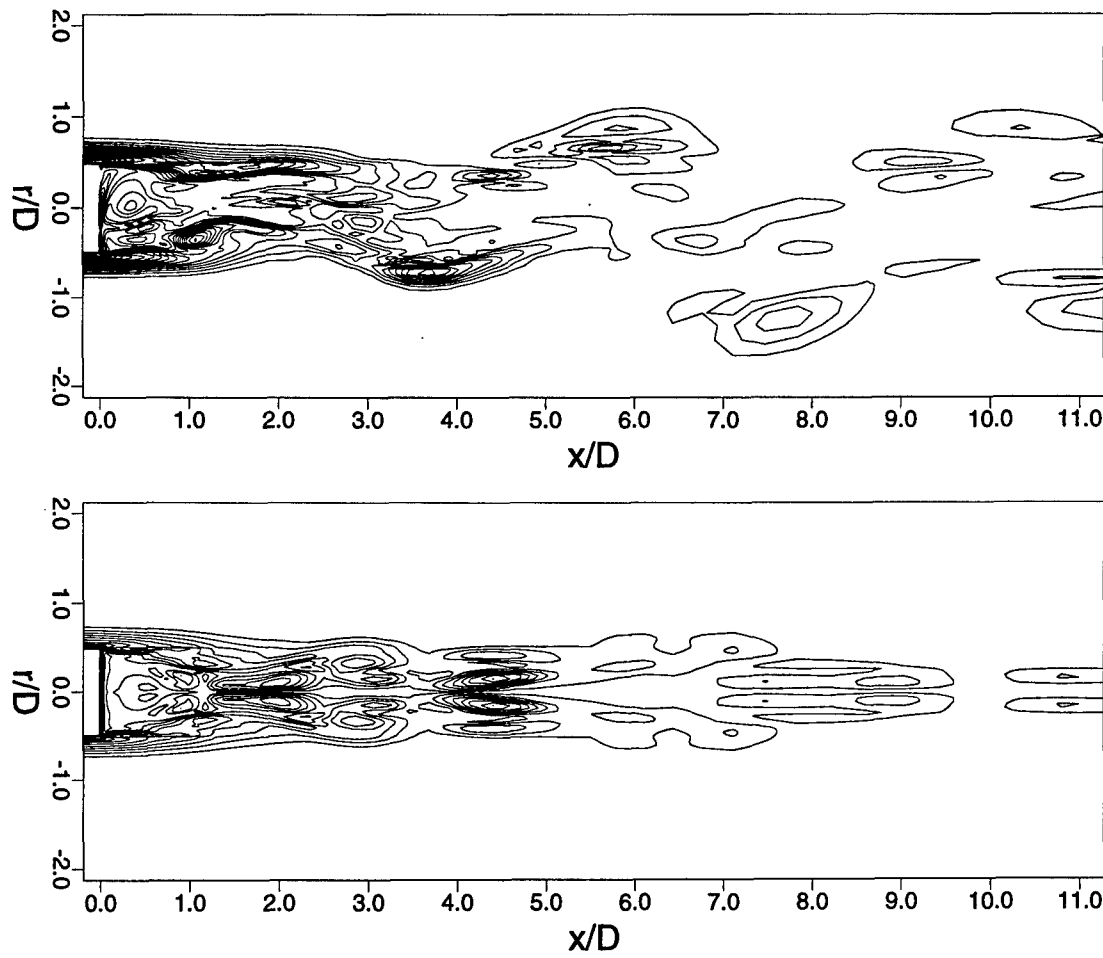


Figure 4.28: Isolines of total vorticity at  $M_\infty = 0.2$  and  $Re_D = 2,000$  at  $\theta = 0$  (top) and  $\theta = \pi/2$  (bottom).



Figure 4.29: Flow visualization using particles for  $M_{\infty} = 0.2$  and  $Re_D = 2,000$ ; simulation (top) and water channel experiment by Siegel (1994) (bottom).

# Chapter 5

## Results

Three-dimensional unsteady flow fields of the wake of an axisymmetric bluff body with a blunt base have been calculated for several combinations of free stream Mach number and global Reynolds number. The main goal for the present calculations was to investigate the existence of large structures and their influence and significance on the characteristics of the global flow field. As a first step, Direct Numerical Simulations (DNS) were performed to investigate the time dependent behavior of laminar flows in order to determine the existence of absolute instabilities and investigate the evolution of large structures in laminar wake flows and their effect on the global flow field. Secondly, although preliminary, the calculations were extended to turbulent flows by employing Large-Eddy Simulations (LES) in order to investigate if absolute instabilities also exist and if large coherent structures are also present in turbulent supersonic wake flows.

### 5.1 Direct Numerical Simulations

As pointed out earlier, the incompressible wake of axisymmetric bodies at a global Reynolds number of  $Re_D = 1,000$  is subject to an absolute instability in the first helical Fourier mode. As a result, the flow is highly unsteady and dominated by large structures. However, the flow remains laminar at all times and does not undergo transition to turbulence. From previous investigations [see, for example, [Schwarz (1996)] and Siegel (1994)] there is a basis of knowledge about the evolution of large structures in the incompressible wake. For that reason, the low Mach number subsonic flow has been used for code validation and is also used here for comparison of the evolution of the structures in supersonic flows. In the following sections results from DNS are presented for three different free stream Mach numbers,  $M_\infty = 0.2$ ,  $M_\infty = 1.2$ , and  $M_\infty = 2.46$ .

#### 5.1.1 Subsonic Flow

##### a) Steady Calculations

The subsonic flow field, that has been evaluated for validation of the DNS code (cases A1 and T3 through T5) is presented here to provide a basis for comparison of the results with

supersonic wake flows. First, additional information on the steady axisymmetric flow field is provided in form of isolines of axial velocity, radial velocity, pressure, density, and temperature. These results are shown in figures 5.1 through 5.5.

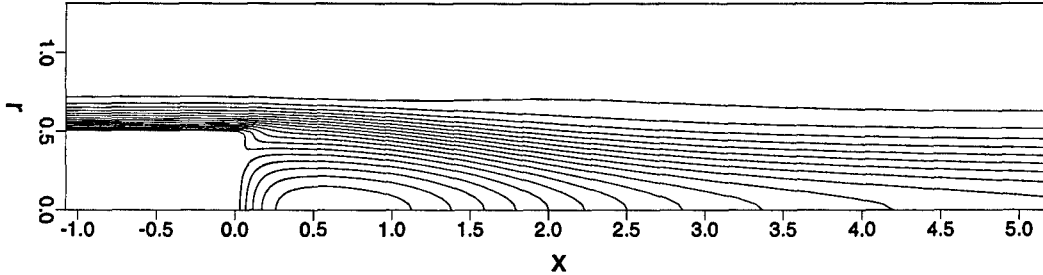


Figure 5.1: Isolines of axial velocity for  $M_{\infty} = 0.2$  and  $Re_D = 1,000$  (axisymmetric unforced calculation).

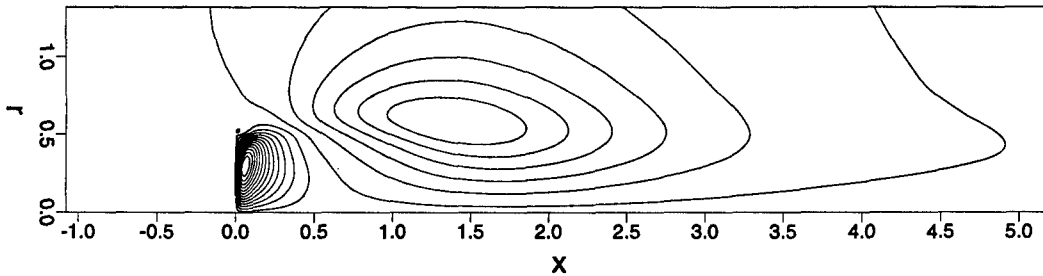


Figure 5.2: Isolines of radial velocity for  $M_{\infty} = 0.2$  and  $Re_D = 1,000$  (axisymmetric unforced calculation).

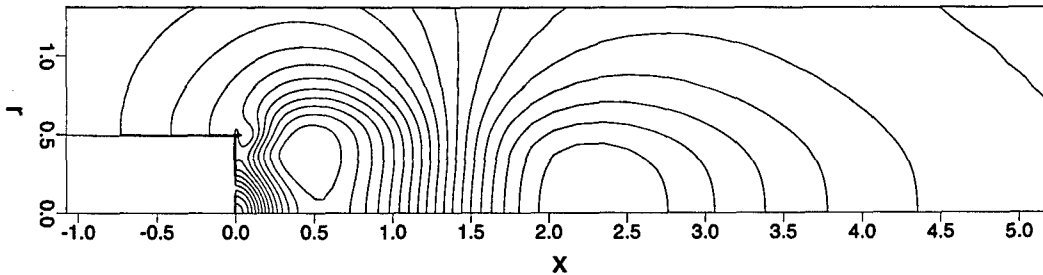


Figure 5.3: Isolines of pressure for  $M_{\infty} = 0.2$  and  $Re_D = 1,000$  (axisymmetric unforced calculation).

The most important feature at this point can be seen in the pressure distribution (figure 5.3). The graph clearly shows the strong pressure drop immediately downstream of the base, which is responsible for the base drag. However, as will be seen in the following sections, the pressure drop is much more pronounced in supersonic flow fields. In addition, the plot reveals an elevated pressure at the base near the axis of symmetry. This can be explained by the stagnation point flow behavior of the recirculating region. This results in the typical base pressure distribution as shown in figure 5.19.

### b) Unsteady Calculations

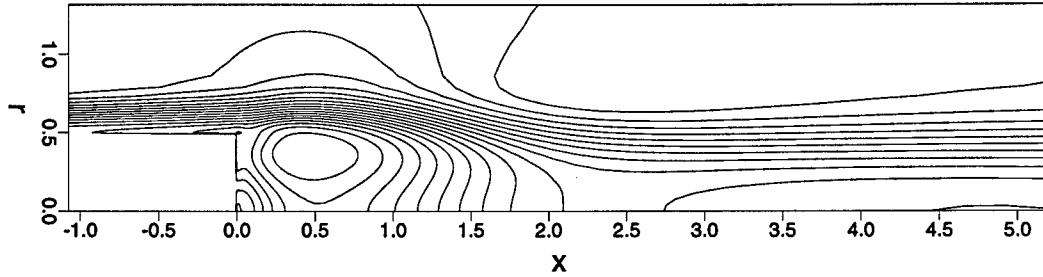


Figure 5.4: Isolines of density for  $M_\infty = 0.2$  and  $Re_D = 1,000$  (axisymmetric unforced calculation).

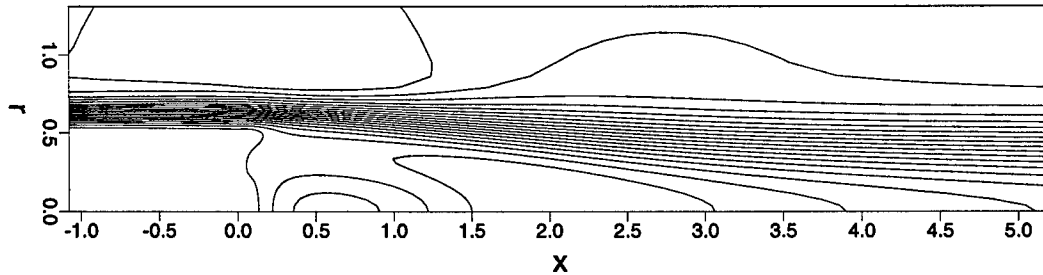


Figure 5.5: Isolines of temperature for  $M_\infty = 0.2$  and  $Re_D = 1,000$  (axisymmetric unforced calculation).

As mentioned in the discussion concerning code validation in section 4.3, for the DNS of the three-dimensional unsteady wake the flow was disturbed by a single pulse disturbance locally within the recirculating region at the location

$$x_{\text{dist}} = 0.25 \quad \text{and} \quad r_{\text{dist}} = 0.25, \quad (5.1)$$

as described in section 3.7. The time dependent response of the flow field at the location of the disturbance is shown in figure 4.13. After a period of time, the signal deviates from the axisymmetric state and starts oscillating in a non-periodic fashion. At this point, large structures are present in the flow.

Four different methods are used here for the identification of vortical structures in the flow field:

- Isolines of instantaneous total vorticity shown in different planes, the x-y plane and the x-z plane through the axis of symmetry, and the y-z plane at 4 different  $x$  locations ( $x = 1.0$ ,  $x = 2.0$ ,  $x = 3.0$ , and  $x = 4.0$ ).
- Visualization of the instantaneous flow field using particles.
- Isosurfaces of instantaneous total vorticity, axial vorticity, and azimuthal vorticity.
- Isosurfaces of instantaneous pressure deviation from the time-averaged flow field.

Figure 5.6 shows isolines of instantaneous total vorticity in two planes perpendicular to each other. The figure reveals that the flow remains symmetric in the second plane. This plane

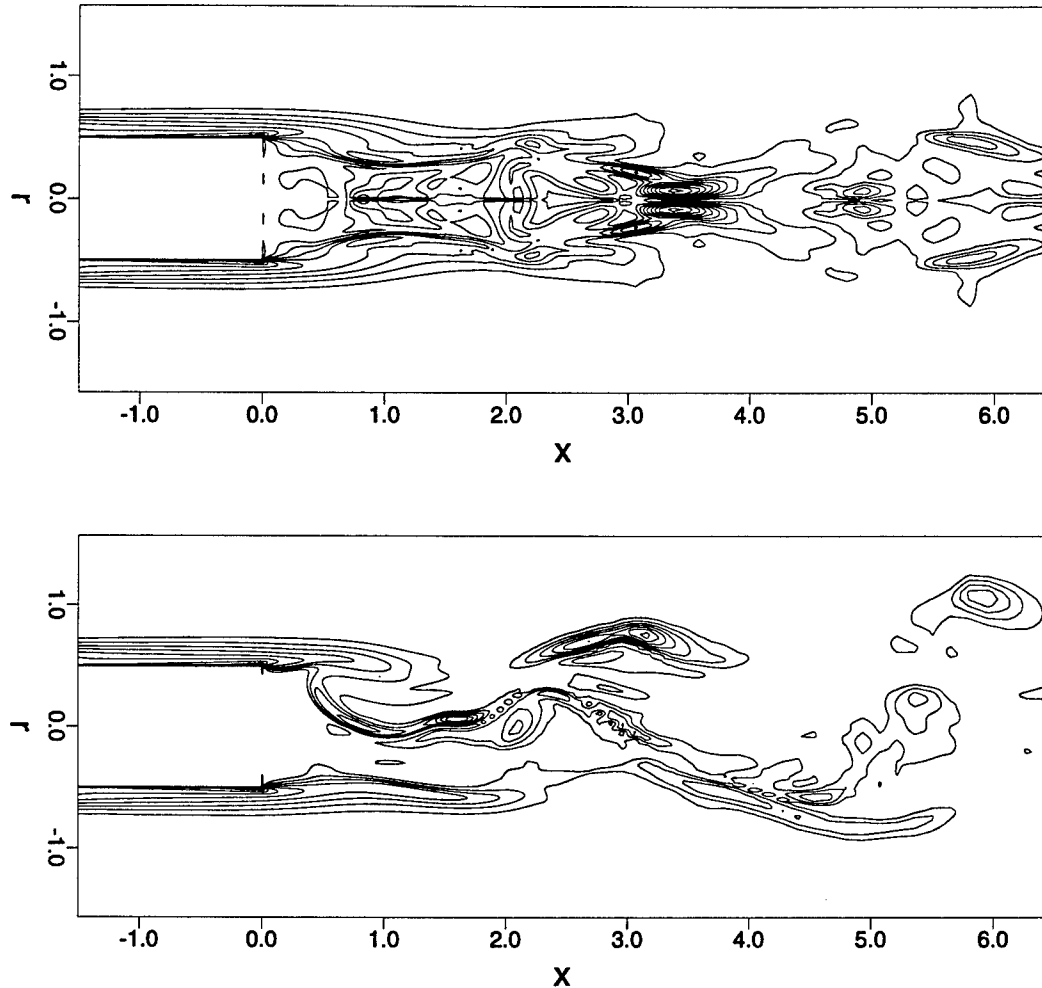


Figure 5.6: Instantaneous total vorticity for  $Re_D = 1,000$  and  $M_\infty = 0.2$ . x-z plane (top) and x-y plane (bottom).

of symmetry has also been observed in the incompressible calculations and in water channel experiments. Therefore, in order to save computer resources a plane symmetry was prescribed in all following calculations.

Strong vortical structures appear which originate near the corner of the base and are convected downstream. These structures have also been observed in water channel experiments. Figure 5.7 shows isolines of the total vorticity at axial cross-sections at four different  $x$  locations. The figures clearly indicate two strong maxima of total vorticity at every cross-section. However, some cross-sections exhibit more than two local maxima (for example at  $x = 3$ ). The structure of the axial vortices will become clearer when looking only at the axial vorticity, which is shown in the next series of figures.

Figures 5.8 through 5.10 show isosurfaces of total vorticity, azimuthal vorticity and total axial vorticity, respectively. Comparing the total vorticity with the azimuthal vorticity, which are both shown at the same level of  $|\omega| = 3.0$ , reveals that the ring-shaped structure consists

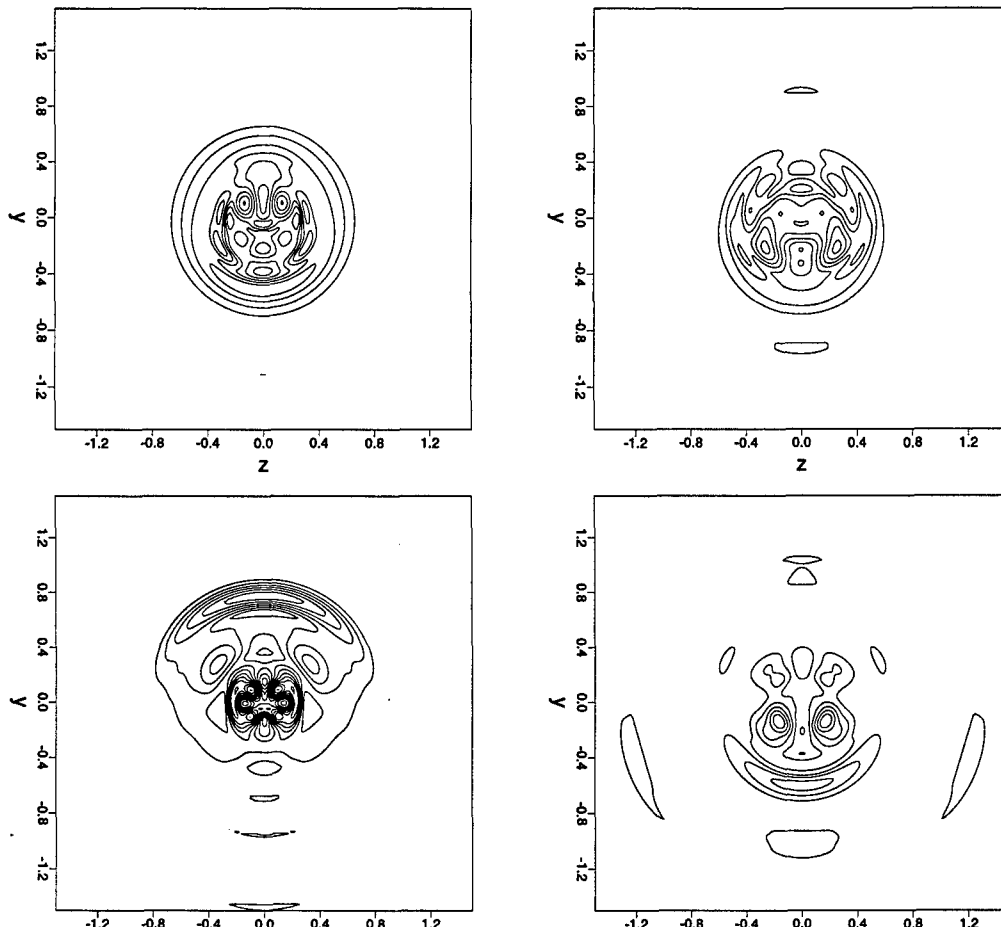


Figure 5.7: Instantaneous total vorticity for  $Re_D = 1,000$  and  $M_\infty = 0.2$ , y-z planes at  $x = 1$  (top left),  $x = 2$  (top right),  $x = 3$  (bottom left), and  $x = 4$  (bottom right).

mainly of azimuthal vorticity. This structure is followed by two structures of axial vorticity (shown here at  $|\omega_x| = 1.0$ ), which are counter-rotating. The connection between the two types of structures becomes clearer when looking at figure 5.11. Here the isosurface of instantaneous pressure deviation from the time-averaged flow field is shown (for  $\Delta p = -0.02$ ). The figure shows, that two ring-shaped structures are connected by two axial structures.

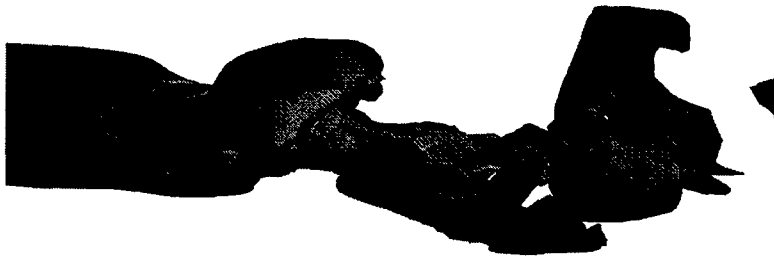


Figure 5.8: Isosurfaces of instantaneous total vorticity ( $|\omega| = 3.0$ ) for  $M_\infty = 0.2, Re_D = 1,000$ .

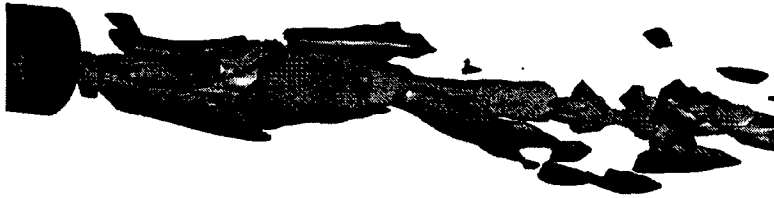


Figure 5.9: Isosurfaces of instantaneous axial vorticity ( $|\omega_x| = 1.0$ ) for  $M_\infty = 0.2, Re_D = 1,000$ .

For a direct comparison with flow visualization in water channel experiments that were carried out by Siegel (1994), particles have been introduced into the flow during the numerical simulations. The locations of the particles are updated at every time step during the numerical simulation. The release of new particles is triggered at a specified number of time steps (typically every 16 to 64 steps). The particles are released at a ring near the corner of the base, such that they enter the recirculation region close to the center of the shear layer. This resembles the introduction of dye at the corner of the base in the water channel experiments.

In figure 4.14 the flow field is shown for two side views perpendicular to each other. As before, the figures show the symmetry to the x-y plane and the appearance of a ring-like structure followed by two axial vortices. In figure 4.15 particles are shown at x locations  $x = 1.0, x = 2.0, x = 3.0$ , and  $x = 4.0$ . This method is similar to a laser sheet illumination of fluorescent dye in a water channel experiment. Again the figures reveal the symmetry to the x-y plane and clearly shows the two rollups which result from a superposition of a  $k = 1$  and a  $k = -1$  helical disturbance mode. Similar structures have been observed in water channel experiments when using a laser sheet illumination technique at cross sections in the y-z plane (compare, for example, figure 5.17).

The three-dimensional time dependent results show that there is a strong unsteady part in the flow. Large structures are present. In order to investigate the influence of the structures on

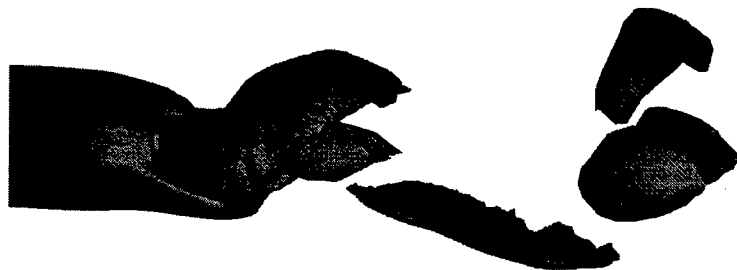


Figure 5.10: Isosurfaces of instantaneous azimuthal vorticity ( $|\omega_\theta| = 3.0$ ) for  $M_\infty = 0.2, Re_D = 1,000$ .

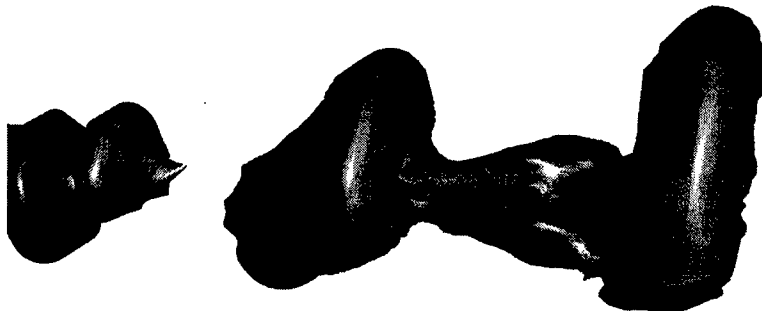


Figure 5.11: Isosurfaces of instantaneous pressure deviation from the time-averaged mean flow ( $\Delta p = -0.02$ ) for  $M_\infty = 0.2, Re_D = 1,000$ .

the global flow field, a time average is performed over a time period from  $t = 80$  to  $t = 150$ . Figures 5.12 through 5.18 show isolines of axial velocity, radial velocity, pressure, density, temperature, azimuthal vorticity and stream lines for the time-averaged flow field, respectively. The strongest changes compared to the axisymmetric steady flow are noticeable in the distribution of the pressure and the density. The streamlines reveal that the recirculation region for the time-averaged flow field is only 1.8 diameters long, compared to the recirculation length of 2.1 diameters for the steady flow.

The pressure distribution along the base has become almost constant, in contrast to the steady calculation which exhibits a strong maximum at the axis of symmetry (see figure 5.19). This phenomenon is even more pronounced in the case of supersonic flows, as will be shown in the following sections.

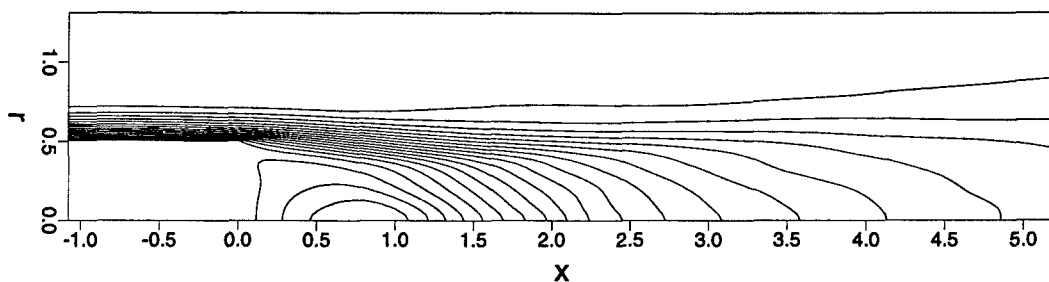


Figure 5.12: Isolines of axial velocity for the time-averaged flow of  $M_\infty = 0.2$  and  $Re_D = 1,000$ .

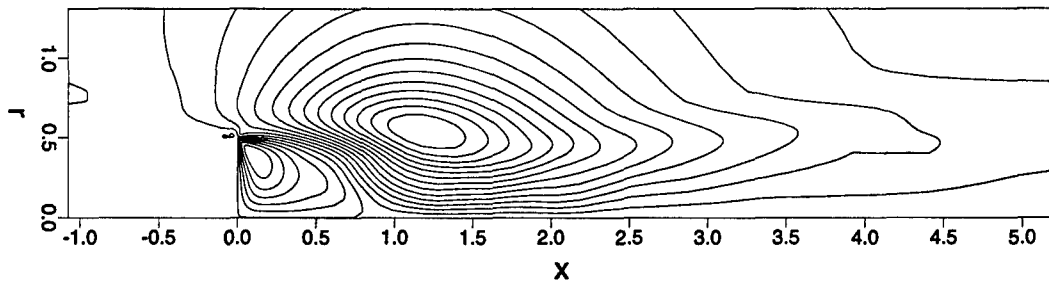


Figure 5.13: Isolines of radial velocity for the time-averaged flow of  $M_\infty = 0.2$  and  $Re_D = 1,000$

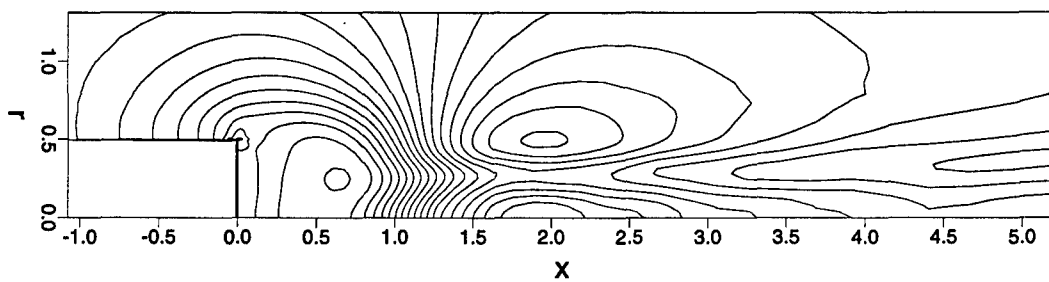


Figure 5.14: Isolines of pressure for the time-averaged flow of  $M_\infty = 0.2$  and  $Re_D = 1,000$

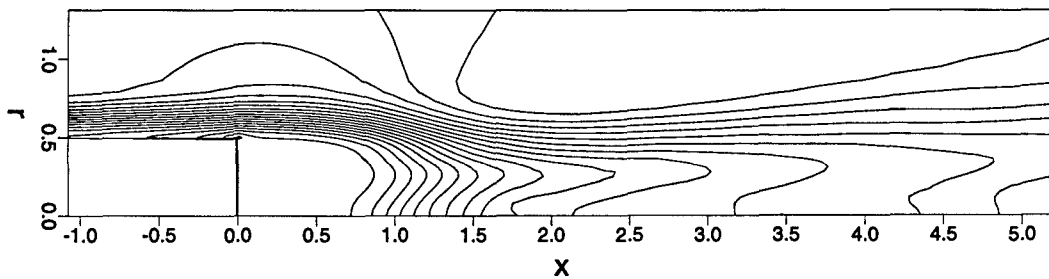


Figure 5.15: Isolines of density for the time-averaged flow of  $M_\infty = 0.2$  and  $Re_D = 1,000$

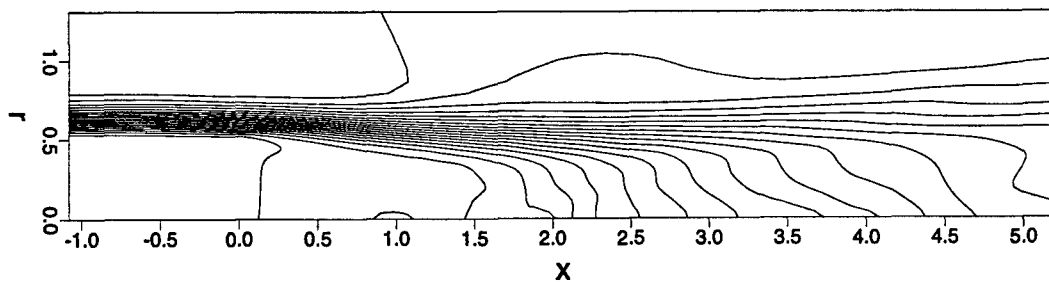


Figure 5.16: Isolines of temperature for the time-averaged flow of  $M_\infty = 0.2$  and  $Re_D = 1,000$

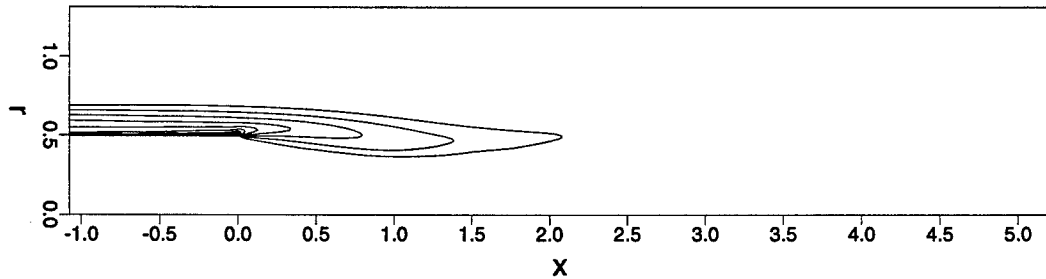


Figure 5.17: Isolines of azimuthal vorticity for the time-averaged flow of  $M_\infty = 0.2$  and  $Re_D = 1,000$

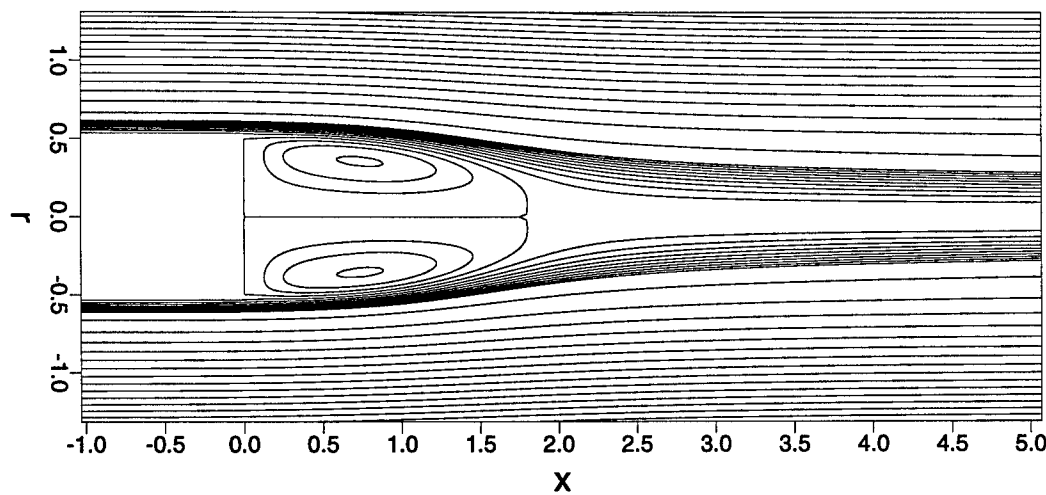


Figure 5.18: Streamlines for the time-averaged flow of  $M_\infty = 0.2$  and  $Re_D = 1,000$

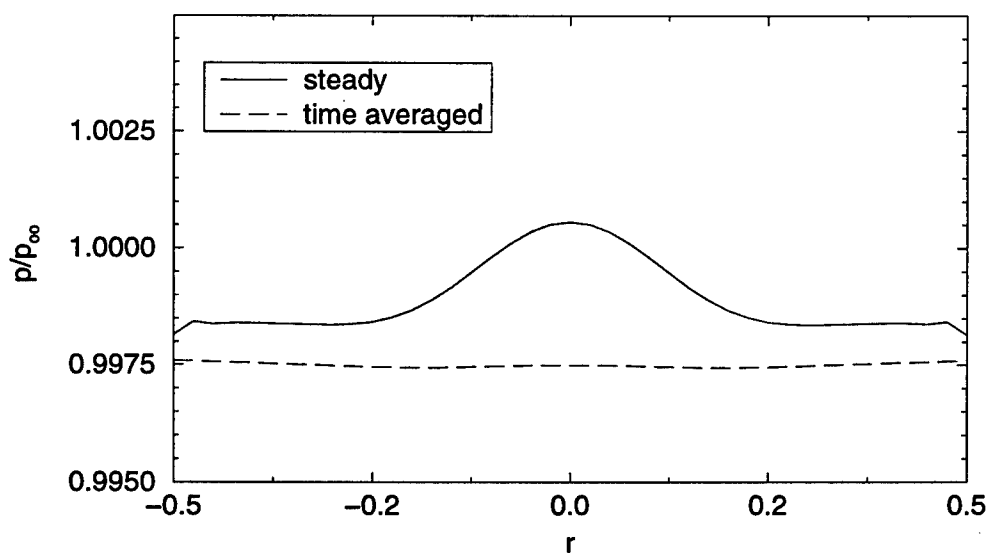


Figure 5.19: Base pressure distributions for  $M_{\infty} = 0.2$  and  $Re_D = 1,000$ .

### 5.1.2 Supersonic Flow at Mach 1.2

For the first simulation of a supersonic wake the free stream Mach number was  $M_\infty = 1.2$  and the global Reynolds number was  $Re_D = 4,000$  (cases A6 and T6).

#### a) Steady Calculations

As for the subsonic case, at first a steady axisymmetric flow was calculated. The resulting flow field is shown in figures 5.20 through 5.26 in form of isolines of axial velocity, radial velocity, streamlines, pressure, density, temperature, and azimuthal vorticity, respectively. The figures indicate that the features of the supersonic flow are different from its subsonic counterpart.

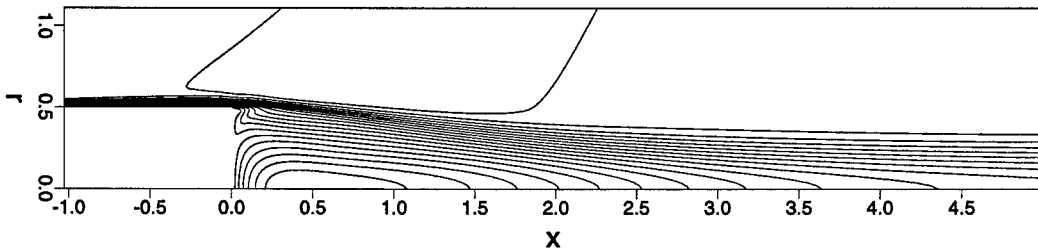


Figure 5.20: Isolines of axial velocity for  $M_\infty = 1.2$  and  $Re_D = 4,000$  (axisymmetric steady calculation).

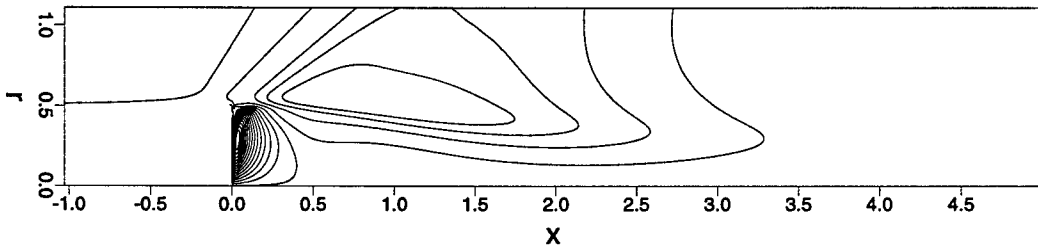


Figure 5.21: Isolines of radial velocity for  $M_\infty = 1.2$  and  $Re_D = 4,000$  (axisymmetric steady calculation).

The figures for the axial velocity do not show significant differences from the subsonic flow. The approaching boundary layer was thinner at the corner for the supersonic flow, as can be seen in figure 5.20. This is determined by the prescribed inflow condition. The radial velocity, however, looks different for the different Mach numbers. Here, the area of negative velocity above the free shear layer extends farther upstream than for the subsonic calculation. It also reveals the existence of expansion waves. The streamlines, shown in figure 5.22, have very similar shapes to the ones of the subsonic flow, with the exception that the curvature of the separating streamline is much weaker for the supersonic case.

The largest difference can be observed in the pressure distribution. Figure 5.23 clearly shows the regions of expansion and of weak re-compression which, of course, are not present in the subsonic flow. In addition, the change in pressure is much stronger for the supersonic flow. This

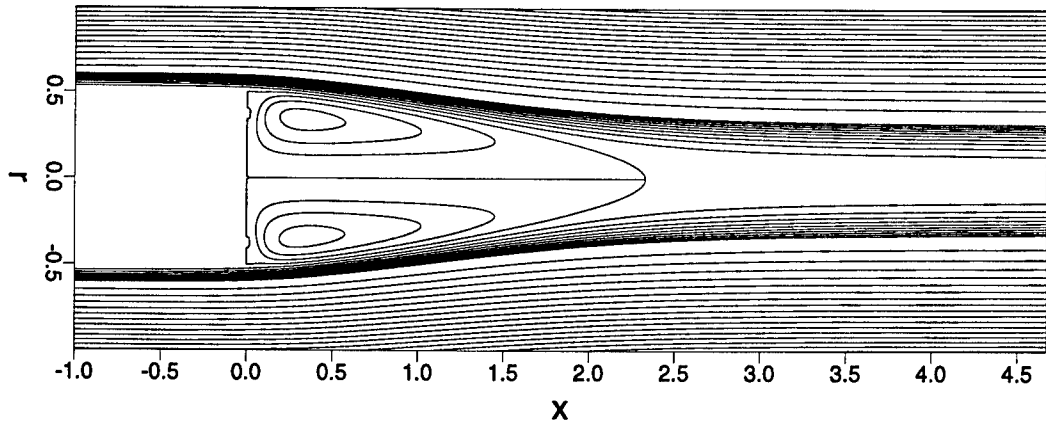


Figure 5.22: Steady streamlines for  $M_\infty = 1.2$  and  $Re_D = 4,000$  (axisymmetric steady calculation).

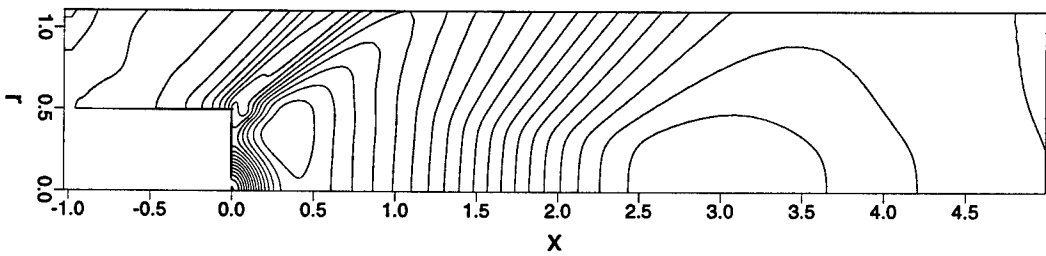


Figure 5.23: Isolines of pressure for  $M_\infty = 1.2$  and  $Re_D = 4,000$  (axisymmetric steady calculation).

results in a much higher base pressure drag, which agrees with observations from experiments (see, for example, [Rollstin (1987)]). Similar features as in the pressure can be seen in the density and temperature distribution, which both show a much stronger variation for the supersonic flow than for the subsonic flow.

The isolines of azimuthal vorticity look very similar to those of the subsonic flow. However, the absolute values of the vorticity are much higher for the present case.

### b) Unsteady Calculations

Similar to the subsonic calculation, as discussed in the preceding section, the flow was disturbed locally with a single pulse disturbance. The location of the disturbance introduction was at  $r = 0.25$  and  $x = 0.25$ . Figure 5.27 shows the time signal of the radial momentum at the location of the disturbance introduction for Fourier modes  $k = 0$ ,  $k = 1$ , and  $k = 2$ . The signal exhibits a behavior similar to that observed for the subsonic calculation. After some time the signal deviates from the axisymmetric state and starts oscillating in a non-periodic fashion.

On a logarithmic scale, which is shown in figure 5.28, the signal of the radial momentum at

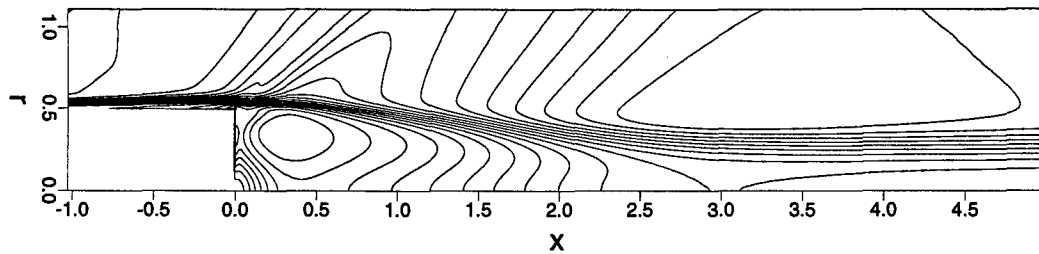


Figure 5.24: Isolines of density for  $M_\infty = 1.2$  and  $Re_D = 4,000$  (axisymmetric steady calculation).

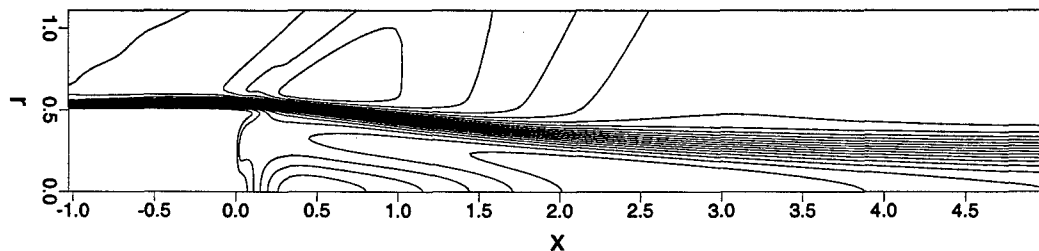


Figure 5.25: Isolines of temperature for  $M_\infty = 1.2$  and  $Re_D = 4,000$  (axisymmetric steady calculation).

$r = 0.25$  and  $x = 0.25$  exhibits an exponential deviation from the axisymmetric state until a state of nonlinear saturation is reached. This is a clear indication that an absolute instability exists. In the following, the response of the flow is further studied in the same fashion as discussed for the subsonic flow field. Figures 5.29 through 5.31 show isolines of instantaneous total vorticity for different time instances. This series reveals the development of vortical structures which originate near the corner of the base and increase in strength while being convected downstream. The structures appear to be similar to the ones observed in the subsonic case, except that they have a much higher concentration of vorticity. In addition, a layer of high vorticity develops near the center line farther upstream (see figure 5.31).

As for the subsonic case, the figures reveal the existence of a plane of symmetry as shown in figures 5.32 through 5.34 in which isolines of instantaneous total vorticity in the x-y plane are

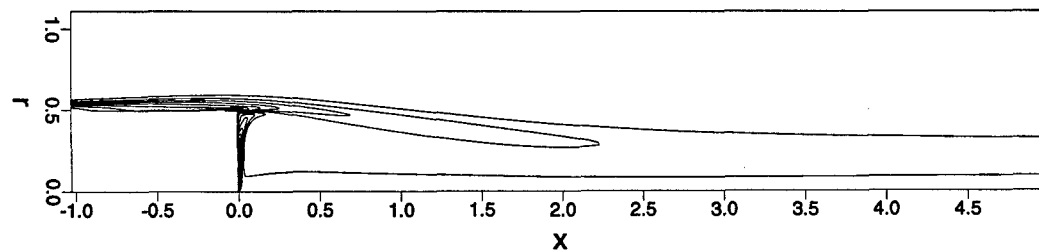


Figure 5.26: Isolines of azimuthal vorticity field for  $M_\infty = 1.2$  and  $Re_D = 4,000$  (axisymmetric steady calculation).

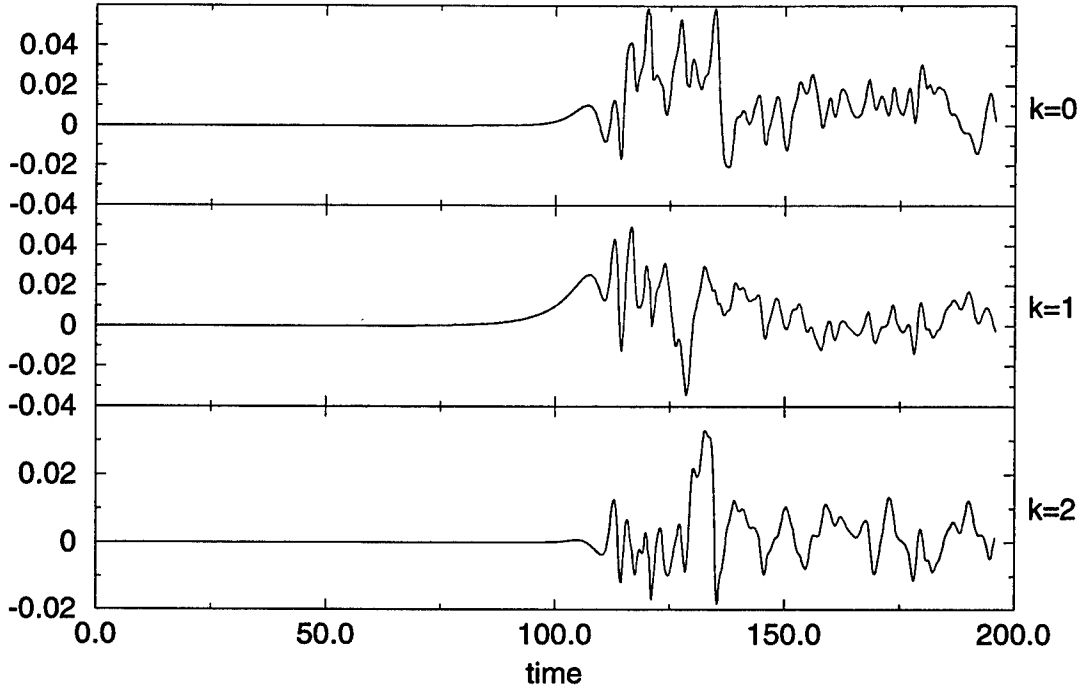


Figure 5.27: Time response of radial momentum to a single pulse of Fourier mode  $k = 1$  at  $r = 0.25$  and  $x = 0.25$  at  $M_\infty = 1.2$  and  $Re_D = 4,000$ .

plotted at four different  $x$  locations. These plots reveal that in addition to the high concentration of vorticity at two locations in a cross section, locations of high concentration of vorticity are also present closer to the axis. These phenomena were also observed for the subsonic case. The three-dimensional shape of the vortical structures can be seen more clearly in figures 5.35 through 5.38, where isosurfaces of instantaneous total vorticity, azimuthal vorticity, axial vorticity and pressure deviation from the time-averaged mean flow are plotted, respectively. As for the subsonic case, the total vorticity and the azimuthal vorticity exhibit ring-shaped structures, which are followed by a pair of axial vortices of lesser strength (see figure 5.36).

Flow visualization by particle introduction as shown in figures 5.39 through 5.40, also reveals the structures. As before, the particles were introduced at a ring near the corner of the base. However, the structures are not as clearly noticeable as in the subsonic case. To date there have been no visualization experiments for flows at this Mach number. Therefore, no direct comparison is possible to experimental observation.

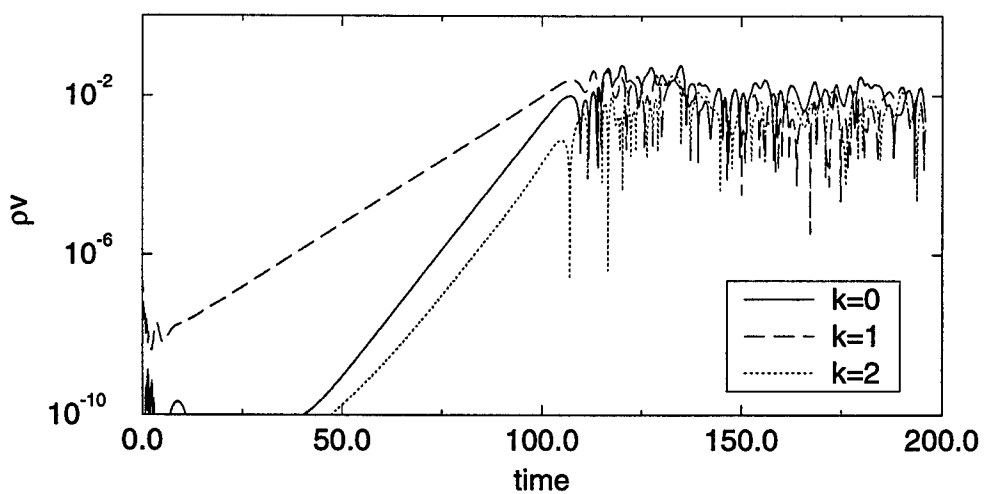


Figure 5.28: Time response of radial momentum to a single pulse of Fourier mode  $k = 1$  at  $r = 0.25$  and  $x = 0.25$  on a logarithmic scale at  $M_\infty = 1.2$  and  $Re_D = 4,000$ .

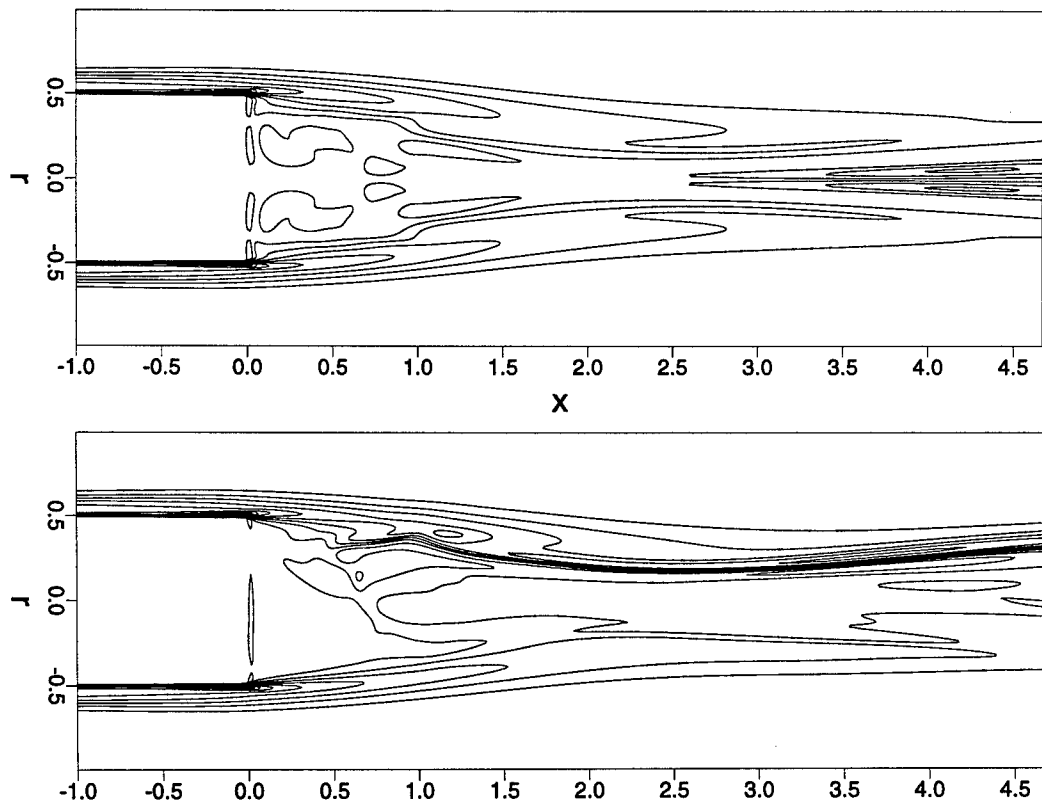


Figure 5.29: Isolines of instantaneous total vorticity for  $Re_D = 4,000$  and  $M_\infty = 1.2$ , at  $\theta = 0$  (top) and  $\theta = \pi/2$  (bottom) at  $t = 121.34$ .

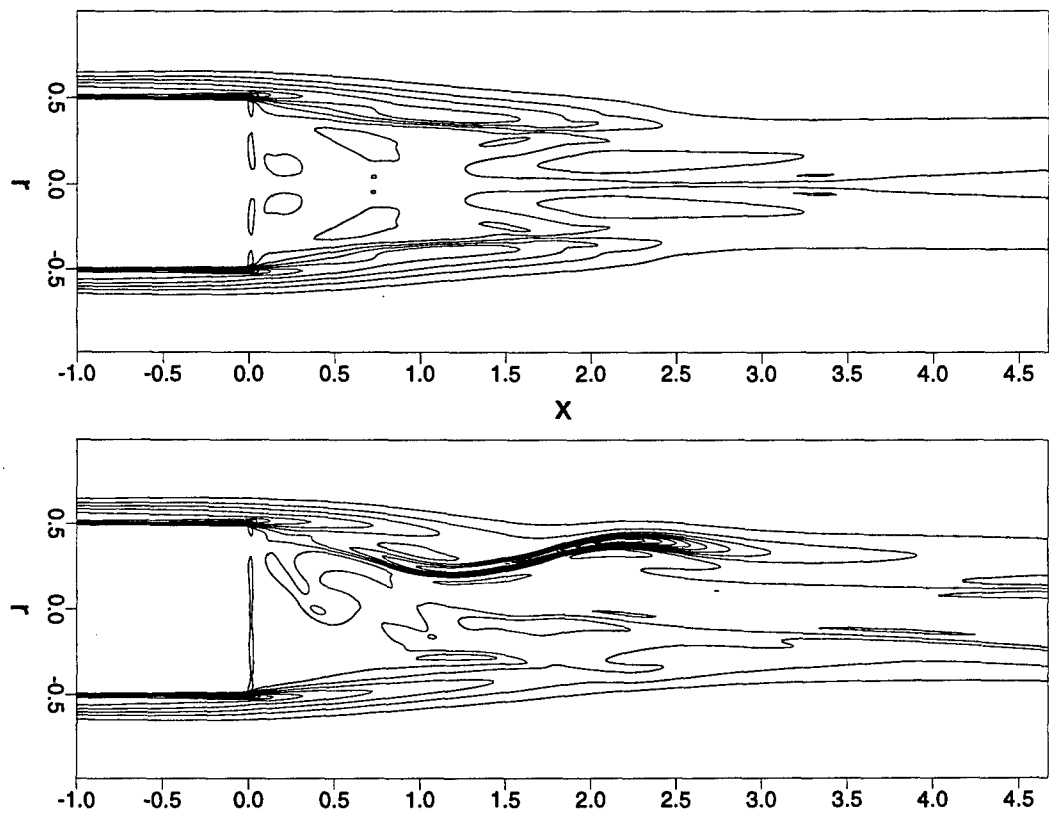


Figure 5.30: Isolines of instantaneous total vorticity for  $Re_D = 4,000$  and  $M_\infty = 1.2$ , at  $\theta = 0$  (top) and  $\theta = \pi/2$  (bottom) at  $t = 127.84$ .

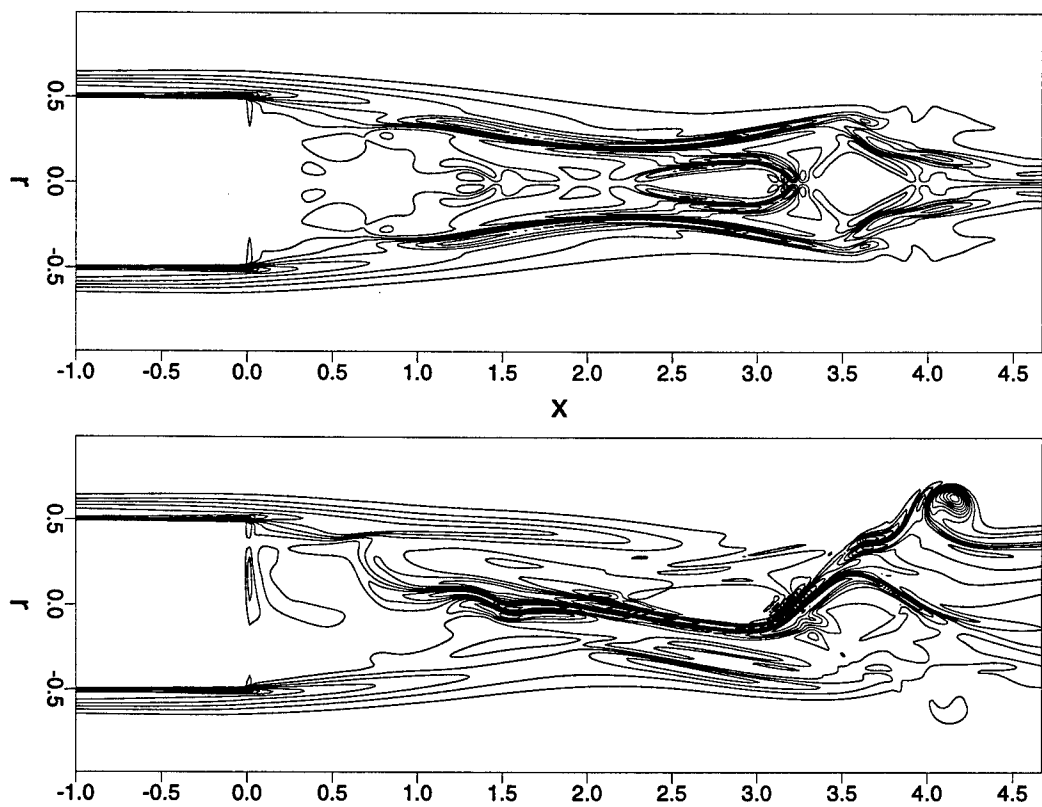


Figure 5.31: Isolines of instantaneous total vorticity for  $Re_D = 4,000$  and  $M_\infty = 1.2$ , at  $\theta = 0$  (top) and  $\theta = \pi/2$  (bottom) at  $t = 135.09$ .

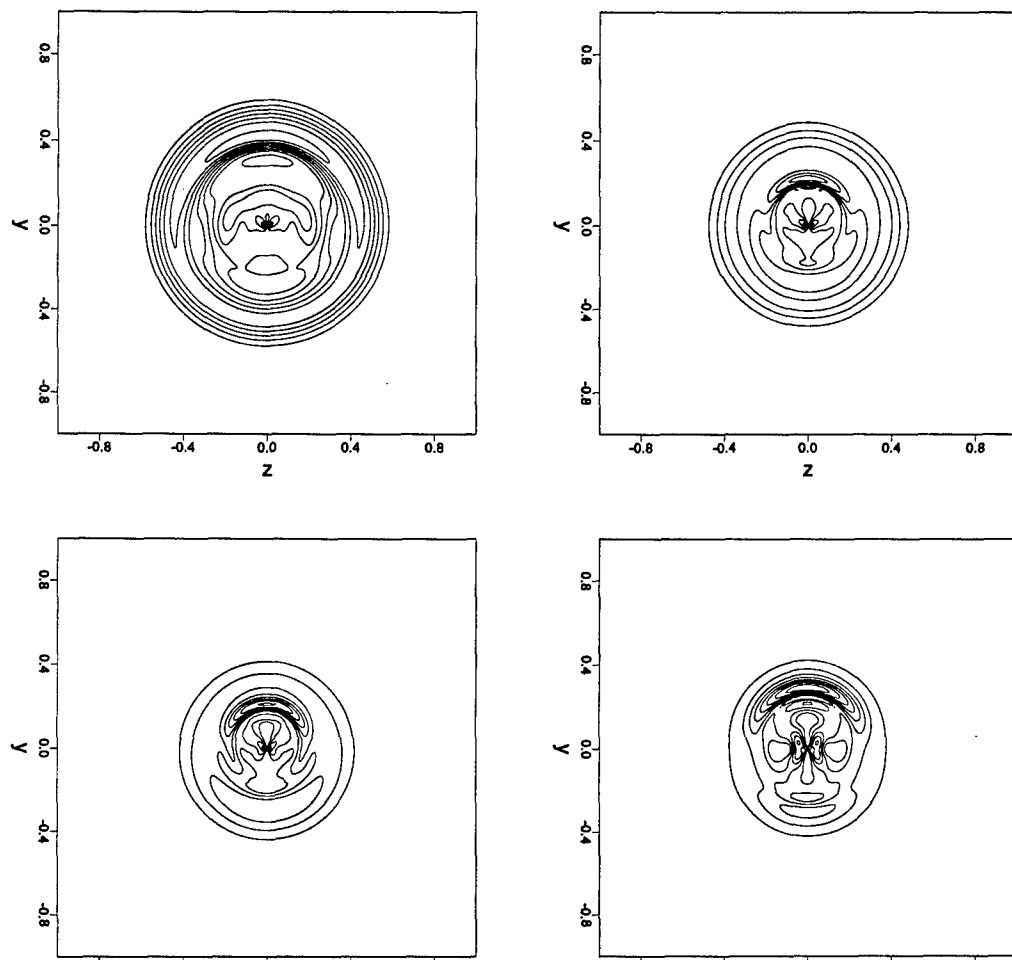


Figure 5.32: Isolines of instantaneous total vorticity for  $Re_D = 4,000$  and  $M_\infty = 1.2$ , y-z planes at  $x = 1$  (top left),  $x = 2$  (top right),  $x = 3$  (bottom left), and  $x = 4$  (bottom right) at  $t = 121.34$ .

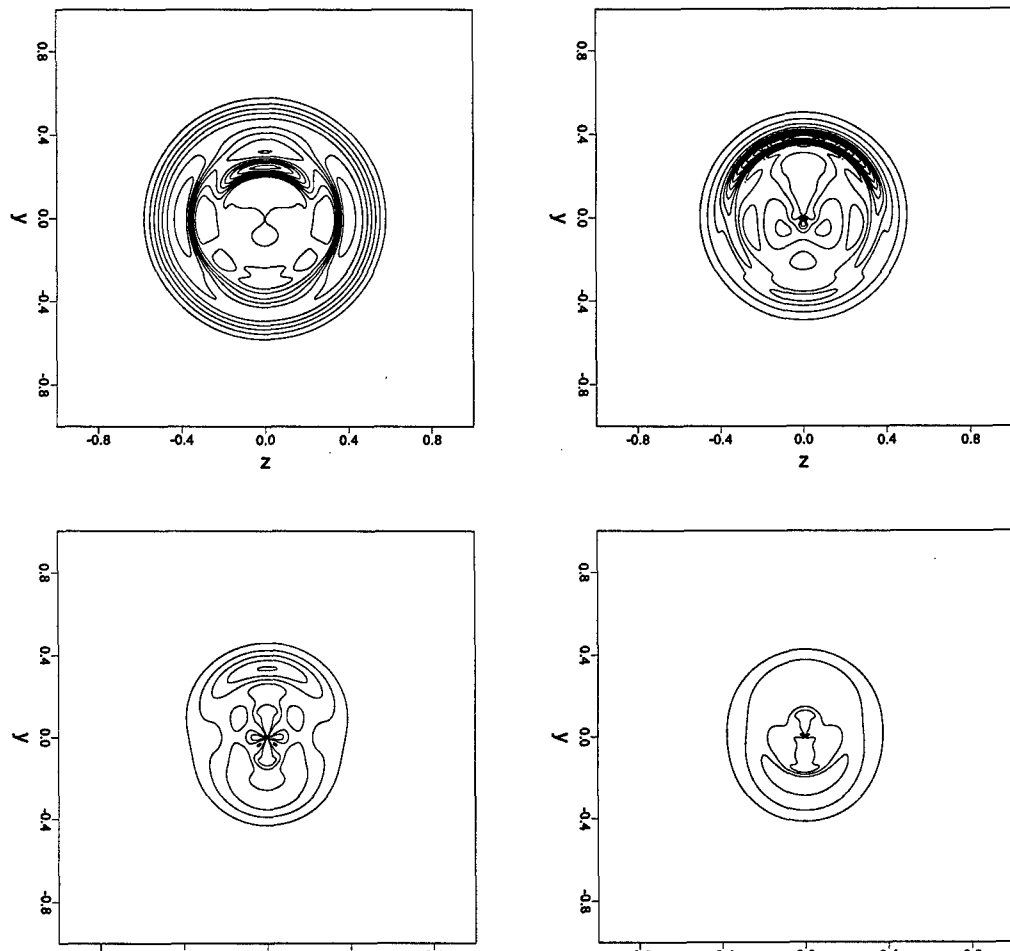


Figure 5.33: Isolines of instantaneous total vorticity for  $Re_D = 4,000$  and  $M_\infty = 1.2$ , y-z planes at  $x = 1$  (top left),  $x = 2$  (top right),  $x = 3$  (bottom left), and  $x = 4$  (bottom right) at  $t = 127.84$ .

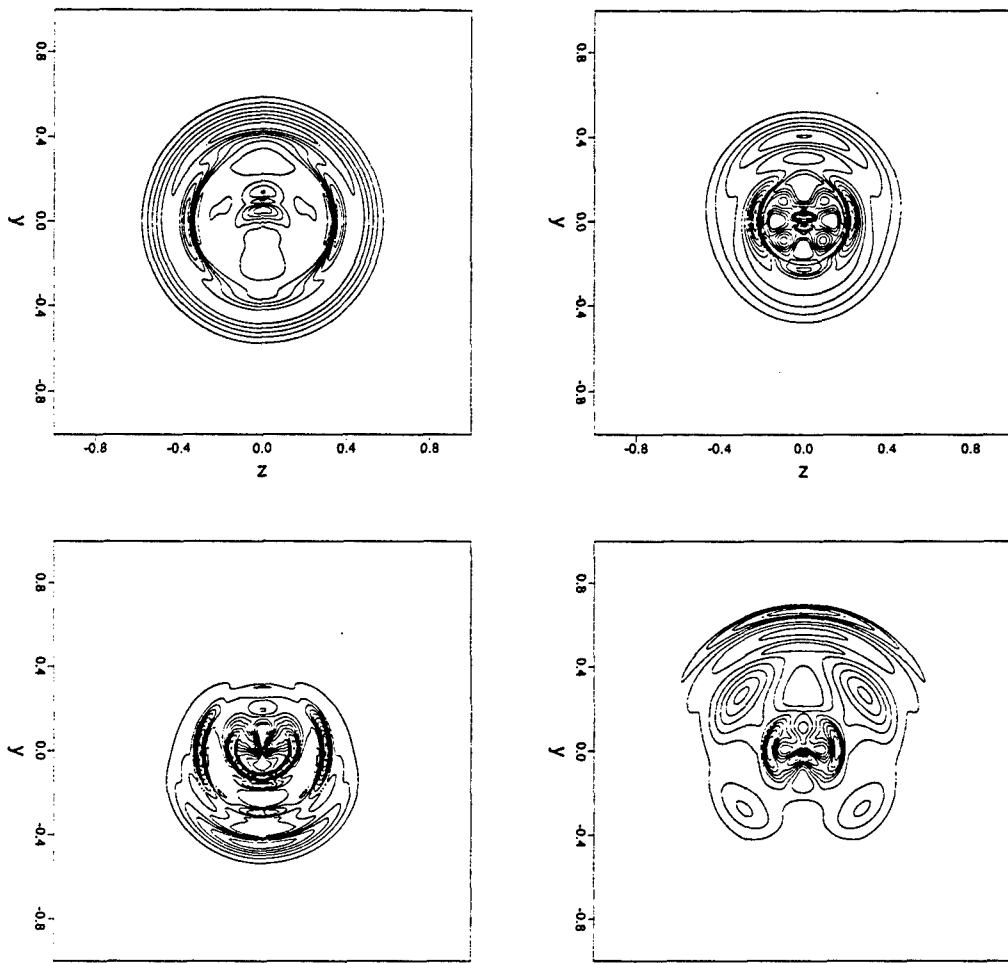


Figure 5.34: Isolines of instantaneous total vorticity for  $Re_D = 4,000$  and  $M_\infty = 1.2$ , y-z planes at  $x = 1$  (top left),  $x = 2$  (top right),  $x = 3$  (bottom left), and  $x = 4$  (bottom right) at  $t = 135.09$ .

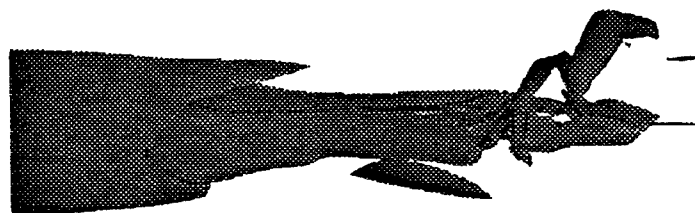


Figure 5.35: Isosurfaces of instantaneous total vorticity ( $|\omega| = 6$ ) for  $M_\infty = 1.2, Re_D = 4,000$  at  $t = 135.09$ .

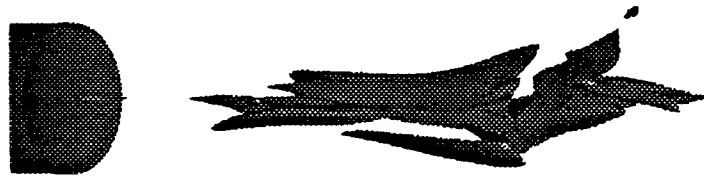


Figure 5.36: Isosurfaces of instantaneous axial vorticity ( $|\omega_x| = 2$ ) for  $M_\infty = 1.2$ ,  $Re_D = 4,000$  at  $t = 135.09$ .

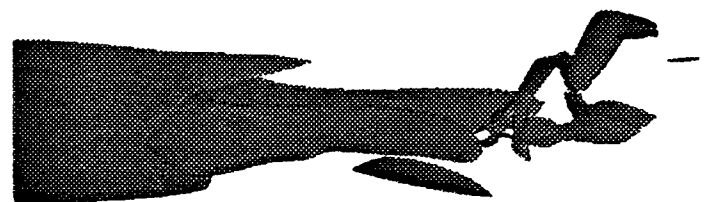


Figure 5.37: Isosurfaces of instantaneous azimuthal vorticity ( $|\omega_\theta| = 6$ ) for  $M_\infty = 1.2$ ,  $Re_D = 4,000$  at  $t = 135.09$ .

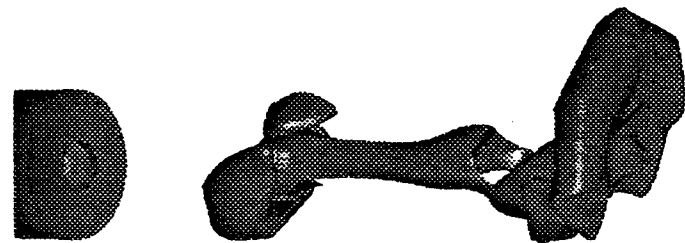


Figure 5.38: Isosurfaces of instantaneous pressure deviation from the time-averaged mean flow ( $\Delta p = -0.02$ ) for  $M_\infty = 1.2$ ,  $Re_D = 4,000$  at  $t = 135.09$ .

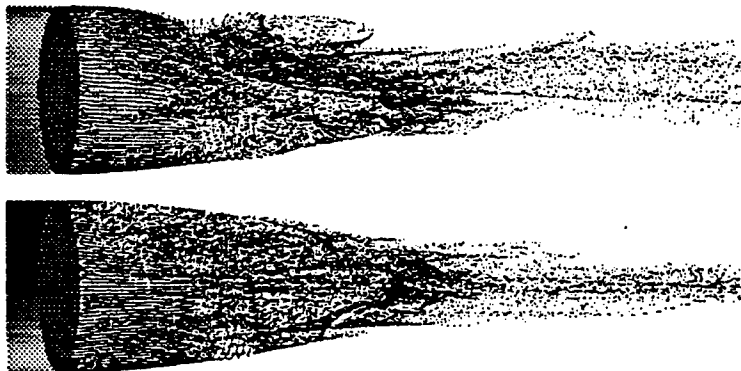


Figure 5.39: Flow visualization of instantaneous flow field via particles for  $M_\infty = 1.2$  and  $Re_D = 4,000$ , viewed from  $\theta = \pi/2$  (top) and from  $\theta = 0$  (bottom) (particles introduced at  $x = 0.025, r = 0.475$ ).



Figure 5.40: Flow visualization of instantaneous flow field via particles for  $M_\infty = 1.2$  and  $Re_D = 4,000$ , sheets of thickness 0.01 at  $\theta = 0$  (top) and  $\theta = \pi/2$  (bottom), (particles introduced at  $x = 0.025, r = 0.475$ ).

The subsonic calculations have shown that the unsteady structures can have a strong influence on the global time-averaged flow. This influence was strongest in the time-averaged pressure and the density. For the case of  $M_\infty = 1.2$ , isolines of the time-averaged pressure and density are shown in figures 5.42 and 5.43, respectively. They indicate that the distribution of the pressure and the density along the base is almost constant. This finding is in good agreement with experimental observations of turbulent supersonic axisymmetric wake flows. The difference between the steady axisymmetric and the time-averaged base pressure is again obvious from figure 5.44. Here the pressure is normalized by the free stream static pressure. The plot shows



Figure 5.41: Flow visualization of instantaneous flow field via particles for  $M_\infty = 1.2$  and  $Re_D = 4,000$ , cross-sectional cuts of thickness 0.01 at  $x = 1.0$ ,  $x = 2.0$ ,  $x = 3.0$ , and  $x = 4.0$  (particles introduced at  $x = 0.025$ ,  $r = 0.475$ ).

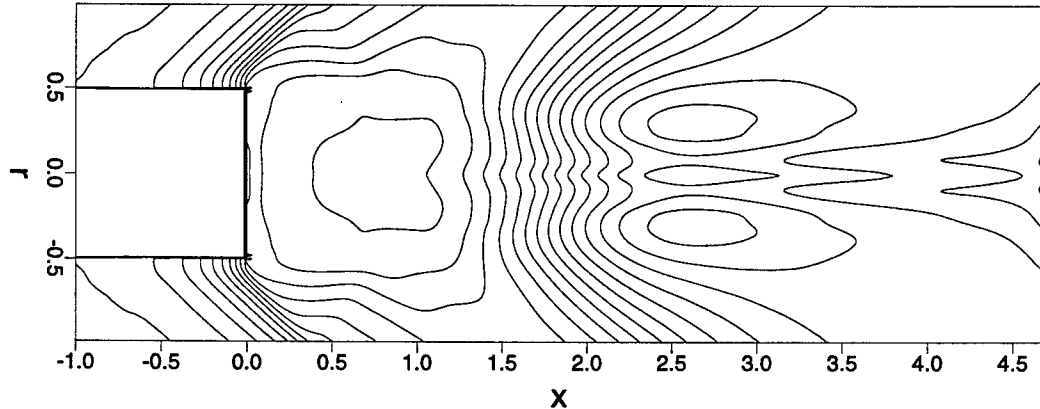


Figure 5.42: Isolines of pressure for a time-averaged flow at  $M_\infty = 1.2$  and  $Re_D = 4,000$ .

that, in addition to a change in shape of the pressure distribution, the average pressure is lower than the average of the steady axisymmetric pressure. This results in a larger base drag, which is caused solely by the unsteady structures.

In summary, the supersonic flow for  $M_\infty = 1.2$  and  $Re_D = 4,000$  shows a behavior that is somewhat similar to that presented previously for the subsonic case. The flow exhibits an absolute instability, which results in the formation of unsteady structures. These structures have a strong influence on the pressure distribution of the time-averaged flow, resulting in a constant base pressure distribution as found in experiments, and a higher base drag than for the steady axisymmetric calculation. The absolute instability causes an exponentially growing deviation from the axisymmetric flow. After a period of time the deviation reaches a nonlinear saturation and the flow field fluctuates in a non periodic way. The unsteady flow remains laminar and does not show any sign of a transition to turbulence.

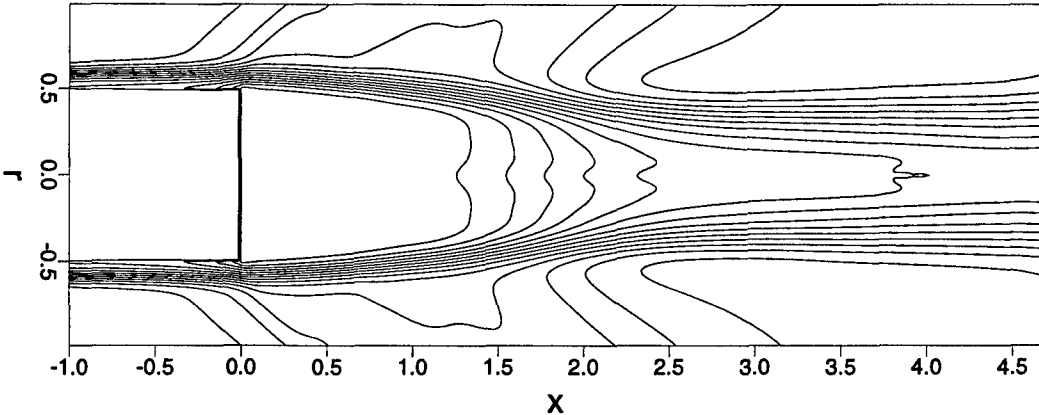


Figure 5.43: Isolines of density for a time-averaged flow at  $M_\infty = 1.2$  and  $Re_D = 4,000$ .

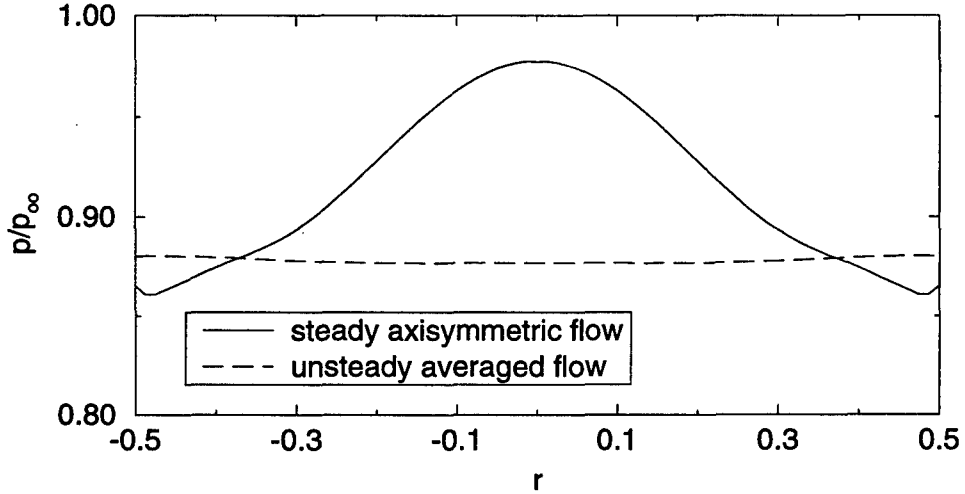


Figure 5.44: Base pressure distributions for  $M_\infty = 1.2$  and  $Re_D = 4,000$ .

### 5.1.3 Supersonic Flow at Mach 2.46

The flow field of case A4, which was calculated for the validation of the DNS code for axisymmetric flow calculations (see section 4.1.2), was used as initial condition for further investigations of the time dependent behavior of the three-dimensional flow.

#### a) Steady Calculations

In addition to the results presented for the steady axisymmetric flow field in chapter 4, figures 5.45 and 5.46 show the streamlines and isolines of vorticity, respectively. As pointed out in the previous section for the flow with free stream Mach number  $M_\infty = 1.2$ , the plot of the streamlines reveals that the curvature of the streamline dividing the recirculating region from the outer region is much smaller for supersonic flow. For the present case at  $M_\infty = 2.46$ , the dividing streamline is almost a straight line.

Also, as already mentioned in the previous section, the pressure distribution is significantly different for the subsonic and supersonic case. This difference becomes even more pronounced for the higher Mach number (comparison of figure 4.9 with figures 5.23 and 5.3). The overall

variation of the pressure is much larger for this case than for the previously shown results. The same effect can be seen in the base pressure variation, which results in a higher base drag for higher free stream Mach numbers. This is indicated by the base pressure distributions shown in figures 5.74, 5.44, and 5.19. The azimuthal vorticity, however, shows very similar characteristics to both flow fields shown previously.

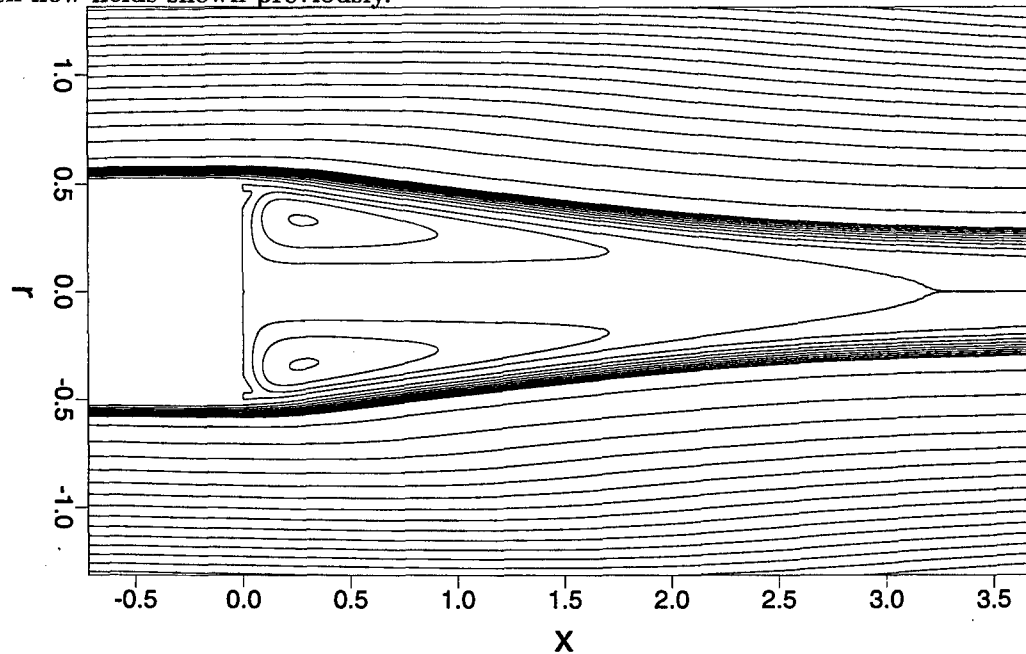


Figure 5.45: Steady streamlines for  $M_\infty = 2.46$  and  $Re_D = 30,000$  (axisymmetric steady calculation).

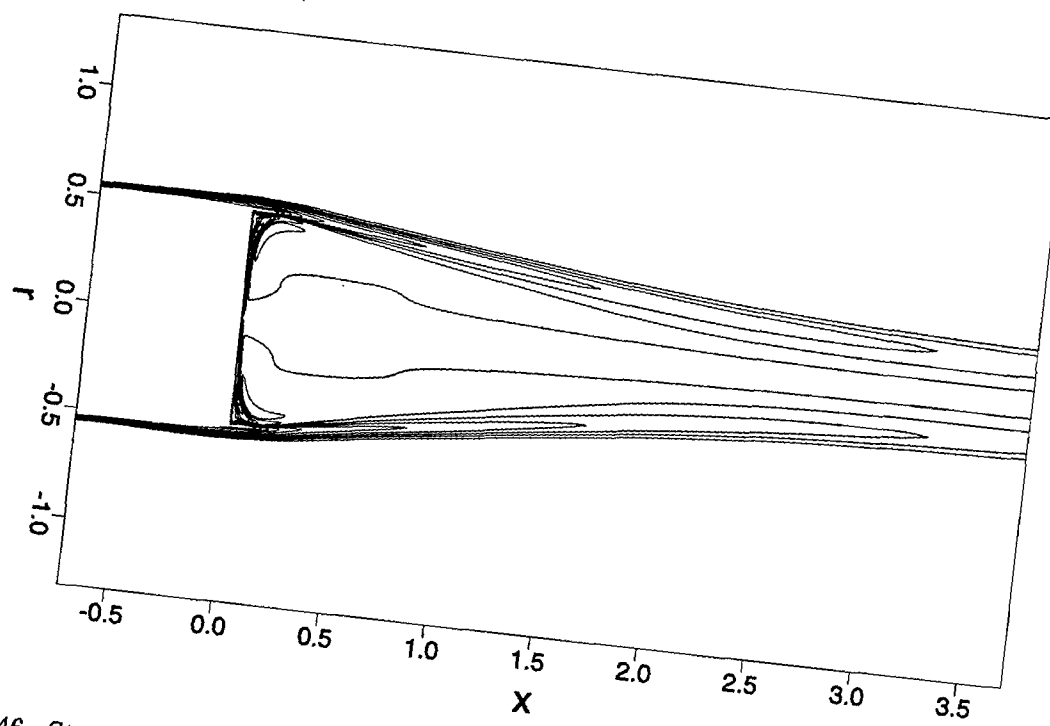


Figure 5.46: Steady azimuthal vorticity field for  $M_\infty = 2.46$  and  $Re_D = 30,000$  (axisymmetric steady calculation)

### b) Unsteady Calculations

In calculations for a free stream Mach number of  $M_\infty = 2.46$  [Turbier & Fasel (1994)], no absolute instability could be observed up to a global Reynolds number of  $Re_D = 3,000$ . Even when increasing the Reynolds number up to  $Re_D = 25,000$  in subsequent calculations, there was no indication of an absolute instability. For all cases with Reynolds numbers lower than  $Re_D = 30,000$  a generated pulse disturbance always decayed in time and the flow field eventually relaxed to the original axisymmetric steady state. The unsteady flow behavior in all these cases was similar to that presented by Turbier & Fasel (1994). The main difference was that the temporal decay rates of the disturbances decreased for increasing Reynolds numbers. This is an indication that the flow becomes less stable when the Reynolds number is increased. Here, results of a DNS are presented at a global Reynolds number  $Re_D = 30,000$ .

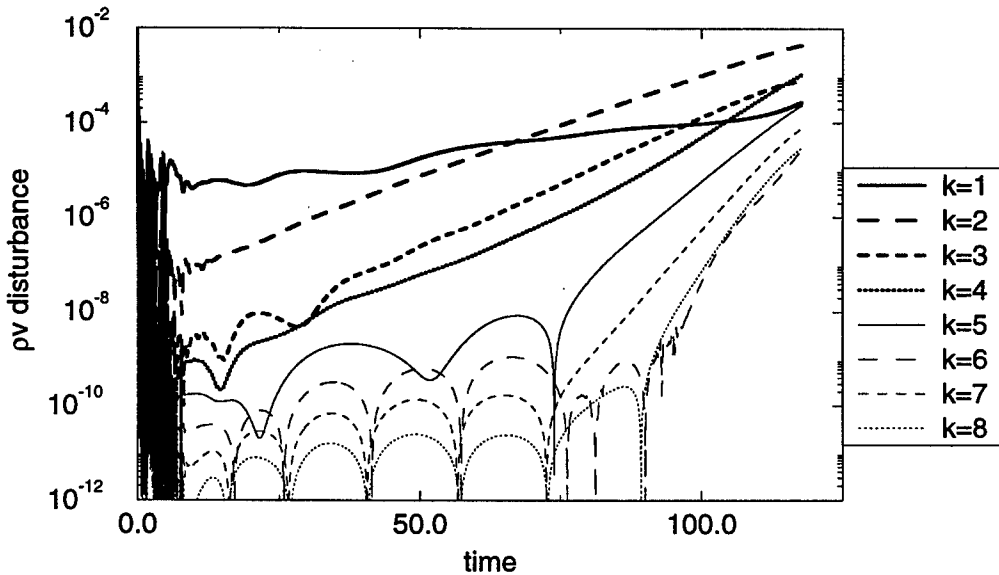


Figure 5.47: Time response of radial momentum to a single pulse of Fourier mode  $k = 1$  at  $r = 0.25$  and  $x = 0.25$  for  $M_\infty = 2.46$  and  $Re_D = 30,000$  (unfiltered DNS).

The axisymmetric flow was disturbed with a single pulse disturbance at  $x = 0.25$  and  $r = 0.25$ . The time signal at the location of the disturbance introduction is shown in figure 5.47. As for both the subsonic case and the supersonic case with  $M_\infty = 1.2$ , the azimuthal decomposition of the time signal exhibits an exponential deviation from the axisymmetric state. Figure 5.47 shows that the Fourier mode  $k = 1$  is not the most amplified for this flow;  $k = 2$ ,  $k = 3$ , and  $k = 4$  show stronger amplification rates. When the first four Fourier modes pass a certain threshold, the higher Fourier modes ( $k = 5$ ,  $k = 6$ ,  $k = 7$ , and  $k = 8$ ) also exhibit strong amplification.

In contrast to the two cases discussed previously, local velocity gradients near the stagnation point ( $x \approx 2.8$ ) kept increasing over time to very high levels. Eventually, the simulation became underresolved and terminated at about  $t = 125$ . Figures 5.48 and 5.49 show instantaneous isolines of total vorticity shortly before the simulation terminated. At this point the flow field

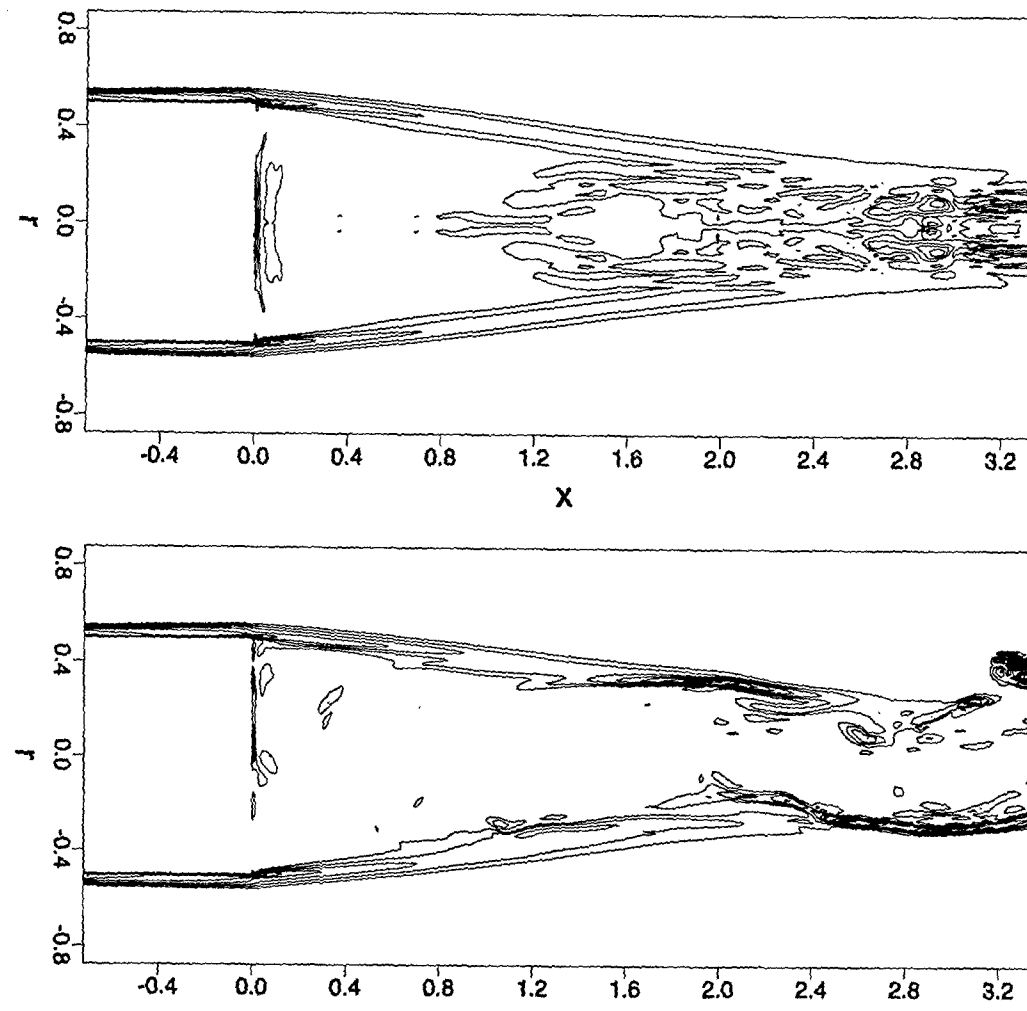


Figure 5.48: Isolines of instantaneous total vorticity for  $Re_D = 30,000$  and  $M_\infty = 2.46$ . x-z plane (top) and x-y plane (bottom) (unfiltered DNS).

exhibits large and small scale structures (see figure 5.48). The simulation is no longer able to handle the large gradients in the flow field, which causes numerical instabilities and finally a termination of the calculation. Also, as can be seen in figure 5.47, all azimuthal Fourier modes fill up rapidly and even the higher modes grow up to the same order of magnitude. All of this is an indication that the spatial resolution of the simulation is inadequate for the occurring small scale structures.

Because of the appearance of small scale structures that could not be resolved with a feasible number of grid points and Fourier modes (for a reasonable computation time on the computer that was used) the flow field was filtered in the axial and radial directions at every time step of the Runge-Kutta integration scheme. For this procedure a sixth-order accurate compact difference filter was applied, which is described in Lele (1992). This filter has been used successfully for Large-Eddy Simulations of incompressible boundary layer flows [Bachman (1996)] and has also been applied for LES in the present work (see section 3.6). In addition, the flow field

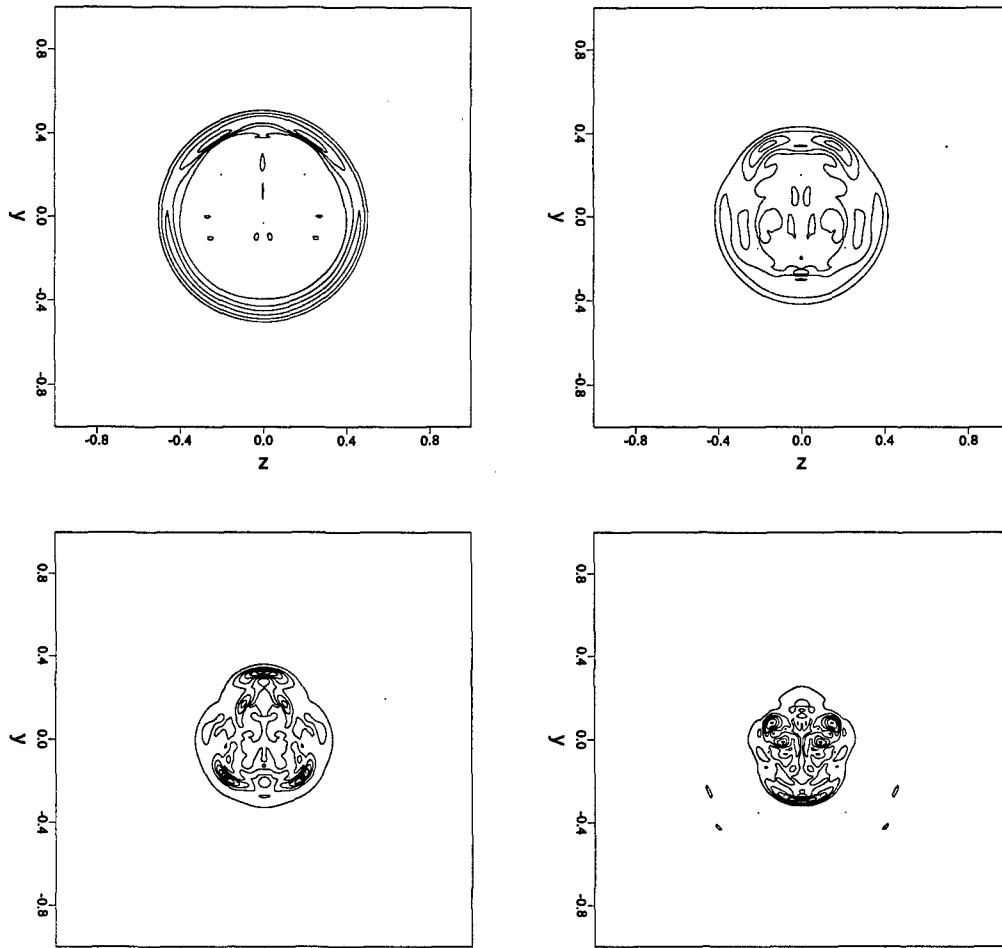


Figure 5.49: Isolines of instantaneous total vorticity for  $Re_D = 30,000$  and  $M_\infty = 2.46$ , y-z planes at  $x = 1$  (top left),  $x = 2$  (top right),  $x = 3$  (bottom left), and  $x = 4$  (bottom right) (unfiltered DNS).

was also filtered at every hundredth time step with an explicit second order central difference filter, because the dissipation provided by the sixth-order compact filter was not sufficient to completely suppress the growth of small scales.

The time signal at the location of the disturbance generation after the introduction of the spatial filtering is shown in figure 5.50. Even with the added dissipation of the filtering the flow field still exhibits non-periodic fluctuations in all Fourier modes that do not decay. In figures 5.51, 5.52, and 5.53 isolines of total vorticity are plotted in the x-y plane and the x-z plane for the spatially filtered calculations for three different instances in time. As for the previous calculations, the figures vortical structures appear in the free shear layer which originate near the corner of the base and are convected downstream. In contrast to the previous cases, the structures are more confined to the shear layer region. This is confirmed by figures 5.54, 5.55, and 5.56 which show isolines of total vorticity in the y-z plane at four different  $x$  locations. The structures that are similar to the ones observed for the lower Mach number cases are now

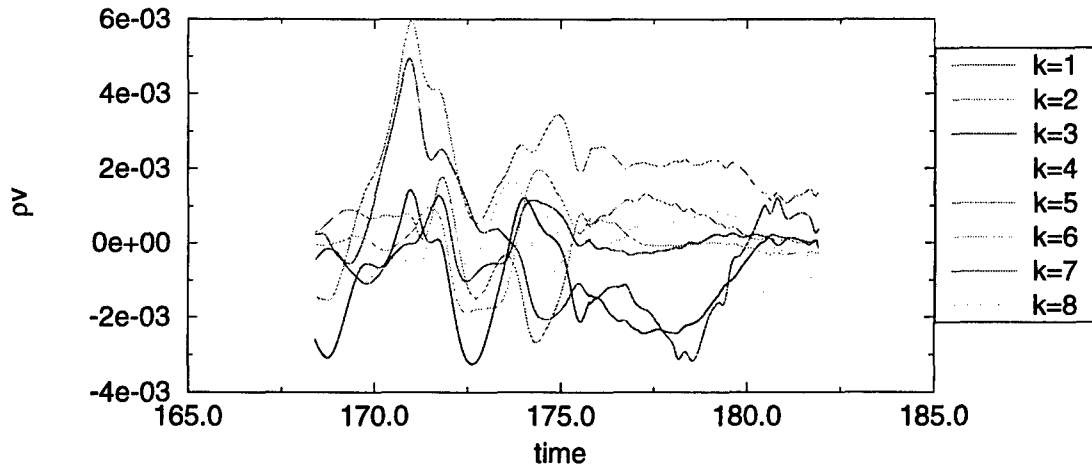


Figure 5.50: Time signal of radial momentum at  $r = 0.25$  and  $x = 0.25$  for  $M_\infty = 2.46$  and  $Re_D = 30,000$  (filtered DNS).

located entirely within the top shear layer. The three-dimensional structures can be seen more clearly in the three-dimensional isosurfaces in figures 5.57 through 5.68. The isosurface for the instantaneous pressure deviation from the time-averaged flow is shown at  $\Delta p = -0.02$  which represents the same level as for the previous cases. It appears that there are still two axial vortices present. The vorticity structures indicate that for this case the level of vorticity is much higher than in the previous two cases. Also, the structures appear to be much thinner and more elongated in the axial direction. Figure 5.65 shows two long axial vortices which are much stronger and much thinner than for the cases with  $M_\infty = 0.2$  and  $M_\infty = 1.2$ .

Flow visualization using particles as shown in figures 5.69 through 5.71 was performed similar to the subsonic case. As before, the particles were introduced at a ring near the corner of the base ( $x = 0.025, r = 0.475$ ). The plots do not indicate the structures as clearly as in the cases for  $M_\infty = 0.2$  and  $M_\infty = 1.2$ . The cross-sectional cuts, however, indicate that the longitudinal vortices are more confined in the shear layer than for the cases with  $M_\infty = 0.2$  and  $M_\infty = 1.2$ .

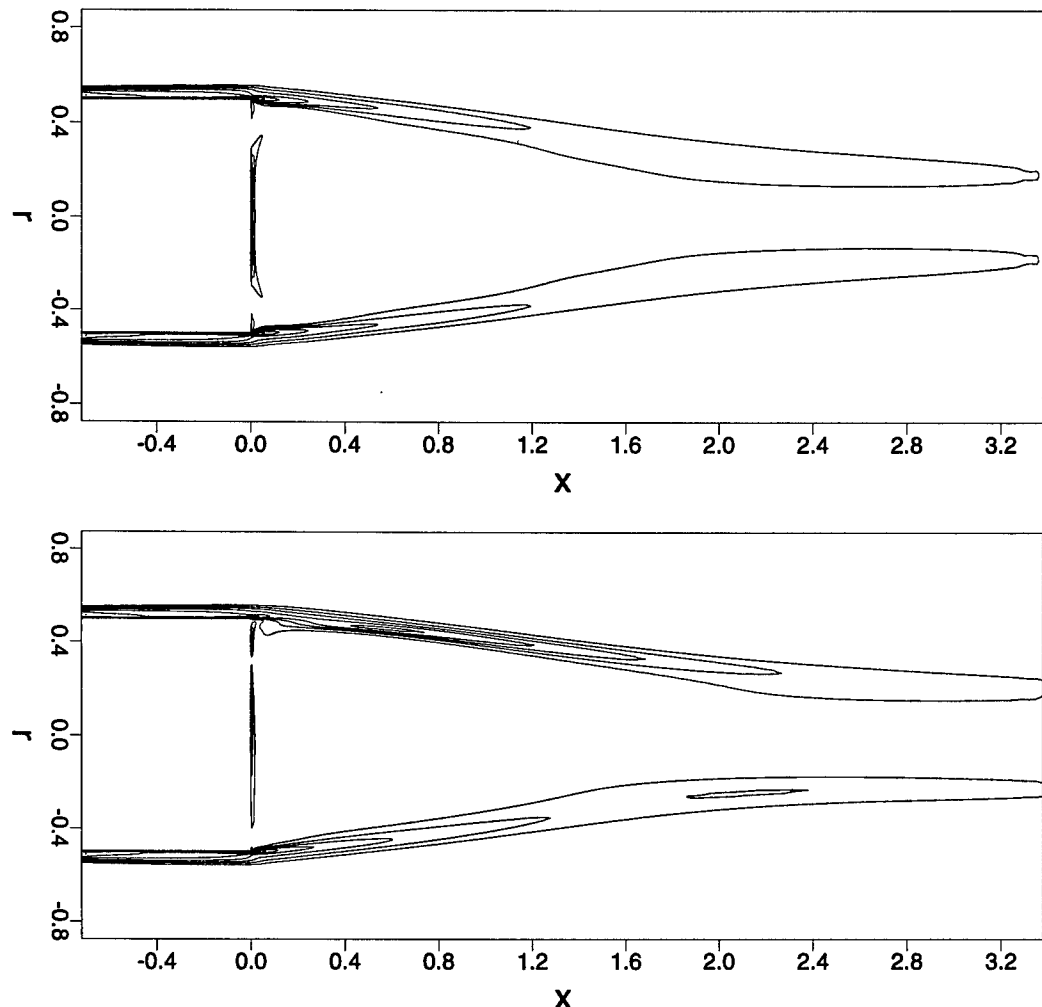


Figure 5.51: Isolines of instantaneous total vorticity for  $Re_D = 30,000$  and  $M_\infty = 2.46$  at  $t = 174.35$ , x-z plane (top) and x-y plane (bottom) (filtered DNS).

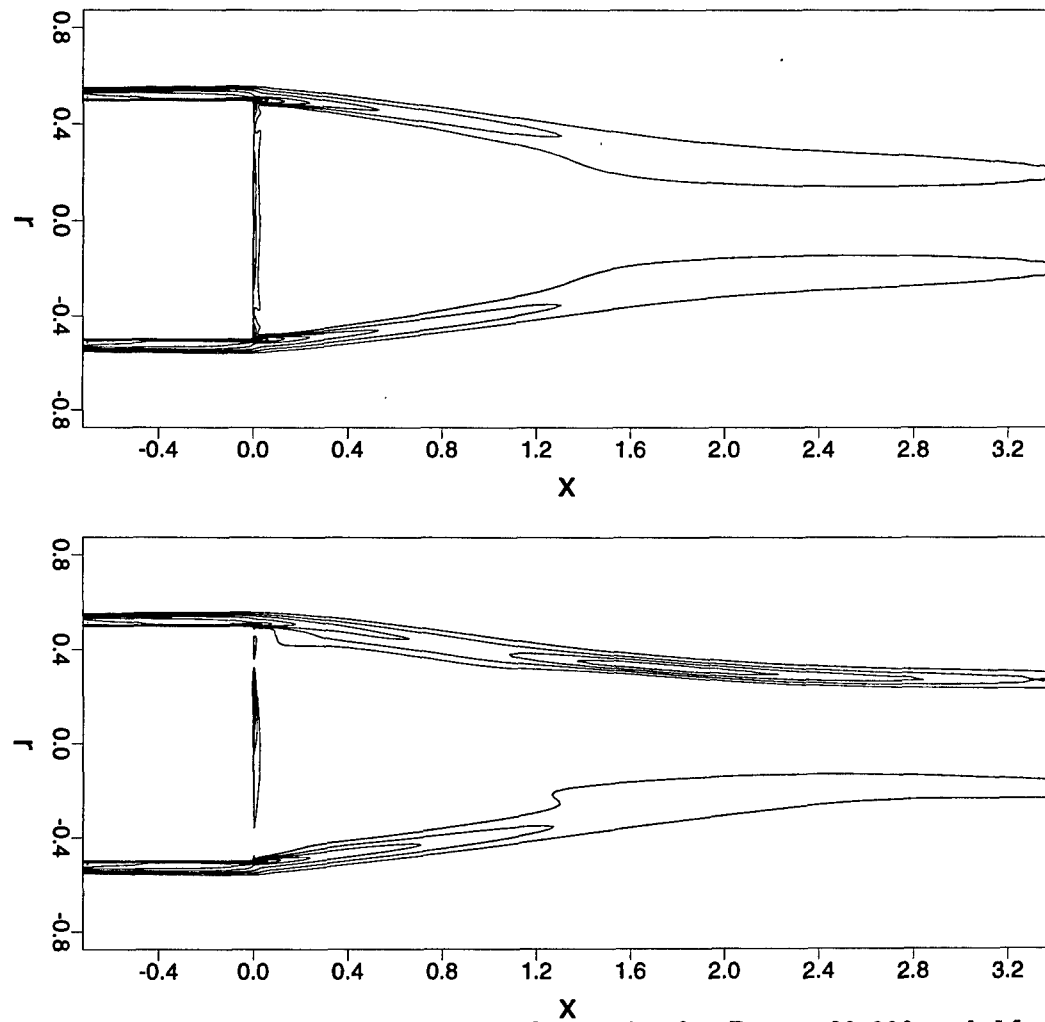


Figure 5.52: Isolines of instantaneous total vorticity for  $Re_D = 30,000$  and  $M_\infty = 2.46$  at  $t = 176.35$ , x-z plane (top) and x-y plane (bottom) (filtered DNS).

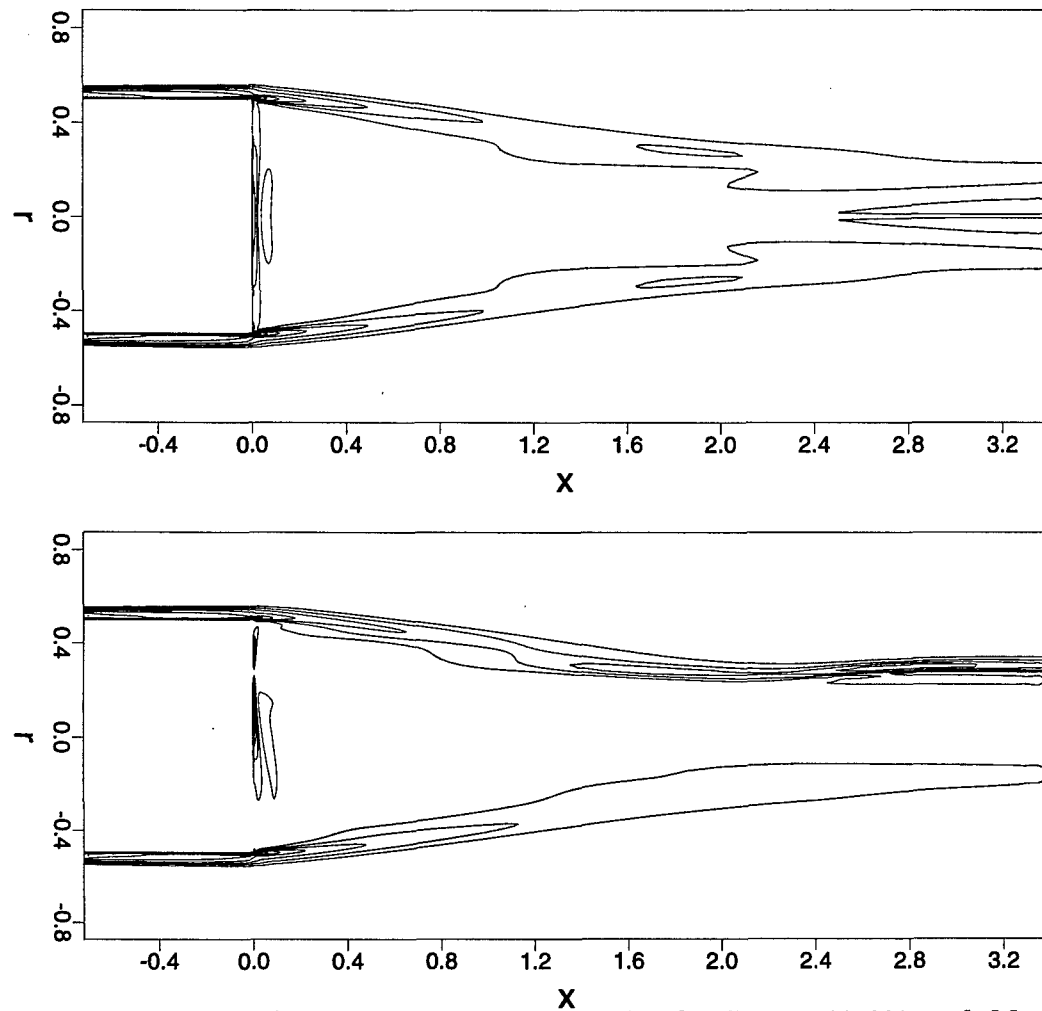


Figure 5.53: Isolines of instantaneous total vorticity for  $Re_D = 30,000$  and  $M_\infty = 2.46$  at  $t = 178.1$ ,  $x$ - $z$  plane (top) and  $x$ - $y$  plane (bottom) (filtered DNS).

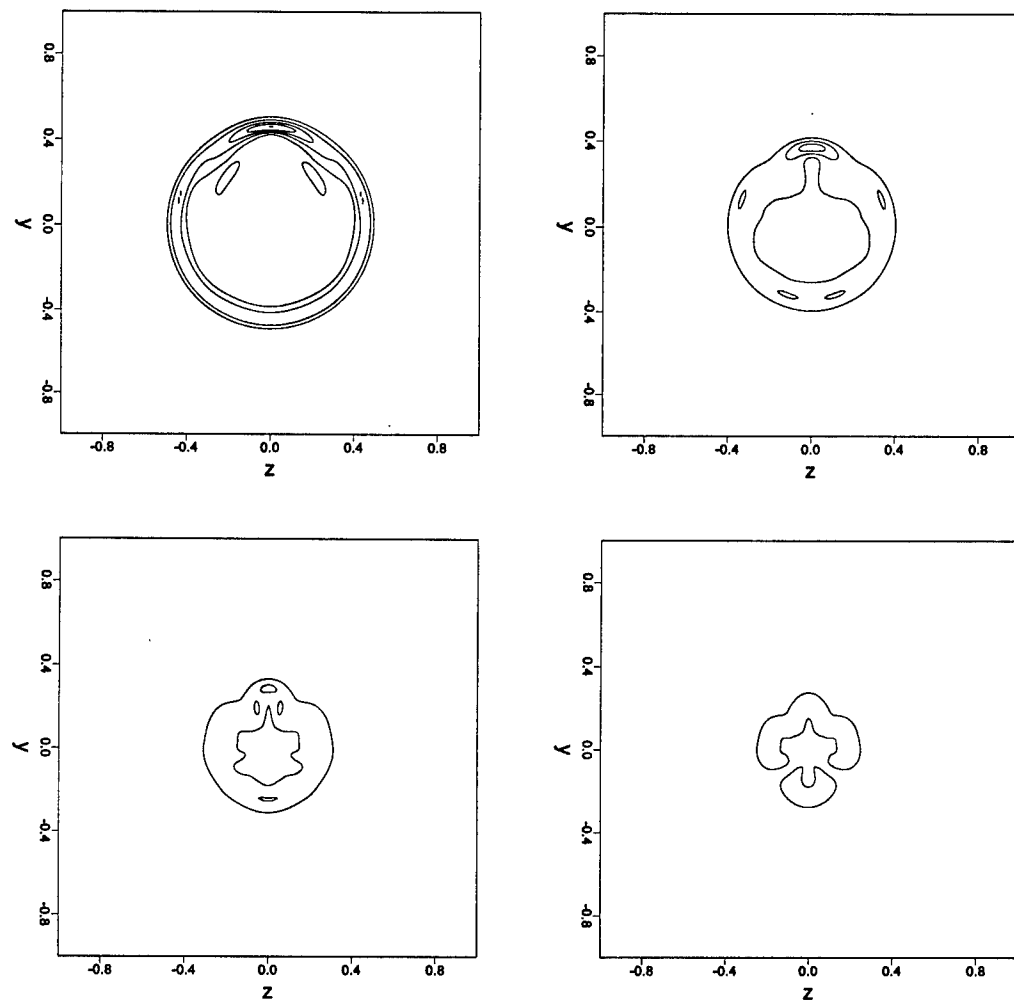


Figure 5.54: Isolines of instantaneous total vorticity for  $Re_D = 30,000$  and  $M_\infty = 2.46$  at  $t = 174.35$ , y-z planes at  $x = 1$  (top left),  $x = 2$  (top right),  $x = 3$  (bottom left), and  $x = 4$  (bottom right) (filtered DNS).

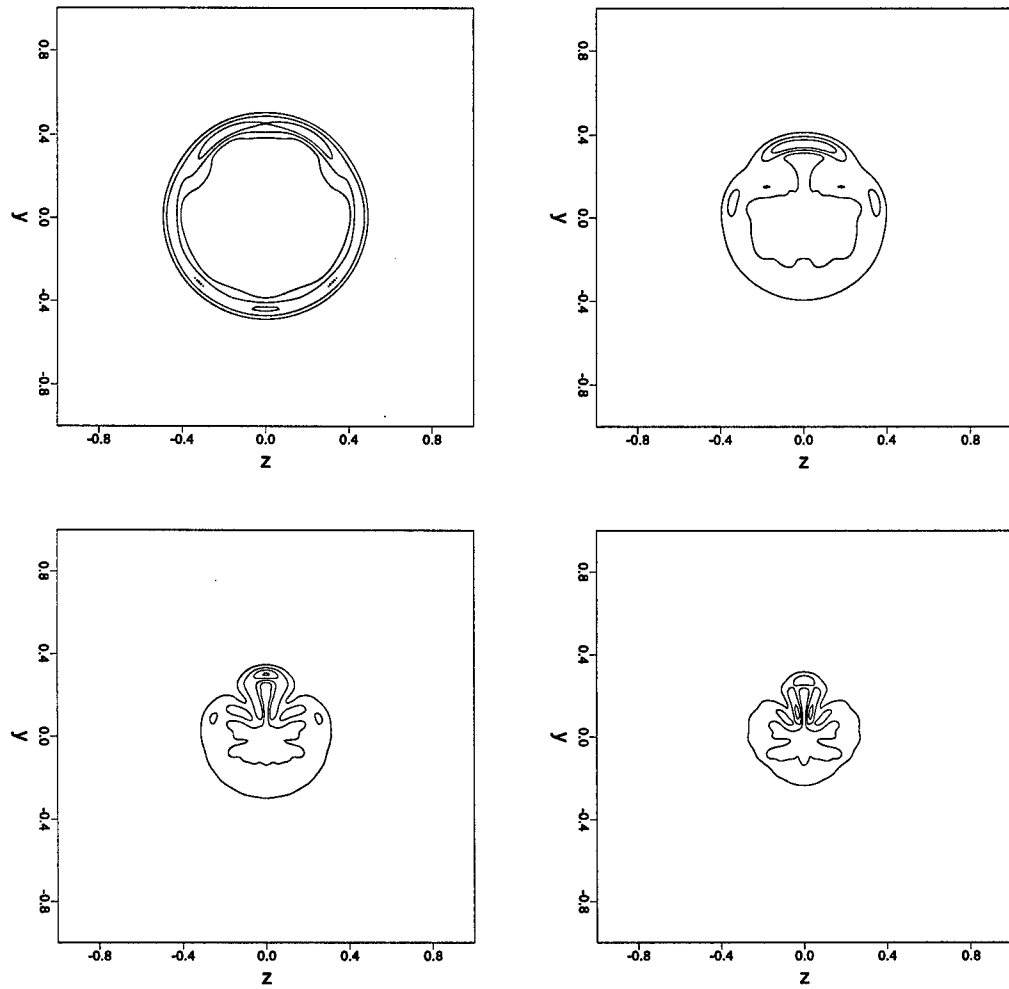


Figure 5.55: Isolines of instantaneous total vorticity for  $Re_D = 30,000$  and  $M_\infty = 2.46$  at  $t = 176.35$ , y-z planes at  $x = 1$  (top left),  $x = 2$  (top right),  $x = 3$  (bottom left), and  $x = 4$  (bottom right) (filtered DNS).

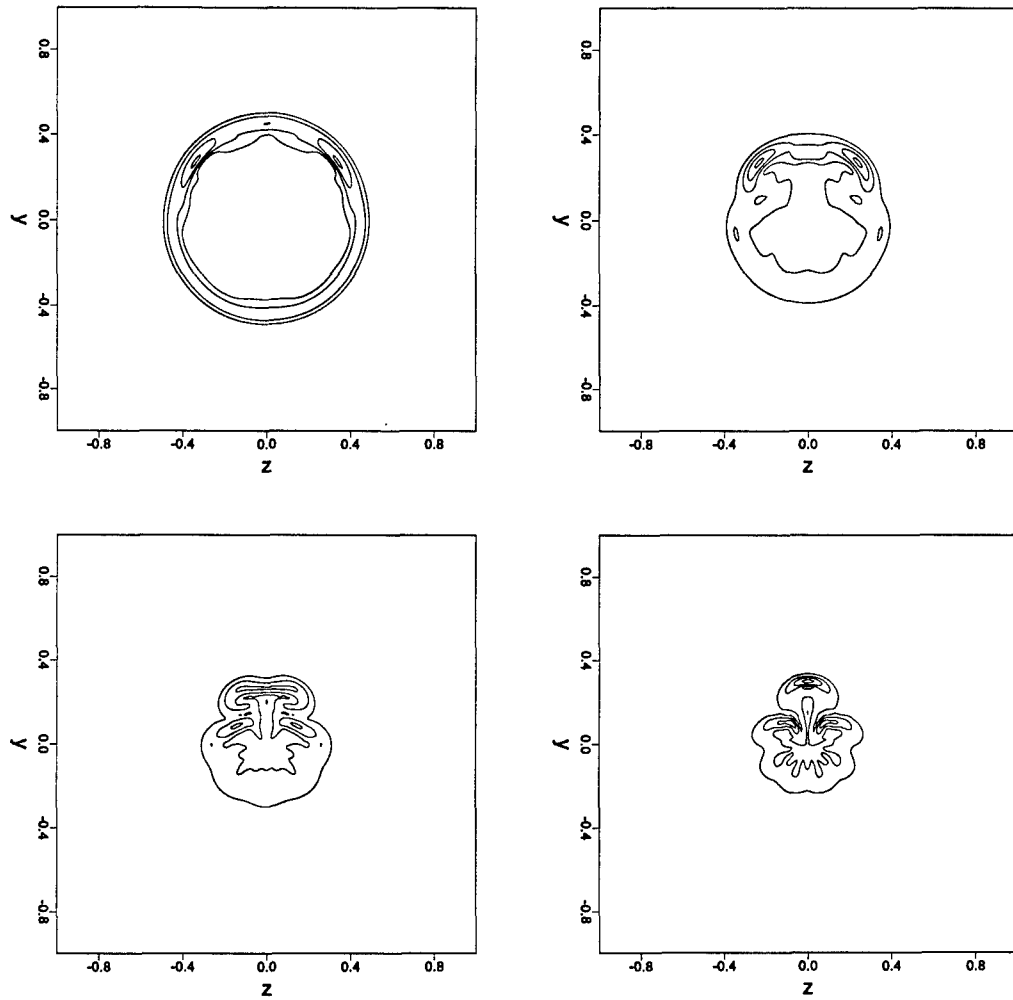


Figure 5.56: Isolines of instantaneous total vorticity for  $Re_D = 30,000$  and  $M_\infty = 2.46$  at  $t = 178.1$ , y-z planes at  $x = 1$  (top left),  $x = 2$  (top right),  $x = 3$  (bottom left), and  $x = 4$  (bottom right) (filtered DNS).

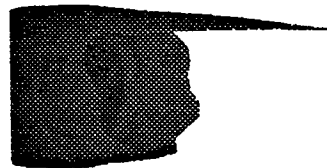


Figure 5.57: Isosurfaces of instantaneous total vorticity ( $|\omega| = 7$ ) for  $M_\infty = 2.46, Re_D = 30,000$  at  $t = 174.35$  (filtered DNS).



Figure 5.58: Isosurfaces of instantaneous total vorticity ( $|\omega| = 7$ ) for  $M_\infty = 2.46, Re_D = 30,000$  at  $t = 176.35$  (filtered DNS).



Figure 5.59: Isosurfaces of instantaneous total vorticity ( $|\omega| = 7$ ) for  $M_\infty = 2.46, Re_D = 30,000$  at  $t = 178.1$  (filtered DNS).

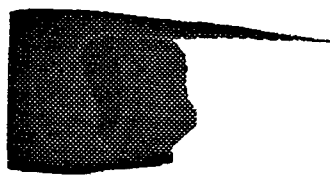


Figure 5.60: Isosurfaces of instantaneous azimuthal vorticity ( $|\omega_\theta| = 7$ ) for  $M_\infty = 2.46, Re_D = 30,000$  at  $t = 174.35$  (filtered DNS).

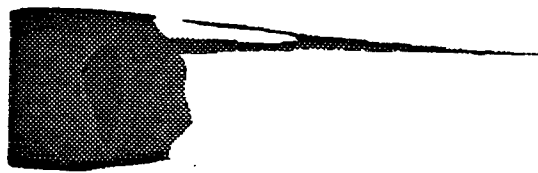


Figure 5.61: Isosurfaces of instantaneous azimuthal vorticity ( $|\omega_\theta| = 7$ ) for  $M_\infty = 2.46, Re_D = 30,000$  at  $t = 176.35$  (filtered DNS).



Figure 5.62: Isosurfaces of instantaneous azimuthal vorticity ( $|\omega_\theta| = 7$ ) for  $M_\infty = 2.46, Re_D = 30,000$  at  $t = 178.1$  (filtered DNS).

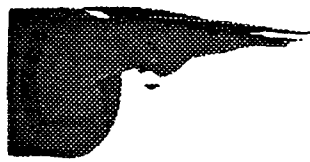


Figure 5.63: Isosurfaces of instantaneous axial vorticity ( $|\omega_x| = 4$ ) for  $M_\infty = 2.46, Re_D = 30,000$  at  $t = 174.35$  (filtered DNS).

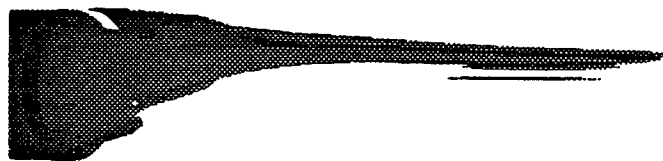


Figure 5.64: Isosurfaces of instantaneous axial vorticity ( $|\omega_x| = 4$ ) for  $M_\infty = 2.46$ ,  $Re_D = 30,000$  at  $t = 176.35$  (filtered DNS).

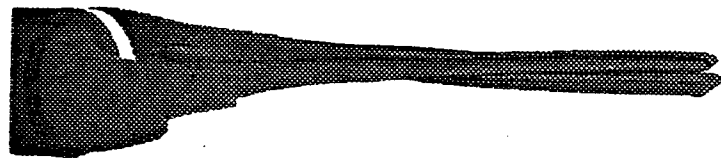


Figure 5.65: Isosurfaces of instantaneous axial vorticity ( $|\omega_x| = 4$ ) for  $M_\infty = 2.46$ ,  $Re_D = 30,000$  at  $t = 178.1$  (filtered DNS).



Figure 5.66: Isosurfaces of instantaneous pressure deviation from the time-averaged mean flow ( $\Delta p = -0.02$ ) for  $M_\infty = 2.46$ ,  $Re_D = 30,000$  at  $t = 174.35$  (filtered DNS).



Figure 5.67: Isosurfaces of instantaneous pressure deviation from the time-averaged mean flow ( $\Delta p = -0.02$ ) for  $M_\infty = 2.46$ ,  $Re_D = 30,000$  at  $t = 176.35$  (filtered DNS).

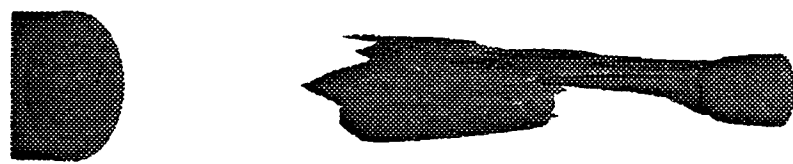


Figure 5.68: Isosurfaces of instantaneous pressure deviation from the time-averaged mean flow ( $\Delta p = -0.02$ ) for  $M_\infty = 2.46$ ,  $Re_D = 30,000$  at  $t = 178.1$  (filtered DNS).

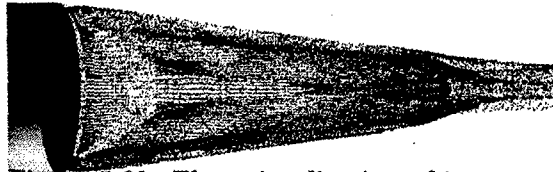
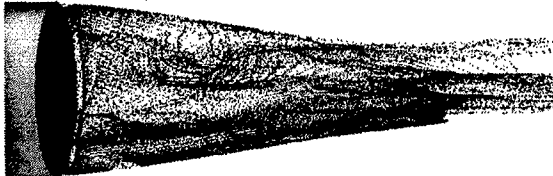


Figure 5.69: Flow visualization of instantaneous flow field via particles for  $M_\infty = 2.46$ ,  $Re_D = 30,000$ , viewed from  $\theta = \pi/2$  (top) and from  $\theta = 0$  (bottom) (particles introduced at  $x = 0.025$ ,  $r = 0.475$ ; filtered DNS).

The previous cases for  $M_\infty = 0.2$  and  $M_\infty = 1.2$  have shown that the unsteady structures have a strong influence on the global time-averaged flow field. For the  $M_\infty = 2.46$  case, the time-averaged flow is shown in figures 5.72 and 5.73 in the form of isolines of the pressure and density. As before, the plots exhibit a drastic difference between the time-averaged flow and the axisymmetric flow (compare figures 4.8 and 4.9). The pressure distribution in the radial direction for the time-averaged flow is almost constant near the base. This is in agreement with experimental observations.

Figure 5.74 shows the pressure distribution along the base normalized by the static pressure in the free stream. The plot confirms that this is due to the presence of the large structures. The base pressure distribution is almost constant over the radius. Averaged over the radius the base pressure is significantly lower than for the axisymmetric steady calculation. This indicates, that for this higher Mach number the dynamic structures also have a large influence on the global flow field which results in a lower base pressure and, consequently, in a higher base drag.

In summary, the calculations indicate that the flow for the higher Mach number,  $M_\infty = 2.46$ , exhibits an absolute instability at a global Reynolds number of  $Re_D = 30,000$ . As for the subsonic case ( $M_\infty = 0.2$ ) and the slightly supersonic case ( $M_\infty = 1.2$ ) the absolute instability leads to large structures. In contrast to the previous cases, the structures tend to break down to smaller scales. This is an indication that the flow might transition to turbulence if the calculations were better resolved. Therefore, further investigation of this flow was performed

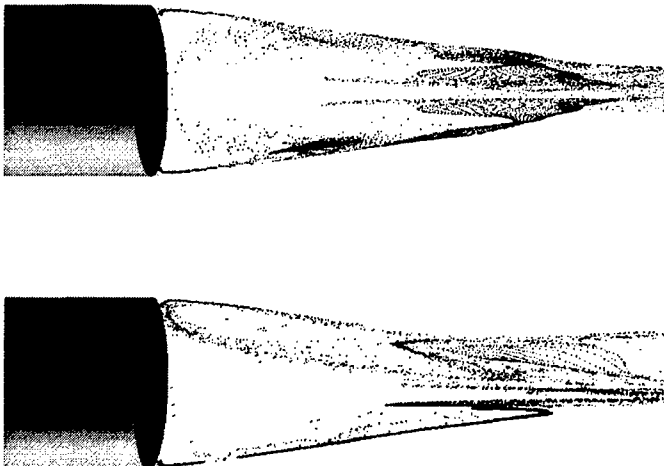


Figure 5.70: Flow visualization of instantaneous flow field via particles for  $M_\infty = 2.46$ ,  $Re_D = 30,000$ , sheets of thickness 0.01 at  $\theta = 0$  (top) and  $\theta = \pi/2$  (bottom), (particles introduced at  $x = 0.025$ ,  $r = 0.475$ ; filtered DNS).

employing LES (see following section).



Figure 5.71: Flow visualization of instantaneous flow field via particles for  $M_\infty = 2.46$ ,  $Re_D = 30,000$ , cross-sectional cuts of thickness 0.01 at  $x = 1.0$ ,  $x = 2.0$ ,  $x = 3.0$ , and  $x = 4.0$  (particles introduced at  $x = 0.025$ ,  $r = 0.475$ ; filtered DNS).

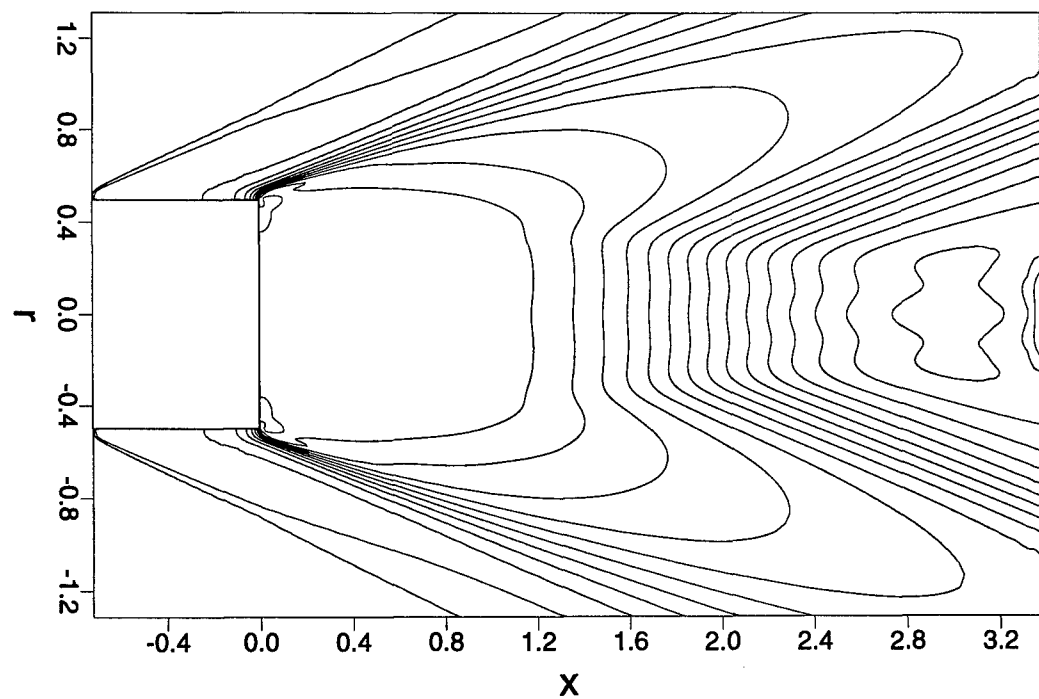


Figure 5.72: Isolines of pressure for the time-averaged flow at  $M_\infty = 2.46$  and  $Re_D = 30,000$ .

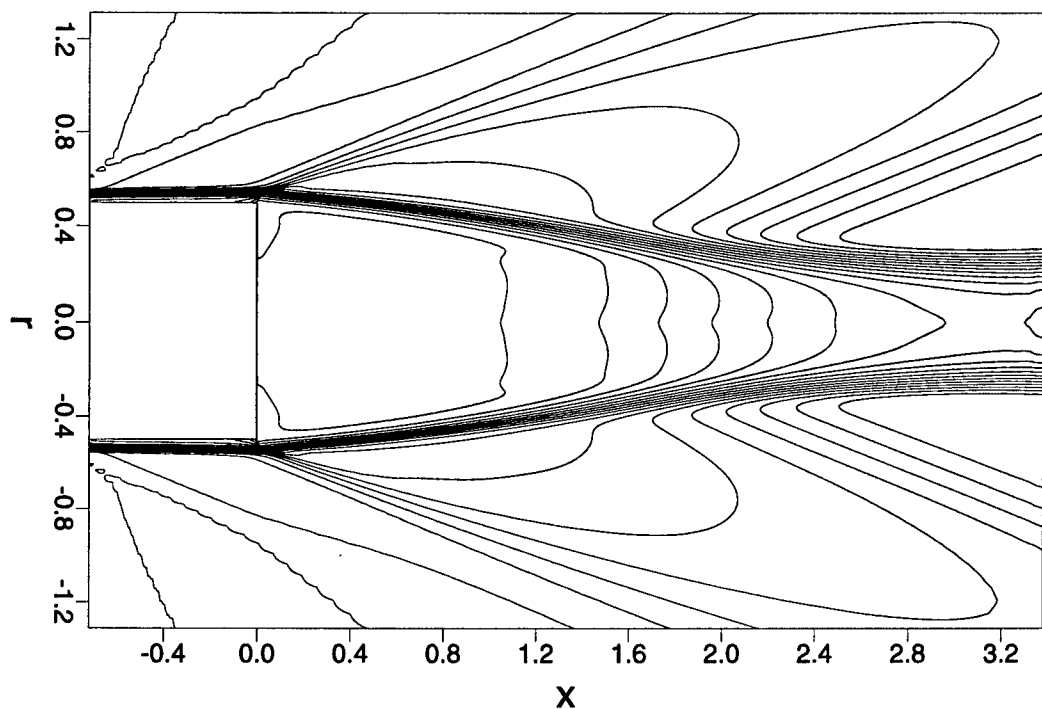


Figure 5.73: Isolines of density for the time-averaged flow at  $M_\infty = 2.46$  and  $Re_D = 30,000$ .

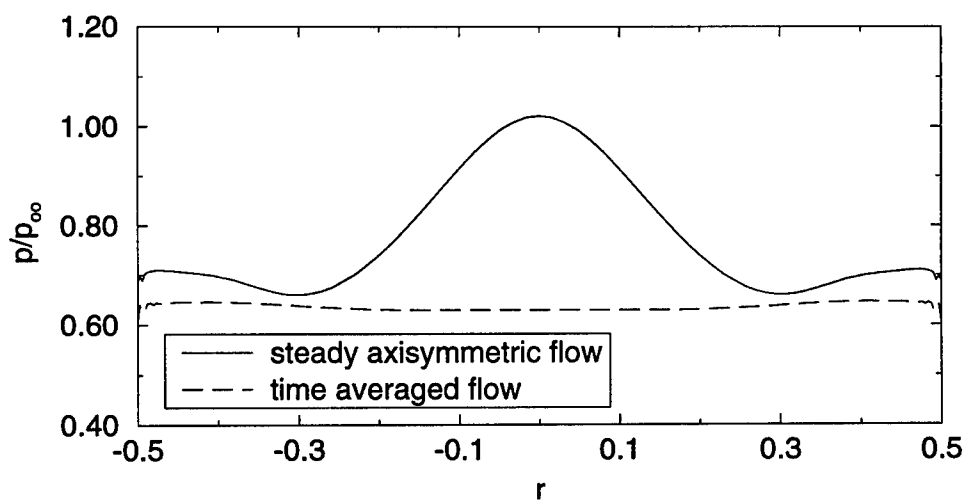


Figure 5.74: Base pressure distributions for  $M_\infty = 2.46$  and  $Re_D = 30,000$ .

## 5.2 Large-Eddy Simulations

As shown in section 5.1.3, the DNS for  $M_\infty = 2.46$  and  $Re_D = 30,000$  without spatial filtering terminated after the local velocity gradients near the stagnation points became too large. Therefore, to extend the calculations, a spatial filter was applied in the axial and the radial directions. The results shown in section 5.1.3 indicate that using the spatial filter (in addition to a very dissipative second-order filter at every 100th time step) the small scale structures could be dissipated. However, the larger structures remained in the flow field (see section 5.1.3).

The application of a second-order filter in order to dissipate the small scale structures is physically not very meaningful. In order to investigate the true behavior of the flow field at this Reynolds number, either a higher resolution for the DNS is necessary or a turbulence model is required to model the unresolved scales. Since the goal is to calculate flow fields at even higher Reynolds numbers (up to  $O(10^6)$ ), a much higher resolution would be required for the DNS. However, the simulation with the spatial and temporal resolution of case T7 (see table A.3) was already very CPU time intensive. A typical calculation for this flow field required about 600 MBytes of main memory and in the order of 500 CPU hours on a single processor of a CRAY C90. Even more memory and CPU time would be required for calculations with higher resolution (about 5 GBytes for twice the resolution in physical space).

As stated in the introduction, with Reynolds-Averaged Navier-Stokes (RANS) it is not possible to capture the relevant physics of this flow. Employing Large-Eddy Simulation (LES), on the other hand, will allow investigation of the dynamics of the large structures and their effect on the local flow behavior. The implementation of LES is discussed in section 2.4. For the LES the same sixth-order accurate compact difference filter was applied in the axial and radial directions (see also section 5.1.3). However, no additional second order central difference filter was applied. The Smagorinsky constant for the sub-grid scale model was chosen to be  $C_S = 0.065$ . This is the same value that has been used for incompressible turbulent boundary layer calculations [[Bachman (1996)]]. It is not clear if this value is also useful for the present case. In addition, a constant value is not realistic for a flow with such complexity. For this case, a dynamic sub-grid scale model would be more appropriate.

In the following, preliminary results are presented for a free stream Mach number of  $M_\infty = 2.46$  and two different global Reynolds numbers,  $Re_D = 30,000$  and  $Re_D = 100,000$ . The results are presented in form of isolines of instantaneous total vorticity, isolines of axial velocity, radial velocity, pressure, density, temperature, local Mach number, and azimuthal vorticity for the time-averaged turbulent flow field, and isolines of root-mean-square values (RMS) of axial, radial and tangential turbulent intensities as well as axial-radial Reynolds stress  $\langle u'v' \rangle$  and turbulent kinetic energy (Here  $\langle \rangle$  denotes the RMS value).

As a first case, the LES was applied to the previously calculated flow field at  $Re_D = 30,000$ . Figure 5.75 shows isolines of instantaneous total vorticity in the flow field. A direct comparison with figures 5.51 through 5.53 for the filtered DNS for  $M_\infty = 2.46$  and  $Re_D = 30,000$  shows that the flow field for the LES looks very similar to that of the spatially filtered DNS. However, in the

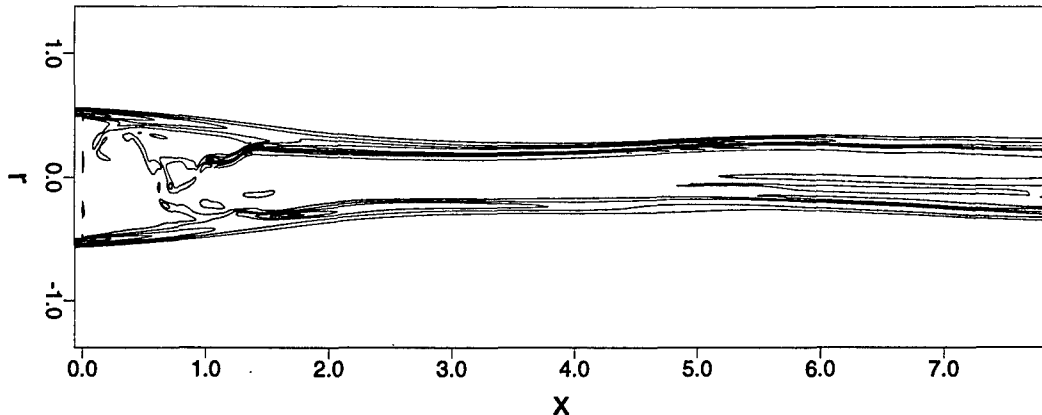


Figure 5.75: Isolines of instantaneous total vorticity for  $M_\infty = 2.46$  and  $Re_D = 30,000$  (LES).

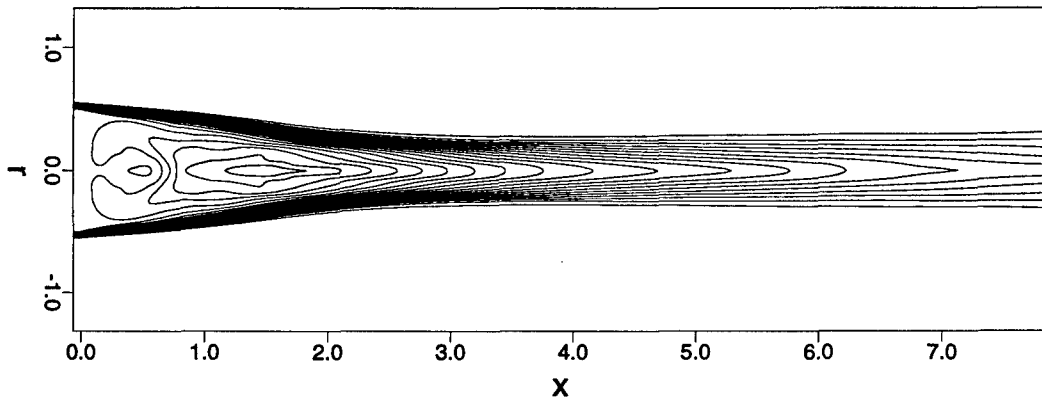


Figure 5.76: Isolines of axial velocity for the time-averaged flow field at  $M_\infty = 2.46$  and  $Re_D = 30,000$  (LES).

DNS, structures appeared in the free shear layer, emanating from the corner. These structures seem to be suppressed in the LES. However, structures are noticeable within the recirculating region which are convected upstream to the base.

As for the time-averaged spatially filtered DNS, the recirculating region of the time-averaged LES is much shorter ( $L_R \approx 2.8$ ) than for the steady laminar calculation ( $L_R \approx 3.5$ ). This can be seen in figure 5.76, where isolines of the axial velocity of the time-averaged turbulent flow field are shown. Figures 5.77 through 5.82 show isolines of time-averaged radial velocity, pressure, density, temperature, local Mach number, and azimuthal vorticity, respectively. Comparison with the results for the steady flow calculation reveals, that the changes in the flow field (for example the pressure drop downstream of the corner) are much more intense for the turbulent flow. In addition, figure 5.78 shows that, similar to the time-average for the unsteady DNS calculations for  $M_\infty = 2.46$  and for  $M_\infty = 1.2$ , the pressure distribution along the base is almost constant. This is in good agreement with experimental observations.

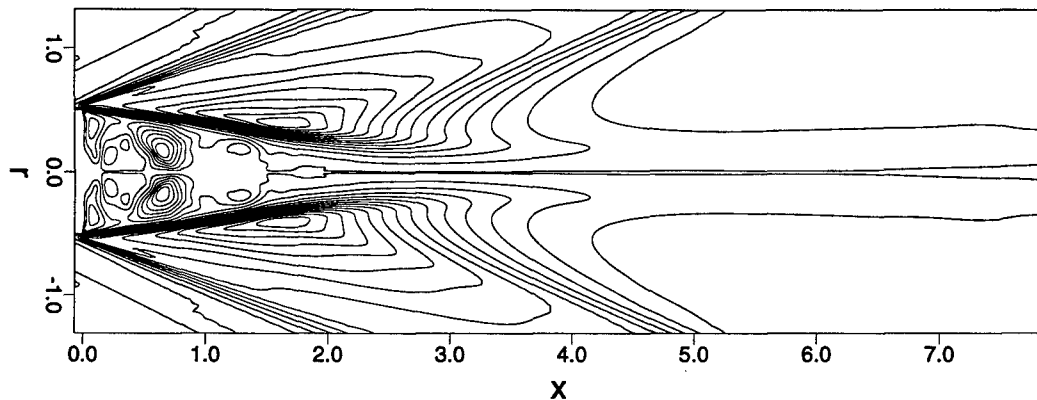


Figure 5.77: Isolines of radial velocity for the time-averaged flow field at  $M_\infty = 2.46$  and  $Re_D = 30,000$  (LES).

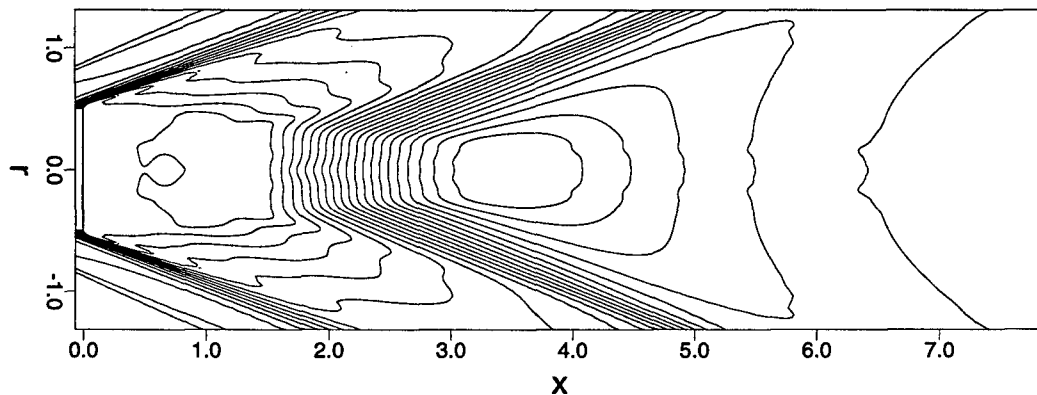


Figure 5.78: Isolines of pressure for the time-averaged flow field at  $M_\infty = 2.46$  and  $Re_D = 30,000$  (LES).

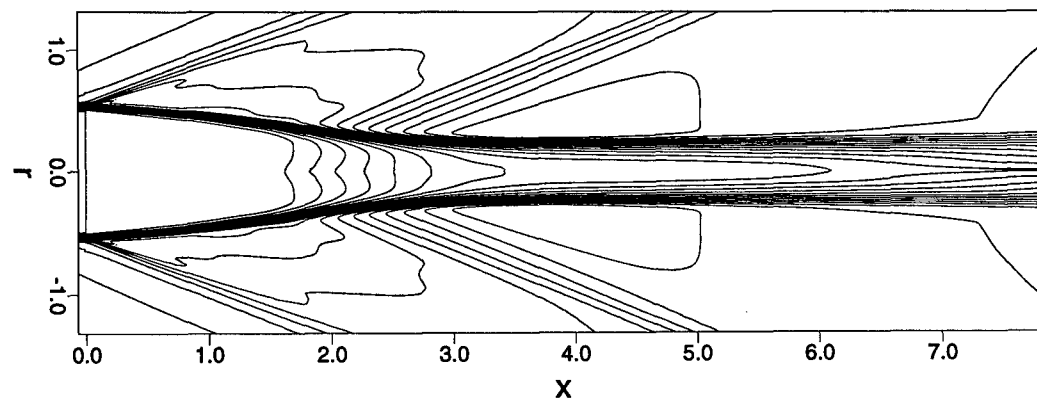


Figure 5.79: Isolines of density for the time-averaged flow field at  $M_\infty = 2.46$  and  $Re_D = 30,000$  (LES).

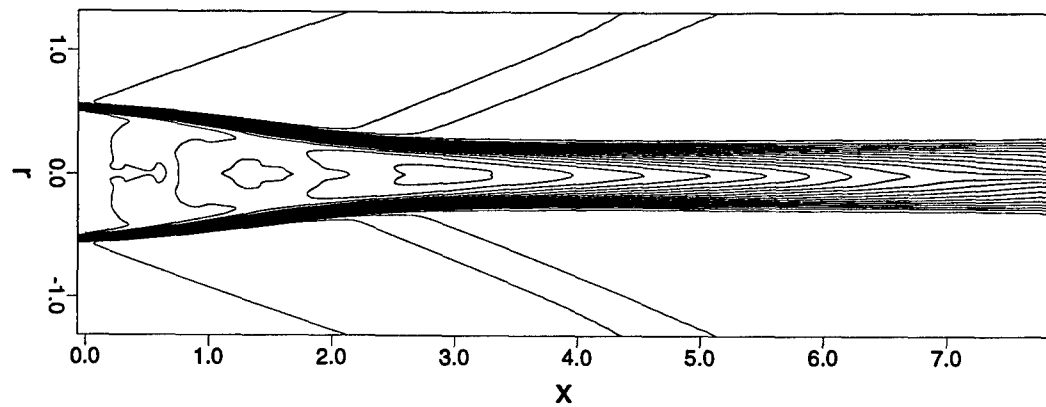


Figure 5.80: Isolines of temperature for the time-averaged flow field at  $M_\infty = 2.46$  and  $Re_D = 30,000$  (LES).

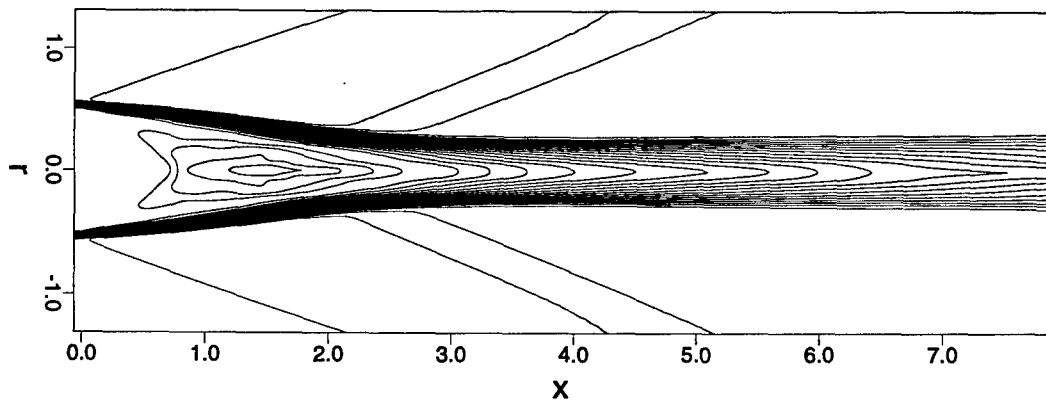


Figure 5.81: Isolines of local Mach number for the time-averaged flow field at  $M_\infty = 2.46$  and  $Re_D = 30,000$  (LES).

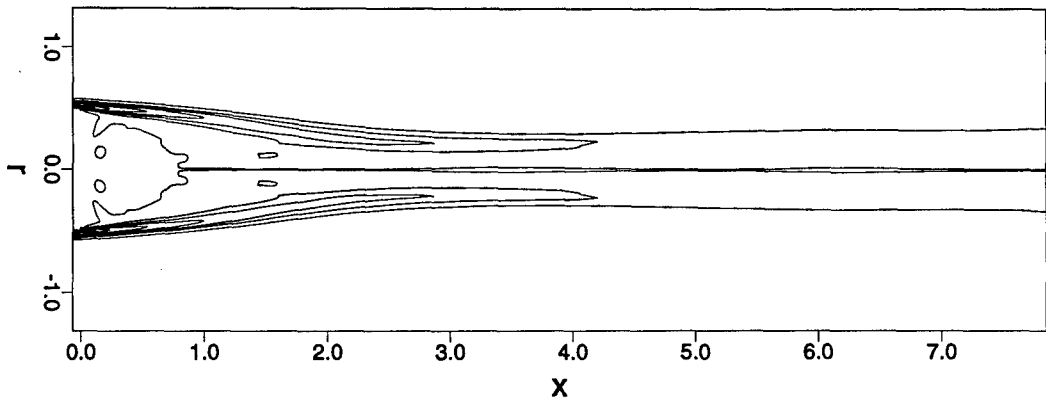


Figure 5.82: Isolines of azimuthal vorticity for the time-averaged flow field at  $M_\infty = 2.46$  and  $Re_D = 30,000$  (LES).

For further comparison with experimental results from Dutton and co-workers [see, for example, [Herrin & Dutton (1994c)]] the RMS values of the turbulent intensities, the Reynolds stress, and the turbulent kinetic energy are shown in figures 5.83 through 5.87, with

$$\begin{aligned} \text{axial turbulence intensity, } \sigma_x &= \sqrt{\langle v'_x v'_x \rangle}, \\ \text{radial turbulence intensity, } \sigma_r &= \sqrt{\langle v'_r v'_r \rangle}, \\ \text{tangential turbulence intensity, } \sigma_\theta &= \sqrt{\langle v'_\theta v'_\theta \rangle}, \\ \text{axial-radial Reynolds stress, } \sigma_{xr}^2 &= \langle v'_x v'_r \rangle, \\ \text{turbulent kinetic energy, } \text{TKE} &= \frac{1}{2} (\sigma_x^2 + \sigma_r^2 + \sigma_\theta^2). \end{aligned}$$

The values of the turbulence intensities, the Reynolds stress and the TKE from the simulation are slightly below the experimental measurements. The highest level of turbulence intensity in the simulations can be found in the free shear layer just upstream of the stagnation point ( $x \approx 2.8$ ). This finding is also in agreement with experimental observations. However, the results in the experimental investigations by Dutton and co-workers were obtained for a global Reynolds number  $Re_D = 1,600,000$  and while the Reynolds number of the simulation was  $Re_D = 30,000$ .

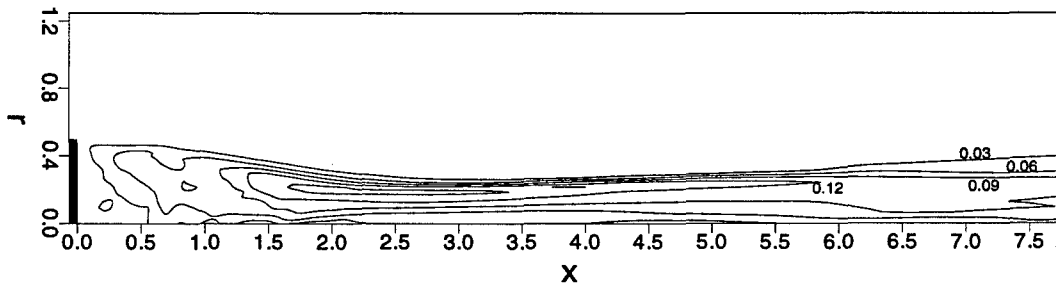


Figure 5.83: Isolines of axial turbulence intensity at  $M_\infty = 2.46$  and  $Re_D = 30,000$  (LES).

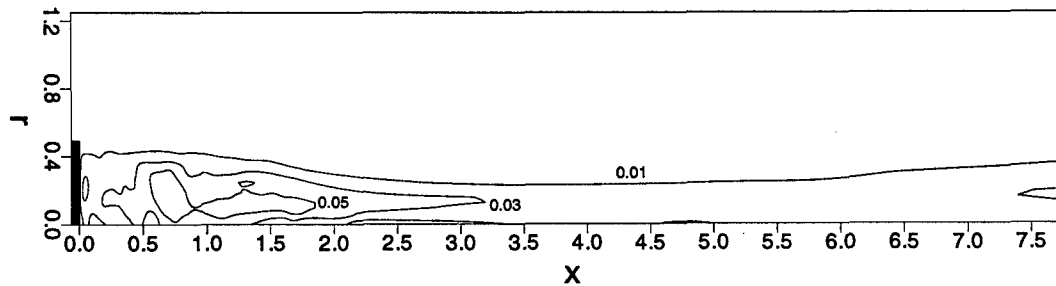


Figure 5.84: Isolines of radial turbulence intensity at  $M_\infty = 2.46$  and  $Re_D = 30,000$  (LES).

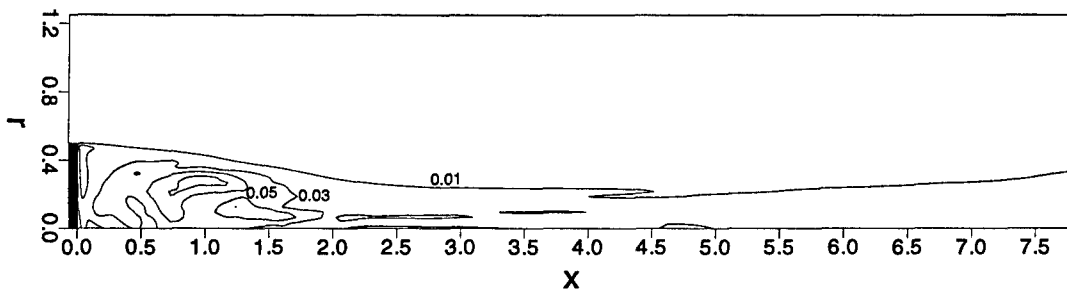


Figure 5.85: Isolines of tangential turbulence intensity at  $M_\infty = 2.46$  and  $Re_D = 30,000$  (LES).

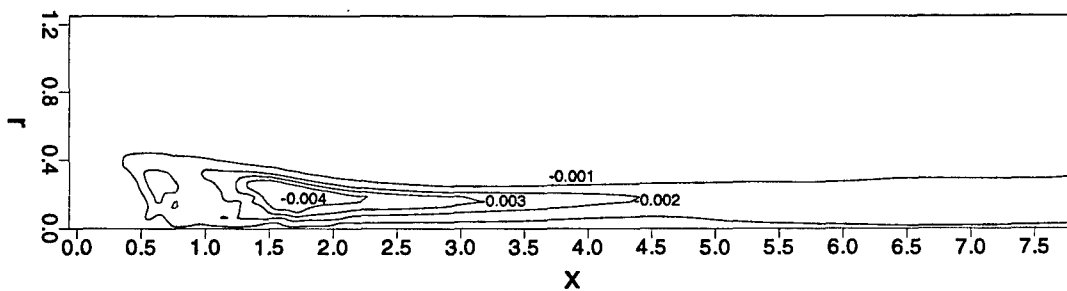


Figure 5.86: Isolines of radial turbulent Reynolds stress at  $M_\infty = 2.46$  and  $Re_D = 30,000$  (LES).

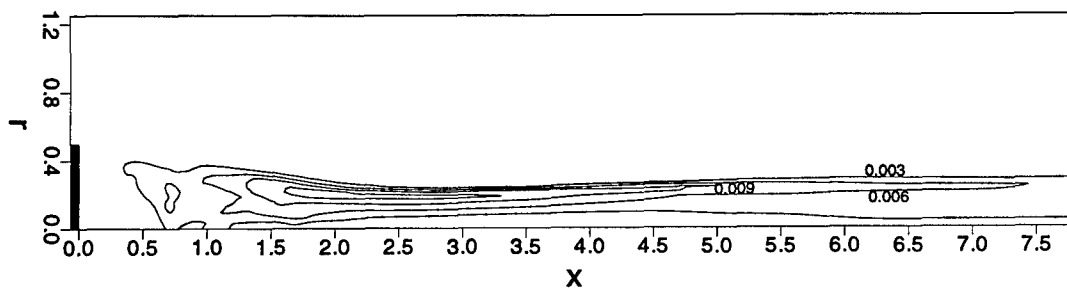


Figure 5.87: Isolines of turbulent kinetic energy at  $M_\infty = 2.46$  and  $Re_D = 30,000$  (LES).

Therefore, other simulations were carried out, where the global Reynolds number was raised to  $Re_D = 100,000$  in order to determine the effect of the global Reynolds number on the flow field behavior. Figure 5.88 shows isolines of instantaneous total vorticity for  $Re_D = 100,000$ . A comparison with figure 5.75 for  $Re_D = 30,000$  shows that more small scale structures appear to be present for the higher Reynolds number case than for the lower Reynolds number case. The time-averaged flow field, which is shown in figures 5.89 through 5.95, is very similar to the flow field at the lower Reynolds number, except that the gradients in the flow field (for example the pressure gradient in the expansion and the recompression region) are more intense for  $Re_D = 100,000$ .

However, at the higher Reynolds number the levels of the RMS values of the turbulence intensities are almost identical with the levels observed in experiments, as shown in figures 5.96 through 5.100, although the Reynolds number in the experiments was considerably larger. The averaged flow field shows a somewhat longer recirculating region than the experimental flow field. This could be a consequence of stronger instabilities in the shear layer for the higher Reynolds number in the experiments. On the other hand, the discrepancy could also be due to the inadequate subgrid-scale model (Smagorinsky, with constant coefficient) and/or insufficient resolution for the calculations of the resolved scale.

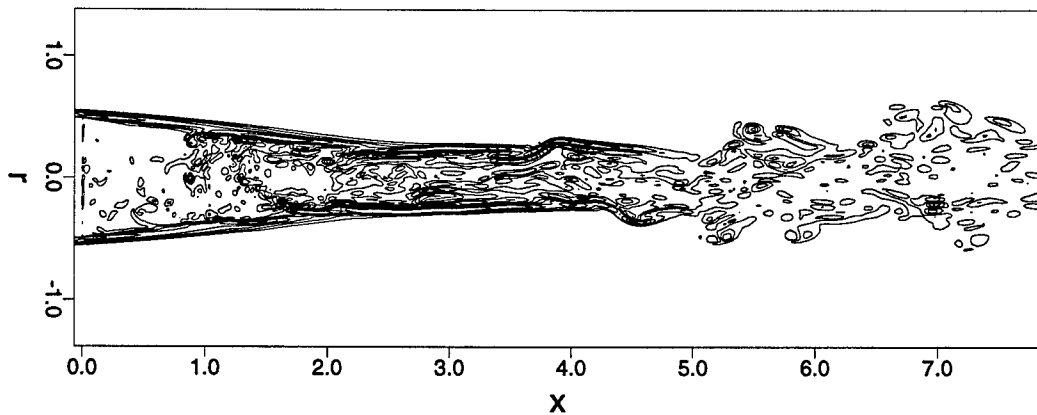


Figure 5.88: Isolines of instantaneous total vorticity for  $M_\infty = 2.46$  and  $Re_D = 100,000$  (LES).

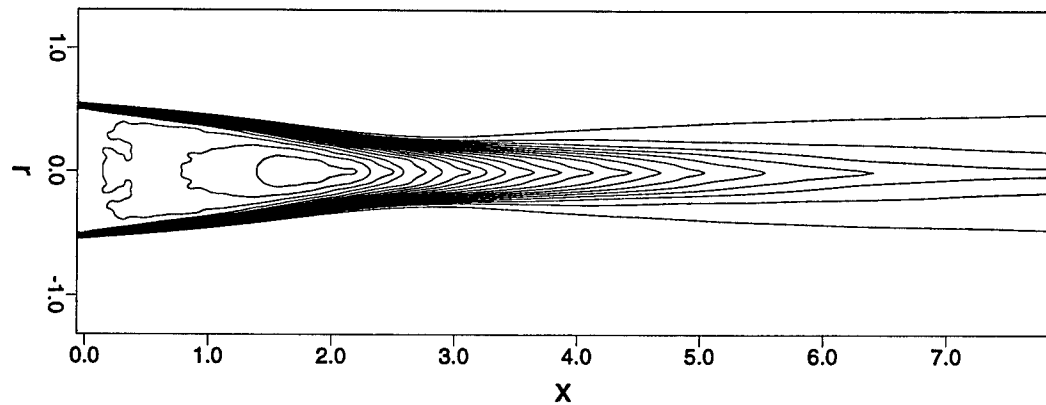


Figure 5.89: Isolines of axial velocity for the time-averaged flow field at  $M_{\infty} = 2.46$  and  $Re_D = 100,000$  (LES).

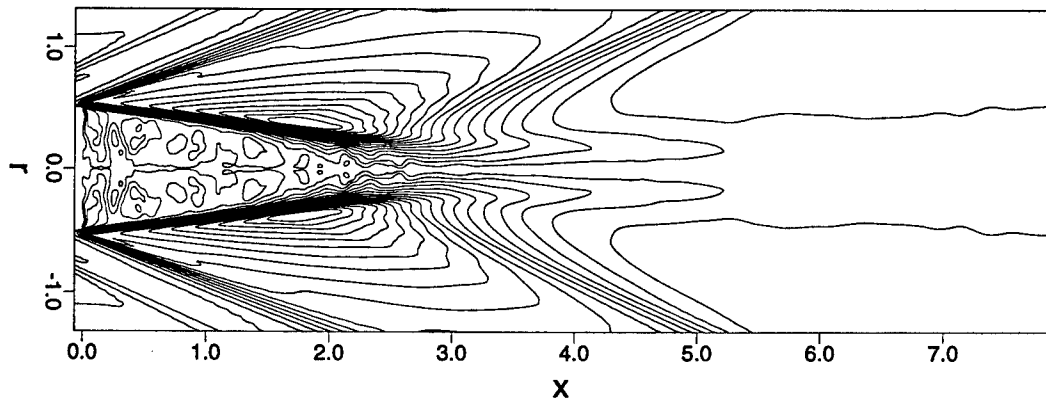


Figure 5.90: Isolines of radial velocity for the time-averaged flow field at  $M_{\infty} = 2.46$  and  $Re_D = 100,000$  (LES).

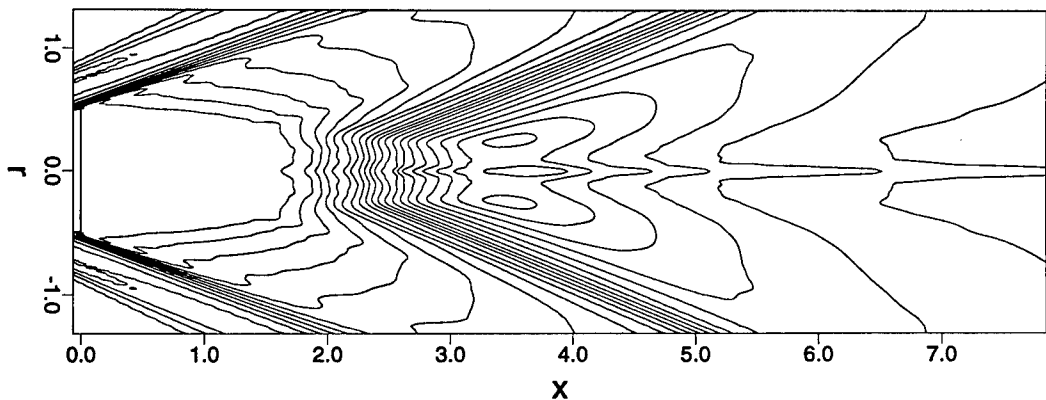


Figure 5.91: Isolines of pressure for the time-averaged flow field at  $M_{\infty} = 2.46$  and  $Re_D = 100,000$  (LES).

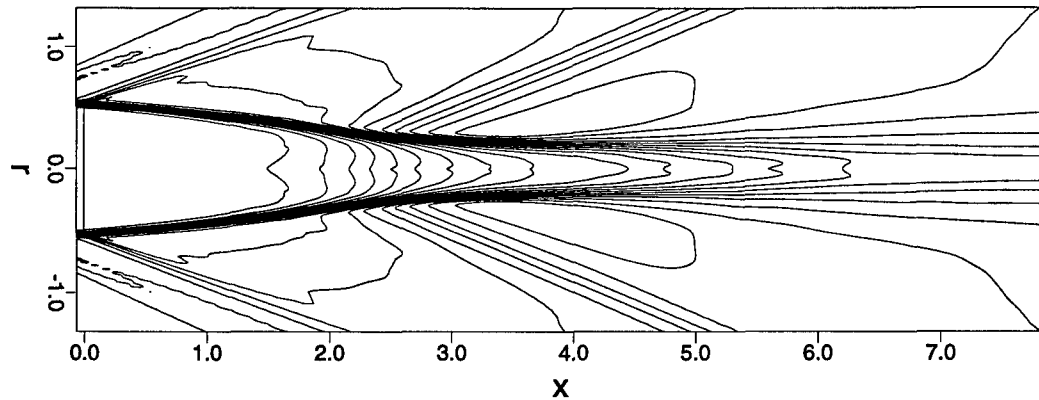


Figure 5.92: Isolines of density for the time-averaged flow field at  $M_\infty = 2.46$  and  $Re_D = 100,000$  (LES).

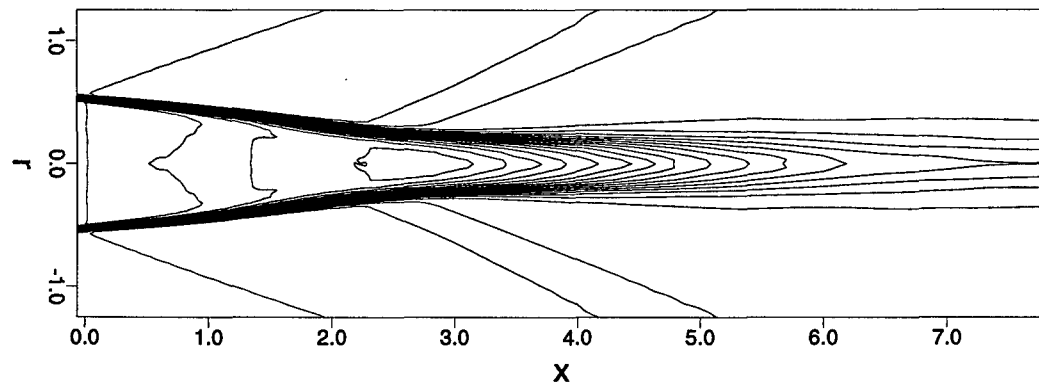


Figure 5.93: Isolines of temperature for the time-averaged flow field at  $M_\infty = 2.46$  and  $Re_D = 100,000$  (LES).

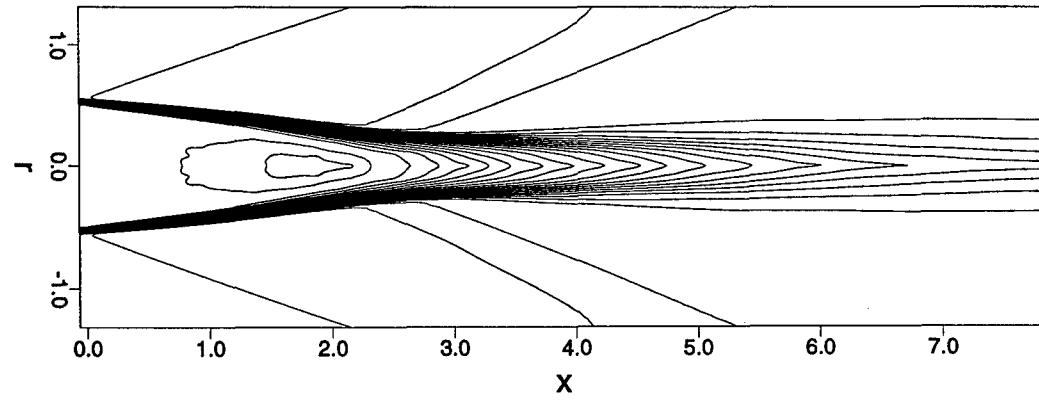


Figure 5.94: Isolines of local Mach number for the time-averaged flow field at  $M_\infty = 2.46$  and  $Re_D = 100,000$  (LES).

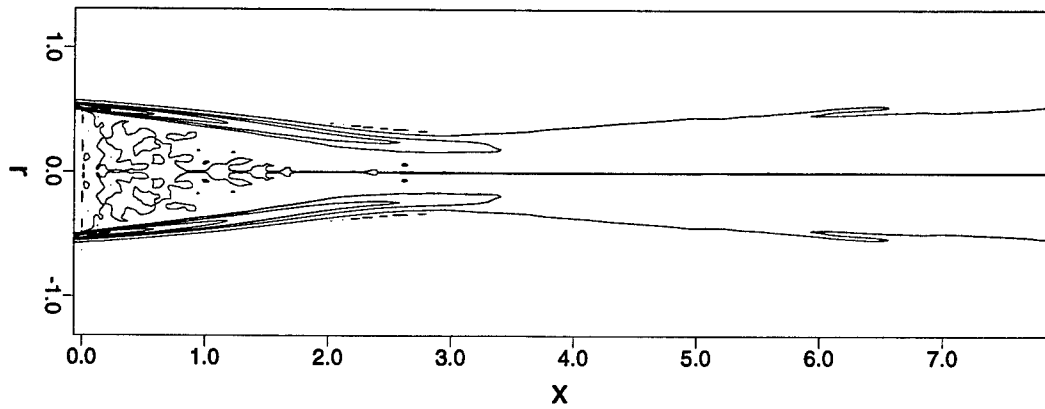


Figure 5.95: Isolines of vorticity for the time-averaged flow field at  $M_\infty = 2.46$  and  $Re_D = 100,000$  (LES).

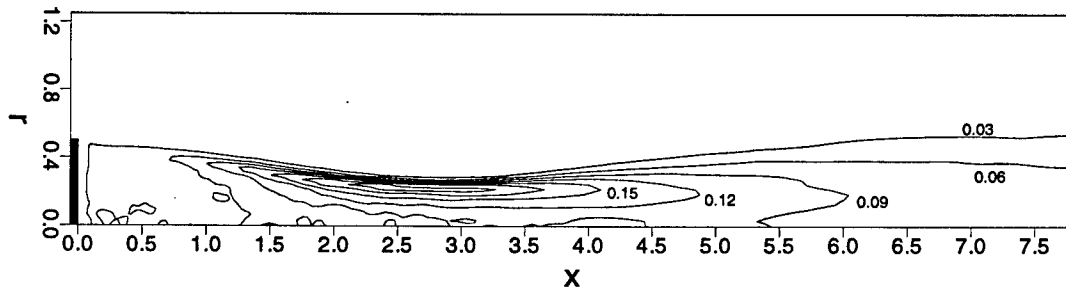


Figure 5.96: Isolines of axial turbulence intensity at  $M_\infty = 2.46$  and  $Re_D = 100,000$  (LES).

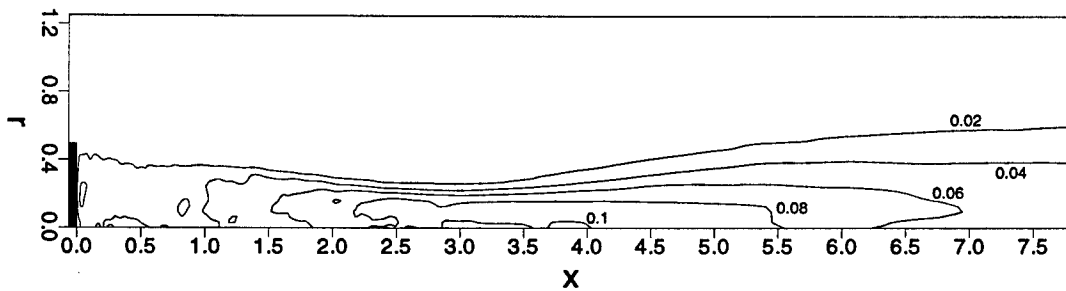


Figure 5.97: Isolines of radial turbulence intensity at  $M_\infty = 2.46$  and  $Re_D = 100,000$  (LES).

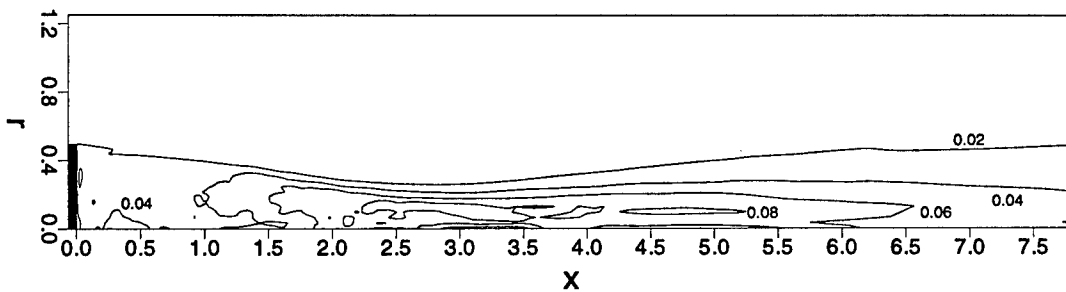


Figure 5.98: Isolines of tangential turbulence intensity at  $M_\infty = 2.46$  and  $Re_D = 100,000$  (LES).

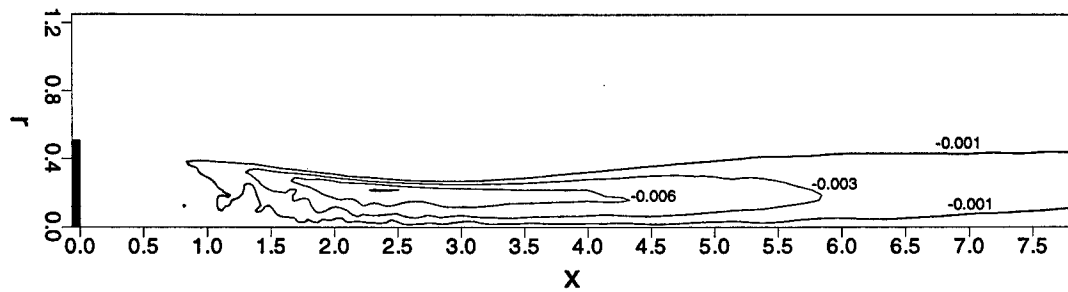


Figure 5.99: Isolines of radial turbulent Reynolds stress at  $M_\infty = 2.46$  and  $Re_D = 100,000$  (LES).

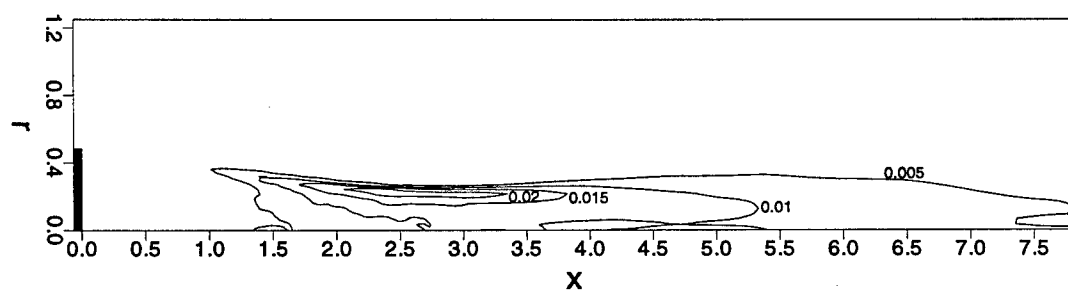


Figure 5.100: Isolines of turbulent kinetic energy at  $M_\infty = 2.46$  and  $Re_D = 100,000$  (LES).

# Chapter 6

## Conclusions

A numerical method has been developed for studying the evolution and propagation of three-dimensional structures in the laminar and the turbulent wake of axisymmetric bluff bodies with a blunt base in supersonic flows. The method is based on the complete compressible Navier-Stokes equations. The equations are solved in a cylindrical coordinate system using finite difference approximations of fourth-order accuracy in the axial and radial directions. In the azimuthal direction a pseudo-spectral method is employed. The method is explicit in time, using a fourth-order accurate Runge-Kutta scheme for the time integration.

Axisymmetric flows have been calculated by solving the axisymmetric Navier-Stokes equations. All axisymmetric flow fields have been found to converge to a steady state. These flow fields are then used as initial conditions for the time-dependent three-dimensional calculations. The evolution of three-dimensional disturbances was investigated by disturbing the axisymmetric flow either through a blowing and suction slot near the base of the body, or by introducing local single pulse disturbances in the flow field.

For code validation, comparison of the results for subsonic calculations was made with water channel experiments and incompressible simulations. It was found that for the absolutely unstable flow at a Reynolds number  $Re_D = 1,000$  the compressible calculations show similar structures as observed in the experiments and the incompressible calculations. For a continuously excited flow field, amplitude distributions of the disturbances in the wake region closely matched those of the water channel experiments.

Direct Numerical Simulations (DNS) were carried out for three different free-stream Mach numbers. Absolute instabilities were observed for the following Mach number – Reynolds number combinations:  $M_\infty = 0.2$  and  $Re_D = 1,000$ ,  $M_\infty = 1.2$  and  $Re_D = 4,000$ , and  $M_\infty = 2.46$  and  $Re_D = 30,000$ . For  $M_\infty = 2.46$ , no absolute instability was found at lower Reynolds numbers ( $Re_D < 30,000$ ). Rather, the flow always returned to the initial axisymmetric steady state. For the three Mach number and Reynolds number combinations shown above, however, the flow deviated from the axisymmetric steady state and reached a state with non-periodic fluctuations. At this point, structures appeared in the flow field, originating near the corner of the blunt base and increasing in strength as they were convected downstream. For all Mach number – Reynolds

number combinations the structures consist of a region of high azimuthal vorticity followed by two regions of axial vorticity of opposite signs (indicating two counter-rotating vortices). For the cases  $M_\infty = 0.2$  and  $M_\infty = 1.2$  the observed structures can be explained by the superposition of two helical modes ( $k = 1$  and  $k = -1$ ). For the higher Mach number case ( $M_\infty = 2.46$ ), however, the vortices are more confined within the shear layer.

The time dependent large structures have a strong influence on the global, time-averaged flow. This can be shown by comparing the time average of the unsteady three-dimensional flow with the initial axisymmetric steady state. For the time-averaged flow the base pressure distribution is almost constant over the radius. In addition, the integral of the base pressure over the entire base area is much lower for the time-averaged flow than for the steady axisymmetric calculations. This indicates that an additional contribution of base drag is added due to the dynamical behavior of the large structures.

For the case of  $M_\infty = 2.46$  and  $Re_D = 30,000$  attempts of DNS were terminated because of lack of resolution in the calculation. Therefore, Large-Eddy Simulations (LES) were employed for this and higher Reynolds numbers. The results of the LES show that dominant large structures exist in the flow, rendering the flow field highly unsteady. However, the evolution of large oscillating structures in the shear layer emanating from the corner appears to be suppressed, possibly due to the inadequacies of the subgrid-scale model used in the LES and/or due to insufficient resolution for the calculation of the resolved scales. For LES at a higher global Reynolds number ( $Re_D = 100,000$ ) turbulence levels are reached that closely match those of the experiments for much larger Reynolds numbers ( $Re_D = 1,600,000$ ) [see, for example, Herrin & Dutton (1994c)].

However, other time-averaged quantities do not agree well with the experimental findings. The length of the recirculating region for the LES calculations is  $L_R \approx 2.8$ , whereas in the experimental investigation it was found to be  $L_R \approx 1.3$  [Herrin & Dutton (1994c)]. In addition, the levels of the kinetic energy and of the Reynolds shear stress in the experiments reveal that the shear layer is highly unstable immediately downstream of the corner. As mentioned above, this instability was also observed in the preliminary DNS for  $Re_D = 30,000$ , but not in the LES calculations. Therefore, further investigations are needed to explore the influence of the subgrid-scale model and/or the resolution used in the calculations.

In general, the results of the simulations indicate that it may be possible to influence the base pressure (i.e. the total aerodynamic drag) of axisymmetric bodies with a blunt base by influencing the generation and/or the dynamics of the large structures. This can be done either by passive means (base bleed, boat-tailing, etc.) which is currently investigated by Dutton and co-workers, or by active means (introducing controlled periodic disturbances).

## Appendix A

# TABLES OF PARAMETERS

Case	Schwarz	A1	A2	A3	A4	A5	A6
$M_\infty$	N/A		0.2		2.46		1.2
$Re_D$			1,000		30,000		4,000
$p_\infty [bar]$	N/A		1.01325		0.3207851		
$T_\infty [K]$	N/A		72.0		133.0		
$c_p \left[ \frac{J}{kgK} \right]$	N/A			1,004.9157			
$Pr$	N/A				0.7		
$\gamma$	N/A				1.4		
$N$	209	112	223	112	640	1279	420
$M$	129	50	99	50	120	239	400
$x_1$			-1.5			-0.71956	-1.5625
$x_N$	5.0		18.15132			14.48345	5.0
$r_M$	4.0		6.2841			6.0435	4.0
$\Delta\xi$	0.03125	0.025	0.0125	0.025	0.004427	0.0022135	0.015625
$\Delta\eta$	0.03125	0.025	0.0125	0.025	0.01	0.005	0.01
$s_x$	1.0		0.4391			0.7	1.0
$s_r$	1.0		0.4			0.3	1.0
$\Delta t$	N/A	0.0014	0.00068	0.0014	0.0019	0.00096	0.0019
$\beta_0$			N/A		1.0		N/A
$A_0$			N/A		0.001		N/A

Table A.1: Parameters for axisymmetric calculations.

	T1	T2	T3	T4	T5
$M_\infty$			0.2		
$Re_D$			1,000		
$p_\infty[\text{bar}]$			1.01325		
$T_\infty[K]$			72.0		
$c_p \frac{\text{J}}{\text{kgK}}$			1004.9157		
$Pr$			0.7		
$\gamma$			1.4		
$N$	112		223	112	
$M$	50		99	50	
$x_1$			-1.5		
$x_N$			18.15132		
$r_M$			6.2841		
$\Delta\xi$	0.025		0.0125	0.025	
$\Delta\eta$	0.025		0.0125	0.025	
$s_x$			0.4391		
$s_r$			0.4		
$\Delta t$	0.0014		0.00068	0.0014	
$k_{\max}$		4		8	
$St_D$	0.0318	$\Delta t$ -Pulse		0.159	
Ampl.	0.001			0.1	

Table A.2: Parameters for three-dimensional subsonic DNS calculations.

	T6	T7
$M_\infty$	1.2	2.46
$Re_D$	4,000	30,000
$p_\infty [bar]$	0.3207851	
$T_\infty [K]$	133.0	
$c_p \frac{J}{kgK}$	1004.9157	
$Pr$	0.7	
$\gamma$	1.4	
$N$	420	640
$M$	400	120
$x_1$	-0.71956	-1.5625
$x_N$	5.0	14.48345
$r_M$	4.0	6.0435
$\Delta\xi$	0.015625	0.004427
$\Delta\eta$	0.01	0.01
$s_x$	1.0	0.7
$s_r$	1.0	0.3
$\Delta t$	0.0019	0.0019
$k_{\max}$	4	8
$St_D$	$\Delta t$ -Pulse	
Ampl.	0.0001	

Table A.3: Parameters for three-dimensional supersonic DNS calculations.

## Appendix B

# FREE STREAM BOUNDARY CONDITIONS

The boundary conditions at the free-stream boundary are discussed in detail in Harris(1995). The equations change only slightly for the axisymmetric coordinate system used here. Depending on the free stream Mach number ( $M_\infty$ ), three different kinds of boundary conditions are considered:

$$M_\infty < 1 \quad : \quad \text{subsonic boundary conditions}, \quad (\text{B.1})$$

$$M_\infty = 1.2 \quad : \quad \text{characteristic boundary conditions}, \quad (\text{B.2})$$

$$M_\infty = 2.46 \quad : \quad \text{Thompson boundary conditions}. \quad (\text{B.3})$$

The three different methods are described in detail in the next sections.

### B.1 Subsonic Boundary Conditions

For subsonic flow fields, where the local Mach number at the free stream is always less than one, the flow field is assumed to have reached nearly axisymmetric state. Therefore, derivatives in radial direction of any flow variable are neglected. This leads to the following boundary conditions:

$$\frac{\partial}{\partial r} [v_x] = 0. \quad (\text{B.4})$$

From continuity it follows that

$$\frac{\partial}{\partial r} [rv_r] = 0. \quad (\text{B.5})$$

### B.2 Characteristic Boundary Conditions

The second free-stream boundary condition (referred to hereafter as the Characteristic Boundary Condition) is applied when the free stream Mach number is  $M_\infty = 1.2$ . For steady, isentropic

two-dimensional flow,

$$\frac{\partial \phi}{\partial \vec{c}} = 0 \quad (\text{B.6})$$

is used for all variables, where  $\vec{c}$  is the outward-travelling characteristic direction along the Mach angle. Corrected for flow direction, the angle of the characteristic is given at the upper free stream by

$$\mu_{n+1}^{i,J} = \sin^{-1} \left( \frac{1}{M_n^{i,J}} \right) + \tan^{-1} \left( \frac{v_n^{i,J}}{u_n^{i,J}} \right), \quad (\text{B.7})$$

where the local Mach number is

$$M_n^{i,J} = \frac{M}{\sqrt{T_n^{i,J}}} \left[ (u_n^{i,J})^2 + (v_n^{i,J})^2 \right]^{1/2}. \quad (\text{B.8})$$

The  $w$ -terms are not included because the flow is presumably (for each  $l$ -plane) steady and axisymmetric, thus  $w = 0$ . The values of  $u, v, w, T$ , and  $\rho$  are thus found using

$$\phi^{i,J} = 2\phi^{i_{c1},J-1} - \phi^{i_{c2},J-2}, \quad (\text{B.9})$$

where  $(i_{c1}, J - 1)$  and  $(i_{c2}, J - 2)$  are backward locations along  $\vec{c}$ , starting from  $(i, J)$ . The values at those locations are found by linear interpolation of the values at surrounding points, e.g., with  $i_{ca} \leq i_{c1} \leq i_{cb}$ ,

$$\phi^{i_{c1},J-1} = (1 - \alpha)\phi^{i_{ca},J-1} + \alpha\phi^{i_{cb},J-1}. \quad (\text{B.10})$$

### B.3 Thompson Boundary Conditions

The third free-stream boundary conditions used were suggested by Thompson [1987]. Here, the integration is extended to the boundary itself, where the integration in the radial direction is done in a manner which should allow disturbances to move out of, but not into the domain.

The method is described in detail in Harris (1995). It is based on the fact that information can travel along the outgoing characteristic, but is not allowed to propagate along the incoming characteristic. Thus, only outgoing information is allowed at the free stream boundary. Therefore, a special treatment is required for the convective terms in the radial direction, while for the viscous terms one-sided differences are applied for derivatives with respect to  $r$ .

This condition was found to lead to reflections of waves for subsonic and slightly supersonic flows. Only for a free stream Mach number of  $M_\infty = 2.46$  no reflections could be observed. For this reason, this boundary condition was only applied for that particular free stream Mach number. For the  $M_\infty = 1.2$  case the Characteristic Boundary Conditions were employed (see section B.2).

## Appendix C

# BOUNDARY CONDITIONS AT THE AXIS OF SYMMETRY

The boundary conditions at the symmetry axis are non-physical and appear in the numerical scheme because of the Fourier decomposition of the flow variables in circumferential direction ( $\theta$ ). The conditions are independent of time. Therefore the time indices are dropped in the following derivation.

The derivation of the boundary condition is similar to the one for incompressible computation as shown for example in Tourbier (1991). For the cylindrical coordinate system  $(x, r, \theta)$  the axis ( $r = 0$ ) forms a singularity, that needs special treatment in the numerical scheme. This results mainly in the treatment of vectors, that are non-parallel to the axis and terms with division by the radial coordinate ( $r$ ).

### a) Velocity Vector at the Axis

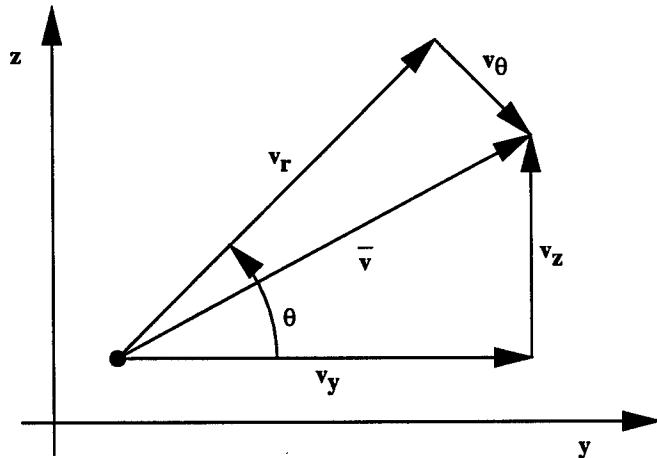


Figure C.1: Decomposition of the velocity vector within the field.

The velocity vector  $(v_x, v_r, v_\theta)$  is related to the cartesian velocity vector  $(v_x, v_y, v_z)$  as follows:

$$v_x = v_x, \quad (C.1)$$

$$v_r = v_y \cos \theta + v_z \sin \theta, \quad (C.2)$$

$$v_\theta = -v_y \sin \theta + v_z \cos \theta, \quad (C.3)$$

or

$$v_x = v_x, \quad (C.4)$$

$$v_y = v_r \cos \theta - v_\theta \sin \theta, \quad (C.5)$$

$$v_z = v_r \sin \theta + v_\theta \cos \theta. \quad (C.6)$$

The Fourier decomposition of the velocity vector components yields

$$v_x(x, r, \theta) = \sum_{k=-K}^K \hat{v}_{x,k}(x, r) e^{ik\theta}, \quad (C.7)$$

$$v_r(x, r, \theta) = \sum_{k=-K}^K \hat{v}_{r,k}(x, r) e^{ik\theta}, \quad (C.8)$$

$$v_\theta(x, r, \theta) = \sum_{k=-K}^K \hat{v}_{\theta,k}(x, r) e^{ik\theta}. \quad (C.9)$$

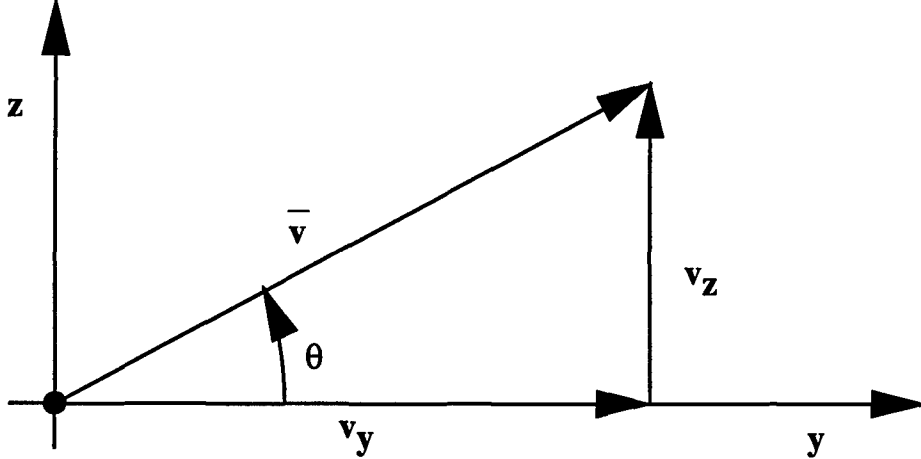


Figure C.2: Decomposition of the velocity vector at the axis of symmetry.

At the axis ( $r = 0$ ) all angles ( $\theta$ ) belong physically to the same point ( $y, z$ ) and to unique values of  $v_y$  and  $v_z$ . In addition, all scalar values as well as the axial velocity component ( $v_x$ ) are the same for all angles ( $\theta$ ). Therefore for all scalar fields and the axial velocity component:

$$\hat{\rho}_0(x, 0) \neq 0, \quad (C.10)$$

$$\hat{T}_0(x, 0) \neq 0, \quad (C.11)$$

$$\hat{p}_0(x, 0) \neq 0, \quad (C.12)$$

$$\hat{e}_0(x, 0) \neq 0, \quad (C.13)$$

$$\hat{v}_{x,0}(x, 0) \neq 0, \quad (C.14)$$

and

$$\hat{\rho}_k(x, 0) = 0, \quad (C.15)$$

$$\hat{T}_k(x, 0) = 0, \quad (C.16)$$

$$\hat{p}_k(x, 0) = 0, \quad (C.17)$$

$$\hat{e}_k(x, 0) = 0, \quad (C.18)$$

$$\hat{v}_{x,k}(x, 0) = 0, \quad (C.19)$$

for  $k \neq 0$ .

The radial and the azimuthal component of the velocity vector at the axis are represented by

$$v_r(x, 0, \theta) = \sum_{k=-K}^K \hat{v}_{r,k}(x, 0) [\cos(k\theta) + i \sin(k\theta)], \quad (C.20)$$

$$v_\theta(x, 0, \theta) = \sum_{k=-K}^K \hat{v}_{\theta,k}(x, 0) [\cos(k\theta) + i \sin(k\theta)]. \quad (C.21)$$

Since the functions  $\sin(k\theta)$  and  $\cos(k\theta)$  build an orthogonal basis, it follows, that only the Fourier components  $k = 1$  and  $k = -1$  can be non-zero when comparing the components to equation C.5. Therefore,

$$v_r(x, 0, \theta) = [\hat{v}_{r,1}(x, 0) + \hat{v}_{r,-1}(x, 0)] \cos \theta [\hat{v}_{r,1}(x, 0) - \hat{v}_{r,-1}(x, 0)] \sin \theta, \quad (C.22)$$

$$v_\theta(x, 0, \theta) = [\hat{v}_{\theta,1}(x, 0) + \hat{v}_{\theta,-1}(x, 0)] \cos \theta [\hat{v}_{\theta,1}(x, 0) + \hat{v}_{\theta,-1}(x, 0)] \cos \theta. \quad (C.23)$$

Combining these results leads to the final conditions for the radial and the azimuthal velocity components at the symmetry axis:

$$\hat{v}_{r,1}(x, 0) + \hat{v}_{\theta,1}(x, 0) = 0, \quad (C.24)$$

$$\hat{v}_{r,-1}(x, 0) - \hat{v}_{\theta,-1}(x, 0) = 0. \quad (C.25)$$

### b) Treatment of the Division by $r$ Near the Axis

For the division by  $r$  at the axis of symmetry the rule of l'Hopital was applied. For the example of the term  $\frac{v_r}{r}$  this leads to

$$\lim_{r \rightarrow 0} \frac{v_r}{r} = \frac{\partial v_r}{\partial r} \quad (C.26)$$

This rule can be applied, as long as the numerator vanishes at  $r = 0$ .

# Bibliography

- [Addy (1970)] Addy, A.L., 1970, "Experimental-Theoretical Correlation of Supersonic Jet-on Base Pressure for Cylindrical Afterbodies", *Journal of Aircraft*, Vol. 7, No. 5, pp. 474-477.
- [Avidor & Schneiderman (1975)] Avidor, J.M. & Schneiderman, A.M., 1975, "Experimental Investigation of High Reynolds Number Compressible Axisymmetric Turbulent Wakes", *AIAA Journal*, Vol. 13, No. 4, pp. 485-489.
- [Bachman (1996)] Bachman, C., 1996, Private Communication, University of Arizona.
- [Bird et al. (1960)] Bird, R.B., Stewart, W.E., and Lightfoot, E.N., 1960, *Transport Phenomena*, John Wiley & Sons Inc..
- [Bowman & Clayden (1968)] Bowman, W.C. & Clayden, W.A., 1968, "Boat-Tailed Afterbodies at M=2 With Gas Ejection", *AIAA Journal*, Vol. 6, p. 2029.
- [Chapman (1951)] Chapman, D.R., 1950, "An Analysis of Base Pressure at Supersonic Velocities and Comparison with Experiment", NACA Report 1051.
- [Chen et al. (1989)] Chen, J.H., Cantwell, B.J. and Mansour, N.N., 1989, "Direct Numerical Simulations of a Plane Compressible Wake: Stability, Vorticity Dynamics, and Topology", Report No. TF-46, Thermosciences Division, Department of Mechanical Engineering, Stanford University, Stanford, CA.
- [Chen et al. (1990)] Chen, J.H., Cantwell, B.J. and Mansour, N.N., 1990, "The effect of Mach number on the stability of a plane supersonic wake", *Physics of Fluids A*, Vol. 2, No. 6.
- [Clayden & Bowman (1968)] Clayden, W.A. & Bowman, J.E., 1968, "Cylindrical Afterbodies at M=2 With Hot Gas Ejection", *AIAA Journal*, Vol. 6, p. 2429.
- [Cortwright & Schroeder (1951)] Cortwright, E.M. & Schroeder, A.H., 1951, "Preliminary Investigation of Effectiveness of Base Bleed in Reducing Drag of Blunt-Base Bodies in Supersonic Stream", NACA RM E51A26.

- [Danberg & Nietubicz (1992)] Danberg, J.E. & Nietubicz, C.J., 1992, "Predicted Flight Performance of Base-Bleed Projectiles", *Journal of Spacecraft and Rockets*, Vol. 29, p. 366.
- [Dayman (1963)] Dayman, B., Jr., 1963, "Support Interference Effects on the Supersonic Wake", *AIAA Journal*, Vol. 1, No. 8, pp. 1921-1923.
- [Demetriades (1968)] Demetriades, A., 1968, "Turbulence Measurements in an Axisymmetric Compressible Wake", *Physics of Fluids*, Vol. 11, p. 1841.
- [Ding et al. (1992)] Ding, Z., Chen, S., Liu, Y., Luo, R., & Li, J., 1992, "Wind Tunnel Study of Aerodynamic Characteristics of Base Combustion", *Journal of Propulsion and Power*, Vol. 8, p. 630.
- [Donaldson (1955)] Donaldson, I.S. , 1955, "The Effect of Sting Supports on the Base Pressure of a Blunt-Based Body in a Supersonic Stream", *The Aeronautical Quarterly*, Vol. 6, pp. 221-229.
- [Dutton & Addy (1993)] Dutton, J.C. & Addy, A.L., 1991, "Fluid Dynamic Mechanisms and Interactions Within Separated Flows", Final Tech. Rept., UILU-ENG 93-4019, University of Illinois, Urbana-Champaign.
- [Erlebacher et al. (1992)] Erlebacher, G., Hussaini, M. Y., Speziale, C. G., & Zang, T. A., 1992, "Toward the large-eddy simulation of compressible turbulent flows", *Journal of Fluid Mechanics*, Vol. 238, pp. 155-185.
- [Ferziger (1981)] Ferziger, J.H., 1981, *Numerical Methods for Engineering Application*, John Wiley & Sons, Inc., NY.
- [Ghosal & Moin (1993)] Ghosal, S. & Moin, P., 1993, "The basic equations for the large eddy simulation of turbulent flows in complex geometry", Center for Turbulence Research Manuscript 143.
- [Hannemann & Oertel (1989)] Hannemann, K. & Oertel, H., Jr., 1989, "Numerical Simulation of the Absolute and Convectively Unstable Wake", *Journal of Fluid Mechanics*, Vol. 199, p. 55.
- [Harris] Harris, P., 1996, Master's Report, University of Arizona.
- [Herrin & Dutton (1991)] Herrin, J.L. & Dutton, J.C., 1991, "An Experimental Investigation of the Supersonic Axisymmetric Base Flow Behind a Cylindrical Afterbody", Tech. Rep. UILU 91-4004, University of Illinois at Urbana-Champaign.

- [Herrin & Dutton (1994a)] Herrin, J.L. & Dutton, J.C., 1994a, "Effect of a Rapid Expansion on the Development of Compressible Free Shear Layers", *AIAA Paper* 94-2229.
- [Herrin & Dutton (1994b)] Herrin, J.L. & Dutton, J.C., 1994b, "Effects of Afterbody Boattailing on the Near-Wake of Axisymmetric Bodies in Supersonic Flow", *AIAA Paper* 94-0029.
- [Herrin & Dutton (1994c)] Herrin, J.L. & Dutton, J.C., 1994c, "Supersonic Base Flow Experiments in the Near Wake of a Cylindrical Afterbody", *AIAA Journal*, Vol. 32, p. 77.
- [Hubbartt et al. (1981)] Hubbartt, J.E., Strahle, W.C., & Neale, D.H., 1981, "Mach 3 Hydrogen External/Base Burning", *AIAA Journal*, Vol. 19, p. 745.
- [Huerre & Monkewitz (1990)] Huerre, P. & Monkewitz, P.A., 1990, "Local and Global Instabilities in Spatially Developing Flows", *Annual Review of Fluid Mechanics*, Vol. 22, p. 473.
- [Israel (1996)] Israel, D., 1996, Private Communication.
- [Korst (1956)] Korst, H.H., 1956, "A Theory for Base Pressures in Transonic and Supersonic Flow", *Journal of Applied Mechanics*, Vol. 23, No. 4, pp. 593-600.
- [Lele (1992)] Lele, S.K., 1992, "Compact Finite Difference Schemes with Spectral-like Resolution", *Journal of Computational Physics*, Vol. 103, pp. 64-42.
- [Marasli et al. (1989)] Marasli, B., Champagne, F.H., & Wygnanski, I., 1989, "Modal Decomposition of Velocity Signals in a Plane Turbulent Wake", *Journal of Fluid Mechanics*, Vol. 198, p. 255.
- [Mathur & Dutton (1995)] Mathur, T. & Dutton, J.C., 1995, "Base Bleed Experiments With a Cylindrical Afterbody in Supersonic Flow", *AIAA Paper* 95-0062.
- [Mathur & Dutton (1996a)] Mathur, T. & Dutton, J.C., 1996a, "Base Bleed Experiments With a Cylindrical Afterbody in Supersonic Flow", *Journal of Spacecraft and Rockets*, Vol. 33, p. 30.
- [Mathur & Dutton (1996b)] Mathur, T. & Dutton, J.C., 1996b, "Velocity and Turbulence Measurements in a Supersonic Base Flow With Mass Bleed", *AIAA Journal*, Vol. 34, p. 1153.

- [Neale et al.(1978)] Neale, D.H., Hubbartt, J.E., Strahle, W.C., & Wilson, W.W., 1978, "Effects of External Compression on an Axisymmetric Turbulent Near Wake", *AIAA Journal*, Vol. 16, No. 9, pp. 940-947.
- [MacCormack (1969)] MacCormack, R.W., 1969, "The Effect of Viscosity in Hypervelocity Impact Cratering", *AIAA Paper* 69-354.
- [McDonald (1965)] McDonald, H., 1965, "An Analysis of the Turbulent Base Pressure Problem in Supersonic Axisymmetric Flow", *The Aeronautical Quarterly*, Vol. 16, pp. 97-121.
- [Mueller (1968)] Mueller, T.J., 1968, "Determination of the Turbulent Base Pressure in Supersonic Axisymmetric Flow", *Journal of Spacecraft and Rockets*, Vol. 5, No. 1, pp. 101-107.
- [Nietubicz & Sturek (1988)] Nietubicz, C.J. & Sturek, W.B., 1988, "Navier-Stokes Code Verification for Projectile Configurations at Supersonic and Transonic Velocities", *AIAA Paper* 88-1995.
- [Putnam & Bissinger (1985)] Putnam, L.E. & Bissinger, N.C., 1985, "Results of AGARD Assessment of Prediction Capabilities for Nozzle Afterbody Flows", *AIAA Paper* 85-1464.
- [Reid & Hastings (1959)] Reid, J. & Hastings, R.C., 1959, "The Effect of a Central Jet on the Base Pressure of a Cylindrical Afterbody in a Supersonic Stream", Reports and Memoranda No. 3224, Aeronautical Research Council, Great Britain.
- [Rollstin (1987)] Rollstin, L., 1987, "Measurement of Inflight Base-Pressure on an Artillery-Fixed Projectile", *AIAA Paper* 87-2427.
- [Sahu (1992)] Sahu, J., 1992, "Numerical Computations of Supersonic Base Flow with Special Emphasis on Turbulence Modeling", *AIAA Paper* 92-4352.
- [Sahu & Heavey (1995)] Sahu, J. & Heavey, K.R., 1995, "Numerical Investigation of Supersonic Base Flow With Base Bleed", *AIAA Paper* 95-3459.
- [Sahu & Nietubicz (1984)] Sahu, J. & Nietubicz, C.J., 1984, "Numerical Computations of Base Flow for a Missile in the Presence of a Centered Jet", *AIAA Paper* 84-0527.
- [Sahu et al. (1985)] Sahu, J., Nietubicz, C.J., & Steger, J.L., 1985, "Navier-Stokes Computations of Projectile Base Flow With and Without Mass Injection", *AIAA Journal*, Vol. 23, p. 1348.

- [Sullins et al. (1982)] Sullins, G.A., Anderson, J.D., Jr., & Drummond, J.P., 1982, "Numerical Investigation of Supersonic Base Flow with Parallel Injection", *AIAA Paper 82-1001*.
- [Schwarz (1996)] Schwarz, V., 1996, "Numerische Untersuchungen zur Instabilität eines rotationssymmetrischen Körpers mit stumpfem Heck", Dissertation, Universität Stuttgart, Germany.
- [Schwarz et al. (1994)] Schwarz, V., Bestek, H., & Fasel, H.F., 1994, "Numerical Simulation of Nonlinear Waves in the Wake of an Axisymmetric Bluff Body", *AIAA Paper 94-2285*.
- [Siegel (1996)] Siegel, S., 1996, Private Communication, University of Arizona.
- [Siegel (1994)] Siegel, S., 1994, "Completion and Optimization of an Open Water Channel and Investigations of the Wake Behind and Axisymmetric Bluff Body", Diplomarbeit, Universität Stuttgart.
- [Smagorinsky (1963)] Smagorinsky, J., 1963, "General circulation experiments with the primitive equations", *Mon. Weather Review*, Vol. 91, pp. 99-165.
- [Smith & Dutton (1996)] Smith, K.M. & Dutton, J.C., 1996, "Investigation of Large-Scale Structures in Supersonic Planar Base Flows", *AIAA Journal*, Vol. 34, p. 1146.
- [Speziale (1996)] Speziale, C.G., 1996, Private Communication, Boston University.
- [Thompson (1987)] Thompson, K.W., 1987, "Time Dependent Boundary Conditions for Hyperbolic Systems", *Journal of Computational Physics*, Vol. 68, pp. 1-24.
- [Thumm (1991)] Thumm, A., 1991, "Numerische Untersuchungen zum laminar-turbulenten Strömungsumschlag in transsonischen Grenzschichtströmungen", Dissertation, Universität Stuttgart, Germany.
- [Toubier (1991)] Toubier, D., 1991, "Numerical Investigation of the Spatial Stability of an Axisymmetric Jet by Solving of the Full Navier-Stokes Equations", Diplomarbeit, Universität Stuttgart, Germany.
- [Toubier & Fasel (1994)] Toubier, D. & Fasel, H.F., 1994, "Numerical Investigation of Transitional Axisymmetric Wakes at Supersonic Speeds", *AIAA Paper 94-2286*.
- [Valentine & Przirembel (1970)] Valentine, D.T. & Przirembel, C.E.G., 1970, "Turbulent Axisymmetric Near-Wake at Mach Four with Base Injection", *AIAA Journal*, Vol. 8, No. 2, pp. 2279-2280.

- [White (1991)] White, F.M., 1991, *Viscous Fluid Flow*, McGraw-Hill.
- [Wygnanski (1994)] Wygnanski, I., 1994, "The Control of Separation by Periodic Oscillation", *AIAA Paper 94-2608* [invited].
- [Zang et al. (1992)] Zang, T. A., Dahlburg, R. B., & Dahlburg, J. P., 1992, "Direct and large-eddy simulations of three-dimensional compressible Navier-Stokes turbulence", *Physics of Fluids A*, Vol. 4, pp. 127-140.